The geochemistry and geochronology of Quaternary collision-related volcanism in the southern Lesser Caucasus: from development of the mantle source to magma generation and eruption

Patrick James Sugden

Submitted in accordance with the requirements for the degree of
Doctor of Philosophy

The University of Leeds

School of Earth and Environment

October, 2019

The candidate confirms that the work submitted is his own, except where work which has formed part of jointly-authored publications has been included. The contribution of the candidate and the other authors to this work has been explicitly indicated below. The candidate confirms that appropriate credit has been given within the thesis where reference has been made to the work of others.

The work in Chapter 3 of the thesis has appeared in publication as follows:

Sugden, P. J., Savov, I. P., Wilson, M., Meliksetian, K., Navasardyan, G., & Halama, R. (2019). The Thickness of the Mantle Lithosphere and Collision-Related Volcanism in the Lesser Caucasus. *Journal of Petrology*, *60*(2), 199-230.

The candidate was responsible for some of the field sampling in September 2015, sample preparation (rock crushing), Sr-Nd isotope analysis and all written text. All ideas presented as new are the candidate's own.

The contribution of the other authors were in: repeated field campaigns between 2004 and 2013; Savov assisted in the preparation of some of these older samples (rock crushing); Savov analysed a small number of the samples for Sr-Nd isotopes; Major and trace element analyses were performed externally at ACME labs, Vancouver, Canada; Navasardyan and co-workers produced the geological map in Figure 4 of the publication.

Acknowledgements

This research has been carried out by a team which has included *Ivan Savov, Marjorie Wilson, Khachatur Meliksetian, Ralf Halama, Gevorg Navasardyan, Samuele Agostini and Dan Barfod.* My own contributions, fully and explicitly indicated in the thesis, have been: (i) taking part in sample collection fieldtrips in 2015 and 2017; (ii) preparing samples from the 2012, 2013, 2015 and 2017 field campaigns for geochemical analysis (rock crushing); (iii) preparing samples for thin sectioning; (iv) strontium and neodymium cation column chemistry; (v) preparing and loading samples onto metal filaments for Sr-Nd isotope analysis; (vi) analysing samples for Sr-Nd isotope ratios on the Triton Thermal Ionisation Mass Spectrometer at University of Leeds; (vii) performing all geochemical calculations and modelling presented in this thesis; (viii) preparing samples for boron isotope analysis at IGG-CNR Pisa using cation and anion exchange columns; (ix) sample preparation for Ar-Ar dating, including rock crushing, magnetic separation, density separation, leaching and hand picking; (x) petrographic imaging of volcanic rocks using both traditional petrographic polarising microscope and the scanning electron microscope at the University of Leeds; (xi) electron probe microanalysis of amphibole and clinopyroxene phenocrysts to measure their major element composition.

The other members of the group and their contributions have been as follows: *Ivan Savov* has worked on all field campaigns from 2004 to 2017, and has prepared samples collected 2004-2010 for geochemical analysis, as well as analysing the Gegham obsidians and Tezhsar alkaline complex samples for B and $\delta^{11}B$ in Pisa; *Marjorie Wilson* has supported Ivan Savov in supervising the candidate's PhD project and providing comments and advice at every stage of the project; *Khachatur Meliksetian* has worked on all field campaigns from 2004 to 2017, providing in depth knowledge of the local geology; *Ralf Halama* provided comments on the Journal of Petrology manuscript which is included here as Chapter 3, as well as providing comments and feedback on Chapter 4; *Gevorg Navasardyan* worked using GIS software, remote sensing and extensive fieldwork to produce the Geological map of Syunik volcanic highland which was adapted for this thesis in Chapters 2 and 5; *Samuele Agostini* conducted boron isotope analyses using the Neptune series multi-collector (MC) inductively coupled plasma mass spectrometer (ICP-MS) at IGG-Pisa; *Dan Barfod* packaged samples for irradiation and then carried out argon isotope analysis at the Scottish Universities Environmental Research centre, before using the in-house software package to calculate the ages presented in Chapter 5.

The 4 years I have spent as a PhD student have been a unique and often rewarding time. While this thesis is the culmination of 4 years of my own struggles and successes, none of it would have been possible without a whole range of people I have tried to thank below. Sincerest apologies if anyone was left off.

First of all, I must thank Ivan Savov and Marjorie Wilson for all their help over these past 4 years in the various aspects of work which have culminated in this thesis. Quite simply, none of it would have been possible without their time, patience and engagement in the project. In particular, I would like to thank them for repeatedly prioritising my various manuscripts and always providing punctual and detailed comments, despite their busy and varied schedules. Thank you Ivan for all that energy, enthusiasm and support in the field, in the lab, at conferences and in science generally. Thanks to Marge for passing on some of that far-reaching experience in igneous petrology, scientific publishing and much else besides. Thanks also for those trips to the Fav and Weetwood Hall, they were some of the most pleasant and enjoyable supervision meetings I ever had!

A mention has to go out to my Armenian colleagues- Khachatur Meliksetian, Gevorg Navasardyan, Edmond Grigoryan and Davit Manucharyan. Without their help and in-depth knowledge of the local geology it would be impossible to have such successful field trips to their beautiful country. Special thanks must go to Gevorg, for all the work he has done to produce the geological map of the Syunik volcanic highland (adapted for Chapters 2 and 4). I must also thank Edmond for opening up his home to me in 2017, while we prepared to head out into the field.

I would like to thank Jason Harvey and Bob Cliff of the University of Leeds for all their help in showing me the ropes of column chemistry and thermal ionisation mass spectrometry. I spent very many long hours in that lab, but Jason and Bob made sure I had some good data to play with at the end of it all. Thank you also to Richard Walshaw for all his help in electron probe micro-analysis.

Samuele Agostini and the others at IGG-CNR-Pisa deserve thanks for all the training they provided in boron isotope analysis, and for showing me their beautiful city (and fantastic pizza). Similarly, Dan Barfod provided me with excellent support at SUERC as I found my feet in preparing samples for Ar-Ar dating.

I would like to thank the Geochemistry Special Interest Group and the Institute of Geophysics and Tectonics for their financial support which allowed me to attend some of the largest international conferences in geoscience- AGU and EGU. Thank you to all the people who stopped for chats about volcanoes, Armenia, and much else besides at both of these conferences.

To the other PhD students I have had the pleasure of knowing and working with these past few years, thank you for being such great colleagues. Special thanks go to Lubka, Eduardo and Autumn for all their advice on labwork, petrology and all things boron!

Personal “thank you”s must go to my housemates Beth, Josh and Louise who have helped keep me sane, and made my time at Leeds a happy one which I will look back on with fond memories. Thanks also to Linda for all the pep talks when being a PhD student was not so easy. The final thanks must go to my parents, Sally and Mark, who have always encouraged me to pursue my passion for Earth Science. I also thank them for the delicious food and home comforts which have kept me going through these final few weeks.

Abstract

The Arabia-Eurasia continent-continent collision zone is unique on Earth for hosting widespread Quaternary post-collisional volcanism. This thesis explores the geochemistry of understudied volcanic rocks from the southern Lesser Caucasus mountains. It builds a holistic model of post-collisional magmatism: from how the magmatic source evolved before and after collision, the mechanism by which this source partially melted, and how magmas were able to ascend through the crust. The thesis also explores how aspects of this model might have changed over the duration of Quaternary volcanism. Major and trace element concentrations, as well as Sr-Nd isotopes are used to build a petrogenetic model for magmatism. Boron isotopes provide further information on the evolution of the mantle source. Ar-Ar ages show how the processes of magma ascent and eruption may have evolved over time. Amphibole and clinopyroxene geothermobarometry establish the pressure-temperature conditions of crystal fractionation.

Southern Lesser Caucasus magmas are not contaminated by assimilation of continental crust. The ubiquitous arc-like geochemistry reflects an inherited subduction component, which is dominated by sediment melts. Metasomatic amphibole stores the component in the lithosphere after collision, and then initiates melting following its heating-induced breakdown. Heating results from small-scale convective removal at the lithosphere-asthenosphere boundary and/or relaxation of non-linear geothermal gradients within the lithosphere. The parental magma produced is a 1% partial melt formed at depths close to the garnet-spinel transition (~80 km). Initial crystal fractionation in mafic magmas occurs over a narrow depth interval, probably in the mid-crust, at temperatures of ~1000˚C. Magmas then ascend from this reservoir, forming polygenetic (> 1 Ma) and monogenetic (< 1 Ma) volcanoes. The polygenetic to monogenetic transition occurred despite a consistent supply of magma, requiring an increased rate of local extension. Magmas ascend vertically, or along normal faults, with no dyke coalescence, preventing the formation of a stable magma plumbing system.

Table of Contents

List of Tables

List of Figures

1. Introduction

Continent-continent collision zones must be regarded as the most enigmatic tectonic setting for volcanic activity on Earth. They lack the unifying theories around which scientific consensus has been built for volcanism in other tectonic settings (Morgan, 1971; Pearce and Peate, 1995; Langmuir and Forsyth, 2000). Researchers investigating post-collisional volcanism are confronted with a plethora of competing models aiming to explain the magmatism (Rotstein and Kafka, 1982; Innocenti et al., 1982; Dewey et al., 1986; Pearce et al., 1990; Keskin et al., 1998; Mitchell and Westaway, 1999; Keskin, 2003; Şengör et al., 2003; Ershov and Nikishin, 2004; Allen et al., 2013; Kaislaniemi et al., 2014). Those models which are most commonly cited today are discussed in section 1.1.

Post-collisional volcanism bears witness to the end of the subduction process, and tracks the evolution of the upper mantle once volatile materials are not being continuously supplied (Agostini et al., 2008). Post-collisional volcanic rocks provide a window into the geodynamic processes occurring at a crucial stage of the Wilson cycle, when active continental margins transition to become the interior of a much larger continent (e.g. Keskin, 2003). The large volumes of magma produced, as well as their relatively high preservation potential makes them a significant contributor to the continued growth of continental crust (Niu et al., 2013). Today, the proximity of large volcanoes with Holocene activity to major cities presents a serious natural hazard to this increasingly densely populated region. For example, the Holocene volcano Damavand is located only 70 km north-east of the Iranian capital Tehran, with a population of nearly 9 million (Davidson et al., 2004). Post-collisional volcanism is important for our understanding of the Earth system and global volcanism, and cannot be ignored.

This thesis enhances our understanding of post-collisional volcanism by expanding the geochemical, geochronological and petrological databases for this setting. This was achieved by field sampling of previously unstudied volcanoes in the Lesser Caucasus mountains, largely contained within the territory of modern-day Armenia. Two of the assets of the Lesser Caucasus as a field area are the widespread young (Pleistocene) volcanic rocks (Philip et al., 2001; Karapetian et al., 2001; Karakhanian et al., 2002; Ollivier et al., 2010; Joannin et al., 2010; Connor et al.,

2011; Lebedev et al., 2013; Gevorgyan et al., 2018), and its semi-arid climate- both of which mean that samples collected in this region showed little to no surface alteration. These samples provide exceptionally high-quality geochemical data and make the Lesser Caucasus an invaluable geochemical laboratory for understanding post-collisional volcanism. The lack of forest cover means that volcanic units are exposed extensively, and parts of the region have been mapped in detail by local geologists (e.g. Kharazyan, 2005).

The Lesser Caucasus occupy a central position in the Arabia-Eurasia collision zone (Fig. 1.1), sandwiched between the large stratovolcanoes of eastern Anatolia and NW Iran. Comparing and contrasting the volcanic rock geochemistry of the Lesser Caucasus with neighbouring regions allows for an analysis of the similarities and differences in the geodynamic processes which contribute to volcanism.

The city of Yerevan, with a population of over a million is in the heart of the Lesser Caucasus. Improving our understanding of the nature of the volcanism will help evaluate the risk it poses to the population of the Armenian capital and surrounding regions. Additionally, as the government of Armenia has developed its nuclear programme over the past 10 years, understanding the hazard volcanism poses to the nuclear power plant is critical for the country's energy security (Aspinall et al., 2016).

The central aim of this thesis is to build a holistic model of volcanism in the Lesser Caucasus, from the nature and evolution of the mantle source, through the mechanism of partial melting, to the processes of magma ascent and ultimate eruption. This chapter aims to put the Lesser Caucasus in their regional geotectonic context by introducing the Arabia-Eurasia collision zone and its associated widespread volcanism. It will then give a detailed synopsis of the aims and objectives of the thesis and how these will be addressed in the subsequent chapters.

1.1 Volcanism in the Arabia-Eurasia collision zone

The Arabia-Eurasia continent-continent collision zone is formed by the northward indentation of the Arabian plate into the Eurasian plate. Collision has led to widespread uplift forming the Turkish-Iranian Plateau (Fig. 1.1), a broad region

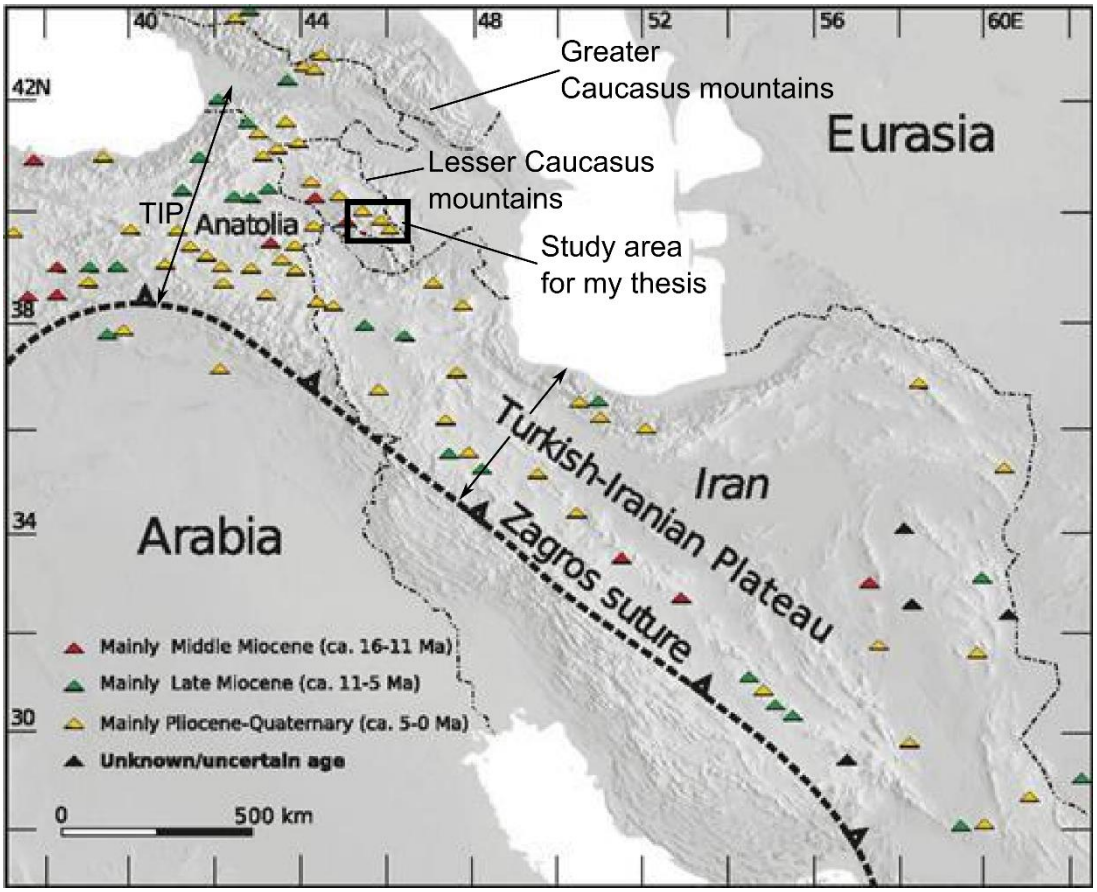

Figure 1.1 Map of volcanoes in the Arabia-Eurasia collision zone.

Triangles show the locations of post-collisional volcanic edifices, colour coded by age. Zagros suture referred to as Bitlis-Zagros suture in the text. Extent of the Turkish-Iranian plateau (TIP) shown by arrows. My study area is outlined by the bold black box. Modified from Kaislaniemi et al. (2014).

uplifted by 1-2 km, which extends for ~ 500 km north of the Bitlis-Zagros suture (Şengör et al., 2008). This plateau has hosted widespread mantle-derived post-collisional volcanism since Miocene times (Fig. 1.1; Innocenti et al., 1980; Pearce et al., 1990; Kaislaniemi et al., 2014). Aside from one isolated example in SW Tibet (Zhu et al., 1983), the Arabia-Eurasia collision zone is unique on Earth as a continent-continent collision hosting volcanism where activity extends into the Holocene (Yilmaz et al., 1998; Karakhanian et al., 2002; Davidson et al., 2004).

Volcanism in the collision zone is widely distributed but predominantly focussed on the Eurasian plate, with only a few volcanic centres on the Arabian foreland (Fig. 1.1; Pearce et al., 1990; Keskin, 2003; Kaislaniemi et al., 2014). As well as the large number of volcanoes (Fig. 1.1), the large size of the post-collisional volcanic edifices (Fig. 1.2) requires a substantial volume of magma to have been produced after the end of subduction. For example, Mt. Ararat volcano, close to the

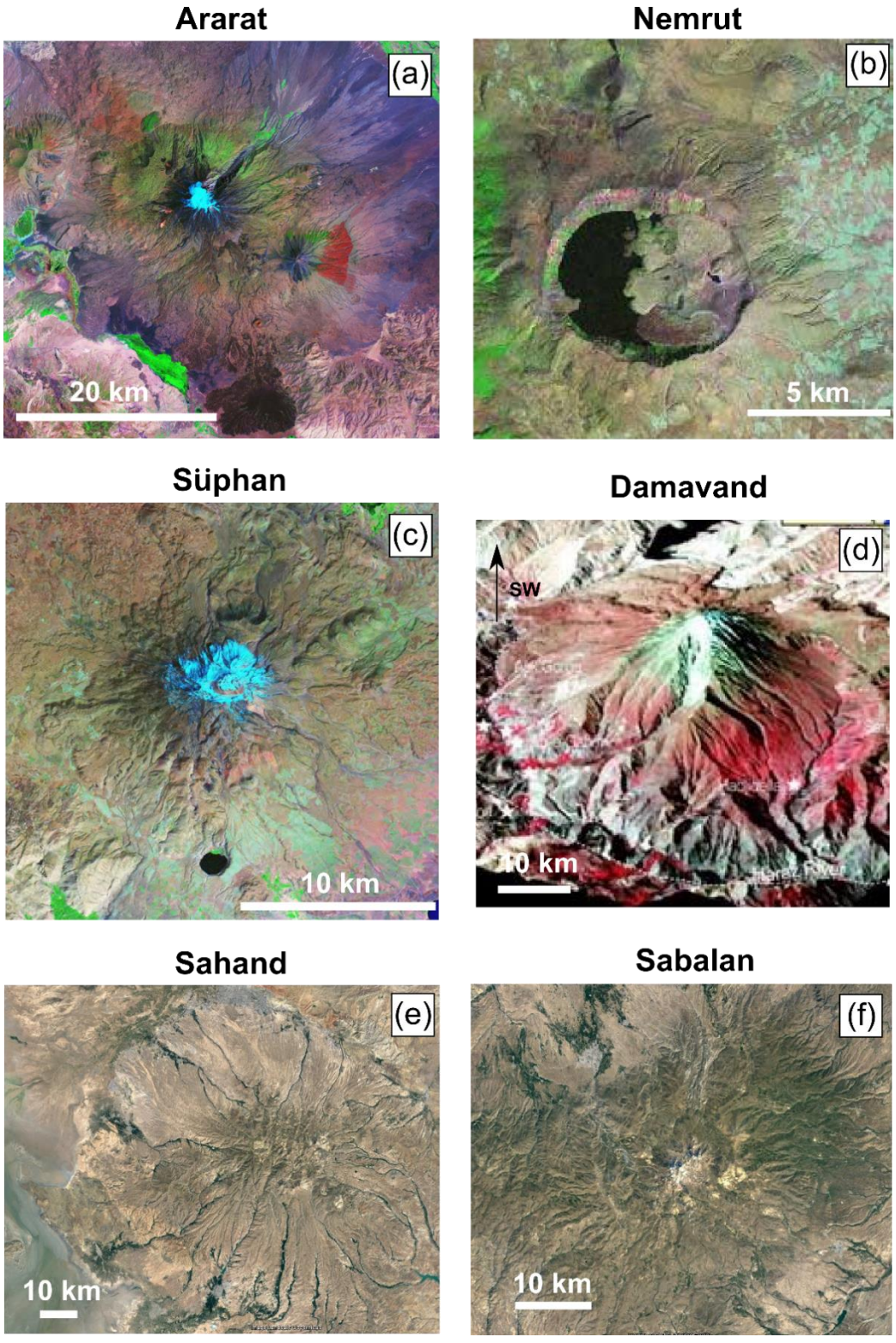

Figure 1.2 sizes of volcanic edifices on the Turkish-Iranian Plateau.

False colour satellite images of eastern Anatolian volcanoes: Ararat (a), Nemrut (b) and Süphan (c) from Keskin (2007). Green colours are vegetated areas, pink colours are basement rocks or sedimentary cover. The grey areas shown the volcanoes. The blue is snow cover. For reference the height of these volcanoes is: Ararat – 5127 m (~4000 m above the surrounding plateau), Nemrut – 2134 m (424 m above plateau) and Süphan - 4058 m (~2000 m above surrounding plateau). d-f show large volcanoes from NW Iran. The image for Damavand (5610 m, ~2000m above the plateau) is a digital elevation model (Davidson et al., 2004). Note the direction of line of sight, for all other figures north is to the top. (e) and (f) show Google Earth™ images of NW Iran volcanoes.

Turkey-Armenia state border, rises to an elevation of 5137 m (over 4 km above the surrounding plateau), with a 60 by 40 km base (Fig. 1.2a). Eastern Anatolia alone has been covered by at least 15000 km^3 of lava flows (Şengör et al., 2008), and with volcanoes in Iran as large as Sabalan (800 km^2, 3km tall; Ghalamghash et al., 2016) and Damavand (volume >400 km^3; Davidson et al., 2004), the volume for the whole collision zone is likely to be much greater (Fig. 1.2). Many of these large volcanoes are still active. For example, Nemrut volcano in eastern Anatolia (Fig. 1.2b) last erupted in 1441 AD (Oswalt, 1912).

In eastern Anatolia (the western part of the collision zone; Fig. 1.1), there is a geochemical distinction between calc-alkaline volcanic rocks of the northern part of the Turkish-Iranian plateau, and the alkaline rocks to the south (Fig. 1.3; Keskin, 2003; Keskin, 2007; Şengör et al., 2008). Incompatible trace element abundances of calc-alkaline volcanic rocks from the north are similar to arc volcanic rocks, with negative Nb-Ta anomalies and enrichments in large ion lithophile (LILE) and light rare earth (LREE) elements (Fig. 1.3a; Pearce, 1982; Keskin et al., 1998). To the south these anomalies are less distinct in trace element patterns (Fig. 1.3b), suggesting an intraplate type mantle source similar to that observed for ocean island basalts (OIB).

The initiation for volcanic activity in eastern Anatolia is younger in the south (3 Ma) compared to the north (11 Ma; Fig 1.4; Keskin, 2003). On this basis of younging volcanism and OIB rather than arc-type geochemistry in volcanic rocks to the south, Keskin (2003) suggested that volcanism in eastern Anatolia is driven by slab-breakoff (Fig. 1.5). He suggested that following the initial collision between Arabia and Eurasia (Fig. 1.5a), the previously subducting oceanic slab rolled back southward, and the mantle wedge was sucked into the space created (Fig. 1.5b). This roll-back and steepening is argued to be the cause of the southward migration of volcanism. Once the slab has steepened sufficiently, it breaks off, introducing convecting mantle (which was previously underneath the subducting slab) from the south (Fig. 1.5c-d). This mantle domain will have been unmodified by previous subduction, and will introduce an intraplate (OIB) component, reflected in the increasingly alkaline volcanic rocks found exclusively in the south (Fig. 1.3).

This model is supported by evidence from seismic receiver functions of

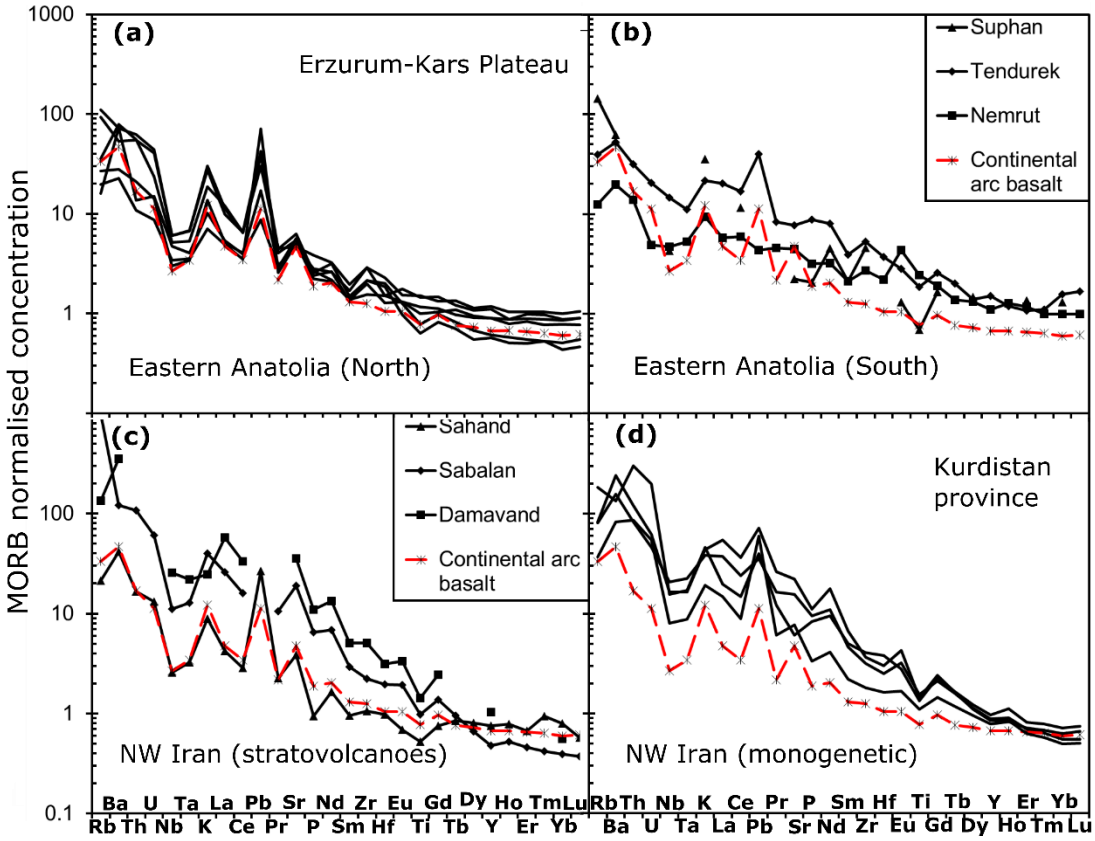

Figure 1.3 geochemistry of mafic volcanic rocks across the collision zone

MORB-normalised (Sun and McDonough, 1989) incompatible trace element patterns for volcanic rocks from eastern Anatolia and NW Iran (Pearce et al., 1990; Keskin et al., 1998; Şen et al., 2004; Davidson et al., 2004; Özdemir et al., 2006; Allen et al., 2013; Ghalamghash et al., 2016; Ghalamghash et al., 2019). Continental arc basalt shown for comparison (Kelemen et al., 2003) (a) The Erzurum-Kars plateau is located in the north of the Turkish-Iranian plateau in eastern Anatolia. The distinct negative Nb-Ta anomaly and LILE enrichments in the most mafic samples are reminiscent of arc rocks. (b) Geochemistry of volcanic rocks from the south of eastern Anatolia. Here any slab signature is much less distinct. Each profile represents one of the most mafic samples from a stratovolcano. (c) and (d) are for volcanic rocks from the eastern part of the Turkish-Iranian Plateau in NW Iran. (c) Showing the geochemistry of volcanic rocks from large stratovolcanoes in NW Iran. Note the Sabalan sample has a trachyandesite composition. All samples show subduction signatures, some are more enriched in the most incompatible elements than is seen in eastern Anatolia. (d) showing some of the most mafic samples from the region- monogenetic cones in the Kurdistan province of NW Iran. All samples are more enriched in incompatible trace elements than continental arc basalt and East Anatolian volcanic rocks.

globally typical crustal thicknesses (~38-50 km; Zor et al., 2003; Angus et al., 2006), and evidence from seismic tomography and shear wave attenuation for total lithospheric thickness that is barely, if at all thicker (~45-50 km; Gok et al., 2000; Al-Lazki, 2003; Zor, 2008; Koulakov et al., 2012). On the basis of this geophysical evidence it seems the crust in eastern Anatolia sits almost directly on the convecting mantle, with little if any mantle lithosphere in between. The lack of mantle lithosphere has been used to support the view that a slab of oceanic lithosphere

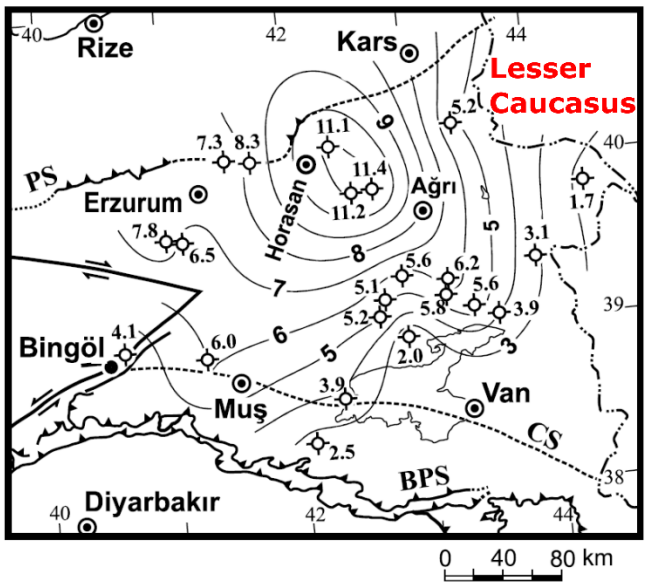

Figure 1.4 ages of initiation of volcanic activity in eastern Anatolia

The age of the first volcanic activity after continent-continent collision is shown, with contours at 1 Myr intervals. Individual points are radiometric ages (Ercan et al., 1990; Pearce et al., 1990; Keskin et al., 1998). After Keskin (2003).

which had previously underplated the crust was removed during slab break-off (Şengör et al., 2003; Keskin, 2003). This makes sense when one considers that the local crust is composed of the East Anatolian Accretionary complex, an accretionary wedge which would have previously sat above a subducting slab (Şengör et al., 2008).

Crustal thickness exhibits only modest variation across the collision zone, with slightly thicker crust (~45-65 km; Paul et al., 2010) in the east (NW Iran). In contrast, the lithosphere thickness differs dramatically between east and west (Fig. 1.6), with lithosphere thicknesses of > 200 km in NW Iran, as opposed to the thin lithosphere of eastern Anatolia (Priestley and McKenzie, 2006; McKenzie and Priestley, 2008; Priestley et al., 2012; Priestley and McKenzie, 2013). If slab break-off removes previously underplated oceanic lithosphere, a thin lithospheric lid is a pre-requisite to the slab break-off model. Slab break-off is therefore not a viable mechanism for magma generation in the eastern part of the collision zone.

Many of the geological observations used to support a slab break-off model in eastern Anatolia do not hold for NW Iran. There are no OIB-type volcanic rocks-instead all samples exhibit an arc-type geochemistry, although with stronger enrichments in the most incompatible trace elements than observed in eastern

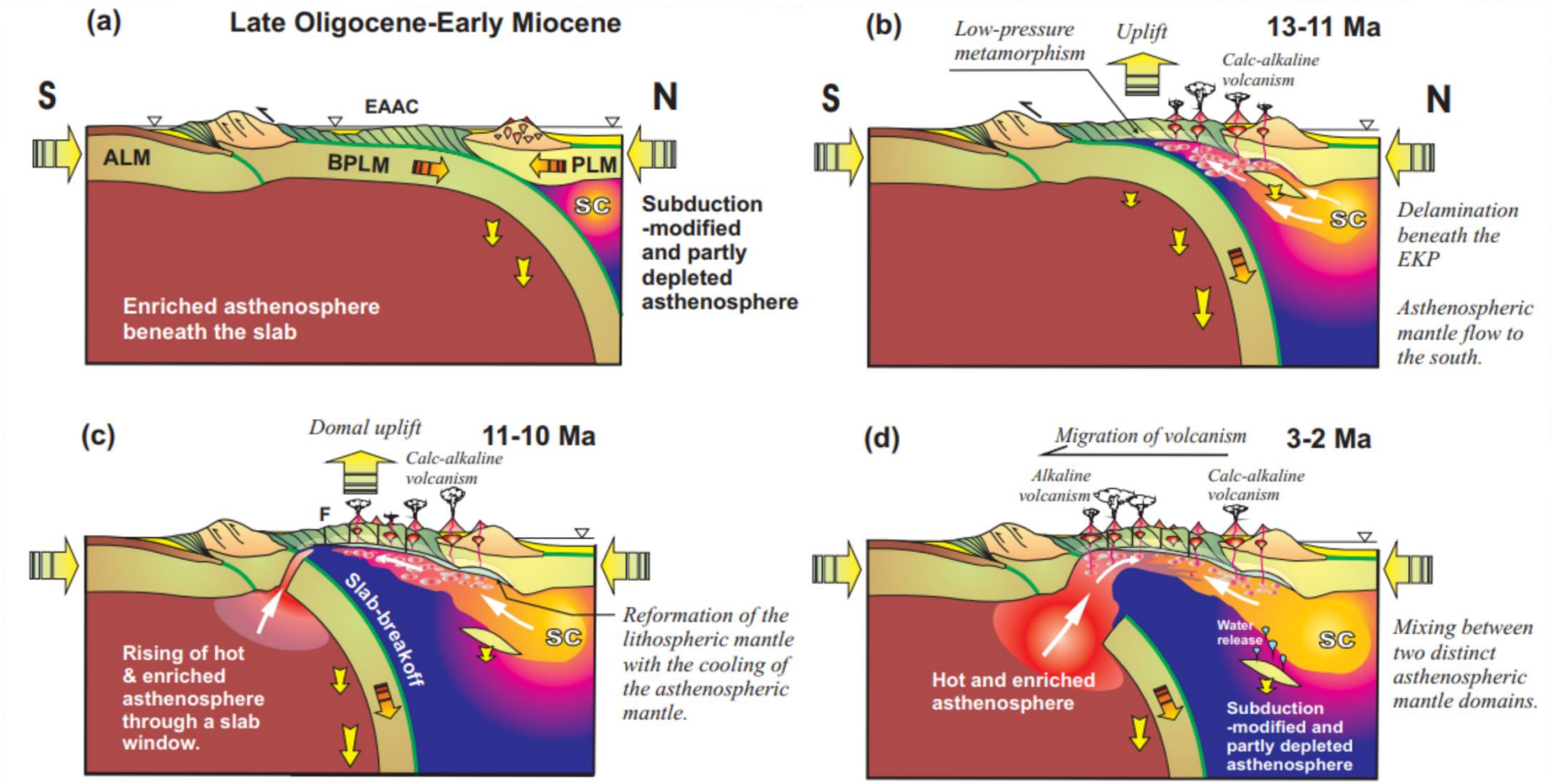
(a)
Late Oligocene-Early Miocene
S
N
EAAC
ALM
BPLM
PLM
SC
Enriched asthenosphere beneath the slab
Subduction -modified and partly depleted asthenosphere
(b)
Low-pressure metamorphism
Uplift
13-11 Ma
Calc-alkaline volcanism
S
N
SC
Delamination beneath the EKP
Asthenospheric mantle flow to the south.
(c)
Domal uplift
11-10 Ma
Calc-alkaline volcanism
F
Slab-breakoff
SC
Rising of hot & enriched asthenosphere through a slab window.
Reformation of the lithospheric mantle with the cooling of the asthenospheric mantle.
(d)
Migration of volcanism
3-2 Ma
Alkaline volcanism
Calc-alkaline volcanism
Water release
SC
Hot and enriched asthenosphere
Subduction -modified and partly depleted asthenosphere
Mixing between two distinct asthenospheric mantle domains.

Figure 1.5 (previous page) Geodynamic model of slab break-off following continental collision

Acronyms are: ALM = Arabian lithospheric mantle; EAAC = East Anatolian Accretionary complex; BPLM = Bitlis-Poturge lithospheric mantle; PLM = Pontide lithospheric mantle; SC = subduction component; EKP = Erzurum-Kars Plateau. After Keskin (2007).

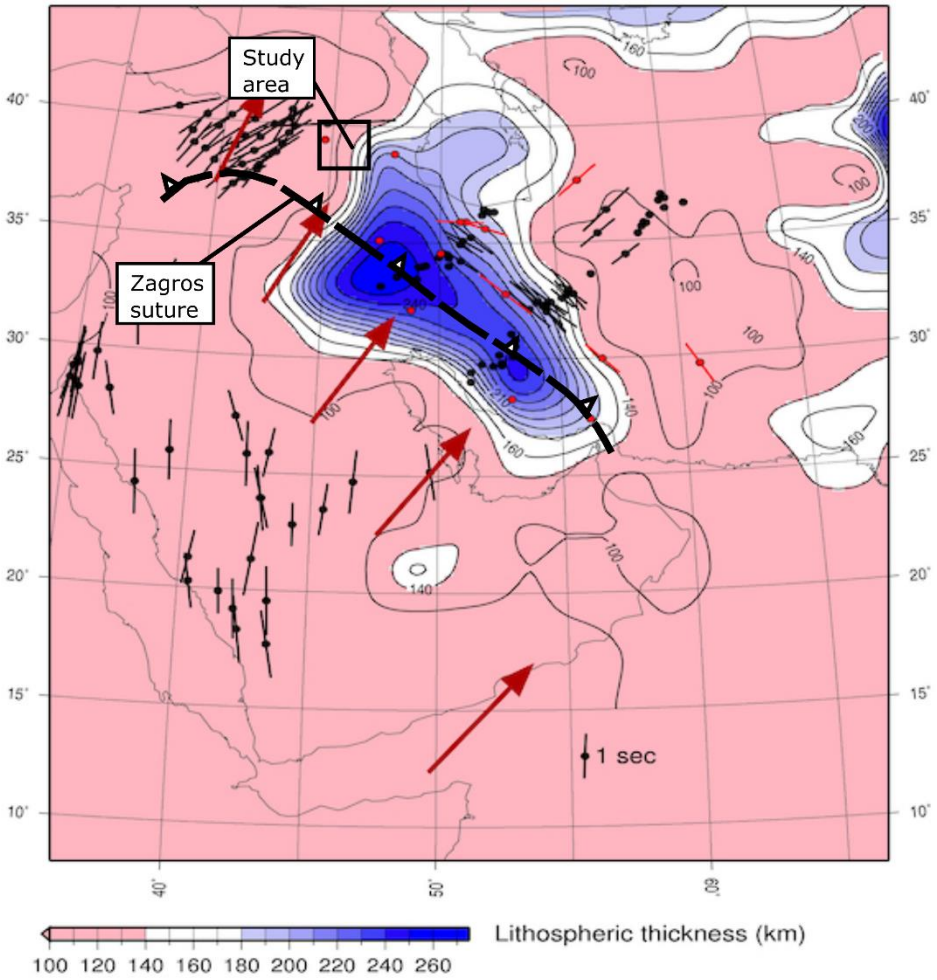

Figure 1.6 lithosphere thickness contours across the Arabia-Eurasia collision zone.

Large red arrows indicate the direction of Arabian plate motion. Black and red circles are seismographs. The circles with bars are SKS splitting measurements of seismic anisotropy. The bold square box indicates the location of the study area for this thesis. Also shown is the location of the Zagros suture. Lithosphere thickness contours are derived from mapped shear wave velocities with depth across the region. These velocities are converted to temperature to construct geotherms which are used to identify the thickness of the lithosphere. Although there will be some errors on the absolute values- the vertical resolution on shear wave velocities at 150 km depth is 25 km- the whole area is treated the same. Relative differences in lithosphere thickness are likely to be real. Modified from Priestley et al. (2012).

Anatolia (Fig. 1.3c, d; Pearce, 1982; Allen et al., 2013; Ghalamghash et al., 2016). Volcanism shows no south-westward migration with time given that both Quaternary and Late Miocene volcanism is seen close to- and away from the Zagros

suture (Fig. 1.1), although a north-westward migration (away from the suture) has recently been suggested (Ghalamghash et al., 2019).

Several alternative models for magma generation in the eastern part of the collision zone, where the lithosphere is thick, have been proposed. One model is compression melting (Fig. 1.7), when as the lithosphere thickens, mantle peridotite is pushed to a higher pressure where amphibole breaks down, inducing dehydration melting (Allen et al., 2013). This invokes the back-bent solidus of amphibole peridotite (Fig. 1.7), to cause melting simply as a result of thickening the lithosphere. This model would require non-linear geothermal gradients to explain such elevated temperatures at the relevant depths in the mid-lithosphere (Allen et al., 2013).

Another model suggests melting occurs in regions of thick lithosphere as a result of small-scale convective removal of lower lithospheric mantle (Kaislaniemi et al., 2014). If a small amount of water (200-600 ppm) is retained in the mantle lithosphere after subduction, it can greatly reduce the viscosity of the peridotite, leading to instabilities at the lithosphere-asthenosphere boundary. This can cause heating and melting at the base of the lithosphere, which is modelled to lead to the spatially sporadic nature of volcanism observed in the Turkish-Iranian plateau (Fig. 1.1; Kaislaniemi et al., 2014).

A single slab break-off event may also be unable to explain volcanism in the far north of the Turkish-Iranian plateau. Neill et al. (2015) argued that volcanic activity is too far north of any slab break-off under the Bitlis-Zagros suture to be explained by such an event. Instead a mixture of small-scale delamination and a second slab break-off event further north have been used to explain volcanism here (Figs 1.8 and 1.9).

Clearly there is no unifying model for the generation of post-collisional magmas. Instead magmatism may come in several different “flavours” (Neill et al., 2014). A key focus of this thesis is how the southern Lesser Caucasus might fit into this varied picture of volcanism.

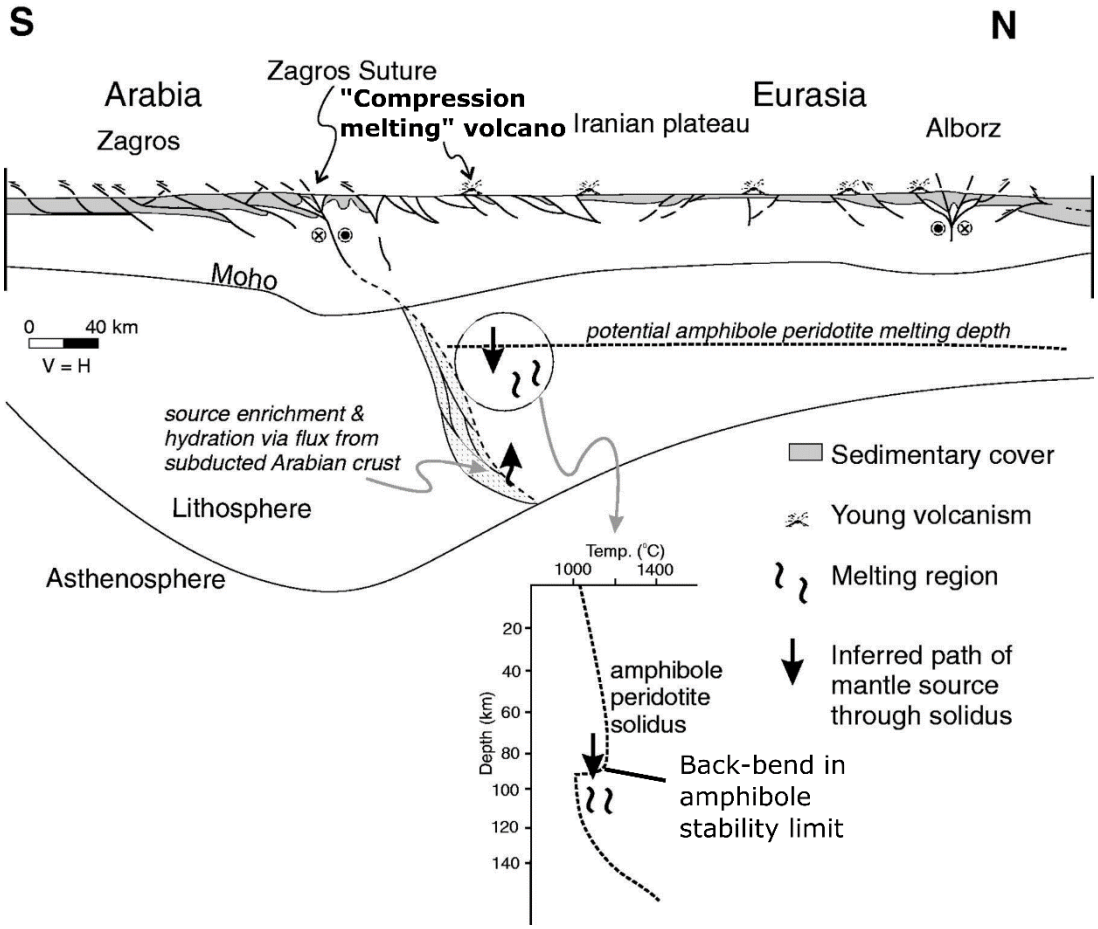

Figure 1.7 amphibole compression melting model.

As the lithosphere thickens, amphibole peridotite is pushed to greater depths. If this peridotite is at ~1000˚C, then a simple increase in depth could lead to melt formation in these regions. This can be achieved as shown in the temperature *vs* depth inset, whereby rocks moving downwards through the back-bent amphibole dehydration solidus will partially melt. After Allen et al. (2013)

1.2 Geochemistry of Lesser Caucasus volcanic rocks

The Lesser Caucasus mountains are located towards the northern edge of the Turkish-Iranian plateau (Fig. 1.9), defined by the Mesozoic-Paleogene Pontide-Lesser Caucasus arc (Mederer et al., 2013). They occupy a central position along the strike of the collision zone, between the Erzurum-Kars plateau of eastern Anatolia, and Sabalan and Sahand volcanoes in NW Iran (Fig. 1.1; Fig. 1.9). The Lesser Caucasus are located at the transition between the thin lithosphere collision tectonics of eastern Anatolia, and the thick lithosphere of NW Iran (Fig. 1.6).

Despite their central position in the collision zone, there are only published geochemical data for the northern part of the region (NLC in Fig. 1.9; Neill et al., 2013, 2015). Volcanic rocks in the northern Lesser Caucasus (Fig. 1.9) exhibit the

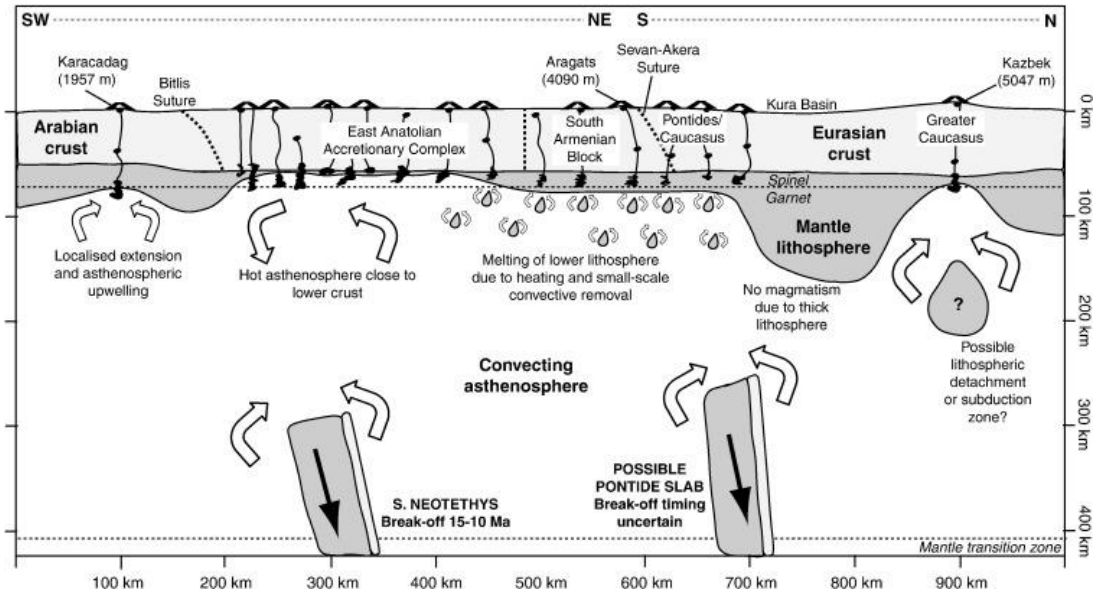

Figure 1.8 Geodynamic model of volcanism across the Arabia-Eurasia collision zone

Showing some of the various processes which might contribute to volcanism. Processes are diverse and include melting of both the lithosphere and asthenosphere, multiple slab break-off events, small scale convective removal and lithospheric detachment. After Neill et al. (2015).

same ubiquitous arc-type geochemistry (Fig. 1.10; Neill et al., 2013, 2015) as samples from neighbouring NE Anatolia (Fig. 1.3a; Keskin et al., 1998). Given that both the northern Lesser Caucasus and eastern Anatolia sit on thin lithosphere, the similar geochemistry is unsurprising. The northern Lesser Caucasus is distinguished from neighbouring regions by the lack of evidence from Sr-Nd isotopes for crustal contamination (Neill et al., 2013, 2015), in contrast to evidence for extensive crustal assimilation in eastern Anatolia (Keskin et al., 2006). If there is a similar lack of evidence for crustal contamination in the southern Lesser Caucasus (SLC in Fig. 1.9) volcanic rocks, this will make the region ideal for studying the post-collisional mantle source.

The southern Lesser Caucasus also host some of the most mafic volcanic rocks in the region (Fig. 1.11), where basanites with SiO_2 ~ 45 wt % can be sampled (Meliksetian, 2013). Such rocks have likely only fractionated olivine, and in the absence of mantle xenoliths provide the most direct means of assessing the composition of the mantle source. Elsewhere in the Lesser Caucasus, magmas generally have > 50 wt % SiO_2, such that even the most mafic samples have fractionated multiple mafic minerals.

Despite hosting > 200 volcanoes, little is known about the composition of

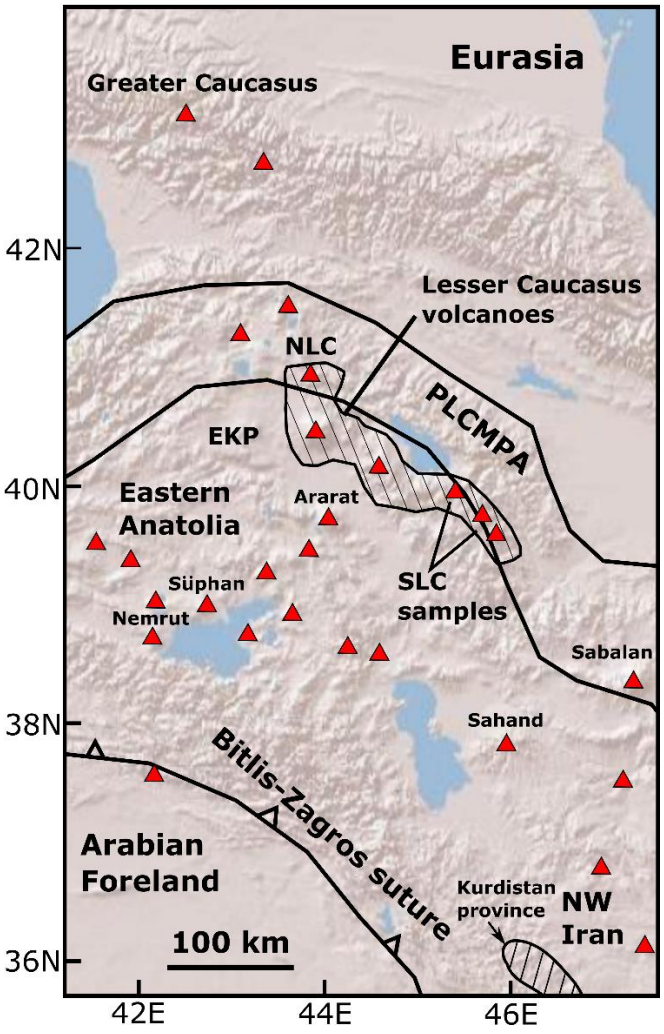

Figure 1.9 Location of the Lesser Caucasus

Locations of Plio-Pleistocene post-collisional volcanoes are shown by the red triangles (Kaislaniemi et al., 2014)- triangles may refer to one polygenetic volcano or numerous monogenetic centres, or both. The region of Lesser Caucasus volcanism is outlined by the striped region. These volcanoes are close to the northern edge of the Turkish-Iranian plateau, which is defined by the Pontide-Lesser Caucasus Mesozoic-Paleogene arc (PLCMPA). The southern Lesser Caucasus (SLC) region is the focus of sampling for this thesis. The region is located between the thin lithosphere of eastern Anatolia and the thick lithosphere of NW Iran. Several locations referred to in this introduction chapter are labelled here. NLC- Northern Lesser Caucasus. EKP- Erzurum-Kars Plateau volcanism in the north of eastern Anatolia. Three stratovolcanoes from eastern Anatolia- Ararat, Süphan and Nemrut are labelled. Sahand and Sabalan stratovolcanoes in NW Iran are also shown. The Kurdistan province is the region of thick lithosphere where amphibole compression melting has been hypothesised to occur. Basemap is "World Topo Map" (Sources: Esri, DeLorme, HERE, TomTom, Intermap, increment P Corp., GEBCO, USGS, FAO, NPS, NRCAN, GeoBase, IGN, Kadaster NL, Ordnance Survey, Esri Japan, METI, Esri China (Hong Kong), swisstopo, MapmyIndia, and the GIS User Community). Maps such as this used throughout the thesis were partly created using ArcGIS® software by Esri. ArcGIS® and ArcMap™ are the intellectual property of Esri and are used herein under license. Copyright © Esri. All rights reserved. For more information about Esri® software please visit www.esri.com.

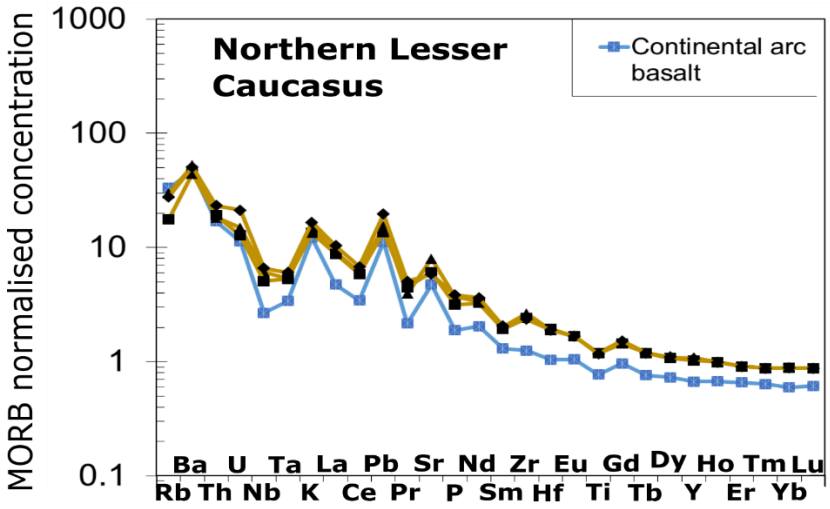

Figure 1.10 geochemistry of mafic volcanic rocks from the northern Lesser Caucasus

Showing the similarity with continental arc basalts (Kelemen et al., 2003). Data (Neill et al., 2015) for mafic (MgO > 6 wt %) volcanic rocks from the northern Lesser Caucasus (labelled NLC in Fig. 1.9) has the typical negative Nb-Ta and Ti anomalies and positive Ba, K, Pb and Sr anomalies of continental arc basalts (Pearce, 1982).

volcanic rocks from the south-eastern part of the Lesser Caucasus, which is partly why they form the main focus of this thesis. Within the Lesser Caucasus, the thickness of the lithosphere is thought to increase from north to south (Fig. 1.6). This could affect the composition of Lesser Caucasus volcanic rocks in some way. The only published study of volcanic rocks from this region (Meliksetian, 2013) shows that lavas from the south have higher K_2O contents than those from the north (Fig. 1.11). This observation suggests magmatism in the south may be more alkaline and sample more enriched mantle sources than magmatism to the north. A more detailed introduction to the geology of the Lesser Caucasus and its Quaternary volcanoes is given in Chapter 2.

1.3 Aims and Objectives

This thesis aims to improve our understanding of some of the most remote and understudied volcanoes in the Arabia-Eurasia collision zone. At the heart of it is a single fundamental question: why are the volcanoes in the southern Lesser Caucasus still active when the subduction process ceased > 20 Myr ago?

The goal of this thesis is to build a holistic model of magma generation and

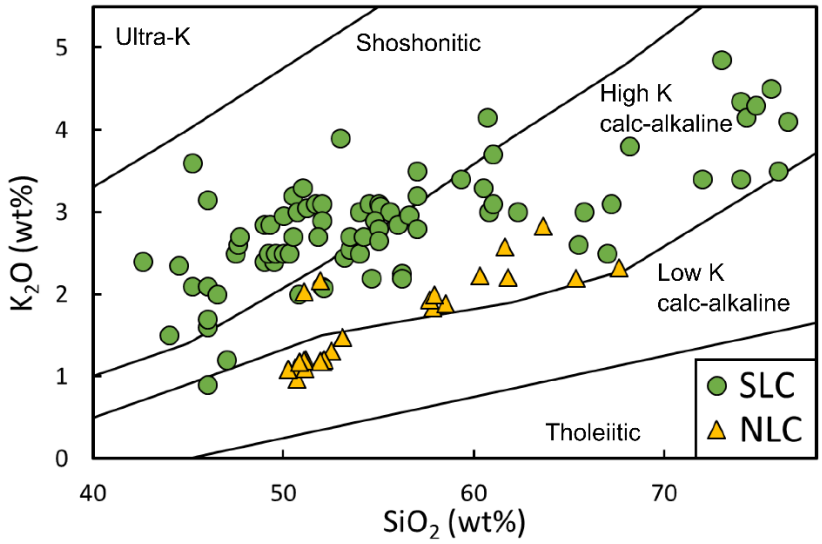

Figure 1.11 K content of volcanic rocks from the northern and southern Lesser Caucasus.

NLC- northern Lesser Caucasus, SLC- southern Lesser Caucasus. NLC data from Neill et al. (2013), SLC data from Meliksetian (2013).

volcanism, from the evolution of the mantle source to eventual volcanic eruption (presented in Chapter 7). This model will explain how the magma source retained sufficient fusible components to produce magma which could be extracted (Chapter 4). It will then constrain the mechanism of melt generation (Chapter 3). Finally, it will elucidate the processes of magma storage (Chapter 6) and transport in the crust, which eventually led to volcanic eruptions (Chapter 5).

Using mafic volcanic rocks as a window on the mantle source is the major tool in developing several aspects of the holistic model. They will be used to gain insights into the nature of the mantle source- in terms of both its mineralogy and geochemistry, which will tell us about its metasomatic history. The other mantle source process this thesis aims to investigate is that of magma genesis. This thesis aims to understand where in the mantle magma was formed, what proportion of this source was melted and what the mechanism of melt generation was.

Once these magmas have formed, they then ascend into the crust. During this ascent they must stall and partially crystallise. The pressure and temperature conditions under which this occurs will help to build a picture of the magma plumbing system which connects the magma source to the volcanoes at the surface. It will also be necessary to account for the processes of crystal fractionation and any associated crustal contamination when constraining the mechanism of melt

generation mentioned above. Finally, magmas must ascend to the surface and erupt. As will be made clear in **Chapter 2**, volcanic eruptions have produced both polygenetic and monogenetic volcanoes in the southern Lesser Caucasus. An important aim is to understand whether there has been a temporal shift in the mode of eruption and why.

The location of the southern Lesser Caucasus in the middle of the Arabia-Eurasia collision zone could mean the insights gained from studying these volcanic rocks might have implications for the generation of post-collisional magmas across the collision zone. The southern Lesser Caucasus could provide a "missing link" between magmatism in the thick lithosphere region of NW Iran, and the thin lithosphere region of eastern Anatolia.

In terms of the analysis of new geochemical data, the main objectives of this thesis are:

- To use the bulk-rock major and trace element systematics of both mafic and felsic rocks to gain an understanding of the process and extent of crystal fractionation.
- To use trace element systematics of the most mafic samples to investigate the composition and mineralogy of the magma source.
- To investigate the location and extent of partial melting using both major and trace element data for the most mafic samples. Combining this with the previous objective will allow for the development of a geodynamic model for the mechanism of magma generation.
- To use bulk-rock Sr-Nd isotope ratios to investigate the extent of crustal contamination and directly characterise the composition of the mantle source. These isotope ratios are not fractionated during the processes of melting or crystallisation, such that they should simply be a reflection of the magma sources.
- To use B isotopes as a quantitative tracer of fluid-mobile components in order to decipher the origin and nature of the subduction signature, and hence the pre-melting history of the magmatic source.
- To use the major element composition of amphibole and clinopyroxene phenocrysts (in mafic igneous rocks) as inputs to empirical

geothermobarometric equations to constrain the *P-T* conditions of the partial crystallisation of the magmas in the crust.

- To determine the ages (via $^{40}Ar/^{39}Ar$) of selected volcanic rocks to investigate a potential transition from polygenetic to monogenetic volcanism and to understand the origins of that transition.
- To investigate the overall occurrence rate of volcanic activity using the new ages and the implications this has for the volcanic hazards posed to the local population.

1.4 Chapter outline

The remainder of this thesis describes the geology of the Lesser Caucasus and its volcanoes, before presenting new geochemical data on volcanic rocks from the south of the region. These data are then carefully interpreted to provide insights on various aspects of post-collisional volcanism. These interpretations are then synthesised into the holistic model of volcanism in the southern Lesser Caucasus.

- **Chapter 2** provides a more detailed background to the geology of the Lesser Caucasus and its Quaternary, post-collisional volcanoes. It also provides some geographical signposting for locations referred to in the text.
- **Chapters 3-6** outline the major results of the thesis:
    - **Chapter 3** introduces the bulk rock major and trace element geochemistry as well as the Sr-Nd isotope ratios of the studied southern Lesser Caucasus samples. These geochemical data are compared with literature data for volcanic rocks in the northern Lesser Caucasus (where the lithosphere is thin) and NW Iran (where it is thick). The chapter examines the mineralogy of the mantle source, conditions of magma generation, and the extent of melting, before presenting a new geodynamic model for magma genesis in the southern Lesser Caucasus
    - **Chapter 4** rewinds the clock to examine how the mantle source developed its distinct composition before the onset of melting. Boron isotopes are used as a tracer of slab material in the mantle source, to understand the nature and origin of the subduction component.
    - **Chapter 5** presents newly determined Ar-Ar ages for southern Lesser Caucasus volcanic rocks and compares them with other ages from the

literature. The rate of volcanic activity is estimated. The chapter then explores a possible transition from polygenetic to monogenetic volcanism and what might have caused it.

    - **Chapter 6** calculates the P-T conditions of amphibole and clinopyroxene crystallisation using geothermobarometry. As well as interpreting the conditions of crystal fractionation, the chapter also considers the implications of these estimates for the conclusions drawn in the previous 3 chapters.

- **Chapter 7** synthesises these results into an overall history of magmatism from metasomatism of the mantle source to the type of volcano formed by the eventual eruptions (the holistic model of volcanism in the southern Lesser Caucasus).

2. The geology of the Lesser Caucasus and its volcanoes

This chapter provides a brief overview of the geology of the Lesser Caucasus, including the subduction history which led to accretion of the pre-Miocene terranes, and a summary of the types of post-collisional volcanic structures and their deposits. There are a substantial number of different locations and sub-locations within the Lesser Caucasus referred to throughout this thesis. For clarity, these locations are signposted in this chapter.

2.1 Pre-collision geological history

The geology of the Lesser Caucasus is defined by the closure of the Neotethys Ocean, which resulted in the Arabia-Eurasia continent-continent collision (Rolland, 2017 and references therein). Its pre-Miocene geology (Fig. 2.1), like much of the interior of the Turkish-Iranian Plateau, is a complex amalgamation of a series of terranes (microplates) which accreted to the Eurasian continental margin during the closure of the Neotethys Ocean (Rolland, 2017). The north and east of the Lesser Caucasus mountains include rocks associated with the Mesozoic- early Cenozoic volcanic arc (known as the Lesser Caucasus arc; Mederer et al., 2013), which constitute an eastern continuation of the Pontides of Anatolia. The Pontide and Lesser Caucasus arcs together formed the active southern margin of the Eurasian Plate (Yilmaz et al., 2000). Figure 2.2 illustrates the various stages of closure of the Neotethys Ocean. During the Mesozoic and Paleogene there were several subduction zones which contributed to the closure of the northern, and later the southern Neotethys basins (Fig. 2.2 panels 1 and 2; Galoyan et al., 2009; Rolland et al., 2010, 2012; Sosson et al., 2010; Topuz et al., 2013a, 2013b, 2014; Karaoğlan et al., 2013, 2016; Mederer et al., 2013; Hässig et al., 2015).

The Sevan-Akera suture zone is defined by the outcropping of several (likely N. Neotethys- derived) ophiolite complexes (Fig. 2.1; Rolland et al., 2010; Hässig et al., 2013). These ophiolites were obducted onto the South Armenian block (SAB) at 88-83 Ma (Rolland et al., 2010; Sosson et al., 2010). The SAB (Fig. 2.1) is a micro-continental fragment composed of Proterozoic metamorphic basement and its sedimentary cover. The SAB rifted from the Arabian margin in the early Mesozoic

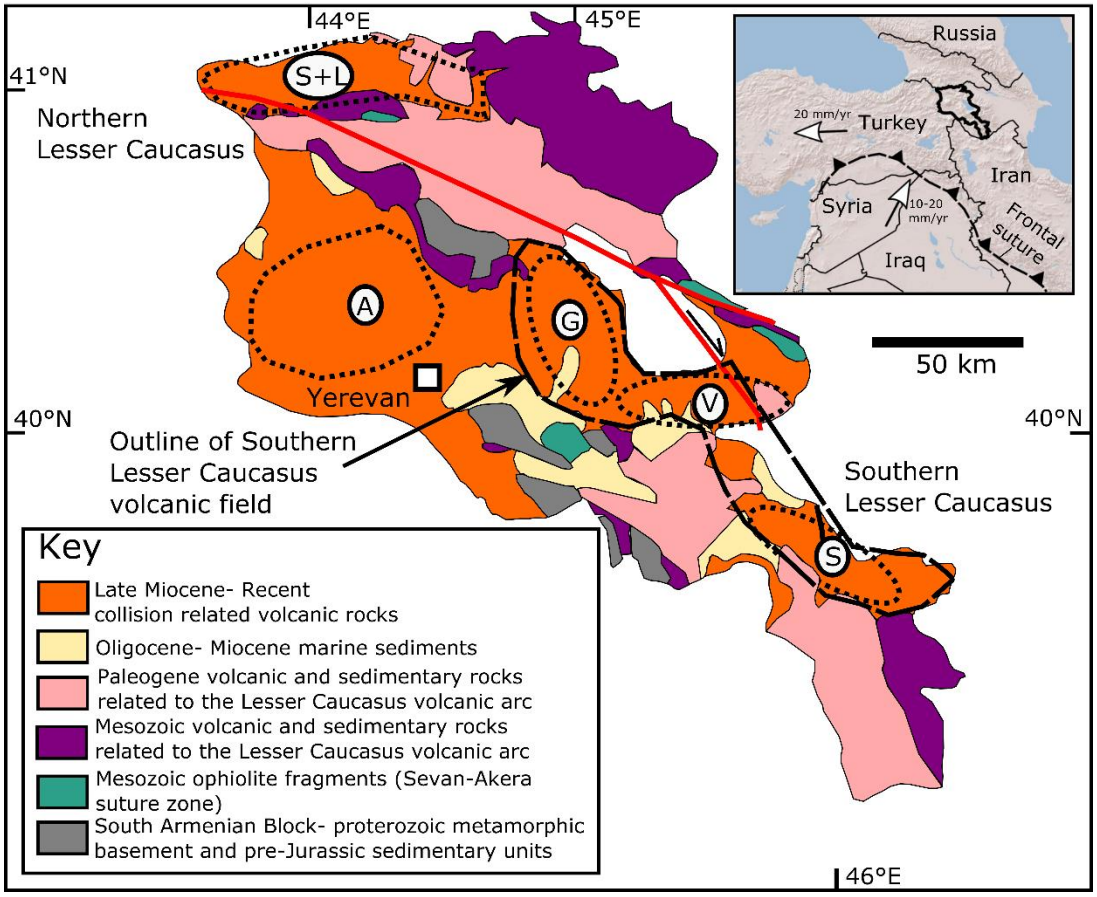

Figure 2.1 Geological map of the territory of Armenia, encompassing most of the Lesser Caucasus

Inset shows the location of Armenia in the Arabia-Eurasia collision zone. Also shown are the location of the Bitlis-Zagros frontal suture and plate velocities for Arabia and Anatolia (Reilinger et al., 2006). The main figure shows a geological map of Armenia showing major tectonic units simplified from Mederer et al. (2013). This figure also includes geographical signposting for the locations of volcanic structures referred to in this Chapter and throughout the thesis. Shirak and Lori provinces (S+L) in NW Armenia are where the samples for geochemical data presented in Neill et al. (2013, 2015) were collected. Aragats polygenetic volcano (A) is probably the largest volcanic structure in the region. Gegham (G), Vardenis (V) and Syunik (S) volcanic highlands together form the southern Lesser Caucasus volcanic field outlined by the dashed line. Each of the volcanic highlands are outlined by a dotted line. The bold red line is the location of the Pambak-Sevan-Syunik strike-slip fault. The labels northern and southern Lesser Caucasus are given to signpost the regions which these terms refer to.

(Sengor, 1984) and is likely continuous with the Taurides-Anatolides of Anatolia (Rolland et al., 2016) and the Cimmerian terrane of Iran (Stampfli et al., 2013). Ophiolite obduction was followed by accretion of the SAB to the Pontide-Lesser Caucasus arc at 80-75 Ma (Rolland et al., 2012) along the Sevan-Akera suture, marking the closure of the N. Neotethys Ocean (Fig. 2.2, panel 2). Subduction then jumped to the south with northward subduction of the Southern Neotethys until its closure with the "soft" collision of Arabia with SAB-Lesser Caucasus along the Bitlis-Zagros suture (Fig. 1.9; Fig. 2.2 panel 3) at ~ 50-40 Ma (Rolland et al., 2012).

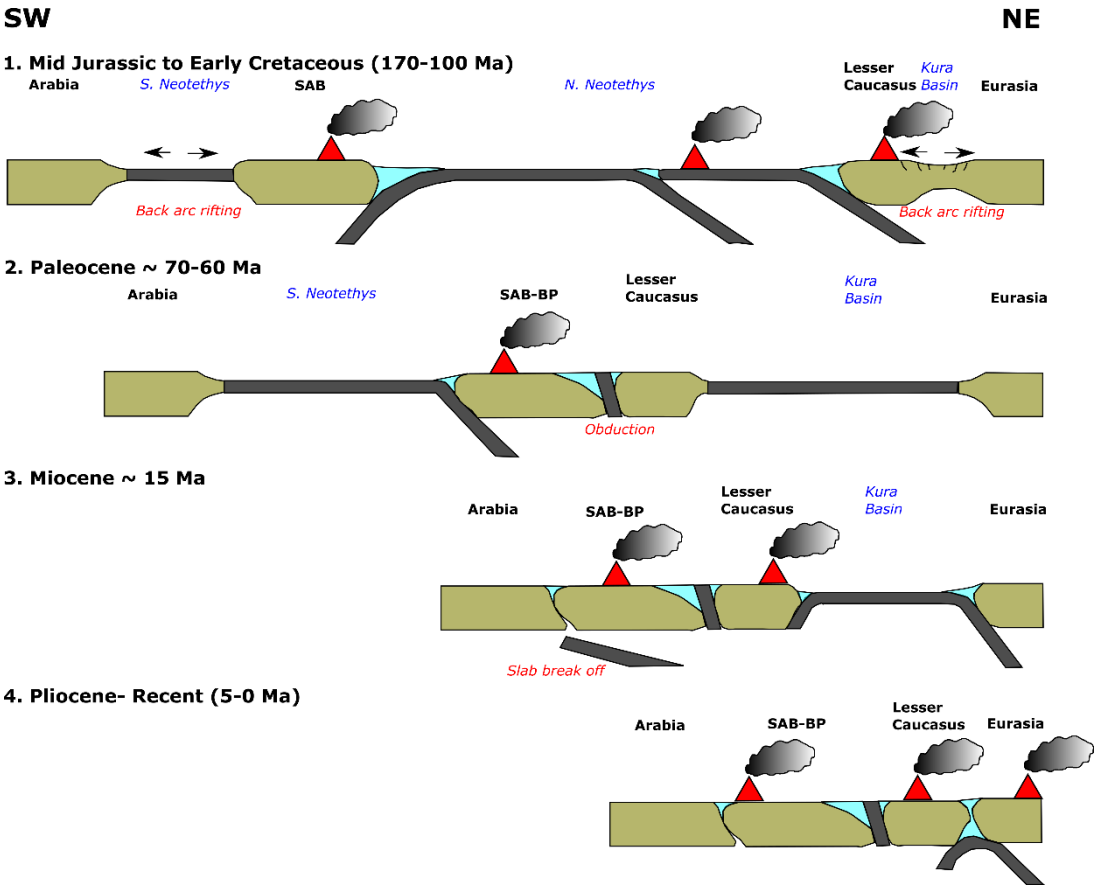

Figure 2.2 Tethyan subduction history for the Arabia-Eurasia collision zone.

Illustration of the progressive closure of the oceanic domains that separated Arabia from Eurasia during the Mesozoic. The movement of the Bitlis-Poturge terrane (BP) from Arabia to the South Armenian Block (SAB) is not shown but occurs between panels 1 and 2. Simplified from Rolland (2017).

However, some authors have posited a much later collision at ~ 25 Ma (Okay et al., 2010). “Hard” collision was delayed until the Pliocene, following the closure of the Kura Basin to the north (Fig. 2.2 panel 4; Rolland, 2017).

The numerous subduction zones illustrated in Fig. 2.2 would have added slab-derived material to the mantle wedge beneath the present-day Lesser Caucasus. It has been suggested that this signature of a subduction-modified mantle has been widely inherited by the post-collisional volcanic rocks in the Arabia-Eurasia collision zone (Pearce et al., 1990; Keskin et al., 1998; Keskin, 2003; Okay et al., 2010; Allen et al., 2013).

2.2 Lesser Caucasus post-collisional volcanism

Post-collisional volcanism within Armenia (which includes most of the Lesser Caucasus; Fig. 2.1), is sufficiently widespread to obscure a significant proportion of the pre-existing geology. Previous studies of volcanism in the Lesser Caucasus focused on the volcanic rocks from the Shirak and Lori provinces in NW Armenia, labelled S+L in Fig. 2.1 (Neill et al., 2013, 2015). Three regions of distributed volcanism (areas with numerous volcanoes which each erupted only once) are the Gegham, Vardenis and Syunik highlands (labelled G, V and S in Fig. 2.1; Karapetian et al., 2001). There are no distinct breaks between these highlands, such that together they can be considered a single volcanic field covering ~8000 km^2, which is referred to in this thesis as the southern Lesser Caucasus volcanic field. The SE of the region (Syunik and Vardenis) is generally referred to as the southern Lesser Caucasus, while the northern Lesser Caucasus generally refers to Shirak and Lori. Gegham highland and Mt. Aragats stratovolcano (labelled A in Fig. 2.1) could be considered to occupy the central Lesser Caucasus in the nomenclature of this thesis. The vast majority of data presented in this thesis are from Vardenis and Syunik. Field photos of various volcanic features from Vardenis and Syunik are shown in Fig. 2.3. A geological map of Syunik volcanic highland is shown in Fig. 2.4.

2.2.1 Style of volcanism in the Lesser Caucasus

The large volcanic edifices of eastern Anatolia: Ararat, Tendurek, Suphan, and Nemrut (Fig. 1.2; Keskin, 2007), all have activity extending into the Holocene (Yilmaz et al., 1998). Similarly, large edifices are present in NW Iran, such as Damavand (Fig. 1.2) which is thought to have erupted in the Holocene (Davidson et al., 2004), and Sabalan (Fig. 1.2) which last erupted at ~ 0.1 Ma (Ghalamghash et al., 2016). All of these volcanoes are polygenetic, meaning they were formed by repeated eruptions from a single vent (Valentine and Connor, 2015). In the Lesser Caucasus, Aragats is the largest polygenetic volcano (70 km basal diameter, 3km tall) and was active from 1.8 to 0.5 Ma (Connor et al., 2011; Gevorgyan et al., 2018), suggesting it is now dormant. To the south-east, there are two polygenetic volcanoes (Tskhouk and Ishkhanasar) in the Syunik volcanic highland (Figs 2.3a & 2.4). These volcanoes are also thought to be dormant (Meliksetian, 2013).

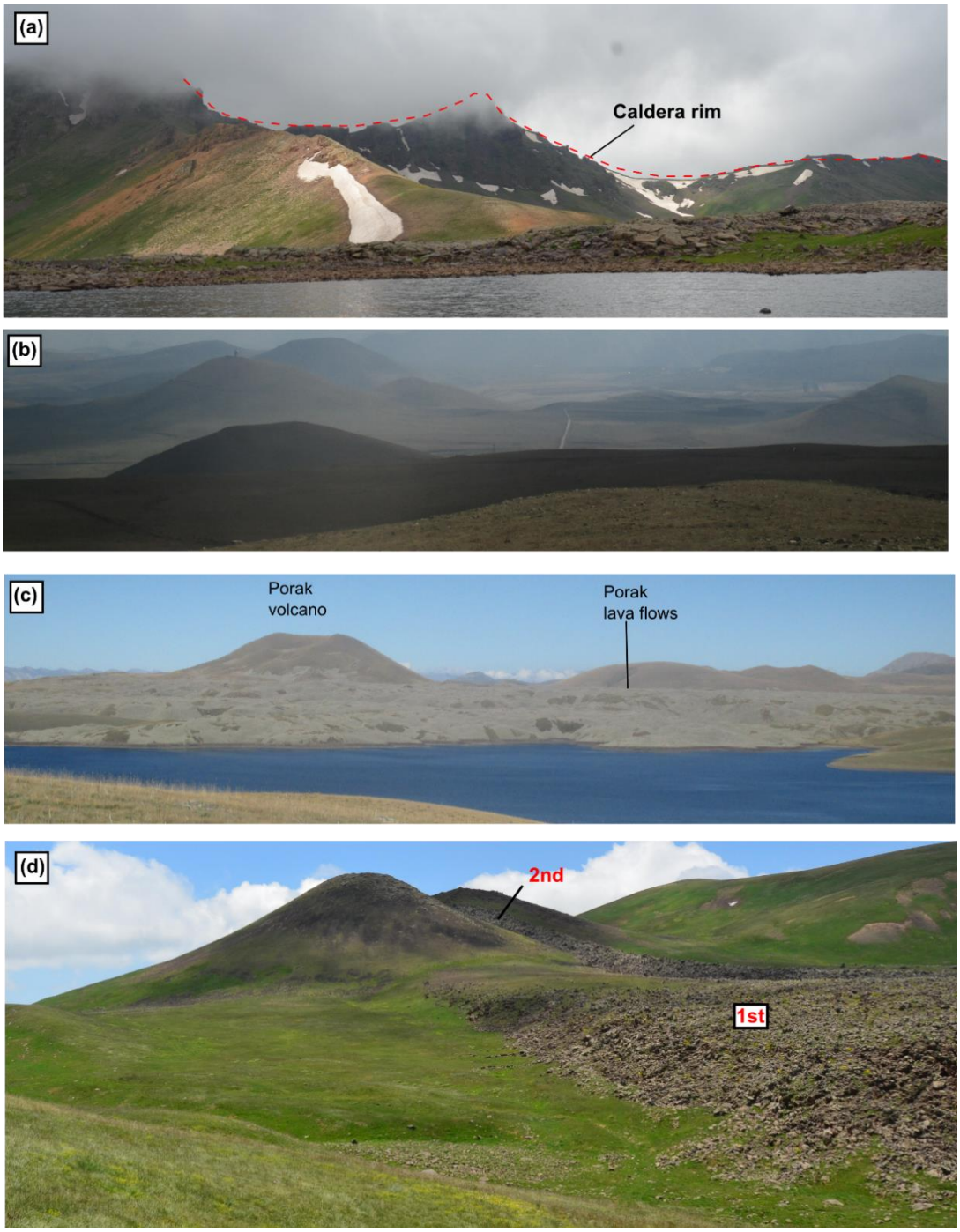

Figure 2.3 Field photographs from Syunik and Vardenis volcanic highlands in the southern Lesser Caucasus

Showing volcanic structures and types of eruptive product. (a) The summit of Tskhouk volcano, one of the polygenetic centres in the Syunik volcanic highland. The caldera rim is shown by the red dashed line. (b) Numerous scoria cones in the south of the Syunik volcanic highland, seen from the lower slopes of Ishkhanasar polygenetic volcano. (c) One of the Holocene volcanic centres, Porak, in Vardenis volcanic highland (Karakhanian et al., 2002). A large area of lava flows are associated with the formation of the volcano travelling up to 20 km from the vent site. (d) Nazelli is another Holocene monogenetic volcano, this time in the Syunik highland. As can be seen the scoria cone has two lava flows extruding from it. The earlier 1st generation lava flow extrudes from a *boca* (a vent close to the base of a scoria cone). The 2nd generation lava flow is much smaller and erupts from the summit producing a narrow tongue down its flanks.

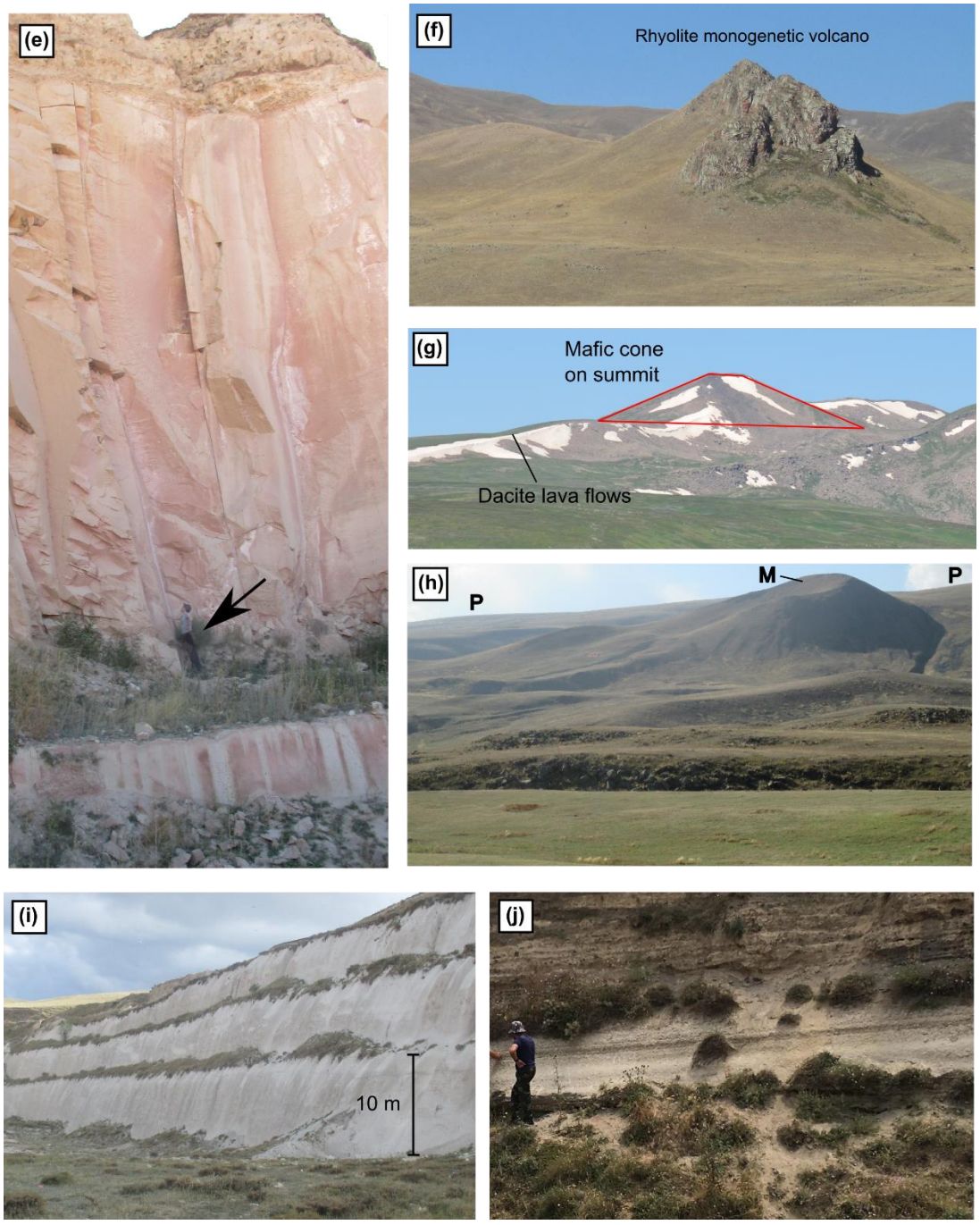

Figure 2.3 continued.

(e) The massive ignimbrite deposit known as the Subatan tuff at the base of the Vardenis volcanic section. A person is shown for scale. It is only exposed in this quarry, such that volume estimates are not possible. (f) Rhyolite lava vent plug of a monogentic volcano in Vardenis; (g) is an image of Torgomayr volcano in Vardenis. Its lower slopes are composed of dacite lava flows, however the summit is a mafic cone emplaced at a later date on top of these dacites. (h) Sherepasar volcano in Syunik. It is on the slopes of the Tskhouk stratovolcano shown in (a). The labels P denote lava flows emanating from the Tskhouk polygenetic volcano. Sherepasar is labelled with an M (monogenetic), and can be clearly seen to overly the polygenetic lava flows. (i) Tsovak quarry pumice fall deposit in Vardenis. (j) A pumice fall-out layer to the east of Syunik volcanic highland.

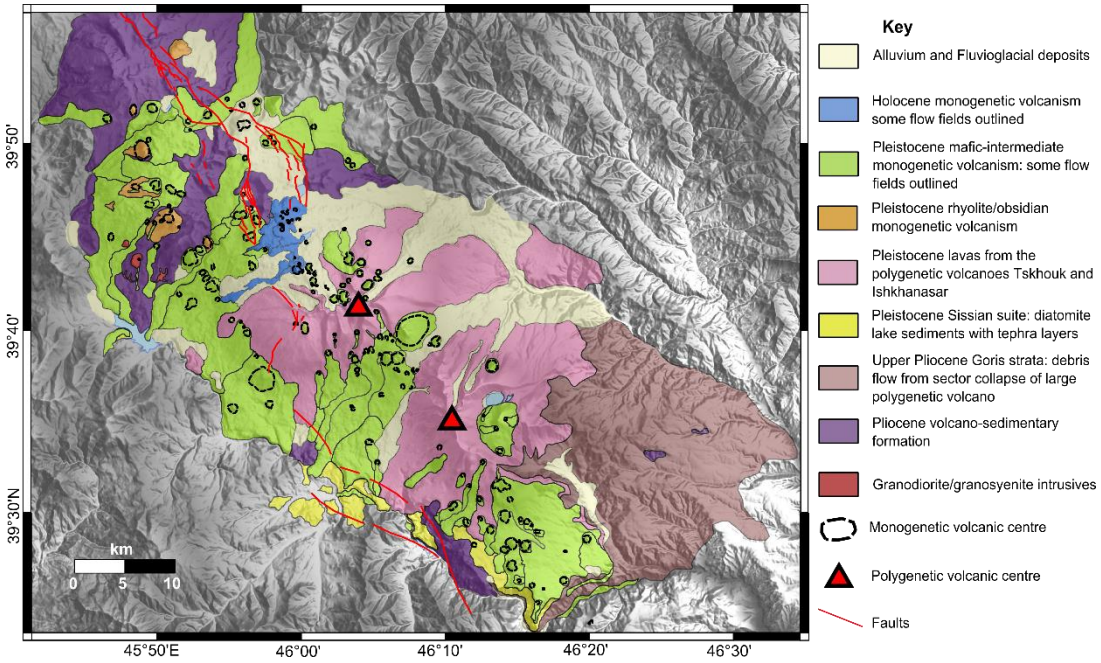

Figure 2.4 Geological map of the Syunik volcanic highland

Map showing the ages of volcanic deposits from Syunik (labelled S in Fig. 2.1). The map is based on the work of S. Karapetyan, R. Jrbashyan and G. Navasardyan of the Institute of Geological Sciences at the Armenian National Academy of Sciences; and Ivan Savov (University of Leeds, main supervisor for this thesis). The two polygenetic volcanoes are shown by red triangles, with Tshkouk in the north-west and Ishkhanasar in the south-east. Note the Sissian suite of sediments shown in yellow, from which tephra layers have been dated by Ar-Ar (Joannin et al., 2010), while several of the lava flows which cap these sediments were dated by K-Ar (Ollivier et al., 2010).

While there are polygenetic volcanoes in the Lesser Caucasus, distributed volcanism is the dominant mode (Figs 2.3b and 2.4). Distributed volcanism involves the formation of numerous small monogenetic volcanoes within a defined region, rather than the development of a single volcanic edifice (Valentine and Connor, 2015). Monogenetic volcanoes are generally thought to form in a single eruptive episode (Smith and Németh, 2017). Unusually for monogenetic volcanism, the Lesser Caucasus eruptive products are not restricted to mafic compositions, with volcanic rocks exhibiting a complete and continuous compositional range from basanite to rhyolite (Figs 2.3b, f and 2.4). In both the north and south of the Lesser Caucasus, this style of volcanism becomes increasingly dominant in the most recent eruptive products (Figs 2.3g, h and 2.4; Neill et al., 2013; Ollivier et al., 2010).

Styles of volcanic eruption in the Lesser Caucasus are diverse, and although lava flows from effusive eruptions dominate the geological landscape (Fig. 2.3c, d), there is clear evidence for very large Neogene explosive volcanic eruptions producing widespread ignimbrites (Karapetian et al., 2001; Karakhanian et al., 2002;

Gevorgyan et al., 2018). There are numerous ignimbrite deposits which have been mapped around Aragats, potentially indicative of repeated caldera-collapse events at this volcano, with ages of 1.8-0.6 Ma (Gevorgyan et al., 2018). These ignimbrites include the Yerevan-Gyumri tuff, with an estimated volume of 5 km^3 (Connor et al., 2011; Gevorgyan et al., 2018). The Subatan tuff outcrops at the base of the volcanic succession in the Vardenis volcanic highland (Fig. 2.3e), and is an at least 25m thick massive ignimbrite deposit which includes both magmatic and lithic fragments. Unfortunately, because a single quarry is the only known outcrop of this ignimbrite, it is not possible to make a volume estimate. This suggests that from early on in the post-collisional volcanic history of the region there were large volcanoes capable of producing caldera-forming eruptions.

A large Pliocene sector collapse volcaniclastic deposit (the "Goris strata") covers ~400 km^2 to the south of the Syunik highland (Fig. 2.4), and also requires a large polygenetic volcano to have formed in the past. Tephra fallout layers, which likely formed in Plinian eruptions are found in sedimentary units at the base of lavas in Syunik (Joannin et al., 2010). They must be older than the monogenetic lava flows which cover these sediments (Ollivier et al., 2010). Other pumice fall deposits are seen in Vardenis, where the deposit thickness is over 20 m (Fig. 2.3i), and to the east of Syunik where a distal deposit (~3m thick) is ~25 km to the east of Ishkhanasar- the nearest large volcano (Fig. 2.3j).

Lava flows have been produced by both polygenetic and monogenetic volcanoes. Holocene lava flows from monogenetic vents (Fig. 2.3c, d) travelled between ~ 100m and ~ 20 km from their eruption vent. Large (2250 km^3), fissure-fed 'flood basalt' style lava flows are found predominantly in some of the older (~3-2.05 Ma) volcanic successions in the northern Lesser Caucasus (Sheth et al., 2015).

Small scoria cones are well preserved across much of the southern Lesser Caucasus volcanic field (183 mapped in Syunik; Fig. 2.3b, c, d, g, h; Fig. 2.4), and are often clustered (Fig. 2.3b; Fig. 2.4). The positive relief of these scoria cones, and the lava flows that extrude from them through *boccas* (a vent on the lower flank of the cone from which lava issues; Fig. 2.3d) are indicative of internally driven, rather than phreatomagmatic eruptive processes.

2.2.2 Geochronological constraints

Previous geochronological studies have constrained the ages of the volcanic deposits upon which this thesis focuses as late Pliocene or younger, although the oldest post-collisional volcanism in the Lesser Caucasus has been dated to 10 Ma (Arutyunyan et al., 2007). Northern Lesser Caucasus data (Neill et al., 2013; Neill et al., 2015) used for comparison with the studied samples in Chapter 3 is ~2.5 Ma or younger, based on a K-Ar age for one of the "valley series" lavas at the base of the sampled section in the Shirak province (Fig. 2.1) of NW Armenia (Jrbashian and Gukasyan, 2002).

Volcanic rocks from further south (the data for which are presented in this thesis) were all collected from Quaternary volcanic highlands. A limited number of ages from the Syunik volcanic highland (S in Fig. 2.1; Fig. 2.3) suggest volcanism ranges from 1.3 to 0.11 Ma. This is based on two Ar-Ar ages of pumice layers in diatomaceous sediments (Fig. 2.4; Joannin et al., 2010), along with K-Ar ages of local lava flows which overlie the sediments (Fig. 2.4; Ollivier et al., 2010). Archaeological evidence from ^{14}C dating of petroglyphs and burial tombs around the youngest lavas in Syunik (Fig. 2.3) suggest volcanism may extend to within the last 5 ka, while in Vardenis there are historical records of an eruption at Porak (Fig. 2.3c) at around 3 ka (Karakhanian et al., 2002). These ages are very similar to the estimated age span of the nearby Gegham volcanic highland (G in Fig. 2.1) of 1.2-0.02 Ma (Lebedev et al., 2013), based on K-Ar dating. See Chapter 5 for more details.

2.3 Summary

The pre-Miocene geology of the Lesser Caucasus consists of three accreted tectonic terranes: the Lesser Caucasus volcanic arc, the Sevan-Akera suture zone and ophiolites, and the South Armenian block micro-continental fragment. These three terranes accreted by the subduction and closure of both the Northern and Southern Neotethys, with closure of the Southern Neotethys ultimately leading to the Arabia-Eurasia continent-continent collision. Following continental collision, post-collisional volcanism has produced widespread volcanic units since 10 Ma. All the post-collisional volcanic rocks for which geochemical data are presented in this

thesis are younger than 3 Ma. Eruptive products range from basanite to rhyolite in composition, and deposit types include lava flows, scoria cones, ignimbrites, volcaniclastic tuff layers, debris flows, and fissure-fed flood basalts. The following chapters explore the geochemistry, geochrononology and petrology of these volcanic rocks, with a strong emphasis on those samples from the southern Lesser Caucasus.

3. The Thickness of the mantle lithosphere and collision-related volcanism in the Lesser Caucasus

3.1 Introduction

The Lesser Caucasus mountains sit close to the edge of the Zagros Core region of thick mantle lithosphere, and therefore close to a transition from thick to thin lithosphere. These mountains thus provide an opportunity to look at the influence of lithospheric thickness on the geochemistry of collision-related magmas. Figure 3.1 shows the four volcanic highlands considered in this study, which form a NW-SE transect almost orthogonal to contours of lithospheric thickness from Priestley et al. (2012), which increase from NW to SE. It should be noted that the resolution on these lithospheric thickness estimates is limited by the 30-50 km vertical resolution of the seismic tomography data (McKenzie and Priestley, 2008). The Priestley et al. (2012) model is used because it is likely to give better local resolution in the Lesser Caucasus region than other global lithospheric thickness studies (Priestley and McKenzie, 2006; Priestley and McKenzie, 2013).

Volcanic rocks from the SE of this transect, where the lithosphere is thought to be thicker, are known to be more potassic than volcanic rocks from the NW (Meliksetian, 2013). This chapter provides the first complete geochemical dataset for volcanic rocks from the SE of the Lesser Caucasus. This dataset includes a complete range of compositions from basanite to rhyolite, which are used to evaluate the extent to which crustal contamination is an important component of magma petrogenesis. The geochemistry of the more primitive mafic volcanic rocks is compared between the NW and SE of the Lesser Caucasus, in order to understand how thicker lithosphere in the SE might influence the geochemistry of volcanic rocks found there. In order to indicate how thicker mantle lithosphere might influence the composition of magmas, volcanic rocks from a region of very thick lithosphere (> 200 km) in NW Iran (Fig. 3.1; Allen et al., 2013) are used as an end-member comparison of melting in a thick lithosphere regime.

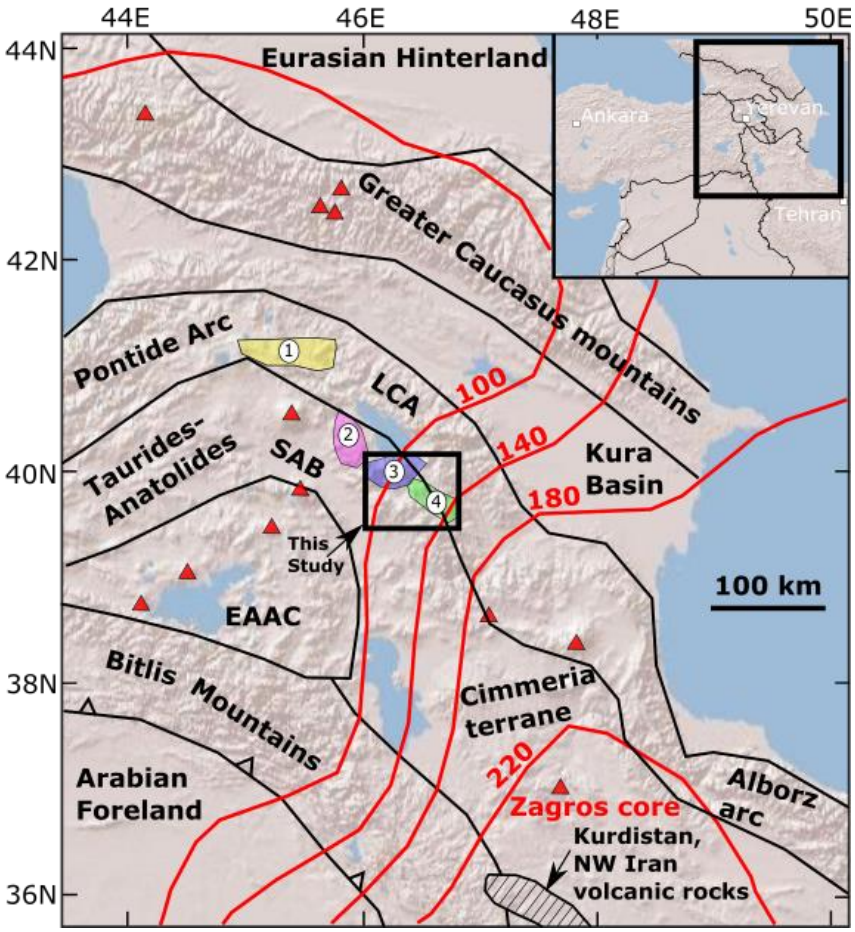

Figure 3.1 Location of tectonic terranes, the region of thick lithosphere, and the Lesser Caucasus volcanic highlands within the Arabia-Eurasia collision zone.

Terrane map of the Caucasus region with inset showing the location of the Caucasus mountains. The major tectonic blocks are labelled, which from north to south are: Greater Caucasus, Kura Basin, Pontides-Lesser Caucasus (LCA)-Alborz Mesozoic-early Cenozoic arc, Taurides-Anatolides-South Armenian Block (SAB)-Cimmeria microcontinent terranes, East Anatolian Accretionary Complex (EAAC), Bitlis Mountains and the Arabian foreland. Terrane boundaries are after Neill et al. (2015). Red triangles denote the locations of major composite volcanoes. The locations of volcanic highlands which are used for the geochemical comparison which forms the focus of this study are shown by the coloured fields. These are labelled as 1- Shirak and Lori (Neill et al., 2013; Neill et al., 2015); 2- Gegham (Savov, unpublished); 3- Vardenis; and 4- Syunik. New data for this study are from volcanic highlands 3 and 4. These volcanic highlands are close to parallel with major tectonic boundaries in the collision zone. Volcanic rocks from NW Iran referred to in the text are from the region labelled at the bottom of the map. Contours of lithospheric thickness from Priestley et al. (2012) are shown in red, numbers give lithospheric thickness in km. The "Zagros Core" refers to the region of maximum lithosphere thickness in the collision zone.

3.2 Analytical Methods

3.2.1 Major and Trace Element concentrations

Sample preparation was done at the University of Leeds. 60-100g of rock was crushed in a TEMA agate mill. The agate was cleaned extensively between the crushing of each sample, including pre-contamination of the agate by the crushing of 50g of sample which was then discarded. Bulk-rock major and trace element

analysis of samples from this study was done at ACME Labs by Bureau Veritas minerals, in Vancouver, Canada, and at Royal Holloway University, London.

For analysis at ACME Labs, samples were heated to 1000°C to determine loss on ignition (LOI), and then fused in a platinum-gold crucible with a lithium tetraborate flux. The resulting fusion beads were then analysed by XRF for major elements. Two internal ACME standards reproduced expected values to better than 3 % (for all oxides > 1 wt %). Trace element concentrations were determined by ICP-MS on the fused beads after digestion in nitric acid. Analysis of Ni concentrations involved digestion in aqua regia at 95°C. Two internal ACME standards reproduced expected values to better than 10% for trace elements. Values for internal and external standard data are shown in Appendix A.

Analysis at Royal Holloway was by inductively coupled plasma optical emission spectroscopy (ICP-OES) for major elements and some high abundance trace elements (Sr, Zr, Ni) and ICP-MS for low abundance trace elements. Major element analyses followed the methods described by Walsh et al. (1981) and Garbe-Schönberg (1993). The relative standard deviation on the external standards NIM-G, NIM-L, BHVO-1, RGM-1 and STM-1, as well as internal standards was better than 5% (for all oxides > 1 wt %). Trace elements were analysed after HNO_3-HF-$HClO_4$ digestions. Prior to analysis, samples were spiked with 5 ng per ml of indium (In) and rhenium (Re) for internal standardization. For analytical quality control, five international reference materials were analysed: NIM-G, NIM-L, BHVO-1, RGM-1 and STM-1. The standards analysed as unknowns generally gave trace element concentrations that deviated by < 15% from literature values- the results of these measurements are also shown in Appendix A.

3.2.2 Sr-Nd isotope ratios

Thermal Ionization Mass Spectrometry (TIMS) was used for the analysis of $^{87}Sr/^{86}Sr$ and $^{143}Nd/^{144}Nd$. Strontium (Sr) and Neodymium (Nd) were extracted from unspiked rock powders that were dissolved in an HNO_3: HF acid mixture (1:4), followed by conventional ion-exchange chromatographic techniques at the University of Leeds. Sr and Nd isotope ratios were measured on a *ThermoScientific* Triton multi-collector mass spectrometer running in static mode. The normalization value for fractionation of $^{87}Sr/^{86}Sr$ was $^{86}Sr/^{88}Sr = 0.1194$; that of $^{143}Nd/^{144}Nd$ was $^{146}Nd/^{144}Nd = 0.7219$.

Instrument errors for determinations of $^{87}Sr/^{86}Sr$ and $^{143}Nd/^{144}Nd$ are reported as the standard error, 2σ, (i.e. 2 standard deviations about the mean using 200-240 measurements). External precision (2σ) for Sr and Nd isotopic ratios from successive replicate measurements of primary standards was better than 35 ppm for the NIST SRM-987 International Reference Standard ($^{87}Sr/^{86}Sr = 0.710260$ for 9 runs averaged, with a standard deviation of 1.1 $x10^{-5}$) and better than 25 ppm for the La Jolla Nd International Reference Standard ($^{143}Nd/^{144}Nd = 0.511842$ for 11 runs averaged, with a standard deviation of 2.5 $x10^{-5}$). USGS standard BHVO-1 was also run as a validation material throughout the run period for both $^{87}Sr/^{86}Sr$ and $^{143}Nd/^{144}Nd$. Once corrected to an NIST SRM 987 preferred value of 0.710246 using the accompanying primary standard measurement, all measurements of $^{87}Sr/^{86}Sr$ for BHVO-1 reproduce a literature value of 0.703475 to within 2σ (Weis et al., 2006). All measured $^{87}Sr/^{86}Sr$ ratios were corrected to the literature NIST SRM 987 only. For Nd isotopes, all samples were corrected to the literature value of BHVO-1 (0.512986) giving an average correction of 0.00002. The total chemistry blanks for Sr and Nd were negligible during the period of measurements (0.4 ng for Sr and 0.3 ng for Nd).

3.3 Petrography

Southern Lesser Caucasus volcanic rocks are generally very fresh, with generally low loss on ignition (LOI) values (usually <1%) for the majority of mafic samples. The groundmass can sometimes contain minor amounts of clay minerals, but in many cases it is very fresh, with small pockets of volcanic glass present in a minority of samples (Table 3.1).

Tephrites, trachybasalts and trachybasaltic andesites from Syunik always contain phenocrysts (>0.3mm) of clinopyroxene, and may have olivine, amphibole and apatite phenocrysts. Clinopyroxene is ubiquitous and normally occurs as glomerocrysts (Fig. 3.2f). Some samples have abundant olivine microphenocrysts (Fig. 3.2d) and phenocrysts (up to 600μm), although olivine is generally restricted to the most mafic samples (low silica trachybasaltic andesite or more mafic).

Amphibole phenocrysts are common (up to 2cm), and occur across the compositional range (Fig. 3.2a). In several samples amphibole is absent, or partially

Table 3.1 Mineralogy of selected southern Lesser Caucasus samples

Phenocryst and groundmass minerals for selected volcanic rocks from the southern Lesser Caucasus. Volcanic field abbreviations: V- Vardenis; S- Syunik. Mineral abbreviations: ol- olivine; cpx- clinopyroxene; plag- plagioclase; ox- Fe-Ti oxide; kspar- potassium feldspar; qtz- quartz; amph- amphibole; bio- gfgfgf biotite; ap- apatite. Mineral texture abbreviations: xen- xenocrystic; pseud- pseudomorphic. Rock name abbreviations: B, basalt; R, rhyolite; TB, trachybasalt; TBA, trachybasaltic andesite; TA, trachyandesite; Tr, trachyte; Te, tephrite/basanite; PTe, phonotephrite.

Sample	High-land	Volcano/place	Eruptive type	Rock name	#Mg	Phenocrysts	Groundmass
6.27.08.	V	Khrbekner	Lava	TBA	56.2	ol, cpx, plag	plag, cpx, ox,
4.1.12	V	Tsovak pyroclastic flow	Pumice	R	17.3	kspar, plag, qtz	glass
5.1.13	V	Smbatasar	Lava	TA	50.9	cpx, plag, amph	plag, ox, cpx
5.1.15	V	Geghagar tuff	Ignimbrite	R	44.5	kspar, plag, phlog, qtz	glass
5.3.15	V	Porak	Lava	TA	53.9	cpx, plag	plag, cpx, ox
5.4.15	V	Zhiligyol	Lava	TA	51.1	cpx, qtz (xen)	plag, glass, ox, cpx
5.5.15	V	Vent W. of Zhiligyol	Plug	R	17.6	kspar, plag, bio, qtz	altered
5.9.15	V	Lake Al-Lich	Plug	Tr	29.5	plag, phlog, kspar, cpx	kspar, qtz, ox, cpx
6.3.15	V	Torgomayr	Lava	TBA	51.4	Cpx	plag, bio, ox
7.2.15	V	Dome E. of Trdatanist	Plug	R	25.4	kspar, qtz, plag, bio	altered
7.4.15	V	S. slopes of V upland	Lava	TA	54.8	cpx, amph (pseud), plag	plag, cpx, ox, glass
7.5.15	V	S. slopes of V upland	Lava	TBA	54.0	cpx, plag, amph	plag, cpx, ox, ol
1.4C.08	S	Garusar	Scoria	TBA	50.8	cpx, amph	plag, cpx, ox
2.5.08	S	Shinuayr	Bomb	TBA	50.5	cpx, amph, ol	glass, plag, ox, cpx
2.6.08	S	Morutumb	Bomb	TBA	48.8	cpx, amph, ol, ap	plag, glass, cpx, ox
2.7.08	S	Yerakov Blur	Bomb	PTe	48.6	amph, cpx	glass, plag, ox, cpx
2.9.08	S	Pokr Chobanasar	Bomb	TBA	52.5	cpx, amph, ol	plag, cpx, ox
2.10.08	S	Barurtumb	Lava	B	66.8	ol, cpx	plag, cpx, ox
5.21.08	S	Berd	Lava	TBA	52.7	ol, cpx	plag, ox
6.24.08	S	Tekblur	Scoria	PTe	48.4	Cpx	glass, plag
3.10.10	S	Unknown	Lava	Tr	42.5	plag, cpx, amph (pseud)	plag, ox, cpx
3.11.10	S	Unknown	Lava	TA	46.5	cpx, amph (pseud)	plag, ox, cpx
4.19.10	S	Ishkhanasar	Lava	TA	44.5	plag, amph	Plag
5.5.12	S	Tshkhouk	Lava	TA	50.0	cpx, plag, ox	plag, ox, cpx
8.2.15	S	Khozazblur	Bomb	TB	54.1	cpx, ol	plag, cpx, ox
8.3.15	S	Verjiblur	Bomb	TBA	52.6	cpx, amph	plag, cpx, ap
8.7.15	S	Marakhlasar	Scoria	PTe	52.8	amph, cpx	glass, plag
9.1.15	S	Spiovblur	Plug	TBA	51.6	cpx, amph, plag, ol, ap	plag, cpx, ox
9.2.15	S	Chobanasar	Bomb	TB	55.3	cpx, ol, amph (pseud)	plag, cpx, ox
10.2.15	S	Kyorpasar	Lava	TBA	51.4	Aphyric	plag, cpx, ol, ox
10.3.15	S	Mets Yerkvoryak	Scoria	TBA	51.5	plag, ol, cpx, ox	glass
10.6.15	S	Mets Yerkoryak	Scoria	TBA	51.6	Cpx	glass, plag, cpx, ox
11.1.15	S	Quarry, Shaqi village	Lava	TBA	46.3	plag, cpx	plag, cpx, ox
11.3.15	S	Sherepasar	Scoria	Te	54.0	cpx, ol, amph	plag, glass, cpx, ox

resorbed (Fig. 3.2c), due to disequilibrium conditions prior to eruption. The apatite phenocrysts can reach up to 2mm in size in some cases (Fig. 3.2b). The common occurrence of hydrous minerals, such as amphibole and apatite, is noteworthy in

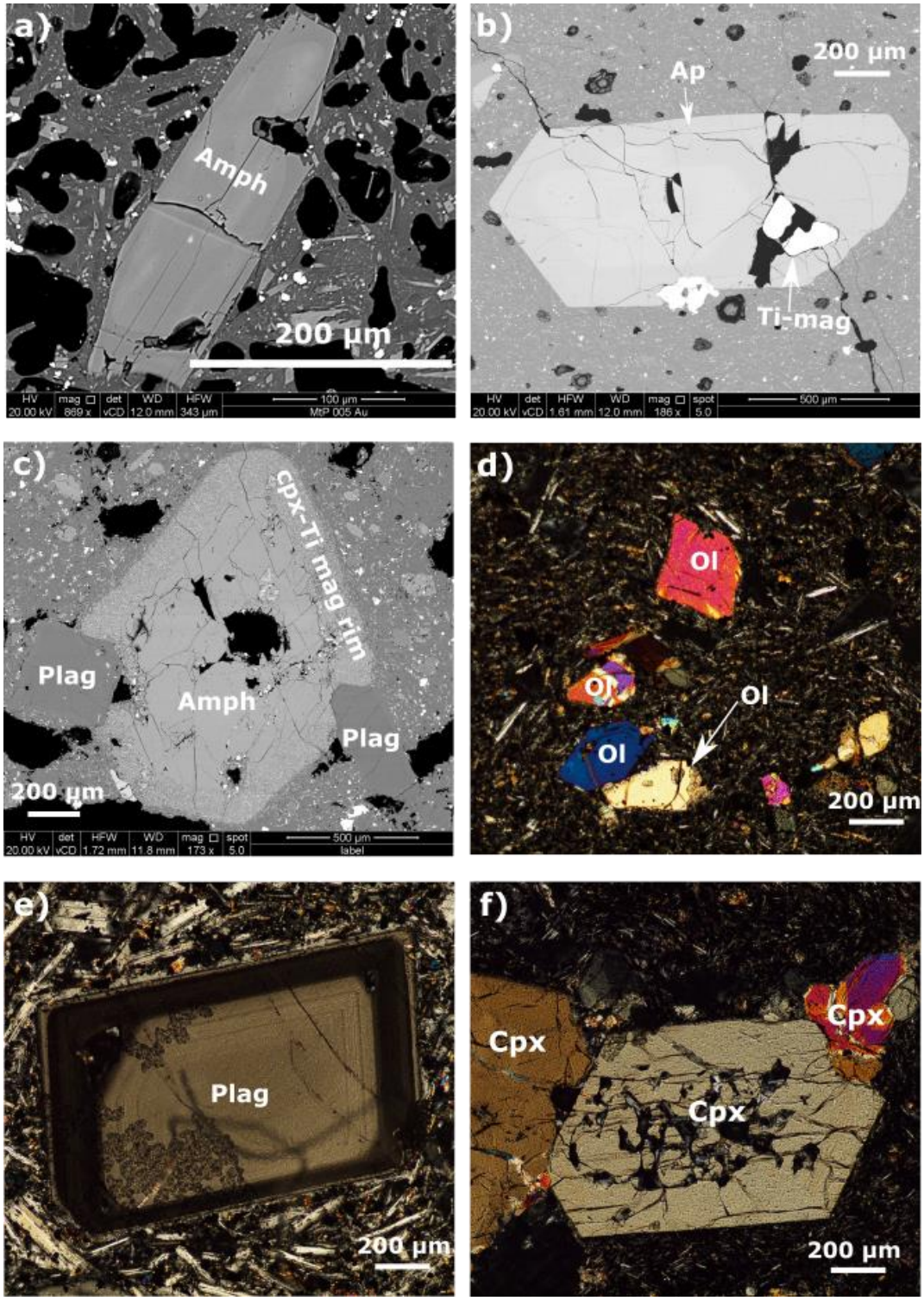

Figure 3.2 Representative back-scattered electron images and photomicrographs.

(a) Unaltered amphibole (amph) phenocryst in trachybasaltic andesite scoria from Syunik. Groundmass composed of clinopyroxene, plagioclase and oxides. (b) Large apatite (Ap) phenocryst >1mm in diameter, with oxide inclusions in trachybasaltic andesite lava, Syunik. (c) Large amphibole phenocryst with overgrowing plagioclase (plag) grains in trachybasaltic andesite lava from Vardenis. The rim of the amphibole is broken down into oxides and clinopyroxene. (d) XPL image of olivine (Ol) phenocrysts in trachybasalt lava from Syunik. (e) XPL image of plagioclase phenocryst in trachybasaltic andesite lava with sharp compositional boundary between the core and rim (in extinction) of this crystal. (f) XPL image of clinopyroxene (cpx) glomerocryst in trachyandesite sample from Vardenis.

comparison to the volcanic rocks from the northern and central Lesser Caucasus, where such mineral phases are less common, certainly in the most mafic samples (Connor et al., 2011; Neill et al., 2013). Typical groundmass in mafic volcanic rocks from Syunik is composed of plagioclase, clinopyroxene, and Fe-Ti oxides, with volcanic glass in some scoria samples. Note that plagioclase is only present in the groundmass and is not a phenocryst phase.

More evolved high-silica trachybasaltic andesites, trachyandesites and trachytes from Syunik show the appearance of abundant plagioclase phenocrysts. In some cases, these plagioclase crystals (up to 2mm) show evidence of multiple stages of crystallisation with distinct core to rim zonation (Fig. 3.2e). Amphibole also becomes a more common phenocryst phase, whereas clinopyroxene is less dominant. The groundmass is increasingly dominated by plagioclase. Rhyolites are common in the northern part of Syunik, where they commonly form obsidian flows.

In Vardenis all samples are trachybasaltic andesites or more evolved, and plagioclase is always a phenocryst phase. In one trachybasaltic andesite (Table 3.1-sample 6.3.15), biotite is also a phenocryst phase. Rhyolites from Vardenis commonly have biotite, plagioclase, quartz and potassium feldspar as phenocrysts, and a groundmass composed of quartz and potassium feldspar.

From the occurrence of different minerals in the range of rock types sampled across the Syunik and Vardenis volcanic highlands (34 samples, Table 3.1), it is possible to suggest a general order of crystallisation for both areas, which would likely have been: olivine + Fe-Ti oxides ± apatite; clinopyroxene + Fe-Ti oxides ± olivine ± amphibole; clinopyroxene + plagioclase + Fe-Ti oxides ± amphibole ± phlogopite; plagioclase + potassium feldspar + Fe-Ti oxides ± phlogopite. The predominant focus of this study is on the mechanism of mantle melting, which requires the effect of fractional crystallisation to be minimised. Based on this crystallisation sequence, the most mafic samples will not have fractionated feldspar, instead only fractionating mafic minerals. Using the major element data presented in section 3.4.2, it was ascertained that feldspar fractionates from 54 wt% SiO_2 and 4 wt% MgO. Only samples with more mafic compositons are used to investigate questions of magma petrogenesis.

3.4 Geochemistry of southern Lesser Caucasus volcanic rocks

3.4.1 New geochemical data

While recent work (Neill et al., 2013; Neill et al., 2015) has provided important new geochemical data for collision-related volcanism in the northern Lesser Caucasus, this chapter presents the first comprehensive dataset for mafic volcanic rocks from the southern part of the Lesser Caucasus (Table 3.2). All samples are from the Vardenis and Syunik volcanic highlands (highlands 3 and 4 in Fig. 3.1; see also Chapter 2). Table 3.2 also gives the co-ordinates for all the mafic samples in the Vardenis and Syunik volcanic highlands. Sampling in the region covers the complete stratigraphic range, but there was a bias towards the relatively young eruptive centres in order to collect the least altered samples for geochemical analysis. The studied rock types range from basanite to rhyolite, although Table 3.2 only includes data for the most mafic samples, which form the main focus of this chapter. The complete dataset (including the more felsic samples) can be found in Appendix A.

3.4.2 Major element characteristics

Across the Lesser Caucasus there is a great diversity in the compositions of the volcanic rocks within each volcanic highland, with most showing a complete compositional range from basalt to rhyolite (Fig. 3.3). Rhyolites are also present in the northern Lesser Caucasus (Karapetian et al., 2001), although they were not sampled for the Neill et al. (2013) study. Southern Lesser Caucasus samples, with Syunik being the most extreme, have more alkaline compositions compared to those from the north, with the largest Na_2O and K_2O variations between north and south in the most mafic samples (Fig. 3.3). Southern Lesser Caucasus samples are also more potassic when compared to their northern counterparts (shoshonitic *versus* calc-alkaline series; Fig. 3.4a). As well as being more alkaline, mafic southern Lesser Caucasus samples extend to lower SiO_2 contents.

On some major element variation diagrams, such as MgO *versus* SiO_2 (Fig. 3.4b) the trends are fairly similar for northern and southern Lesser Caucasus samples. However other elements, notably P, display a significant geographic gradient in concentration for the most mafic samples, from 0.4 wt % P_2O_5 in the

Table 3.2 Major and Trace Element compositions of mafic volcanic rocks from the Vardenis and Syunik volcanic fields in the Southern Lesser Caucasus

Volcanic field	Vardenis	Vardenis	Vardenis	Vardenis	Vardenis	Vardenis	Vardenis
Sample	6.27.08	7.29.08	7.30.08	7.32.08	2.1.12	1.1.13	1.2.13
Erup. type	Lava	Lava	Bomb	Lava	Lava	Lava	Lava
Latitude	40.0905	40.14205	40.0768	40.07712	40.10283	40.02458	40.08497
Longitude	45.414	45.6192	45.51587	45.5256	45.39072	45.83628	45.83638
Elevation (m)	2257	2101	2340	2280	2188	2347	2375
Lab analysis[1]	RH	RH	ACME	RH	ACME	ACME	ACME
SiO_2	51.62	50.94	53.96	52.87	52.17	51.71	51.93
TiO_2	1.20	1.34	1.01	1.23	1.11	1.39	1.38
Al_2O_3	16.31	16.37	16.47	16.93	17.40	17.31	17.39
Fe_2O_3 (tot)[2]	9.61	9.69	6.82	9.49	7.77	8.34	8.39
MnO	0.13	0.14	0.12	0.14	0.13	0.13	0.13
MgO	6.23	6.36	4.08	4.40	4.60	4.15	4.12
CaO	8.54	8.43	7.97	7.93	8.27	7.34	7.32
Na_2O	3.93	4.54	4.36	4.61	4.62	4.52	4.61
K_2O	2.27	2.00	3.37	2.13	2.76	3.08	3.08
P_2O_5	0.52	0.72	0.61	0.77	0.95	1.23	1.23
Total	98.45	99.56	99.49	99.56	100.25	100.09	100.34
LOI			0.59		0.35	0.75	0.61
#Mg	56.2	56.5	54.2	47.9	54.0	49.6	49.3
Ni	77.6	86.8	18.8	45.9	32.8	12	32
La	39	57	52	58	84	64	96
Ce	76	99	91	102	148	112	180
Pr	9.0	10.8	9.9	11.0	16.3	12.1	20.6
Nd	37	41	34	42	57	41	73
Sm	6.6	7.3	5.5	7.6	8.0	6.4	10.0
Eu	1.9	2.1	1.5	2.1	2.2	1.7	2.6
Gd	5.0	5.8	4.5	5.9	6.1	5.0	7.4
Tb	0.8	1.0	0.6	1.0	0.7	0.7	0.8
Dy	3.6	4.3	3.7	4.7	3.8	3.5	4.5
Ho	0.7	0.8	0.7	0.9	0.7	0.6	0.7
Er	1.9	2.2	2.0	2.3	1.7	1.8	1.9
Tm	0.3	0.4	0.3	0.4	0.3	0.3	0.3
Yb	2.0	2.5	1.9	2.4	1.6	1.7	1.7
Lu	0.3	0.4	0.3	0.4	0.3	0.3	0.3
Ba	778	754	768	707	1098	881	1184
Hf	3.4	4.1	4.4	4.1	4.3	4.5	4.6
Nb			18.9		28.3	22.2	31.6
Rb			67.7		41.1	56.9	35.4
Sr	1161	1217	845	1142	1890	1026	2084
Pb	15.9	18.23		14.43			
Ta	1.1	1.1	0.9	1.0	1.2	1.2	1.5
Th	6.3	5.7	11.8	5.9	9.4	9.4	5.9
U	1.5	1.5	3.3	1.2	1.9	2.4	1.4
Zr	141	188	187	187	195	209	213
Y	19.4	24.9	19.9	26.8	18.9	18.5	21.2

[1]Laboratory where samples were analysed: ACME- ACME labs, Bureau Veritas minerals, Vancouver, Canada; RH- Royal Holloway University, UK.
[2]Royal Holloway major element data report Fe as FeO*, which was recalculated to Fe_2O_3 (tot)

Table 3.2 continued.

Volcanic field	Vardenis	Vardenis	Vardenis	Vardenis	Vardenis	Syunik	Syunik
Sample	3.2.13	3.3.13	4.02.15	5.06.15	6.03.15	1.4A.08	2.6.08
Erup. type	Lava	Lava	Lava	Lava	Lava	Scoria	Bomb
Latitude	40.05927	40.07163	40.17904	39.96908	39.98746	39.44133	39.48285
Longitude	45.79923	45.78805	45.6186	45.68293	45.61326	46.08888	46.2693
Elevation (m)	2538	2539	1956	2872	3454	1876	1969
Lab analysis[1]	ACME	ACME	ACME	ACME	ACME	RH	RH
SiO_2	52.81	51.60	51.51	51.47	53.73	50.52	53.23
TiO_2	1.29	1.37	1.33	1.52	1.08	1.43	1.12
Al_2O_3	16.42	17.23	16.77	16.47	17.09	16.31	17.11
Fe_2O_3 (tot)[2]	7.87	8.25	8.57	8.60	7.60	9.97	8.65
MnO	0.14	0.13	0.14	0.14	0.13	0.14	0.13
MgO	4.03	4.12	6.15	4.56	4.06	5.20	4.15
CaO	7.49	7.34	8.33	8.59	7.24	8.74	6.87
Na_2O	4.65	4.85	4.66	4.20	4.79	4.36	5.03
K_2O	3.11	3.13	2.04	2.26	2.75	2.73	3.20
P_2O_5	0.97	1.21	0.73	0.93	0.90	1.02	0.96
Total	99.62	99.66	100.41	99.46	99.78	99.40	99.59
LOI	0.7	0.27	0.06	0.62	0.27		
#Mg	50.4	49.7	58.7	51.2	51.4	50.8	48.8
Ni	7.1	23.1	16.3	18.8	23.7	49.9	52.4
La	21	79	89	75	75	89	95
Ce	35	151	167	138	132	170	172
Pr	3.7	16.8	19.4	15.7	14.5	18.8	18.0
Nd	13	59	68	58	50	73	67
Sm	2.5	8.9	9.9	8.6	8.0	11.3	10.3
Eu	0.8	2.4	2.7	2.4	2.0	2.9	2.7
Gd	2.5	6.7	7.7	7.1	5.8	8.0	7.5
Tb	0.4	0.8	0.9	0.8	0.7	1.1	1.0
Dy	2.1	4.5	4.6	4.6	3.8	4.3	4.0
Ho	0.4	0.8	0.7	0.9	0.7	0.8	0.7
Er	1.3	2.3	2.1	2.4	2.0	2.0	2.0
Tm	0.2	0.3	0.3	0.3	0.3	0.3	0.3
Yb	1.2	2.1	2.0	2.1	1.8	2.0	2.0
Lu	0.2	0.3	0.3	0.3	0.3	0.3	0.3
Ba	563	1162	1171	947	962	1109	1057
Hf	2.8	4.4	5.5	4.5	4.3	4.5	5.1
Nb	8.2	27.6	28.3	20.0	25.8		
Rb	57.3	42.5	47.9	37.4	43.4		
Sr	495	1932	1899	1537	1411	2003	1722
Pb						15.2	18.0
Ta	0.6	1.2	1.2	1.0	1.0	1.6	1.8
Th	6.6	6.9	7.1	6.9	7.1	6.5	8.2
U	1.6	1.7	1.6	1.5	1.4	1.4	1.7
Zr	114	210	245	202	215	199	234
Y	12.5	23.6	21.9	25.0	21.4	23.3	23.4

Table 3.2 Continued.

Volcanic Field	Syunik	Syunik	Syunik	Syunik	Syunik	Syunik	Syunik
Sample	2.7.08	2.8.08	2.9.08	2.10.08	5.21.08	6.24.08	6.25.08
Eruptive type	Bomb	Lava	Bomb	Lava	Lava	Scoria	Bomb
Latitude	39.4587	39.4601	39.48452	39.46787	39.75548	39.68745	39.68745
Longitude	46.24037	46.26768	46.2177	46.25762	45.85745	45.91403	45.91403
Elevation (m)	1849	1958	2107	1956	2871	2514	2514
Lab analysis[1]	RH	RH	RH	RH	RH	RH	RH
SiO_2	50.44	51.74	51.58	47.08	53.46	48.97	48.91
TiO_2	1.32	1.14	1.07	1.31	1.05	1.56	1.60
Al_2O_3	16.82	16.26	16.49	14.39	16.41	16.28	16.37
Fe_2O_3 tot[2]	9.31	8.75	8.46	11.45	8.62	10.06	10.14
MnO	0.14	0.13	0.13	0.15	0.13	0.14	0.14
MgO	4.44	4.77	4.71	11.65	4.84	4.77	4.66
CaO	8.16	8.61	7.03	9.83	7.12	8.63	8.81
Na_2O	5.12	4.76	4.90	3.29	4.45	4.47	4.02
K_2O	3.25	2.89	3.33	1.19	3.02	3.03	3.07
P_2O_5	1.12	1.00	0.93	0.53	0.92	1.30	1.36
Total	99.20	99.17	97.78	99.74	99.15	98.19	98.05
LOI							
#Mg	48.6	51.9	52.5	66.8	52.7	48.4	47.6
Ni	45.0	56.7	85.1	275.5	66.9	38.3	38.6
La	99	93	89	32	85	97	98
Ce	193	175	159	66	150	194	198
Pr	21.4	18.7	16.8	8.3	15.9	21.8	22.1
Nd	84	72	63	34	60	86	87
Sm	12.7	11.1	9.5	6.5	9.4	13.2	13.5
Eu	3.3	2.9	2.6	1.8	2.4	3.3	3.4
Gd	8.7	7.7	7.0	4.9	7.0	8.9	9.3
Tb	1.2	1.1	1.0	0.9	1.1	1.2	1.3
Dy	4.3	4.0	3.7	4.0	4.1	4.5	4.7
Ho	0.8	0.7	0.7	0.8	0.8	0.8	0.8
Er	2.0	1.9	1.8	2.1	2.0	2.1	2.1
Tm	0.3	0.3	0.3	0.4	0.3	0.3	0.3
Yb	2.0	1.9	1.9	2.2	2.1	1.9	2.0
Lu	0.3	0.3	0.3	0.4	0.4	0.3	0.3
Ba	1220	1107	1192	430	1102	1176	1211
Hf	4.9	5.4	4.7	3.0	4.3	4.7	4.6
Nb							
Rb							
Sr	2531	1998	2050	1073	1585	2358	2576
Pb	16.7	17.5	19.9	9.0	15.7	17.2	23.2
Ta	1.7	1.7	1.6	0.7	1.3	1.7	1.8
Th	6.8	8.4	7.8	2.6	8.3	6.1	6.0
U	1.5	1.5	1.7	0.7	1.4	1.4	1.3
Zr	224	246	220	126	192	198	198
Y	24.1	20.6	20.5	22.2	23.0	24.3	23.5

Table 3.2 continued.

Volcanic Field	Syunik	Syunik	Syunik	Syunik	Syunik	Syunik	Syunik
Sample	4.16.10	8.02.15	8.03.15	8.04.15	8.05.15	8.06.15	8.07.15
Eruptive type	Lava	Bomb	Bomb	Lava	Bomb	Lava	Bomb
Latitude	39.56577	39.42896	39.4141	39.49615	39.49431	39.50412	39.50771
Longitude	46.21687	46.27307	46.28308	46.24583	46.24621	46.20926	46.20948
Elevation (m)	2731	1896	1603	2168	2185	2237	2314
Lab analysis[1]	RH	ACME	ACME	ACME	ACME	ACME	ACME
SiO_2	53.53	49.16	51.58	52.01	45.80	50.11	49.81
TiO_2	1.13	1.43	1.21	1.12	1.58	1.14	1.37
$A_{l2}O_3$	17.08	16.91	16.65	16.68	14.92	15.92	16.80
Fe_2O_3 tot[2]	8.48	9.03	7.66	7.26	9.56	7.28	8.15
MnO	0.12	0.14	0.13	0.13	0.16	0.13	0.13
MgO	4.02	5.37	4.29	4.54	7.77	4.44	4.55
CaO	7.71	8.66	8.01	7.23	10.02	8.60	8.29
Na_2O	4.75	4.23	4.48	4.31	4.30	4.78	4.62
K_2O	3.20	2.54	3.14	3.24	2.64	3.75	3.50
P_2O_5	0.93	1.24	1.06	0.98	1.27	1.18	1.17
Total	100.10	99.83	99.76	99.60	98.90	98.42	98.91
LOI		0.98	1.41	1.92	0.73	0.88	1.07
#Mg	48.4	54.1	52.6	55.3	61.7	54.7	52.8
Ni	37.5	66.3	25	66.3	117.1	19.9	29.6
La	82	101	94	94	75	103	98
Ce	152	197	175	177	158	190	193
Pr	16.0	23.1	20.0	19.6	19.6	21.3	22.7
Nd	60	81	71	68	75	76	82
Sm	9.0	11.7	9.7	9.5	11.0	10.4	11.7
Eu	2.4	3.1	2.6	2.5	3.0	2.8	3.0
Gd	6.5	8.0	6.8	6.6	7.6	7.4	7.6
Tb	0.8	0.9	0.8	0.7	0.9	0.9	0.9
Dy	3.9	4.6	4.0	3.8	4.7	4.3	4.6
Ho	0.8	0.7	0.7	0.7	0.8	0.7	0.7
Er	2.1	1.9	1.7	1.8	2.1	1.9	1.9
Tm	0.3	0.3	0.3	0.3	0.3	0.3	0.3
Yb	1.6	1.7	1.7	1.6	1.9	1.7	1.7
Lu	0.2	0.3	0.2	0.3	0.3	0.3	0.2
Ba	1152	1181	1180	1363	1093	1705	1446
Hf	4.3	4.5	4.5	4.6	3.7	4.7	4.6
Nb	24.5	37.8	28.4	31.1	24.1	31.8	28.8
Rb	37.0	34.9	43.0	46.7	31.3	53.3	44.2
Sr	1827	2150	2161	2198	2325	2812	2504
Pb							
Ta	0.9	1.4	1.2	1.4	0.9	1.4	1.2
Th	5.5	6.6	6.6	7.9	3.6	7.8	5.1
U	1.0	1.4	1.2	1.5	0.8	1.9	1.1
Zr	201	204	217	244	166	236	210
Y	23.6	21.7	19.5	20.0	23.4	21.1	20.3

Table 3.2 Continued.

Volcanic Field	Syunik	Syunik	Syunik	Syunik	Syunik	Syunik	Syunik
Sample	9.01.15	9.02.15	10.01.15	10.02.15	10.03.15	11.02.15	11.3.15
Eruptive type	Plug	Bomb	Bomb	Lava	Scoria	Lava	Scoria
Latitude	39.53042	39.51419	39.64401	39.64359	39.6413	39.62041	39.63605
Longitude	46.22106	46.23795	46.102	46.10184	46.10138	46.02615	46.03841
Elevation (m)	2738	2608	2811	2693	2614	2321	2536
Lab analysis[1]	ACME	ACME	ACME	ACME	ACME	ACME	ACME
SiO_2	51.60	47.68	47.89	51.35	51.44	49.60	47.27
TiO_2	1.22	1.78	1.26	1.48	1.46	1.25	1.80
Al_2O_3	17.40	15.80	15.58	16.93	16.91	16.87	15.49
Fe_2O_3 tot[2]	8.20	10.07	8.14	8.96	8.92	8.49	10.07
MnO	0.13	0.15	0.14	0.14	0.14	0.14	0.15
MgO	4.42	6.28	4.45	4.78	4.79	5.09	5.97
CaO	7.51	9.54	9.64	8.23	8.07	8.48	9.87
Na_2O	4.50	4.24	4.47	4.85	4.81	4.87	4.50
K_2O	3.06	2.10	3.87	2.11	2.13	2.75	2.52
P_2O_5	1.26	1.14	1.54	0.81	0.82	1.27	1.17
Total	99.94	99.68	97.74	99.93	99.9	99.19	99.04
LOI	0.49	0.77	0.55	0.18	0.29	0.22	0.08
#Mg	51.6	55.3	52.0	51.4	51.5	54.3	54.0
Ni	41.6	60.8	12.1	34	35.8	49	41.7
La	104	75	102	61	64	95	88
Ce	189	151	195	115	114	175	187
Pr	21.2	18.0	22.9	12.9	13.0	20.3	22.3
Nd	72	68	81	48	47	71	82
Sm	10.1	10.4	11.6	8.0	7.6	10.0	11.7
Eu	2.7	2.9	3.1	2.3	2.4	2.7	3.1
Gd	7.7	8.1	8.6	6.9	7.1	7.1	8.6
Tb	0.9	0.9	0.9	0.8	0.9	0.8	0.9
Dy	4.8	4.9	4.8	5.0	4.9	4.4	4.8
Ho	0.7	0.8	0.8	0.9	0.9	0.7	0.7
Er	2.1	2.0	2.1	2.6	2.5	1.8	2.0
Tm	0.3	0.3	0.3	0.4	0.4	0.3	0.3
Yb	1.8	2.0	2.0	2.4	2.3	1.7	1.7
Lu	0.3	0.3	0.3	0.4	0.4	0.2	0.2
Ba	1201	1022	1795	924	915	1301	1151
Hf	4.3	4.0	4.5	5.1	4.8	3.9	3.9
Nb	31.3	21.9	28.7	19.4	20.5	23.2	33.4
Rb	41.5	26.9	51.2	34.0	33.7	33.2	33.8
Sr	2032	2128	2889	1413	1363	2185	2348
Pb							
Ta	1.2	0.9	1.1	0.8	0.8	1.0	1.3
Th	6.0	3.2	7.1	4.8	4.9	5.5	5.5
U	1.1	1.0	1.1	1.0	1.1	1.0	1.3
Zr	218	177	202	240	235	169	190
Y	22.3	24.0	25.0	26.6	26.3	21.6	22.0

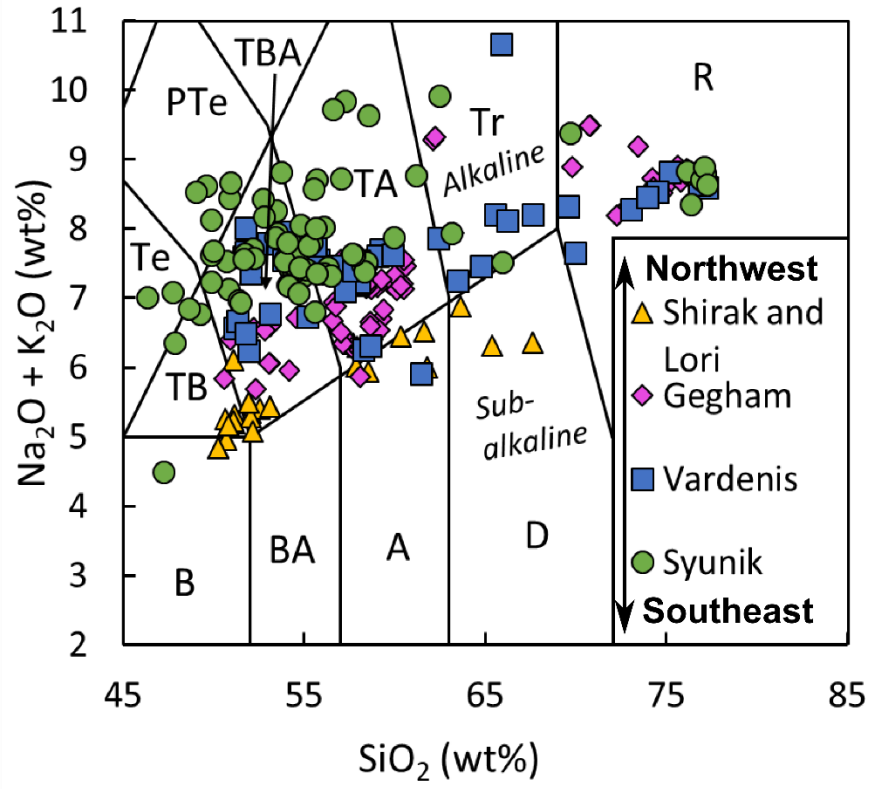

Figure 3.3 Total alkalis *vs* silica classification diagram

For volcanic rocks from across the Lesser Caucasus mountain chain. Classification boundaries are from Le Bas et al. (1986). Data for Syunik and Vardenis are from this study, while Shirak and Lori data are from Neill et al. (2013, 2015), in this and all subsequent figures. Gegham data are from Savov et al., (unpublished). Abbreviations for classification fields are as follows: B, basalt; BA, basaltic andesite; A, andesite; D, dacite; R, rhyolite; TB, trachybasalt; TBA, trachybasaltic andesite; TA, trachyandesite; Tr, trachyte; Te, tephrite/basanite; PTe, phonotephrite.

north to as high as 1.6 wt % in the south (Fig. 3.4c).

3.4.3 Trace element characteristics

MORB-normalised trace element patterns all show profiles typical of subduction-related volcanic rocks, with positive anomalies for Ba, K, Pb and Sr and negative anomalies for the high field strength elements (HFSE) Nb, Ta and Ti (Fig. 3.5). Superimposed on this is an additional enrichment in incompatible trace elements, in particular the light rare earth elements (LREE; Fig. 3.6), Sr, Ba and P, which becomes increasingly pronounced to the south of the transect. Due to the LREE enrichment, as well as a more moderate depletion in heavy rare earth elements (HREE), REE profiles become increasingly steep towards the south (Fig. 3.6)- with CI- normalised La/Yb ratios of 5 in the northern Lesser Caucasus compared to values as high as 40 in the south.

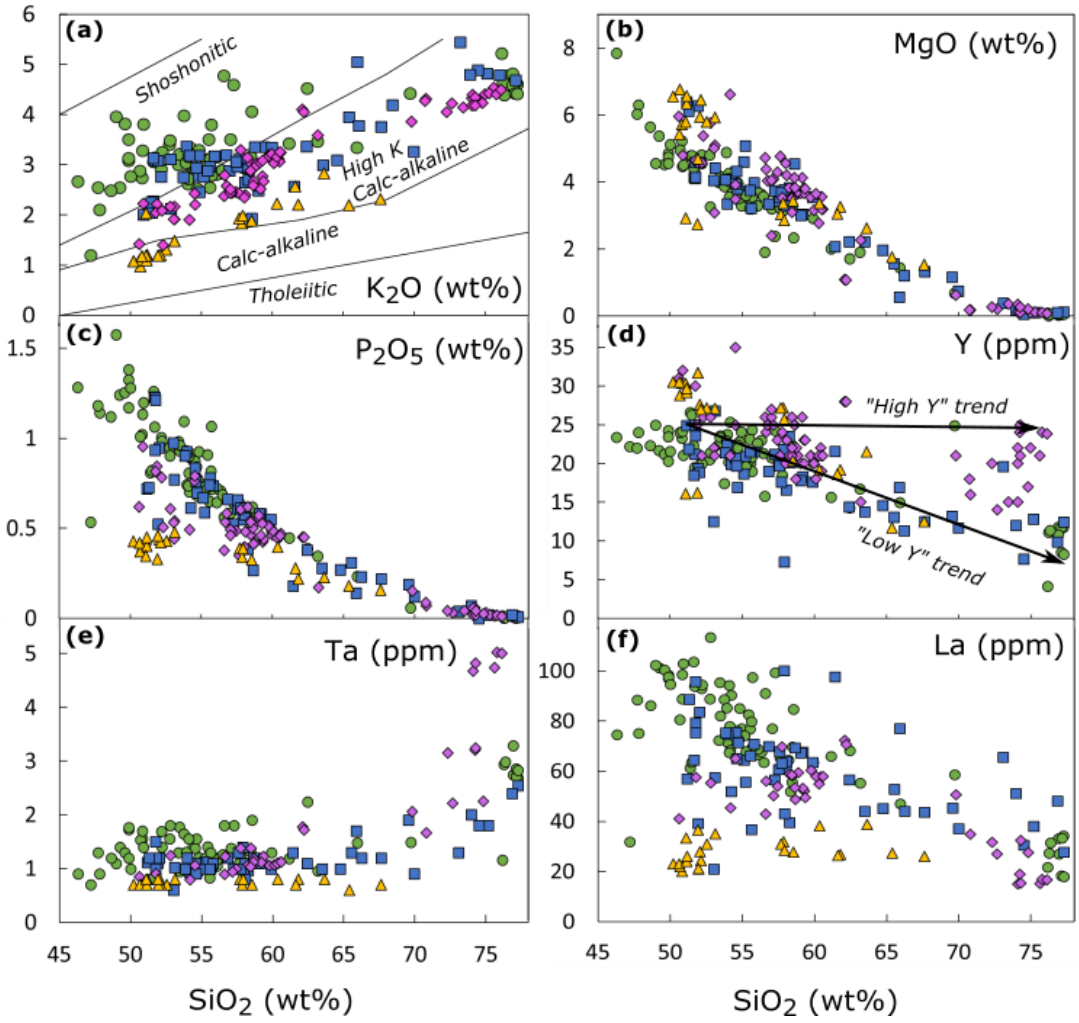

Figure 3.4 Major and trace element Harker diagrams

Selected major and trace elements plotted against SiO_2. a) K_2O, b) MgO, c) P_2O_5, d) Y, e) Ta, f) La. All major elements are recalculated to 100% on an anhydrous basis. Symbols and data sources are as in Fig. 3.3.

These additional enrichments do not resemble those of typical intraplate ocean island basalts (OIB), which show uniform enrichments in all the most incompatible trace elements, rather than the larger enrichments seen in the LREE relative to the HFSE (Fig. 3.5e), as exemplified by Ta and La in Figs 3.4e and f, respectively. These additional enrichments are seen most clearly in volcanic rocks from NW Iran (Fig. 3.5e), a region of very thick lithosphere- up to 220 km (Priestley et al., 2012). Figs 3.5a-d show that the variations in the composition of basalts within individual volcanic highlands are small, relative to the variations in composition between the highlands. Both the ubiquitous subduction ("arc") signatures, and additional enrichment are highlighted in Fig. 3.7. All samples plot

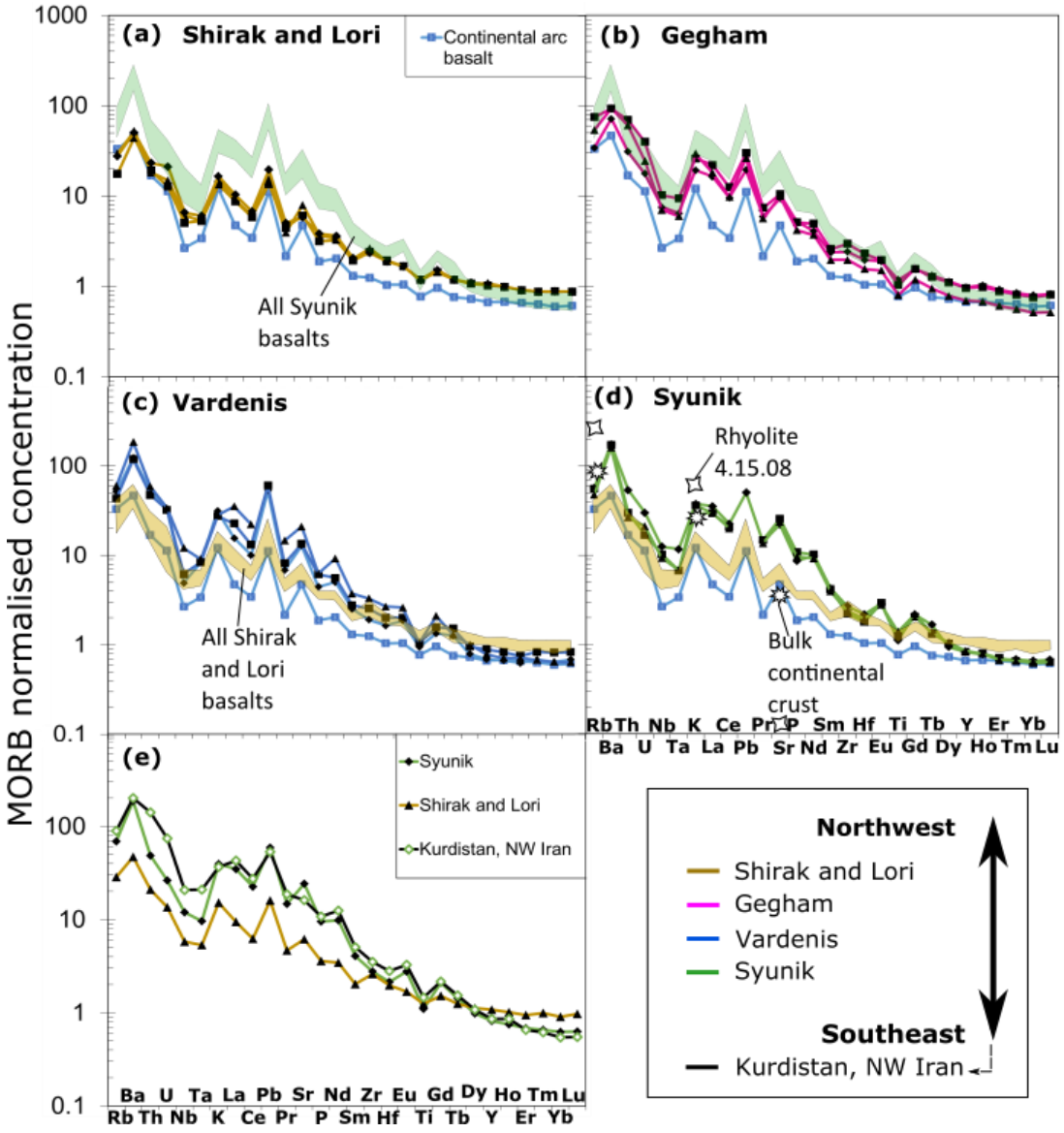

Figure 3.5 MORB-normalised trace element patterns of mafic end-member samples

Patterns for the Shirak and Lori (a), Gegham (b), Vardenis (c), and Syunik (d) volcanic highlands, which correspond to regions 1 to 4 in Fig. 3.1 respectively. The selected samples are the three samples with the highest MgO content (wt %) in each volcanic highland. Data sources are as in Fig. 6. For comparison, the total range of 'basalts' (< 52% SiO_2) from the Syunik volcanic highland is shown in (a) and (b) as the pale green field. The total range of Shirak and Lori basalts is shown as a gold field in (c) and (d). (d) also shows the composition of a Syunik rhyolite (diamonds) and bulk continental crust (stars) for Rb, K and Sr, in order to demonstrate whether these rhyolites are likely to be formed by assimilation and/or melting of continental crust. Composition of the continental crust from Rudnick and Gao (2014). The total compositional variability is illustrated in (e) where averages from the geographic extremes (Shirak in the north and Syunik in the south) are compared. Also shown here is a sample from Kurdistan, NW Iran from Allen et al. (2013), formed from melting in a region of very thick lithosphere. Normalisation factors from Sun and McDonough (1989). The average composition of Continental Arc basalt is from Kelemen et al. (2003).

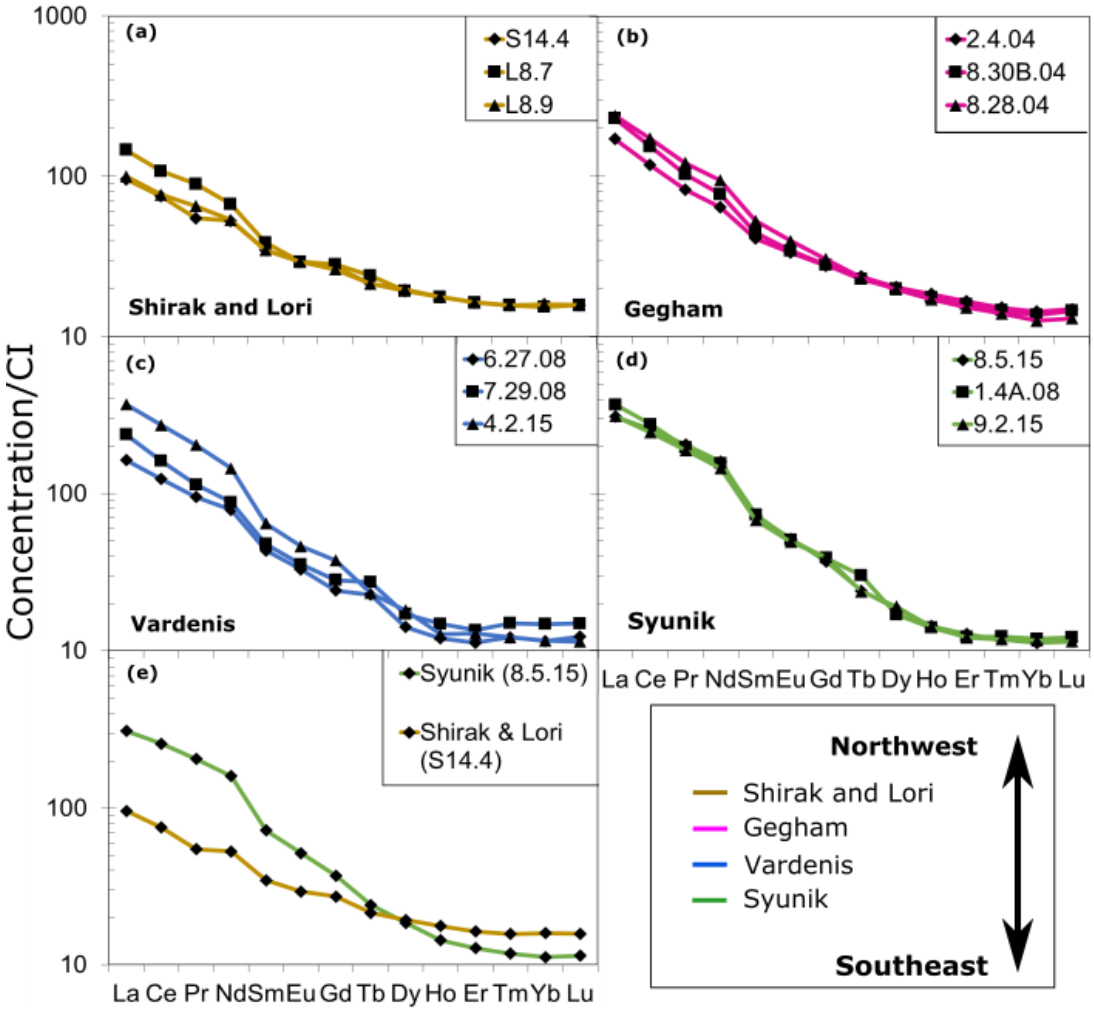

Figure 3.6 Chondrite normalised REE profiles of mafic end member samples

Samples from Shirak and Lori (a), Gegham (b), Vardenis (c) and Syunik (d) volcanic highlands. The total compositional variability is illustrated in (e) where samples from Syunik and Shirak are compared. Normalisation factors from Sun and McDonough (1989). Data sources as in Fig. 3.3.

above the mantle array, typical for rocks from volcanic arcs. However, the samples from the southern Lesser Caucasus have higher Th/Yb and Ta/Yb relative to their northern counterparts (Fig. 3.7). Volcanic rocks from the thick lithosphere Zagros Core region of NW Iran, again plot as a compositional end-member.

Given that amphiboles are relatively common in the southern Lesser Caucasus rocks, it should be noted that low Y (amphibole fractionation) trends dominate the Y *vs.* SiO_2 plot for these rocks (Fig. 3.4d). Samples from further north, in which anhydrous mineral assemblages are more common, show both high Y (anhydrous assemblage) and low Y (hydrous) fractionation trends.

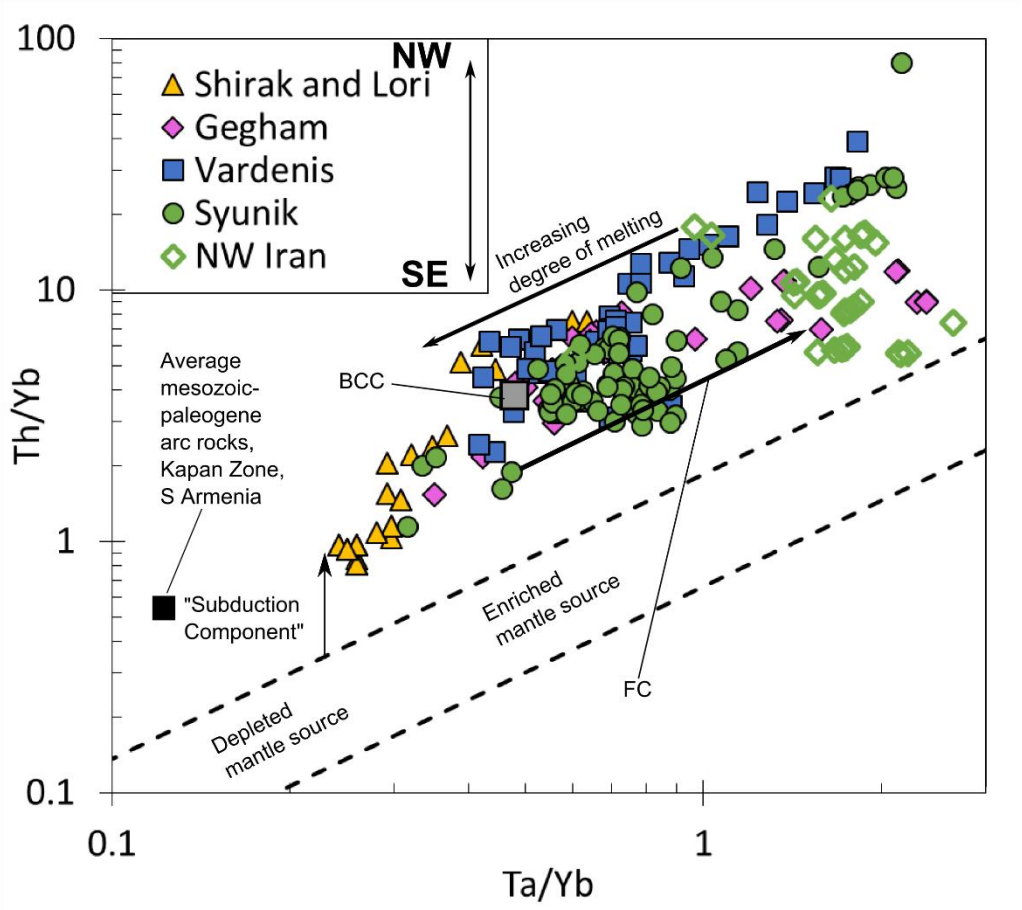

Figure 3.7 Th/Yb *vs* Ta/Yb variations in the volcanic rocks of the Lesser Caucasus

Mantle Source array and enrichment vectors after Pearce (1983). Lesser Caucasus data sources as in Fig. 3.3. NW Iran data from Allen et al. (2013). Fractional crystallisation (FC) vector: from basalt to andesite uses 50% amphibole, 50% clinopyroxene assemblage taking basaltic melt partition coefficients; from andesite to rhyolite uses 50% plagioclase, 50% amphibole assemblage taking andesite melt partition coefficients. The vector has a starting composition as the most mafic sample. Partition coefficients for Ta are: clinopyroxene-basalt = 0.017; amphibole-basalt = 0.05; amphibole-andesite = 0.21; plagioclase-andesite = 0.03. For Th: clinopyroxene-basalt = 0.007; amphibole-basalt = 0.05; amphibole-andesite = 0.16; plagioclase-andesite = 0.01. For Yb: clinopyroxene-basalt = 0.28; amphibole-basalt = 0.59; amphibole-andesite = 1.25; plagioclase-andesite = 1.25. All partition coefficients from the GERM database (earthref.org/GERM/). The average composition of Mesozoic arc rocks from the Kapan zone arc rocks are from Mederer et al. (2013). The grey box labelled BCC is the composition of bulk continental crust from Rudnick and Gao (2014).

3.4.4 Sr-Nd isotope systematics

The Sr-Nd isotope compositions of the southern Lesser Caucasus samples are shown in Table 3.3. $^{87}Sr/^{86}Sr$ varies from 0.7043 to 0.7047, while εNd varies from +2.2 to +4.2. All mafic volcanic rocks from the Lesser Caucasus plot along the mantle array with compositions more enriched than N-MORB, but more depleted than Bulk Earth (Fig. 3.8). In general, those samples from the south-east have higher (more radiogenic) $^{87}Sr/^{86}Sr$, and less radiogenic εNd than those samples from the north-

Table 3.3 Sr-Nd isotope compositions for lavas from the southern Lesser Caucasus.

Rock types use the same abbreviations as Fig. 6 and Table 2. All Sr ratios are normalised to NIST SRM 987, and all Nd ratios are normalised to La Jolla corrected BHVO-I (see Methods). Epsilon values are calculated for the present day using $(^{143}Nd/^{144}Nd)_{CHUR} = 0.512638$ for Chondritic Earth (Jacobsen and Wasserburg, 1980). Samples marked with an asterisk are from the east side of the Sevan-Akera suture- see text for discussion

	Rock type	$^{87}Sr/^{86}Sr$	± 2σ ($x10^{-6}$)	$^{143}Nd/^{144}Nd$	± 2σ ($x10^{-6}$)	εNd
Vardenis						
4.2.15*	TBA	0.704356	10	0.512802	12	3.20
5.3.15*		0.704461	8	0.512803	10	3.22
5.6.15	TBA	0.704505	12	0.512789	10	3.24
5.9.15	Tr	0.704506	12	0.512805	10	3.26
6.3.15		0.704429	8	0.512796	10	3.08
1.1.13*	TBA	0.704432	10	0.512808	10	3.32
1.2.13*	TBA	0.704420	8	0.512781	6	2.79
3.3.13*	TBA	0.704399	12	0.512798	10	3.12
5.1.13		0.704351	8	0.512805	6	3.26
5.2.13		0.704181	8	0.512836	10	3.86
6.2.13	TBA	0.704455	8	0.512815	8	3.45
6.27.08	TBA	0.704307	12	0.512783	12	2.83
7.29.08	TBA	0.70433	8	0.512799	14	3.51
Syunik						
8.3.15	TBA	0.704438	8	0.512785	8	2.87
8.4.15	TBA	0.704466	8	0.512794	9	3.04
8.5.15	Te	0.704615	8	0.512779	10	2.75
8.6.15	PTe	0.704553	10	0.512779	12	2.75
9.1.15	TBA	0.704439	10	0.512803	8	3.22
9.2.15	TB	0.704407	14	0.512801	8	3.18
10.1.15	PTe	0.704660	10	0.512761	10	2.40
10.2.15	TBA	0.704262	10	0.512856	10	4.25
10.3.15	TBA	0.704245	10	0.512821	10	3.57
11.1.15	TA	0.704378	10	0.512806	8	3.28
11.2.15	PTe	0.704595	12	0.512781	11	2.79
11.3.15	Te	0.704277	12	0.512795	5	3.06
5.5.12	TA	0.704432	10	0.512783	10	2.83
2.3.10	R	0.704425	8	0.512788	8	2.93
3.10.10	Tr	0.704419	8	0.512796	4	3.08
3.11.10	TA	0.704530	10	0.512783	4	2.83
4.19.10.	TA	0.704330	8	0.512801	12	3.18
1.4A.08	TBA	0.704317	6	0.512792	10	3.00
1.4B.08. (xenolith)	G	0.704981	32	0.512797	12	3.10
2.7.08.	PTe	0.704440	10	0.512797	7	3.10
2.8.08.	TBA	0.704381	10	0.512799	10	3.14
2.10.08.	B	0.704396	14	0.512827	12	3.69
4.15A.08.	R	0.705207	6	0.512783	8	2.83
4.18A.08.	R	0.704857	8			
5.20A.08	R	0.705482	14	0.512770	14	2.57
5.21.08.	TBA	0.704475	9	0.512767	10	2.52
6.26.08.	TA	0.704273	8			

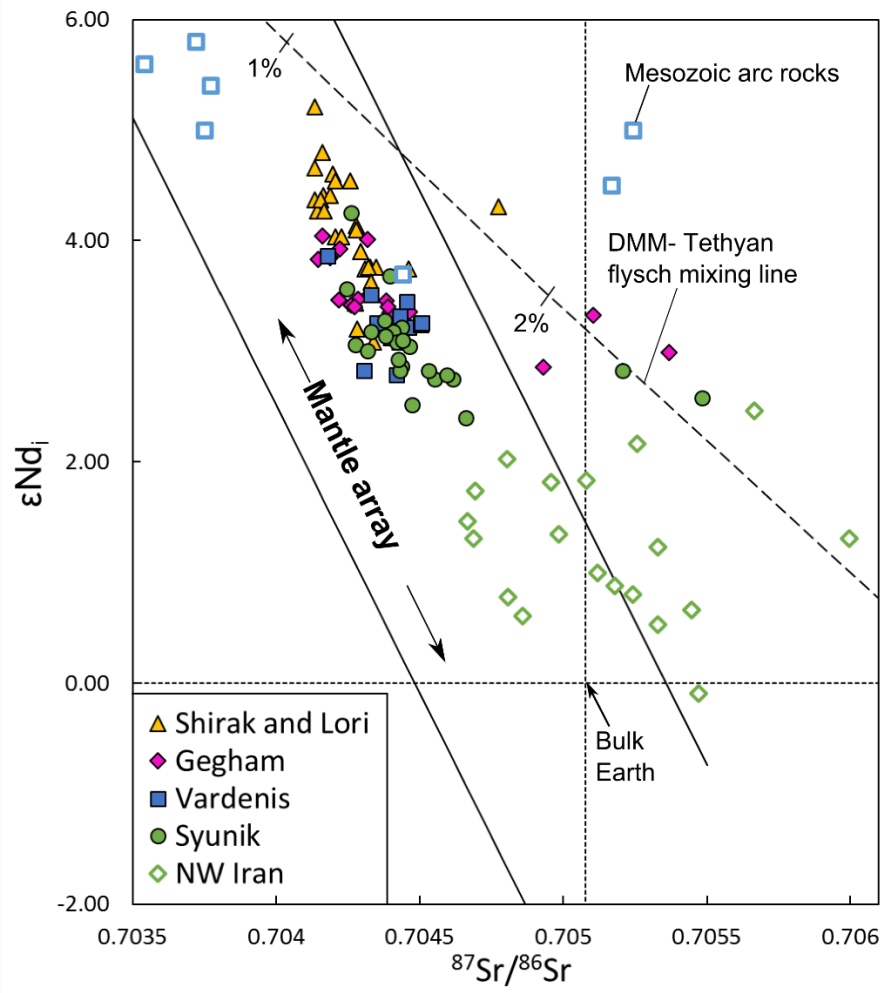

Figure 3.8 εNd *vs* $^{87}Sr/^{86}Sr$

Bulk Earth value and mantle array after Rollinson (1993). NW Iran data is from Allen et al. (2013). Mixing line shown between depleted MORB mantle (DMM) and Tethyan Flysch (Prelević et al., 2008): DMM [Sr] = 21 ppm, [Nd] = 1.35 ppm, $^{87}Sr/^{86}Sr$ = 0.7028, $^{143}Nd/^{144}Nd$ = 0.5131; Tethyan Flysch [Sr] = 349.2 ppm, [Nd] = 25.9 ppm, $^{87}Sr/^{86}Sr$ = 0.7112, $^{143}Nd/^{144}Nd$ = 0.512107.

west, defining a steep gradient on the Sr-Nd isotope diagram (Fig. 3.8). A few samples plot away from this trend to higher $^{87}Sr/^{86}Sr$ (see Crustal contamination section of Discussion below). Lesser Caucasus volcanic rocks are isotopically more depleted than volcanic rocks formed above very thick lithosphere in NW Iran (> 200 km; Priestley et al., 2012). They are also more depleted than volcanic rocks from the Lake Van area, which commonly display significantly more variable Sr-Nd isotope compositions (not shown), probably because those magmas interacted extensively with continental crust during ascent (Pearce et al., 1990; Şen et al., 2004; Özdemir et al., 2006; Oyan et al., 2017).

3.5 Discussion

3.5.1 Crustal contamination

Volcanic rocks produced within the thicker lithosphere of the southern Lesser Caucasus have higher concentrations of incompatible trace elements, more radiogenic $^{87}Sr/^{86}Sr$, and lower $^{143}Nd/^{144}Nd$ ratios. All of these features could be produced by crustal contamination during magmatic evolution, as has been suggested for various parts of eastern Anatolia, where assimilation of radiogenic ancient continental crust gives $^{87}Sr/^{86}Sr$ ratios of up to 0.7065 and marked variation of these ratios with SiO_2 (Pearce et al., 1990; Keskin et al., 2006). All Sr-Nd isotope ratios for the Lesser Caucasus volcanic rocks show small variations compared to what would be expected if magmas had been contaminated by continental crust. The crust in the Lesser Caucasus is composed of a mixture of felsic metamorphic basement (South Armenian Block), arc volcanics and Mesozoic-Cenozoic sediments (Fig. 2.1). Only the arc-related volcanic rocks would have similar isotope compositions to the collision-related magmas, such that assimilation of any of the other lithologies would alter, often dramatically, the isotope composition of the host magma. The majority of samples show insignificant variability in $^{87}Sr/^{86}Sr$ and $^{143}Nd/^{144}Nd$ with SiO_2 within individual volcanic highlands (Fig. 3.9), suggesting that isotope ratios are not being modified significantly during magma evolution and storage in the crust prior to eruption. The lack of isotopic variability with SiO_2 content suggests that assimilation of South Armenian Block crust (Fig. 2.1)- which with a basement $^{87}Sr/^{86}Sr$ ratio of ~0.7303 (Baghdasaryan and Ghukasyan, 1985) should be easily identified- is unlikely. Similarly, assimilation of sedimentary material is also unlikely, given typical Tethyan (Mesozoic) flysch $^{87}Sr/^{86}Sr$ of 0.7112 (Prelević et al., 2008).

One sample from the Syunik volcanic highland (1-4A-08), which was sampled from a scoria cone containing large (cm-sized) felsic xenoliths entrained within the trachybasaltic andesite scoria, has trace element and isotopic characteristics indistinguishable from the other mafic samples. The Sr-Nd isotope composition of one of the xenoliths (sample 1-4B-08, Table 3.3) is also shown in Fig. 3.9, and is only slightly elevated in $^{87}Sr/^{86}Sr$ (0.7049) above that of the quaternary basalts, suggesting that an unrealistically high degree of assimilation would have to occur for the composition of the magma to be significantly affected.

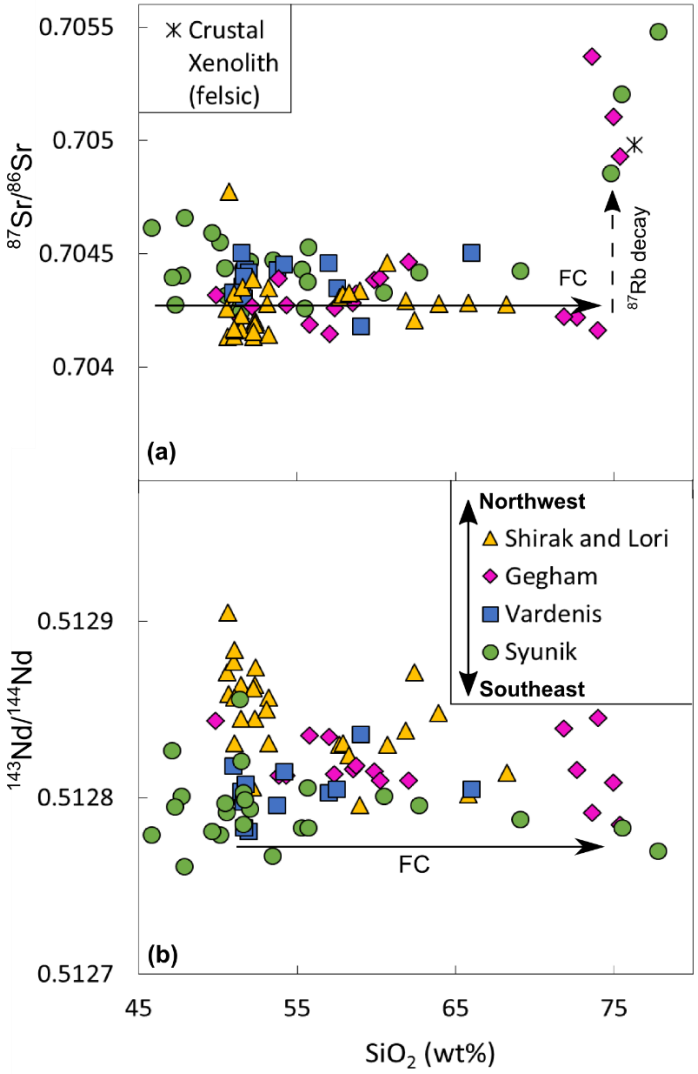

Figure 3.9 Using Sr-Nd isotopes vs SiO_2 to investigate potential crustal contamination

(a) $^{87}Sr/^{86}Sr$ *vs* SiO_2 (wt %) for all samples across the Lesser Caucasus. Fractional crystallisation is denoted by a horizontal arrow labelled "FC". The dashed line labelled ^{87}Rb decay refers to the effect of post-crystallisation radioactive decay in rocks with very high Rb/Sr ratios (see text for discussion). The crustal xenolith was collected in association with sample 1-4A-08 in the Syunik volcanic highland. It has a granitic texture. (b) $^{143}Nd/^{144}Nd$ *vs* SiO_2 (wt %).

The $^{143}Nd/^{144}Nd$ (0.5128) is indistinguishable from Syunik basalts. It is likely the felsic xenolith is cogenetic with the trachybasaltic andesite scoria host. It provides evidence that basaltic magmas in the southern Lesser Caucasus are interacting with felsic igneous rocks in the crust which have a similar origin, rather than interacting with ancient crust which would have strongly impacted the Sr-Nd isotope ratios.

The curved patterns for major element variations *versus* SiO_2, including MgO (Fig. 3.4b), P_2O_5 (Fig. 3.4c) and Al_2O_3 (not shown), suggest the rhyolites are derived from extreme degrees of magmatic differentiation, rather than being crustal

melts. These rhyolites also do not appear to be mixtures between primitive magmas and continental crust (Rudnick and Gao, 2014). The Rb and Sr contents of a rhyolite from Syunik are actually more extreme relative to the basalts than average continental crust (Rb more strongly enriched, Sr more strongly depleted in the rhyolite; Fig. 3.5d). K_2O is more enriched in the rhyolite than in the basalts, whereas continental crust has lower K_2O than the basalts (Fig. 3.5d). The lack of evidence for extensive assimilation of continental crust in the petrogenesis of the rhyolites suggests that these processes are likely to be unimportant in the petrogenesis of the more primitive magmas.

It is also possible that the magmas may have been contaminated by Mesozoic-Paleogene arc crust (Fig. 2.1) on their ascent, as has been suggested for the northern Lesser Caucasus in some isolated cases (Neill et al., 2015). The similar Sr-Nd isotope ratios of these arc rocks (Mederer et al., 2013) to the collision-related magmas means that assimilation could be "cryptic", without obvious modification of Sr-Nd isotope ratios. Given the arc-like incompatible trace element geochemistry of Lesser Caucasus volcanic rocks, arc-crust assimilation is unlikely to significantly alter trace element composition, although it is possible that such assimilation could explain some of the spread in the southern Lesser Caucasus data. The average composition of Mesozoic arc rocks from the southern Lesser Caucasus (Kapan Zone) is shown in Fig. 3.7 (Mederer et al., 2013). The Th/Yb ratio of the arc rocks is elevated above the mantle array like for post-collisional Lesser Caucasus samples. However, the low Ta/Yb ratios of these arc rocks make them unlikely candidates to explain the more enriched composition of southern Lesser Caucasus magmas.

There are a few examples of elevated $^{87}Sr/^{86}Sr$ ratios in evolved samples above the background range. In most cases, it seems that the Nd isotopes are unaffected. Some ancient arc samples from the Kapan zone, southern Lesser Caucasus have very high initial $^{87}Sr/^{86}Sr$, but $^{143}Nd/^{144}Nd$ does not vary significantly in the same samples (Mederer et al., 2013). Extensive assimilation of such material would be required to explain the elevated $^{87}Sr/^{86}Sr$ of these samples. Worthy of note however, are the very high Rb/Sr ratios (7-23) in these rhyolites- sometimes 1000x greater than typical basalts (Table 3.2). While decay of ^{87}Rb over the relatively short timeframe (< 2 Myr) since cooling and crystallisation of lavas will be a process which has negligible effects on the $^{87}Sr/^{86}Sr$ of basaltic rocks, such high Rb/Sr ratios mean that post-crystallisation decay will have a significant effect for rhyolites (Fig.

3.9a). Indeed, minimum ages for the rhyolites of between 0.6 and 1.4 Myr are sufficient to give initial $^{87}Sr/^{86}Sr$ within the range observed for basalts. As such, even in these rhyolites, crustal contamination may have played an unimportant role in magma evolution. It should be noted that the lower Rb/Sr ratio of the felsic xenolith (0.12) means that its elevated $^{87}Sr/^{86}Sr$ ratio was likely present during emplacement of the host quaternary mafic magma.

In summary, assimilation of crustal rocks with markedly distinct geochemistry is unlikely, and although assimilation of igneous rocks with similar petrogenetic origins cannot be precluded, such processes would be incapable of driving the enrichment in incompatible trace element concentrations and Sr-Nd isotope ratios observed from north to south in the volcanic rocks of the Lesser Caucasus. The lack of evidence for crustal contamination, along with the gradient in Sr-Nd isotope ratios in Fig. 3.8, requires that there must be variation in the composition of the mantle source.

3.5.2 Subduction modification of the mantle source in the Lesser Caucasus

All mafic samples show distinct negative Nb-Ta and Ti anomalies (Fig. 3.5), and positive spikes in Ba, K, Pb and Sr in normalised trace element patterns, such that the overall pattern, if not the absolute concentrations, are typical of arc magmas. In the absence of evidence for widespread crustal contamination, it is likely that these features are inherited from the mantle source. Collision between Arabia and Eurasia was preceded by subduction of various Tethyan ocean basins along several convergent margins (Fig. 2.2). These subducting slabs would likely have contributed slab material to the mantle below the collision zone.

Following the approaches of Turner et al. (2017) and Hofmann (2003), Fig. 3.10 illustrates how the ratios Ba/La, Ce/Pb, Sr/Nd and Nb/U in mafic samples (< 54 wt % SiO_2, > 4 wt % MgO) vary with latitude. These ratios show little variation within all MORB and OIB, but are much more variable in volcanic arc rocks due to the subducted slab contribution, such that they can be used here as proxies. In all of the plots in Fig. 3.10 these ratios deviate from those of MORB/OIB, demonstrating the presence of a slab component in their mantle source. These ratios do not show consistent variability between the volcanic highlands (Fig. 3.10), although Sr/Nd

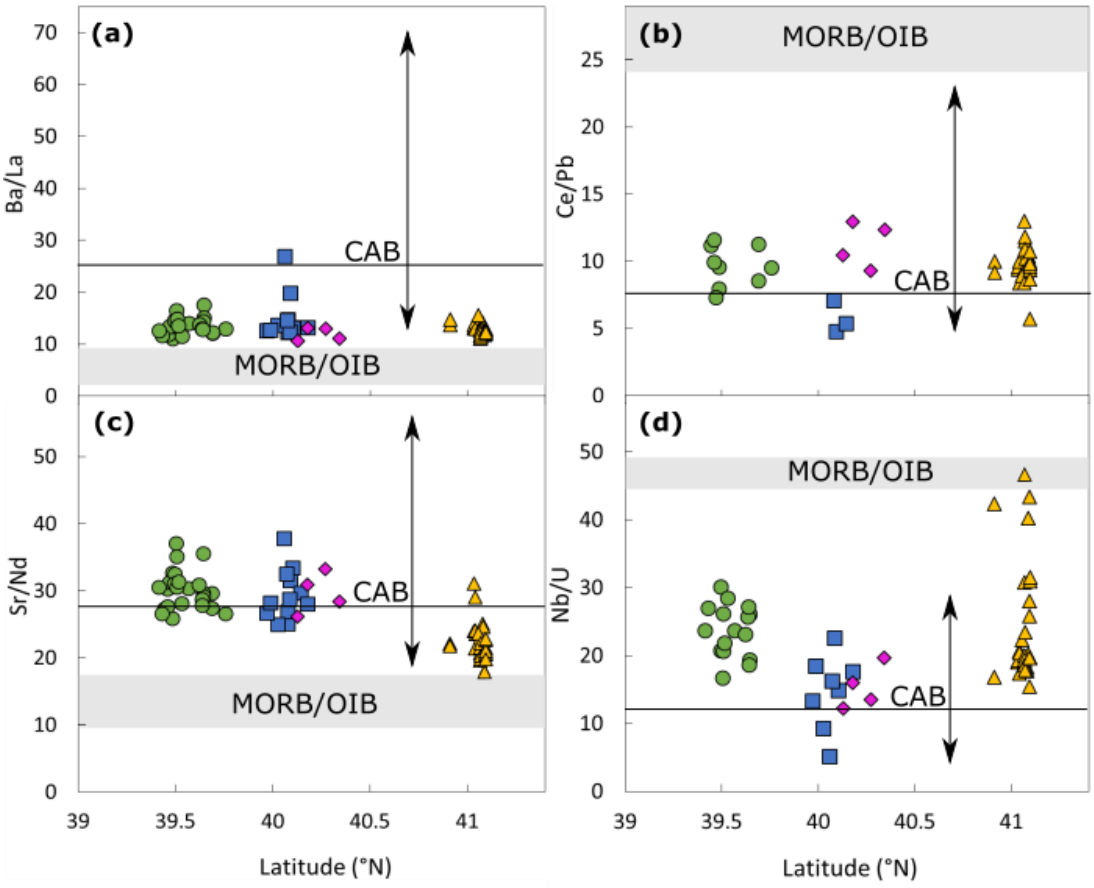

Figure 3.10 Tracing slab input variation with latitude using trace element ratios

The latitudinal variation in the ratios Ba/La (a), Ce/Pb (b), Sr/Nd (c) and Nb/U (d) of mafic volcanic rocks along the Lesser Caucasus mountain chain. These ratios are nearly invariant in MORB and OIB (shaded fields), but arc basalts show substantial variability in these ratios (CAB- continental arc basalt, with the arrows showing the ranges across several arcs from Kelemen et al. (2003)). As such, they are a proxy for slab input, and show a uniform input across the Lesser Caucasus. After Turner et al. (2017).

ratios are slightly elevated to the south (Fig. 3.10c) and the Nb/U ratio reaches a minimum (highest slab contribution) in the central Lesser Caucasus. The lack of a consistent trend in these ratios between volcanic highlands means the slab contribution is likely to be fairly uniform.

Although mixing between a depleted mantle source and the likely composition of subducted sediment, e.g. Tethyan flysch (Prelević et al., 2008), comes close to explaining the Sr and Nd isotopic composition of the least enriched samples in Fig. 3.8, such mixing is unable to explain the trend towards the higher $^{87}Sr/^{86}Sr$ and lower $^{143}Nd/^{144}Nd$ seen in the SE. This enrichment in the southern Lesser Caucasus must be driven by some other process. Pre-collision subduction events have likely imparted a subduction signature on the mantle source across the Lesser Caucasus. However, the geochemical gradient between volcanic rocks of the

northern and southern Lesser Caucasus cannot be explained by differences in the composition, or size of the slab contribution to the mantle source.

3.5.3 Modelling the conditions of mantle melting

It is possible to investigate how a thicker lithosphere effects the conditions of melting by using the approach of Shaw (2005) to forward model the composition of the samples using a non-modal batch melting model (Table 3.4), with the equation:

$$\frac{C_l}{C_0} = \frac{1}{D + F(1 - P)} \qquad (3.1)$$

where C_l is the concentration of an element in the liquid, C_0 is the concentration of that element in the source, D is the element's bulk partition coefficient (based on the source mode in Table 3.4), F is the fraction of melting, and P represents the partitioning of the element into the melt according to the proportion in which each mineral enters the melt (the melt mode in Table 3.4). None of the samples in the region are in equilibrium with mantle olivine, so all must have undergone some fractional crystallisation between last equilibration with the mantle and eruption. This is accounted for by assuming 8% fractional crystallisation of an assemblage composed of 90% olivine and 10% spinel (following the approach of Shaw, 2005). From equation 3.1 it can be seen that there are three parameters which can each be varied to generate the trace element concentration of the most primitive southern Lesser Caucasus samples. Firstly, the fraction of melting (F) could vary, impacting the concentration of all incompatible trace elements. Secondly, if the modal mineralogy is changed then the partitioning of elements between source and melt (D and P in equation 3.1) will change. Thirdly, the concentration of elements in the source rock (C_0) could be changed.

The approach taken here is to take the equivalent model of Neill et al. (2015) for the most geochemically depleted samples from the northern Lesser Caucasus and iteratively vary two of these parameters to attempt reproduce the average composition of primitive basalts in the south. Variations in the mineralogy of the melt source are simplified to spinel *versus* garnet peridotite melting. Spinel peridotite modal mineralogy and melting proportions are from Shaw (2005) and Neill et al. (2015) respectively, while for the garnet peridotite they are from Thirlwall et al. (1994) and Allen et al. (2013), respectively (Table 3.4). Varying the

Table 3.4 Parameters used for non-modal batch melt modelling

The source modes for spinel and garnet peridotite are from Shaw (2005) and Thirlwall et al. (1994) respectively. Melt modes are from Neill et al. (2015) and Allen et al. (2013). The starting composition of the mantle source is the same as that used in Neill et al. (2015). Partition coefficients are from Ionov et al. (2002), except for those for garnet which comes from Mckenzie and O'Nions (1991) and Green et al. (2000). The most primitive Syunik sample used for comparison is 8-5-15 (see Table 3.2). OL- olivine; OPX- orthopyroxene; CPX- clinopyroxene; AMPH- amphibole; SP- spinel; GRNT- garnet.

Lithology		**OL**	**OPX**	**CPX**	**AMPH**	**SP**	**GRNT**	**Sum**
Spinel peridotite	Source mode	0.794	0.123	0.03	0.042	0.011	0	1
	Melt mode	0.15	0.15	0.22	0.42	0.06	0	1
Garnet peridotite	Source mode	0.569	0.212	0.077	0.026	0	0.116	1
	Melt mode	0.05	0.19	0.28	0.06	0	0.42	1
		La	**Gd**	**Dy**	**Yb**	**Zr**	**Hf**	**Nb**
Starting composition		0.5869	0.321	0.317	0.202	7	0.172	0.3635
Kd values		**La**	**Gd**	**Dy**	**Yb**	**Zr**	**Hf**	**Nb**
Olivine		0.0001	0.00076	0.0014	0.00364	0.004	0.006	0.0002
Orthopyroxene		0.0002	0.0128	0.0261	0.0986	0.005	0.01	0.0005
Clinopyroxene		0.054	0.4	0.442	0.427	0.13	0.2	0.0077
Amphibole		0.086	0.64	0.707	0.683	0.156	0.24	0.2
Spinel		0.0004	0.00042	0.0004	0.00053	0.005	0.01	0.001
Garnet		0.01	0.498	1.06	4.03	0.12	0.23	0.00054
Melting models		**La**	**Gd**	**Dy**	**Yb**	**Zr**	**Hf**	**Nb**
1. 3% melting spinel lherzolite (Neill et al., 2015)	Initial	17.3	5.3	4.9	2.7	169.0	3.6	10.0
	After 8% fractionation	18.8	5.8	5.3	2.9	183.6	3.9	10.9
2. 1% melting spinel lherzolite	Initial	39.5	6.8	5.9	3.2	299.9	5.6	20.2
	After 8% fractionation	42.9	7.3	6.5	3.5	325.9	6.1	21.9
3. 1% melting garnet lherzolite	Initial	34.0	2.8	1.7	0.4	175.3	2.8	23.1
	After 8% fractionation	37.0	3.1	1.9	0.4	190.5	3.1	25.1
4. 1% melting of 65% garnet lherzolite, 35% spinel lherzolite	Initial	35.9	4.2	3.2	1.4	218.9	3.8	22.1
	After 8% fractionation	39.1	4.6	3.5	1.5	237.9	4.1	24.0
Most primitive Syunik sample for comparison		74.8	7.6	4.7	1.9	166.0	3.7	24.0

fraction of melting is self-explanatory. Disparities which remain between the model and observed trace element concentrations are likely to be due to differences in the composition of the mantle source. The different stages of melt modelling are shown in Table 3.4.

REE chemistry is used to obtain a qualitative understanding of the changing conditions of melting between the northern and southern Lesser Caucasus (Fig. 3.11). In Fig. 3.11a, two vectors are plotted which show how the composition of the magmas should change with the degree of melting *versus* source mineralogy (presence/absence of garnet) and/or changes in source composition. Davidson et al. (2013) showed that REE partitioning between clinopyroxene and basaltic magma means that melting curves for peridotites will be very steep on a Dy/Dy* *versus* Dy/Yb plot. The assumption that clinopyroxene is a residual phase is reasonable

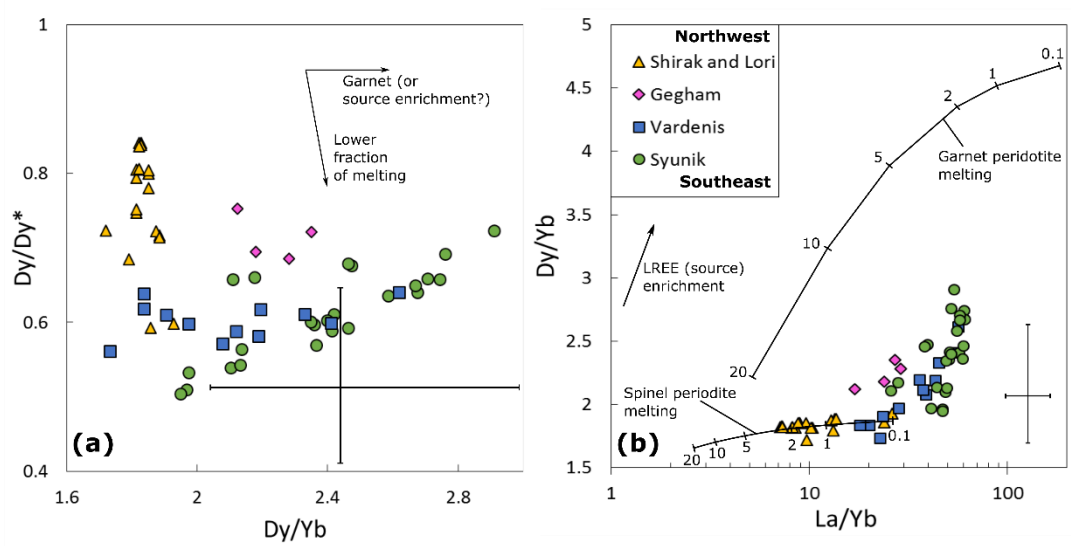

Figure 3.11 rare earth element ratios and the conditions of melting

(a) Dy/Dy* *vs* Dy/Yb after Davidson et al. (2013). The two arrows depict the expected vectors from changing the fraction of melting or source mineralogy/composition. The vector for a lower fraction of melting after Davidson et al. (2013), based on melting of olivine-pyroxene-amphibole dominated mantle source. The presence of garnet in the melt source should follow a horizontal vector (Davidson et al., 2013). (b) Dy/Yb *vs* La/Yb, melting curves based on modal mineralogies, melting modes, and partition coefficients given in Table 3.4. Indicative error bars shown in both figures represent the analytical error, which is estimated on the basis of the standards data shown in Appendix A. Maximum error is estimated as the 90th percentile of percentage error on both the internal and external standards from both ACME and Royal Holloway.

given the low degrees of melting (3% or less) previously estimated for the northern Lesser Caucasus (Neill et al., 2015). Amphibole is also likely to be an important residual phase given the positive correlation between Dy/Dy* and Ti/Ti* (the size of the Ti anomaly in Fig. 3.5; not shown here). It is unclear from Fig. 3.11a whether garnet in the mantle source, or a LREE enriched source is responsible for the high Dy/Yb ratio in southern Lesser Caucasus samples. Both should give vectors close to horizontal in Fig. 3.11a, as both changes will steepen the REE profile rather than changing its curvature (Davidson et al., 2013). The southern Lesser Caucasus samples have lower heavy rare earth element (HREE) abundances than samples from the north (Fig. 3.6). HREE all behave incompatibly during melting of spinel peridotite (Table 3.4), such that lower degrees of melting as suggested by the lower Dy/Dy* ratio should only increase the concentration of HREE. Therefore, garnet as a residual phase during melting must explain at least some of the increase in Dy/Yb in Fig. 3.11a. In Fig. 3.11b, the northern Lesser Caucasus samples sit close to the spinel peridotite melting curve, but the southern Lesser Caucasus samples are intermediate between the spinel and garnet melting curves, suggesting melting of a

mixed source involving both garnet and spinel peridotite. This could be a consequence of polybaric melting across the spinel-garnet transition at ~ 75 km depth (Robinson and Wood, 1998), suggesting melting at greater depths in the south.

It should be noted however, that the analytical uncertainties of the REE concentrations give significant errors for the ratios (Fig. 3.11). While this may well account for some of the variability we see in southern Lesser Caucasus data, it is unlikely to account for the systematic offset between northern and southern Lesser Caucasus data.

Returning to the partial melting model, the melt fraction was estimated on the basis that the Nb concentration (Table 3.4) is not affected by the mineralogy of the source rock, and assuming that its concentration in the source rock is constant along the transect. Utilising this assumption gives 3% melting in the north, *versus* 1% melting in the south (Fig. 3.12). The proportions of garnet peridotite and spinel peridotite which contribute to the total mantle source are estimated from the Hf and Yb concentrations. Both elements are assumed to have constant concentrations in the mantle source because HFSE and HREE would be less affected by metasomatic events which could alter the source composition. The best fit to the Hf and Yb data is a magma source which is 65% garnet lherzolite and 35% spinel lherzolite (Fig. 3.12).

Across the Lesser Caucasus, as lithosphere thickness increases, the degree of melting decreases and melting occurs at greater depths, with garnet as a residual phase for a significant portion of the melting interval. However, the model is still unable to explain the high concentrations of several of the LREE (La, Gd and Dy, Fig. 3.12- black line), and requires changes in the composition of the mantle source with lithospheric thickness as well.

In order to understand how melting is occurring, it is important to understand where magma is forming with respect to the lithospheric structure. For this, major element thermobarometry has been used to estimate the conditions of last equilibration between magmas and the mantle.

3.5.4 Pressure and temperature of melting

In order to calculate these intensive parameters, the parameterisations of Plank and Forsyth (2016) are used, which are based on the major element chemistry of

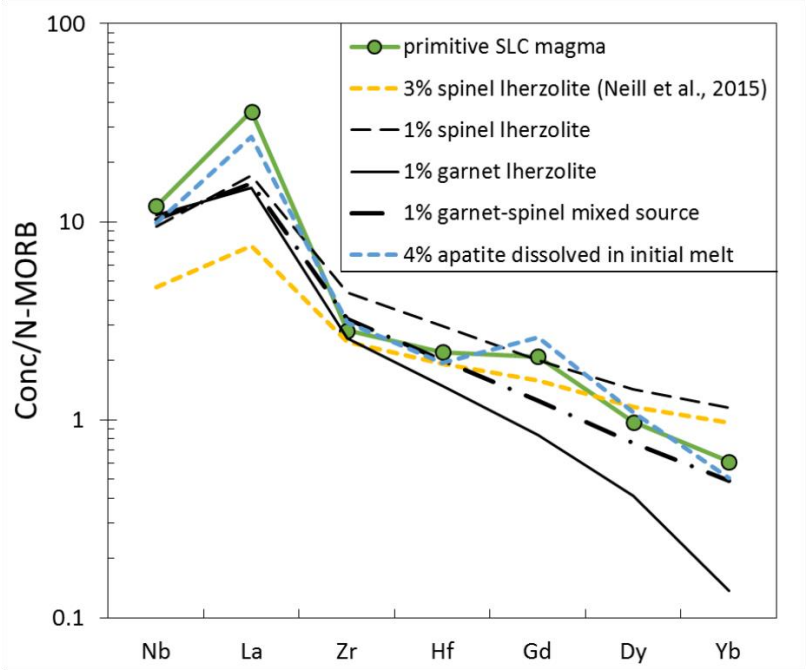

Figure 3.12 Non-modal batch melting modelled trace element concentrations

N-MORB normalised concentrations of Nb, La, Zr, Hf, Gd, Dy and Yb for the average of mafic samples from Syunik volcanic highland (green line) and several non-modal batch melting models which attempt to explain these trace element concentrations. Melting models: spinel peridotite at 3% melting (yellow dashed line), 1% melting of spinel peridotite (dashed black line), 1% melting of garnet peridotite (black solid line) and 1% melting of a source composed of 65% garnet peridotite and 35% spinel peridotite (dash-dot line). The blue dashed line represents a magma derived from the same 65% garnet peridotite source, with 4% apatite dissolved in the melt. Apatite composition is for magmatic apatite from Western Turkey in Prelevic et al. (2015).

primitive magmas, building on the work of Lee et al. (2009). These calculations are for magmas produced from a peridotite mantle source at pressures below 3 GPa (Plank and Forsyth, 2016). The temperature (T) dependence of Mg partitioning between olivine and melt (Roeder and Emslie, 1970), and the pressure (P) dependence of silica activity in melts co-saturated in olivine and orthopyroxene (Carmichael et al., 1970), are exploited to give the equations:

$$T = 1264.5 + 7.85(Mg_4Si_2O_8) + \frac{8545}{Si_4O_8} - 5.96(Al_{16.3}O_8) - \Delta T_{H_2O} - \Delta T_{CO_2}, \quad (3.2)$$

$$P = \frac{\ln(Si_4O_8) - 4.045 + 0.0114(Fe_4Si_2O_8) + 0.00052(Ca_4Si_2O_8)^2 + 0.0024(Mg_4Si_2O_8)}{-336.3T^{-1} - 0.0007T^{1/2}} \quad (3.3)$$

All major element oxides are calculated in mol % as described in Lee et al. (2009), except that they are calculated on an anhydrous basis. The two terms ΔT_{H_2O} and ΔT_{CO_2} account for the lower temperature and higher pressure melting in the presence of volatiles as follows:

$$\Delta T_{H_2O} = 40.4(H_2O) - 2.97(H_2O)^2 + 0.0761(H_2O)^3 \quad (3.4)$$

$$\Delta T_{CO_2} = \frac{(SiO_2) - 50.3}{0.12(-1.067)} \quad (3.5)$$

where H_2O and SiO_2 are in wt %. In order to use these equations, the composition of the primary melt must be known. Given that no samples from the Lesser Caucasus have #Mg>67, it is clear that all the studied samples have undergone some degree of fractional crystallisation. If only olivine has fractionated, then it is a simple process to add olivine incrementally to the melt until it is in equilibrium with mantle olivine of Fo_{90} (Lee et al., 2009). If, however, other phases, such as amphibole or clinopyroxene have also fractionated, then this calculation becomes non-trivial. In a study on the collision-related volcanism of Anatolia, McNab et al. (2018) took 8.5 wt % bulk-rock MgO as a reasonable lower limit for magmas which have only fractionated olivine. Only two such samples exist in the Lesser Caucasus, and it is likely they have both been affected by olivine accumulation rather than being truly primitive melts. Instead, the complete sample suite from the Shirak and Lori, and Syunik volcanic highlands (1 and 4 in Fig. 3.1) is used to project back to the likely composition at 8.5 wt % MgO of two end-member primitive magmas for the Lesser Caucasus. This correction is shown in Appendix B.

In order to calculate the pressures and temperatures of melting, two magma composition parameters must be constrained: $Fe^{3+}/\Sigma Fe$ and water content. The water content of the primary magma has a large effect on the temperature estimate through equation 3.4 (~25°C/wt %), but a smaller effect on the pressure estimate (~30 MPa/wt %). The presence of hydrous mineral phases in mafic rocks (as opposed to only in more evolved samples), only in the southern Lesser Caucasus (Fig. 3.2), suggests higher water contents in the south. Based on previous studies of amphibole peridotite xenoliths (Thirlwall et al., 1994; Ionov and Hofmann, 1995), it is assumed that the mantle source contains between 2 and 10 modal % amphibole, which is assumed to contain 2 wt % H_2O, such that the mantle source could have up to 0.2 wt % H_2O. Using Ce partition coefficients for water during mantle melting (Thirlwall et al., 1994; Dixon et al., 2002; Ionov et al., 2002), and the melting models shown in Table 3.4, gives 2-7 wt % H_2O for southern Lesser Caucasus primary magmas, and 1-4.6 wt% in the north.

As only ferrous iron substitutes in olivine, a higher $Fe^{3+}/\Sigma Fe$ increases the apparent melt Mg#, and so reduces the amount of olivine addition required to produce the primary magma, the MgO content of the primary magma, and thus the calculated pressure and temperature. The $Fe^{3+}/\Sigma Fe$ ratio varies from a minimum of 0.1 in MORB (Cottrell and Kelley, 2011) to as high as 0.3 in some arc basalts (Brounce et al., 2014). Given the ubiquitous arc-type geochemical signatures in Lesser Caucasus volcanic rocks, 0.25 is taken as a conservative estimate of the $Fe^{3+}/\Sigma Fe$ ratio (Brounce et al., 2014).

It should be noted that equations 3.2 and 3.3 will only give meaningful estimates of the pressure and temperature of melting if the mantle source is peridotitic, because the parameterisations assume the melt is saturated in both orthopyroxene and olivine (Plank and Forsyth, 2016). The use of these equations on magmas derived from a pyroxenite source would yield meaningless results. Figure 3.13 shows that for Lesser Caucasus and NW Iran samples, pyroxenite is not a major component of the mantle source. Pyroxenite partial melts have much higher Ni/MgO ratios. As magmas fractionate, those derived from a peridotite source should evolve along a trajectory below the dashed line in Figure 3.13, those from a pyroxenite source would plot above the line.

Based on the water content estimates, southern Lesser Caucasus magmas last equilibrated with the mantle at between 1198 and 1292°C, while northern Lesser Caucasus magmas last equilibrated at between 1174 and 1267°C. Given the observation that amphibole is likely to be a residual phase in the mantle source (see previous section), it is likely melting was occurring at temperatures close to the amphibole dehydration solidus, because amphibole is likely to completely breakdown within a few 10s °C of crossing the dehydration solidus (Green and Falloon, 2005; Mandler and Grove, 2016). As such, it is likely that the minimum temperatures of these ranges are the more realistic. Using these temperatures gives pressure estimates of 2.1 GPa (~75 km) in the southern Lesser Caucasus, and 1.2 GPa (~45 km) in the north. These estimates are shown in Fig. 3.14, along with the position of the amphibole dehydration solidus. Southern Lesser Caucasus magmas are produced deeper, but at similar temperatures to those in the north.

The parameterisations first developed by Lee et al. (2009) were designed to expand the applicability of basalt melt geothermobarometry beyond mid-ocean ridge systems to any setting which involves the melting of terrestrial peridotite. Both the

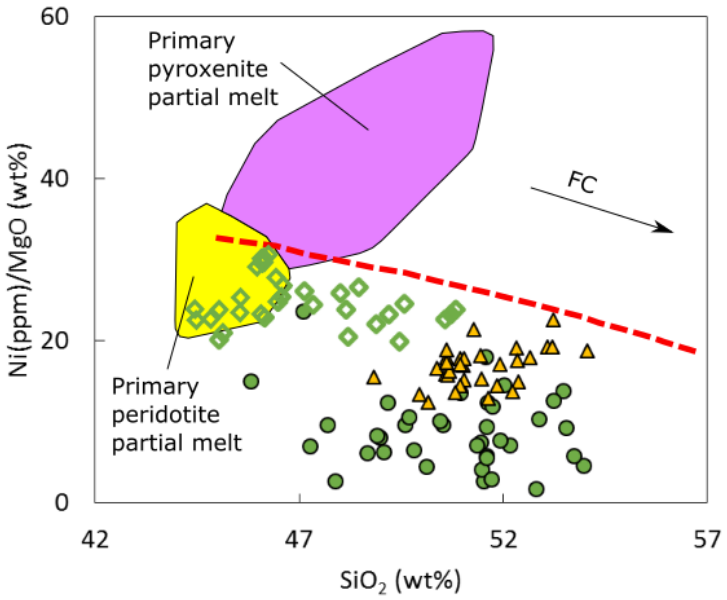

Figure 3.13 Ni content of mafic volcanic rocks as evidence of peridotite source lithology

Ni/MgO *vs* SiO_2 in primitive Lesser Caucasus and NW Iran bulk-rock samples (<54% SiO_2, > 4% MgO), after Allen et al. (2013). Pyroxenite melting should generate compositions above the bold red dashed line (Sobolev et al., 2005). Primary melts of peridotite and pyroxenite (from Hawaii) after Sobolev et al. (2005). FC- fractional crystallisation. Syunik, Shirak and Lori and NW Iran data shown with the same symbols as other figures.

modelled major element compositions, and the pressure and temperature calculated fall within the experimental range of the dataset in Lee et al. (2009), and to this extent the approach is justified.

However, the presence of metasomatic phases such as amphibole in the mantle source means the pressures and temperatures calculated here must be interpreted with caution. Alkaline volcanic rocks from monogenetic volcanic fields in Western Mexico, geochemically similar to those from volcanic highlands in the Lesser Caucasus, have very high $Fe^{3+}/\Sigma Fe$ ratios and whole rock #Mg in excess of the ~72 value normally assumed to be in equilibrium with mantle peridotite (Carmichael et al., 1996). The effects of a potential underestimation of both $Fe^{3+}/\Sigma Fe$, and of the amount of olivine addition required to produce the primary magma will tend to counteract each other, where the former would give an overestimation of temperature, and the latter an underestimate. In the case of Western Mexico, both of these observations are ascribed to the incongruent melting of phlogopite (Carmichael et al., 1996), which does not seem to be a major metasomatic phase in the Lesser Caucasus (see Fig. 3.18 below).

Even if these issues are relevant to the Lesser Caucasus, the constraint

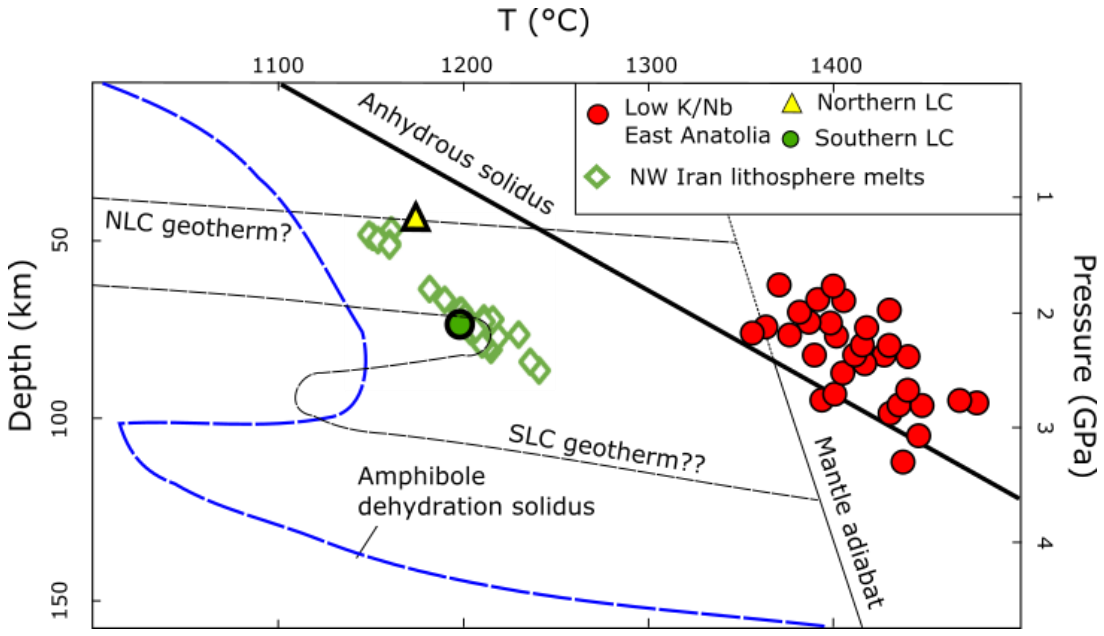

Figure 3.14 P-T estimates of mantle melting in the northern and southern Lesser Caucasus and NW Iran

Also shown are the anhydrous peridotite solidus (1100°C+3.5°C/km) after Plank and Forsyth (2016), the wet solidus (amphibole present) after Green and Falloon (2005), samples from East Anatolia with low K/Nb (red circles) from McNab et al. (2018). The pressures and temperatures of melting of NW Iran magmas were calculated for this study, assuming $Fe^{3+}/\Sigma Fe$ of 0.25 and melt water contents of 7 wt%, as were used for the southern Lesser Caucasus estimate. See text for discussion.

provided by the position of the amphibole dehydration solidus shows the temperature estimates provided here to be reasonable, although some of the ~50°C disparity with the dehydration solidus could be explained by these issues. The sensitivities of the pressure estimate to $Fe^{3+}/\Sigma Fe$ (-0.2 GPa/0.1 increase), primary melt Mg# (+0.5 GPa/10% increase) and estimated temperature (+0.1 GPa/100°C) are all small. The pressure estimate is primarily based on silica activity in a system co-saturated in olivine and orthopyroxene. Given the indications from Fig. 3.13, and reasonably successful trace element modelling of partial melting of a peridotite mantle source, it seems likely that these pressure estimates are robust.

Further constraints on the thickness of the crust are required to interpret these results. Crustal thickness is estimated using the formulations of Hu et al. (2017), which link the Sr/Y and $(La/Yb)_N$ ratios of intermediate magmatic rocks from continental collision zones with the crustal thickness. The basis of this technique is the polarising effects different fractionating mineral assemblages have on the Sr/Y and $(La/Yb)_N$ ratios in shallow *versus* deep storage reservoirs. To the nearest 5 km,

crustal thickness is estimated as: 45 km in Shirak and Lori, 55 km in Gegham and 60 km in both Vardenis and Syunik.

The depth of melting in the northern Lesser Caucasus is very similar to the ~45 km Moho depth, possibly suggesting the presence of a very thin mantle lithosphere. It is instructive to compare this result with recent estimates of melting conditions in neighbouring eastern Anatolia from McNab et al. (2018). East Anatolian magmas can be split into high K/Nb (>500) and low K/Nb types. Low K/Nb magmas generally have OIB-like geochemistry, and are considered to be directly derived from melting of the convecting mantle, which is apparently anomalously hot in the region, plotting to the right of the ambient mantle adiabat (Fig. 3.14), at a much higher temperature than any temperatures modelled for the northern Lesser Caucasus. This can be interpreted as northern Lesser Caucasus magmas being derived from the lithosphere, and not the convecting mantle.

Deeper melting in the south is associated with thicker crust, but magma generation is occurring at much shallower depths than the > 100 km lithosphere-asthenosphere boundary estimated by Priestley et al. (2012). The depth of melt equilibration is much deeper than the anhydrous solidus, confirming the need for a volatile-enriched lithospheric mantle root.

These P-T conditions of melting can be compared with estimates made for this study of the melting conditions of samples from NW Iran, based on the data of Allen et al. (2013). The P-T conditions of melting of NW Iran volcanic rocks were estimated using the same $Fe^{3+}/\Sigma Fe$ and water contents as southern Lesser Caucasus magmas (0.25 and 7 wt% respectively). This is on the basis that the geochemistry of NW Iran magmas is similar to southern Lesser Caucasus magmas (Fig. 3.5), and both formed in a thicker lithosphere regime. Most of the magmas in NW Iran formed under similar conditions to southern Lesser Caucasus magmas, with a small subsidiary group of samples which formed at shallower depths similar to northern Lesser Caucasus magmas, possibly representing magmas which re-equilibrated with the mantle at the base of the crust during their ascent to the surface.

The melting depth in both the southern Lesser Caucasus and NW Iran is significantly shallower than the estimated lithospheric thicknesses. One possible explanation for what these melting conditions represent could be a thermal maximum in a back-bent non-linear geothermal gradient (Fig. 3.14). In recently

thickened orogenic lithosphere, this type of kinked profile is probably more realistic than the linear geothermal gradient more typical of a cratonic region (Mather et al., 2011).

It is worth noting that these differences in melting conditions probably reflect variations in the location of magma generation today, and are not the product of temporal changes in lithosphere structure. This is because in Fig. 3.5, the trace element compositions of basalts from each volcanic highland are distinct, with each having a fairly narrow range of trace element compositions, despite all the volcanic highlands spanning an age range > 1 Myr, and with the Gegham and Syunik highlands thought to have very similar timespans of activity (Joannin et al., 2010; Lebedev et al., 2013).

3.5.5 Geodynamic Implications

Using constraints from geochemistry and the estimated pressures and temperatures of melting, it is possible to develop a model of how melting occurs under the Lesser Caucasus region. It seems clear that a majority of melting is taking place in the lithosphere for two reasons. Firstly, all samples display an arc-type geochemistry. Subduction ceased around 35 Ma (Rolland et al., 2012), such that these arc signatures will likely only be preserved in the lithosphere. It is possible that the mantle lithosphere retains phases such as amphibole and rutile, which if equilibrated with the magmas, are sufficient to impart the arc-type geochemical signature (Allen et al., 2013). Secondly, both northern and southern Lesser Caucasus magmas appear to be produced at significantly lower temperatures than the low K/Nb magmas of eastern Anatolia, which are thought to be derived from the convecting mantle (McNab et al., 2018), such that the Lesser Caucasus magmas have either re-equilibrated in colder lithosphere or are entirely derived from the lithosphere.

Based on the smooth trend in $^{87}Sr/^{86}Sr$ *versus* $^{143}Nd/^{144}Nd$ in Fig. 3.8 and the gradational changes in trace element patterns (Fig. 3.5), it appears that magmas are produced from melting of two source types in varying proportions. If these two source types reflect geochemical end-members, one would be typified by the northern Lesser Caucasus volcanic rocks, whereas the other end-member would be most clearly seen in NW Iran.

Unfortunately constraints on the lithospheric thickness are very limited for the northern Lesser Caucasus (Fig. 3.1), with the Priestley et al. (2012) model showing only that it is <100 km. Taking a typical conductive geothermal gradient for this lithosphere, melting would be expected to occur close to the lithosphere-asthenosphere boundary. Mantle-melt equilibration close to the base of the crust (Fig. 3.14) suggests that the lithosphere is very thin. If this were the case it is likely that there would be some melting of the convecting mantle based on elevated mantle T_p in the region (McNab et al., 2018). However, such a thin lithosphere would make it difficult to insulate the crust from heating, such that more crustal contamination would be expected. As was noted above, this mantle source type appears also to be present in the southern Lesser Caucasus, where the lithosphere is sufficiently thick to supress melting of anhydrous convecting mantle, but where melting of a hydrous lithospheric source would still be possible. It is likely that this magma type is derived from melting of the base of the lithosphere in response to small scale convective removal, as suggested by Neill et al. (2015). This is shown in Figure 3.15a as melt zone 1, with small portions of lithosphere being delaminated. This type of delamination is suggested to occur because a very small amount of water (a few hundred ppm) left over from previous subduction lowers the viscosity of the mantle sufficiently to allow more vigorous convection to render the lithosphere-asthenosphere boundary unstable (Kaislaniemi et al., 2014). Small scale convective removal is preferred over catastrophic large scale delamination because volcanism in the Lesser Caucasus is generally small-scale and sustained, with no evidence of crustal contamination, consistent with a continuous, less invasive process. While this magma type is a mixing component in the southern Lesser Caucasus, it is not seen in NW Iran because the lithosphere is too thick for wet or dry melting at its base (Green and Falloon, 2005; Priestley et al., 2012). As the lithosphere is thickened, the degree of melting in response to convective removal will decrease as the wet peridotite solidus is approached with depth (Fig. 3.15a), which may help to explain the lower degrees of melting in the south.

The second melting zone is the sole magma source for volcanic rocks in NW Iran (Fig. 3.15b). Despite very different lithosphere thicknesses, both NW Iran and southern Lesser Caucasus magmas formed under similar conditions within the lithosphere (Fig. 3.14). It is suggested that continental collision could have led to the formation of a kinked geothermal gradient (Fig. 3.15c). A linear craton-style

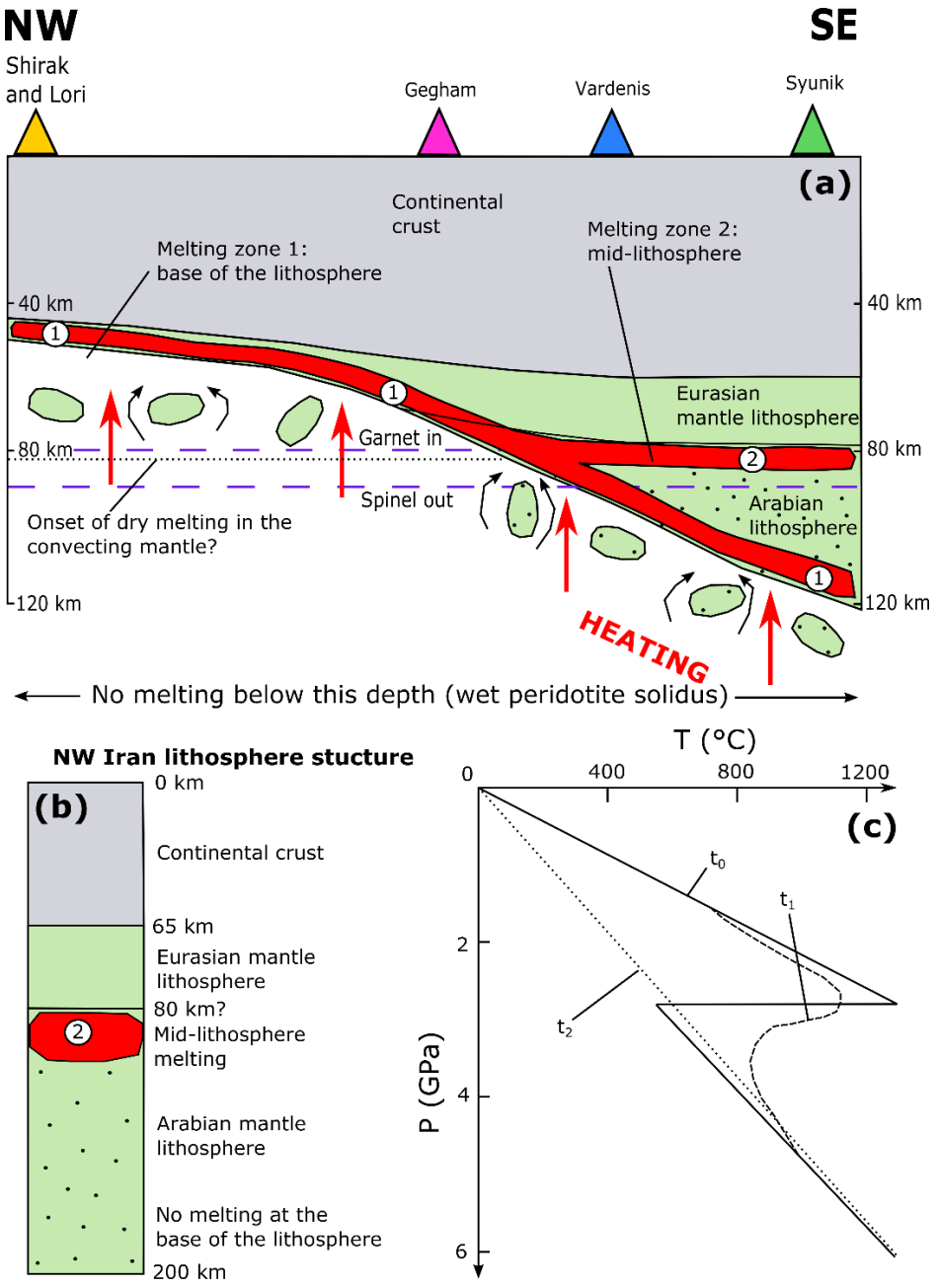

Figure 3.15 Geodynamic model of magmatism showing the lithosphere and upper mantle across the Lesser Caucasus

(a) Crustal thickness is estimated on the basis of formulations relating the Sr/Y and $(La/Yb)_N$ ratios in intermediate volcanic rocks to Moho depth (Hu et al., 2017). Data filtering follows the approach outlined in Hu et al. (2017). Each volcanic highland has a range of moho depth estimates of around 20 km. For both the Sr/Y and $(La/Yb)_N$ the median value for each volcanic highland is taken and then the two values are averaged to give an estimate of crustal thickness. Lithosphere thickness estimates are from Priestley et al. (2012). It is noted that they only estimate thicknesses where the lithosphere >100 km, so the lithospheric thickness in the NW is schematic after Neill et al. (2015). Melting at the wet peridotite solidus lower depth limit is on the basis of upwelling convecting mantle at 1300-1400°C T_p, which would lead to the wet solidus being crossed at ~ 140 km depth (Green and Falloon, 2005). Also shown are the two melting zones (labelled 1 and 2) which are discussed in the text. Melting zone 1 is along the base of the lithosphere, and is suggested to be in response to small scale convective removal of the lithosphere. Melting zone 2 is in the mid-lithosphere. (b) Sketch column of the lithospheric structure of NW Iran and the location of melting in the mid-lithosphere (c) schematic illustration for the thought experiment of the thermal relaxation of a kinked geothermal gradient leading to melting in the mid-lithosphere from initial under-plating at time t_0, though thermal evolution at time t_1, to establishing a cratonic geotherm by time t_2.

geothermal gradient is likely to be unrealistic for orogenic lithosphere (Allen et al., 2013). It has been suggested that orogenesis may proceed by underthrusting of mantle lithosphere from the oncoming plate (e.g. Willett et al, 1993). In this case under-thrusting of Arabian mantle lithosphere, with its own pre-existing geothermal gradient, may lead to a kinked geothermal gradient with the kink forming along the subduction plane between overlying Eurasian lithosphere and underlying Arabian lithosphere. Upon initial collision, this kink will be very sharp (t_0 in Fig. 3.15b), but over time the gradient will thermally relax (t_1) towards a gradient that resembles the one characteristic for cratons (t_2). This thermal relaxation would heat the lithosphere just under the kink, which would previously have been cool. Dewatering and melting of this horizon would follow, which is argued to be seen here in the P-T estimates of magma generation in Fig. 3.14. Given the lower degrees of melting in the southern Lesser Caucasus, it appears that this mechanism only develops low degree melts.

To summarise, in the northern Lesser Caucasus magma is generated by small-scale delamination events heating the base of the lithosphere. This process also occurs in the southern Lesser Caucasus, but at greater depths. Magmas generated by this mechanism mix with a second type of magma produced in the mid-lithosphere from thermal relaxation of a kinked geotherm. Further south, in NW Iran, melting of the base of the lithosphere is suppressed due to the depth being too great even for wet melting. However, melting in the mid-lithosphere continues.

3.5.6 How does thicker mantle lithosphere influence the composition of the mantle source?

The gradient in Sr-Nd isotope ratios in Fig. 3.8, along with a lack of evidence for crustal contamination, requires that there be some variation in the composition of the mantle source. One possibility is that magmas are tapping different lithosphere domains. Northern Lesser Caucasus magmas are exclusively found on Mesozoic arc lithosphere (Fig. 2.1), whereas southern Lesser Caucasus magmas are on South Armenian Block lithosphere, or else are very close to the suture. However, crossing such lithospheric sutures would likely result in a step-change in isotope ratios, rather than the smooth gradation observed in the Lesser Caucasus. A minority of samples from Vardenis volcanic highland (Fig. 3.1) are thought to be on the east (Mesozoic arc) side of the suture, these are shown by a * in Table 3.3. As Table 3.3 shows,

these samples have Sr-Nd isotope compositions indistinguishable from other Vardenis samples, suggesting the suture zone is not a major dividing line in isotope composition. This suggests that melting zone 2 in the mid-lithosphere has a different composition to melting zone 1 at the base of the lithosphere. In this discussion on the nature of the mantle sources, only the most mafic samples (> 4 wt % MgO, < 54% SiO_2) are used in order to try and minimise the effects of fractional crystallisation on trace element contents.

The lower crust is thought to behave as a weak layer during continental collision (Bürgmann and Dresen, 2008). This could lead to some lower crust being incorporated into the mantle lithosphere perhaps during underthrusting of Arabian lithosphere, as has been suggested for numerical models of other collision zones such as the Himalayas (Toussaint et al., 2004; Li et al., 2011). This could lead to the addition of lower continental crust (LCC) to melting zone 2 in the middle of the lithosphere, and hence enrichment of the mantle source of the southern Lesser Caucasus. Incorporation of LCC into the mantle source could result in significant enrichments in all of the most incompatible trace elements, as in Fig. 3.5e, given the much higher concentrations of most incompatible trace elements in the lower crust relative to the primitive mantle (Sun and McDonough, 1989; Rudnick and Gao, 2014).

The La/Nb ratios of the least enriched samples from the northern Lesser Caucasus and the same ratio estimated for the LCC (Rudnick and Gao, 2014) provides a serendipitous coincidence, with both around 1.6 (Fig. 3.16). Given that La/Nb is unaffected by melting and crystallisation (i.e. both elements have similar bulk partition coefficients with respect to the melt) regardless of source mineralogy (Thirlwall et al., 1994; Ionov et al., 2002), any variations in the La/Nb ratio should reflect variations in the source La/Nb. If the lower crust was responsible for the source enrichment, La/Nb should be near-constant along the transect. Samples from the southern Lesser Caucasus have much higher La/Nb ranging from 2.5 to 5 (Fig. 3.16), which cannot be explained by the addition of average LCC.

However, it is worth noting that several estimates of the composition of individual lower crust sections do give higher La/Nb of up to 4.9 (Weaver and Tarney, 1984; Villaseca et al., 2007; Jagoutz and Schmidt, 2013), such that the involvement of lower crust in the southern Lesser Caucasus magma source cannot

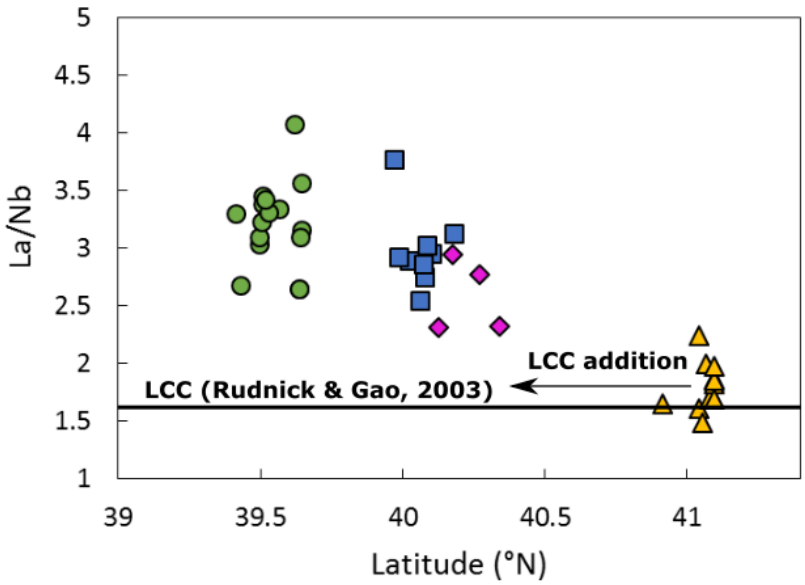

Figure 3.16 La/Nb *vs* latitude and the potential addition of lower crust to the mantle source

The least enriched Shirak and Lori samples have a La/Nb ratio of ~1.6. Fraction of melting and garnet *vs* spinel lherzolite melting have a limited effect on this ratio. Lower continental crust (LCC) has a La/Nb ratio with a similar value of around 1.6 (Rudnick and Gao, 2014). Therefore if LCC is enriching the melt source, the La/Nb ratio should be close to invariant.

be precluded.

Lithospheric mantle which is significantly shallower than the lithosphere-asthenosphere boundary (melting zone 2) is expected to be colder than the deep lithosphere (melting zone 1) prior to any heating, even if the lithosphere does have a kinked geothermal gradient (Fig. 3.14). These lower temperatures should stabilise minerals such as amphibole and phlogopite which can retain chemical components derived from mantle metasomatism (Luth, 2003; Frost, 2006; and references therein). In the deep lithosphere, these components would be subject to upward mobilization by fluid release following dehydration at higher pre-melting temperatures. Under-thrusting of Arabian lithosphere, as suggested in Fig. 3.15, would also introduce a new lithospheric domain, which could have a different composition (including isotopically) to the Eurasian lithosphere.

If this metasomatic material is responsible for the enrichments in the southern Lesser Caucasus, then it must have a composition capable of producing those most enriched melts. La/Yb and Sr/Y are two ratios which increase most dramatically with latitude as shown in Figs 3.17a and b. Both of these ratios show excellent correlations with P_2O_5 content (Figs 3.17c and d) within all Lesser Caucasus samples. The La/Yb ratios and P_2O_5 contents of the NW Iran samples

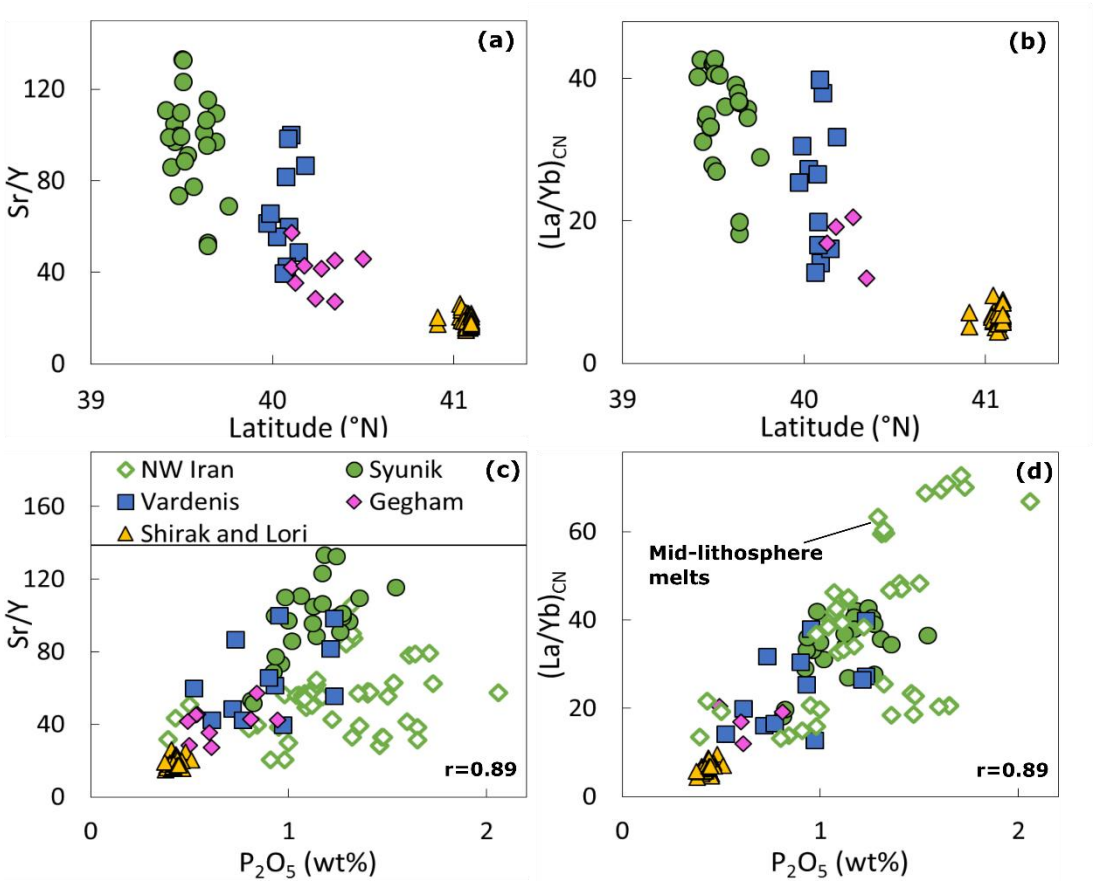

Figure 3.17 Sr/Y and La/Yb variations with latitude and P_2O_5 (wt %)

Sr/Y and La/Yb show strong variations between the northern and southern Lesser Caucasus as shown in (a) and (b). Both of these ratios show strong correlations with P_2O_5 (wt %) (c and d), r=0.89 in both cases. NW Iran data (Allen et al., 2013) in c and d represent melting in a region of very thick lithosphere.

(interpreted to be pure melting zone 2 magmas) appear as end-members on the Lesser Caucasus mixing line (Fig. 3.17d), suggesting apatite may be a metasomatic phase in the host rock of melting zone 2 (Fig. 3.15). This is consistent with the presence of large apatite crystals in some southern Lesser Caucasus samples (up to 2mm across; Fig. 3.2b). It is also consistent with previous suggestions that metasomatic apatite may be an important phase in the Iranian sub-continental lithospheric mantle (Pang et al., 2013). As was shown in Fig. 3.12 it is difficult to produce such high LREE concentrations (shown by La in Fig. 3.12) simply by lower degrees of melting or more garnet in the mantle source. Apatite is soluble in melts with a low SiO_2 content (Watson, 1980), such that apatite may simply be added to the initial modelled melt composition, as shown by the blue dashed line in Figure 3.12, producing a much improved agreement with natural southern Lesser Caucasus samples.

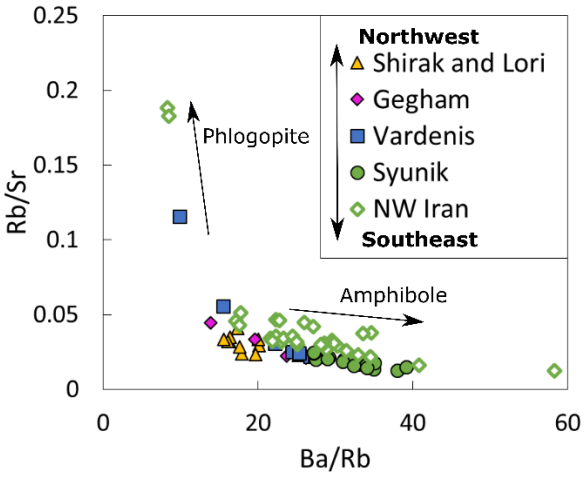

Figure 3.18 Rb/Sr *vs* Ba/Rb for Lesser Caucasus and NW Iran samples. After Furman and Graham (1999). See text for discussion.

While apatite can explain the enrichment in LREE, it cannot explain the large enrichment in other elements such as Ba, which likely requires wider metasomatic reworking. Two minerals which could explain this enrichment in Ba are amphibole and phlogopite. As Fig. 3.18 shows, the high Ba/Rb ratio favours amphibole as the major metasomatic phase in the source of both the Lesser Caucasus and NW Iran. However, in both the southern Lesser Caucasus and NW Iran there are a minority of samples for which phlogopite could be an important metasomatic phase. It is noteworthy that the presence of phlogopite in the mantle source is indicated in a minority of cases for Vardenis, but not Syunik (Fig. 3.18), given biotite is only found as a phenocryst phase in mafic samples in Vardenis (see Section 3.3). The presence of these metasomatic signatures in the southern Lesser Caucasus and NW Iran is consistent with melting zone 2 being host to apatite, amphibole, and occasionally phlogopite prior to melting.

Sr/Y is a ratio which does not follow a simple mixing pattern. It increases across the Lesser Caucasus, but is actually lower in NW Iran compared to the southern Lesser Caucasus. This ratio probably reflects the involvement of garnet in the mantle source (Defant and Drummond, 1990), which should become dominant at greater depths. In NW Iran, all melting is occurring in the mid-lithosphere, however in the southern Lesser Caucasus magmatism is driven by melting in both the mid-lithosphere and at the base of the lithosphere (Fig. 3.15). This means that in the southern Lesser Caucasus, the average depth of melting may actually be greater than

in NW Iran, despite the thinner lithosphere, leading to the mantle source being more dominated by garnet, increasing the Sr/Y ratio of the resulting magmas.

High Sr/Y ratios have been associated with adakites and the melting of oceanic slabs (Defant and Drummond, 1990). Adakitic signatures have been seen in some volcanic suites from NW Iran (e.g. Ghalamghash et al., 2016), suggesting that the Iranian enriched signature could somehow derive from slab melting. These adakites are generally andesites and dacites. The more primitive NW Iran lavas of Allen et al. (2013) and the southern Lesser Caucasus lavas have higher Y contents than true adakites, and it is likely the adakite-like compositions of andesites and dacites are derived from fractional crystallisation processes (e.g. Chiaradia et al., 2009), rather than slab melting.

Melting zone 2 does appear to have a more enriched composition than melting zone 1, as demonstrated by signatures of the metasomatic minerals apatite and amphibole in rocks derived from the southern Lesser Caucasus and NW Iran. However, variations between the chemistry of the northern and southern Lesser Caucasus volcanic rocks do not just reflect mixing of source reservoirs, but also changes in the degree of melting (lower degree of melting will increase La/Yb and Sr/Y ratios), and the mineralogy of the melt source (garnet in the melt source of the southern Lesser Caucasus also increases Sr/Y and La/Yb). The multiple parameters controlling the trace element composition of Lesser Caucasus volcanic rocks means that variations between the northern Lesser Caucasus, southern Lesser Caucasus and NW Iran are often non-linear.

3.6 Summary and Conclusions

Magmas generated in the thicker lithosphere of the southern Lesser Caucasus have higher incompatible trace element concentrations, higher $^{87}Sr/^{86}Sr$ ratios and lower $^{143}Nd/^{144}Nd$ ratios than volcanic rocks from the northern Lesser Caucasus. A lack of consistent variation between the isotope compositions of basalts and rhyolites and SiO_2 suggests crustal contamination is unimportant in generating the enriched geochemistry. The negative Nb-Ta anomalies, and enrichments in large-ion-lithophile elements and LREE are instead likely to be produced by partial melting of a subduction modified mantle source. This subduction component is uniform across

the Lesser Caucasus and is likely inherited from Mesozoic (Tethyan) slab subduction prior to continental collision. The more enriched geochemistry of southern Lesser Caucasus rocks is the result of lower degrees of melting, an increased proportion of garnet in the mantle source, and also a distinct mantle source composition.

The temperatures of melt formation in the mantle are all less than 1200°C, which when compared with the much higher temperatures for magmas formed in the asthenosphere below nearby eastern Anatolia, suggests magma generation occurs in the lithosphere, which is also consistent with the ubiquitous subduction signature. Very similar conditions of melt generation in NW Iran and the southern Lesser Caucasus, as well as several similarities in geochemistry, suggest a common magma generation mechanism in the mid-lithosphere, despite very different lithospheric thicknesses. This magma type appears to mix in the southern Lesser Caucasus with magma from a second source, which probably originates at the base of the lithosphere. This latter magma source is the sole site of magma generation in the northern Lesser Caucasus, where melting occurs at the base of a ~50 km thick lithosphere. In the southern Lesser Caucasus melting occurs at ~75 km depth, significantly shallower than the estimated 120 km thick lithosphere. Melting in the mid-lithosphere occurs due to relaxation of a kinked geothermal gradient, whereas melting at the base of the lithosphere is the result of small-scale delamination events. This latter melting mechanism only proceeds until the point where the lithosphere becomes too thick to melt at its base, even if the mantle peridotite is hydrated. The enriched composition of the mid-lithospheric mantle source could be derived from the incorporation of weak lower crust during collision. However, several signatures of the metasomatic minerals amphibole, apatite and occasionally phlogopite suggest that the enriched nature of the mantle source in the mid-lithosphere is derived from the increased retention of metasomatic components in hydrous minerals prior to the post-collisional magmatism.

Interestingly, it appears that a melt source exists at somewhat less than 100 km depth regardless of the lithospheric thickness across the Anatolian-Armenian-Iranian plateau. This is consistent with the geophysical observations of which show a low shear wave velocity at around 100 km depth below the entire plateau (Maggi and Priestley, 2005). Further work on understanding the interplay between lithospheric thickness and melt generation in continental collision zones would

benefit from detailed tomographic work in the critical region of the Lesser Caucasus to help us better understand how the thickness of the lithosphere varies along this mountain range. Investigations of the petrogenesis of primitive magmatic rocks from NW Iran, could elucidate whether thermal relaxation of a kinked geothermal gradient is a viable mechanism to generate magma in the mid-lithosphere. Studies of stable fluid-sensitive isotopes systems such as O and B would help decipher the nature and role of inherited subduction components in the generation of collision-related magmas.

4. Boron isotope insights into the origin of subduction components in a continent-continent collision zone

4.1 Introduction

Boron (B) and its stable isotopes ^{10}B and ^{11}B are a key tracer for the fate of subduction components under volcanic arcs (De Hoog and Savov, 2018). This is due to a scarcity of boron in the mantle (<0.1 ppm; Leeman et al., 2004; Marschall et al., 2017) and its strong fluid partitioning, with concomitant isotope fractionation during metamorphic slab dehydration reactions which release aqueous fluids at T < 800°C (Konrad-Schmolke and Halama, 2014). B isotope fractionation is largely controlled by the preferential incorporation of ^{11}B into trigonal over tetrahedral sites (Kakihana et al., 1977). Thus B is strongly fractionated between mostly tetrahedrally co-ordinated B in silicate minerals and trigonally co-ordinated B in aqueous fluids (Peacock and Hervig, 1999). This fractionation is preserved in arc magmas because later mantle melting should not lead to isotope fractionation as B is substantially tetrahedrally co-ordinated in both mantle minerals and magmas (Tonarini et al., 2001; Maner and London, 2018).

Only a handful of studies have used B to explore the impact of subduction components on the upper mantle (magma source) composition in regions where subduction has ceased (e.g. Tonarini et al., 2005). This chapter presents whole-rock [B] and $\delta^{11}B$ data for well-studied collision-related igneous rocks from the Lesser Caucasus (Sokół et al., 2018; Sugden et al., 2019), representing the first boron isotope data for young volcanic rocks from an active continent-continent collision (Fig. 4.1). This collision zone is unique on Earth as a modern continental collision zone associated with widespread mantle-derived magmatism. The arc-like geochemistry of volcanic rocks from the Lesser Caucasus (Fig. 4.2, Table 4.1) reflects a subduction-modified mantle source (see Chapter 3). The [B] and $\delta^{11}B$ data presented in this study come from 1.5-0 Ma post-collisional volcanic rocks, as well as ~ 41 Ma alkaline igneous rocks. The latter are used to investigate the $\delta^{11}B$ variations in the subduction-modified mantle since the onset of continental collision. The new [B] and $\delta^{11}B$ data, alongside previously published trace element and Sr- Nd isotope data are used to investigate the nature of the subduction component.

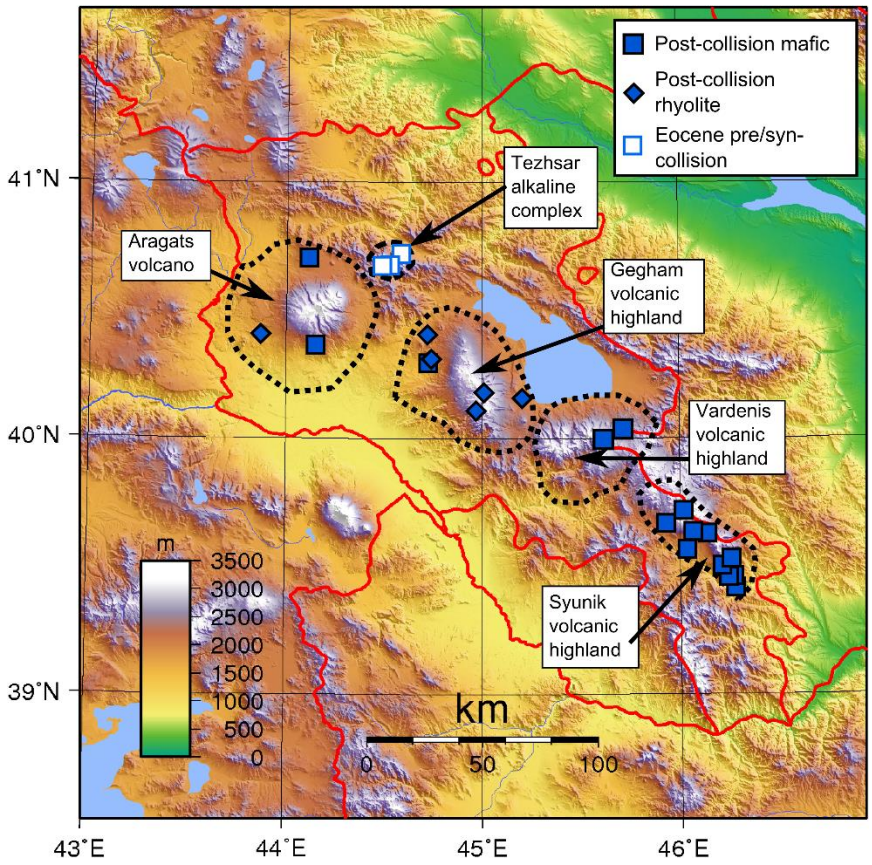

Figure 4.1 Location map of the Lesser Caucasus showing locations of samples analysed for B. Also shown are locations of volcanic regions referred to in the text. Basemap image freely available from https://commons.wikimedia.org/wiki/User:Sadalmelik

4.2 Sample selection for B isotope analyses

The investigated Plio-Pleistocene post-collisional volcanic rocks are from 3 volcanic highlands of monogenetic volcanism (Syunik, Vardenis and Gegham) and the large Aragats stratovolcano (Fig. 4.1). Most of the samples have mafic compositions (Fig. 4.1) and an arc-type geochemistry (Fig. 4.2a), revealing a subduction component in the mantle source. There is a disproportionate number of samples from the Syunik volcanic highland, where mafic lava flows are most abundant. Several of the samples from Gegham volcanic highland, and one sample from Aragats are rhyolite obsidians. The use of obsidian samples is justified given the lack of evidence for crustal contamination (Neill et al., 2015; Sugden et al., 2019), and because boron isotopes do not fractionate during crystal fractionation. The full major and trace element data for all samples measured for boron are shown in Table 4.1.

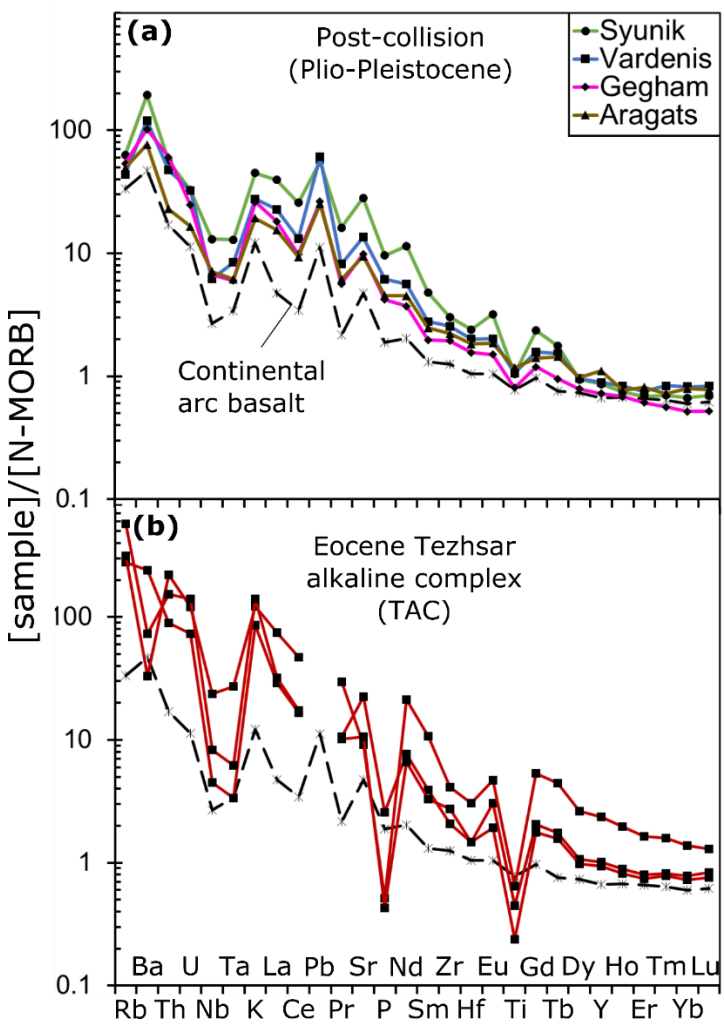

Figure 4.2 N-MORB normalised trace element systematics of Plio-Pleistocene (post-collisional) and Eocene (pre- to syn-collision) volcanic rocks from the Lesser Caucasus

All samples normalised to N-MORB (Sun and McDonough, 1989). (a) Plio-Pleistocene post-collisional (Sugden et al., 2019) and (b) Eocene TAC (Sokół et al., 2018) volcanic rocks from the Lesser Caucasus. Average continental arc basalt is shown for comparison (Kelemen et al., 2003). Note the negative Nb-Ta and Ti anomalies observed in all samples, as well as the positive spikes in LILE and LREE. In the absence of evidence for crustal contamination in the Lesser Caucasus, such "spiky" trace element profiles are commonly interpreted as derivation of the magmas from a subduction-modified mantle source. The more unusual trace element composition of the TAC samples is likely a result of these samples having intermediate compositions (phonolite).

Data from the Tezhsar alkaline complex (TAC) are also presented (Figs 4.1 & 4.2; Table 4.1). The TAC contains trachyte-phonolite volcanic rocks and syenite intrusives from an ~10 km wide shallow plumbing system of an extinct large stratovolcano (Sokół et al., 2018). Although there are some differences in the trace element composition of TAC samples (Fig. 4.2b) when compared to the post-collision samples, they still have the characteristic (if larger) negative Nb-Ta and Ti anomalies and a general enrichment in large ion lithophile (LILE) and light rare

Table 4.1 Major and trace element compositions of samples analysed for B isotopes

Region	Gegham	Gegham	Gegham	Gegham	Gegham	Gegham	Gegham
Sample	4.20.04	6.26.04	8.29B.04	8.30A.04	9.31A.04	9.31B.04	9.31D.04
Latitude (°N)	40.16617	40.4079	40.18125	40.12737	40.27525	40.27122	40.30775
Longitude (°E)	45.20602	44.68053	45.00992	45.00173	44.70115	44.69962	44.71902
Lithology	Rhyolite	Rhyolite	Rhyolite	Rhyolite	Rhyolite	TBA	Rhyolite
Erup. type	Obsidian	Obsidian	Obsidian	Obsidian	Obsidian	Lava	Obsidian
SiO_2 (wt%)	74.15	73.99	74.51	75.90	73.89	53.83	73.69
TiO_2	0.08	0.18	0.07	0.08	0.10	1.02	0.15
Al_2O_3	13.55	13.86	13.64	13.15	13.86	15.86	13.98
Fe_2O_3 (tot)*	0.63	1.25	0.64	0.60	0.97	7.59	1.32
MnO	0.11	0.08	0.11	0.09	0.07	0.12	0.06
MgO	0.10	0.24	0.12	0.07	0.20	6.57	0.35
CaO	0.56	0.99	0.57	0.59	1.00	8.19	1.32
Na_2O	4.27	4.49	4.21	4.35	4.22	4.03	4.66
K_2O	4.35	4.21	4.38	4.48	4.18	1.89	4.15
P_2O_5	0.03	0.06	0.02	0.01	0.03	0.49	0.05
Total	98.88	99.66	98.99	99.71	98.75	99.36	99.74
LOI	1.07	0.31	0.75	0.42	0.31	0.15	0.23
La	N.D.	18.8	N.D.	16.7	27.5	45.4	N.D.
Ce	N.D.	33.4	N.D.	31.0	44.0	73.6	N.D.
Pr	N.D.	3.4	N.D.	3.2	4.1	7.4	N.D.
Nd	N.D.	11.4	N.D.	11.2	13.2	27.1	N.D.
Sm	N.D.	2.5	N.D.	3.0	2.7	5.2	N.D.
Eu	N.D.	0.4	N.D.	0.2	0.5	1.5	N.D.
Gd	N.D.	2.3	N.D.	3.0	2.4	4.4	N.D.
Tb	N.D.	0.4	N.D.	0.6	0.4	0.6	N.D.
Dy	N.D.	2.9	N.D.	3.8	2.7	3.6	N.D.
Ho	N.D.	0.6	N.D.	0.8	0.5	0.7	N.D.
Er	N.D.	1.8	N.D.	2.2	1.5	1.8	N.D.
Tm	N.D.	0.3	N.D.	0.4	0.2	0.3	N.D.
Yb	N.D.	2.0	N.D.	2.4	1.6	1.6	N.D.
Lu	N.D.	0.3	N.D.	0.4	0.3	0.2	N.D.
Ba	47.0	422.1	N.D.	11.8	530.8	642.0	538.0
Hf	N.D.	4.5	N.D.	3.0	3.1	3.2	N.D.
Nb	45.0	36.4	N.D.	50.8	22.8	15.7	22.0
Rb	168.0	132.4	N.D.	196.0	108.8	30.0	99.0
Sr	8.0	114.1	N.D.	10.1	104.0	885.3	147
Pb	N.D.	20.1	N.D.	27.4	21.9	7.9	N.D.
Ta	N.D.	3.2	N.D.	5.0	2.3	0.8	N.D.
Th	N.D.	14.2	N.D.	27.9	17.9	7.2	N.D.
U	N.D.	7.5	N.D.	13.5	8.5	1.2	N.D.
Zr	64.0	157.4	N.D.	59.9	91.7	143.5	109.0
Y	22.0	20.4	N.D.	23.8	16.7	20.3	15.0

Fe reported as FeO was recalculated to Fe_2O_3 (tot) by dividing by a factor of 0.89981. Totals are the original totals prior to Fe_2O_3 (tot) recalculation

Table 4.1 continued.

Region	Syunik	Syunik	Syunik	Syunik	Vardenis	Syunik	Syunik
Sample	2.7.08	2.10.08	6.26.08	5.3.15	6.3.15	8.3.15	8.5.15
Latitude (°N)	39.4587	39.46787	39.68872	40.03073	39.98746	39.4141	39.49431
Longitude (°E)	46.24037	46.25762	45.91847	45.69655	45.61326	46.28308	46.24621
Lithology	PT	Basalt	TA	TA	TBA	TBA	Basanite
Erup. type	Bomb	Lava	Lava	Lava	Lava	Bomb	Bomb
SiO_2 (wt%)	50.44	47.08	55.45	56.98	53.73	51.58	45.80
TiO_2	1.32	1.31	1.08	0.91	1.08	1.21	1.58
Al_2O_3	16.82	14.39	16.97	15.71	17.09	16.65	14.92
Fe_2O_3 (tot)*	9.31	11.45	8.26	6.30	7.60	7.66	9.56
MnO	0.14	0.15	0.12	0.11	0.13	0.13	0.16
MgO	4.44	11.65	3.62	3.72	4.06	4.29	7.77
CaO	8.16	9.83	6.68	6.84	7.24	8.01	10.02
Na_2O	5.12	3.29	4.70	4.19	4.79	4.48	4.30
K_2O	3.25	1.19	3.12	2.88	2.75	3.14	2.64
P_2O_5	1.12	0.53	0.91	0.52	0.90	1.06	1.27
Total	99.20	99.74	100.1	99.5	99.78	99.76	98.90
LOI	N.D.†	N.D.	N.D.	1.3	0.27	1.41	0.73
La	99	32.0	82.6	56.6	75	94.0	75.0
Ce	193	66	149.8	99.5	132	175.0	158.0
Pr	21.4	8.3	16.0	10.8	14.5	20.0	19.6
Nd	84	34	60.2	37.4	50.0	71.0	75.0
Sm	12.7	6.5	9.5	6.0	8.0	9.7	11.0
Eu	3.3	1.8	2.5	1.6	2.0	2.6	3.0
Gd	8.7	4.9	6.9	5.3	5.8	6.8	7.6
Tb	1.2	0.9	1.0	0.7	0.7	0.8	0.9
Dy	4.3	4.0	3.8	4.3	3.8	4.0	4.7
Ho	0.8	0.8	0.7	0.8	0.7	0.7	0.8
Er	2.0	2.1	1.8	2.3	2.0	1.7	2.1
Tm	0.3	0.4	0.3	0.3	0.3	0.3	0.3
Yb	2.0	2.2	1.7	2.1	1.8	1.7	1.9
Lu	0.3	0.4	0.3	0.3	0.3	0.2	0.3
Ba	1220.0	430.0	1147.0	819.0	962.0	1180.0	1093.0
Hf	4.9	3.0	4.8	4.7	4.3	4.5	3.7
Nb	N.D.	N.D.	N.D.	21.0	25.8	28.4	24.1
Rb	N.D.	N.D.	N.D.	72.2	43.4	43.0	31.3
Sr	2531.0	1073.0	1588.8	954.9	1411.0	2161.0	2325.0
Pb	16.7	9.0	28.7	N.D.	N.D.	N.D.	N.D.
Ta	1.7	0.7	1.4	1.0	1.0	1.2	0.9
Th	6.8	2.6	7.3	12.6	7.1	6.6	3.6
U	1.5	0.7	1.6	4.0	1.4	1.2	0.8
Zr	224.0	126.0	220.8	207.5	215.0	217.0	166.0
Y	24.1	22.2	20.3	21.2	21.4	19.5	23.4

Table 4.1 continued.

Region	Syunik	Syunik	Syunik	Syunik	Syunik	Aragats
Sample	9.1.15	10.2.15	11.1.15	11.4.15	6.2.17	11.35A.04
Latitude (°N)	39.53042	39.64359	39.57705	39.63671	39.71918	40.40487
Longitude (°E)	46.22106	46.10184	45.99658	46.04296	46.00917	43.81503
Lithology	TBA	TBA	TBA	Tephrite	TBA	Rhyolite
Erup. type	Plug	Lava	Lava	Lava	Lava	Obsidian
SiO_2 (wt%)	51.6	51.35	55.65	48.67	54.14	76.02
TiO_2	1.22	1.48	1.08	1.73	1.14	0.06
Al_2O_3	17.4	16.93	17.52	15.86	16.92	13.13
Fe_2O_3 (tot)[2]	8.2	8.96	7.38	9.77	7.41	0.49
MnO	0.13	0.14	0.12	0.14	0.13	0.09
MgO	4.42	4.78	3.21	5.65	3.67	0.04
CaO	7.51	8.23	6.07	9.69	7.18	0.48
Na_2O	4.50	4.85	4.90	4.37	4.89	4.35
K_2O	3.06	2.11	3.12	2.49	3.21	4.31
P_2O_5	1.26	0.81	0.82	1.12	1.06	0.01
Total	99.94	99.93	100.0	100.06	99.76	99.02
LOI	0.49	0.18	0.0	0.44	0.19	2.94
La	104.0	61.0	79.9	86.0	105.0	11.6
Ce	189.0	115.0	138.4	175.0	182.1	24.9
Pr	21.2	12.9	15.7	20.9	19.6	2.8
Nd	72.0	48.0	55.8	77.0	70.9	9.8
Sm	10.1	8.0	7.8	10.7	9.8	3.3
Eu	2.7	2.3	2.2	2.9	2.5	0.3
Gd	7.7	6.9	6.2	7.8	7.0	3.7
Tb	0.9	0.8	0.7	0.9	0.8	0.8
Dy	4.8	5.0	4.0	4.6	4.1	5.4
Ho	0.7	0.9	0.7	0.8	0.7	1.1
Er	2.1	2.6	2.1	1.9	1.9	3.2
Tm	0.3	0.4	0.3	0.3	0.3	N.D.
Yb	1.8	2.4	1.9	1.7	1.6	3.2
Lu	0.3	0.4	0.3	0.3	0.3	0.5
Ba	1201.0	924.0	1125.0	1105.0	1267.0	35.9
Hf	4.3	5.1	5.1	4.0	5.1	3.1
Nb	31.3	19.4	25.6	32.6	29.6	38.7
Rb	41.5	34.0	51.5	34.1	49.9	141.7
Sr	2032.0	1413.0	1332.8	2131.0	1869.1	9.8
Pb	N.D.	N.D.	N.D.	N.D.	N.D.	20.0
Ta	1.2	0.8	1.3	1.2	1.2	3.0
Th	6.0	4.8	7.8	5.8	6.9	15.5
U	1.1	1.0	1.5	1.2	1.4	7.4
Zr	218.0	240.0	238.6	186.0	227.4	67.8
Y	22.3	20.3	21.2	22.3	20.1	32.0

Lithology abbreviations: TBA- trachybasaltic andesite; PT- phonotephrite; TA- trachyandesite; TB- trachybasalt; TP- tephriphonolite.

Table 4.1 continued.

Region	Aragats	Aragats	Tezhsar (TAC)	Tezhsar (TAC)	Tezhsar (TAC)	Tezhsar (TAC)
Sample	NPP 11	NPP 241	10.43.08	10.45.08	2.11.09	3.3.09
Latitude (°N)	40.29927	40.57763	40.639	40.639	40.64063	40.65353
Longitude (°E)	44.09498	44.11612	44.58325	44.58325	44.59755	44.62075
Lithology	TB	TBA	TP	Phonolite	Phonolite	Phonolite
Erup. type	Lava	Lava	Lava	Lava	Lava	Lava
SiO_2 (wt%)	50.92	52.53	53.90	58.66	54.78	55.14
TiO_2	1.49	1.35	0.57	0.82	0.30	0.36
Al_2O_3	17.31	16.78	19.95	20.07	21.73	21.91
Fe_2O_3 (tot)[2]	10.44	9.91	5.54	3.57	2.11	2.17
MnO	0.15	0.14	0.19	0.19	0.13	0.22
MgO	5.58	5.22	1.21	0.62	0.21	0.16
CaO	9.12	8.56	4.43	2.02	1.72	2.13
Na_2O	4.14	4.38	5.26	4.68	5.88	7.63
K_2O	1.39	1.85	6.23	8.82	10.16	7.94
P_2O_5	0.53	0.60	0.30	0.06	0.05	0.03
Total	101.07	101.32	101.39	100.25	99.91	98.69
LOI	N.D.	N.D.	4.19	0.99	2.98	1.15
La	38.8	48.4	72.5	186.0	80.2	N.D.
Ce	69.9	93.6	125.0	354.0	130.0	N.D.
Pr	8.1	10.9	14.0	39.3	13.4	N.D.
Nd	32.9	43.3	56.2	155.0	48.5	N.D.
Sm	6.5	7.8	10.3	28.1	8.7	N.D.
Eu	1.9	2.2	3.1	4.8	2.0	N.D.
Gd	5.2	6.1	7.6	19.7	6.5	N.D.
Tb	1.0	1.0	1.2	3.0	1.1	N.D.
Dy	4.4	4.8	4.9	11.9	4.5	N.D.
Ho	0.8	0.9	0.9	2.0	0.8	N.D.
Er	2.4	2.5	2.4	4.9	2.2	N.D.
Tm	0.3	0.4	0.4	0.7	0.4	N.D.
Yb	2.4	2.7	2.4	4.2	2.2	N.D.
Lu	0.4	0.4	0.4	0.6	0.3	N.D.
Ba	481.0	604.5	1510.0	208.0	460.0	N.D.
Hf	3.8	3.4	3.0	6.3	3.0	N.D.
Nb	17.0	15.0	10.5	55.0	19.2	N.D.
Rb	28.0	23.0	157.0	175.0	321.0	N.D.
Sr	852.4	973.4	2010.0	817.0	956.0	N.D.
Pb	7.6	N.D.	N.D.	N.D.	N.D.	N.D.
Ta	0.8	0.9	0.4	3.6	0.8	N.D.
Th	2.8	4.5	10.8	26.6	18.4	N.D.
U	0.8	1.2	3.4	5.7	6.6	N.D.
Zr	164.4	208.7	153.0	304.0	204.0	N.D.
Y	31.0	29.0	28.4	66.0	26.4	N.D.

[†]N.D. = not determined

earth elements (LREE) indicative of a subduction-modified mantle source. The studied samples have intermediate (phonolite) compositions, such that crystal fractionation is likely to be partly responsible for the trace element signature, as well as the composition of the mantle source and the melting process. An ^{40}Ar-^{39}Ar age of 41.0 ±0.5 Ma for the TAC reveals its formation either precedes, or is contemporaneous with, Arabia-Eurasia collision. An earlier 50-40 Ma collision would make the TAC syn-collisional, while a 25 Ma Eurasia/SAB-Arabia collision, would mean that Southern Neotethys subduction was still ongoing. TAC magmatism has been attributed to small degrees of decompression melting of subduction-modified lithospheric mantle in response to localised extension (Sokół et al., 2018), rather than the classic flux melting model for subduction zones. Taken together, the post-collisional and TAC rocks represent two instances of melting of a previously metasomatised mantle source separated by 40 Myr, making it possible to investigate how the inherited subduction component has changed since initial continental collision.

One of the key considerations in choosing samples for [B] and $\delta^{11}B$ analysis is to choose those least affected by alteration. This is because B is highly fluid mobile and its isotope ratio is strongly fractionated by fluid alteration at the surface (e.g. Muttik *et al.*, 2011). The fresh groundmass of samples selected for [B] and $\delta^{11}B$, with microlites and small pockets of glass preserved, is testament to the unaltered nature of the samples selected (Fig. 4.3). This groundmass is also likely to be where the majority of B is hosted, given its incompatibility in most common igneous phases (Brenan et al., 1998). Samples measured for boron isotopes in this study were specifically selected based on the lack of secondary phases observed during petrographic inspection.

Loss on ignition (LOI) is another tool commonly used to assess the level of alteration in samples. Most of the Plio-Pleistocene samples have low LOI (<1 wt%; Fig. 4.4), and there is no discernible correlation between LOI and $\delta^{11}B$ or [B] (Fig. 4.4), suggesting there has been no post-emplacement alteration of these samples and it has not affected the sample $\delta^{11}B$.

LOI values for TAC samples range from close to zero to several percent (Sokół et al., 2018), with the sub-set of samples analysed for boron exhibiting a similar range (Fig. 4.4). However, if surface alteration alone was responsible for

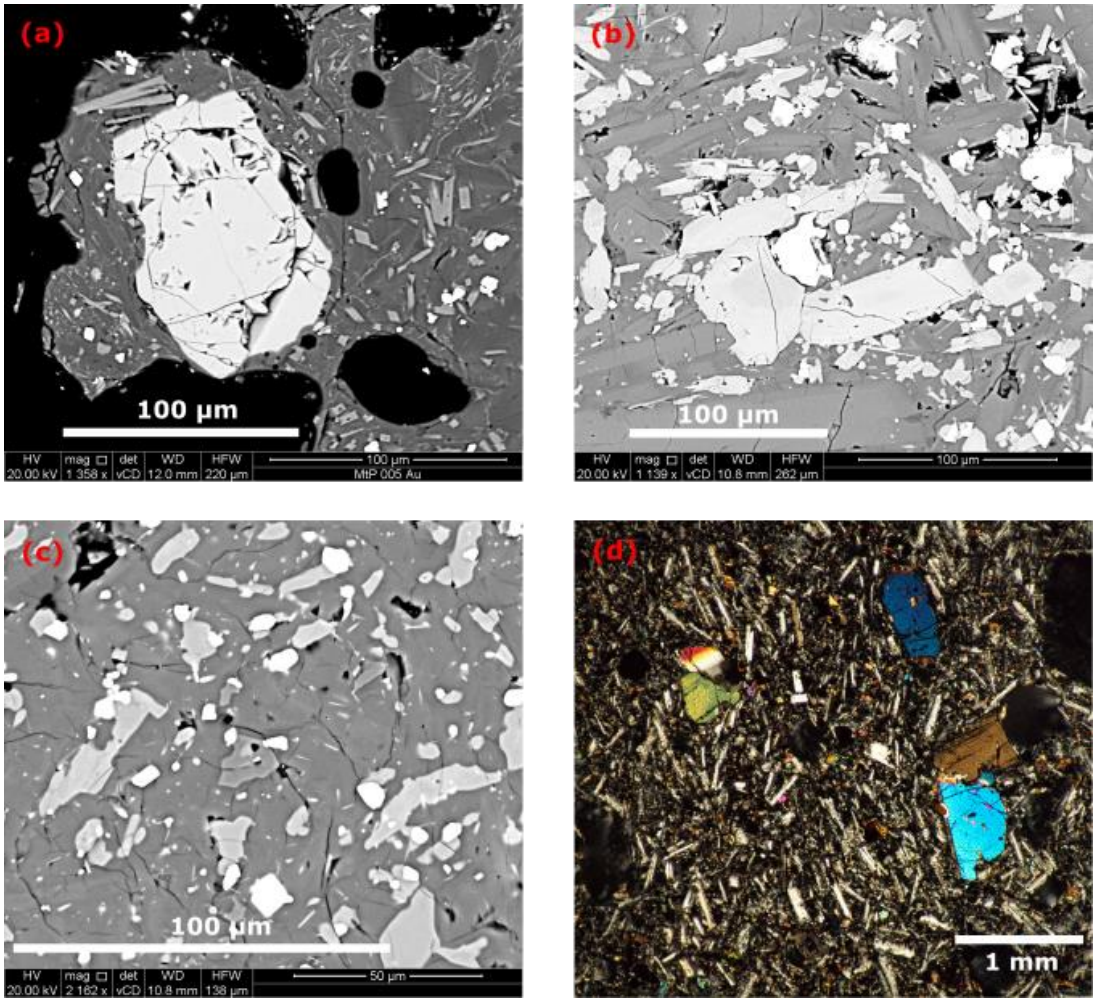

Figure 4.3 Groundmass textures of post-collisional samples selected for $\delta^{11}B$ analysis**.**

Back-scattered electron (BSE) images from scanning electron microscope work (a-c) and a cross-polarised light photomicrograph (d). (a) apatite microphenocryst in the groundmass of scoria sample 8-3-15. Notice in the groundmass the plagioclase (dark), clinopyroxene (medium) and oxide (bright) crystals with some interstitial glass present. (b) groundmass of lava sample 10-2-15. Crystals of plagioclase, clinopyroxene and oxide occurring at various scales with some interstitial glass. (c) groundmass of sample 6-3-15 noteworthy for the very small microlites which preserved suggesting limited alteration given these would be some of the first primary textures to be altered. (d) view under cross-polars of sample 9-1-15 at x4 magnification. Holocrystalline groundmass of plagioclase microlites with smaller clinopyroxene and oxide crystals also present. The phenocryst phases are olivine and clinopyroxene

high LOI, one would expect to see higher K_2O in the high LOI samples (e.g. Zhang and Smith-Duque, 2014), when in fact no correlation is observed (not shown). The high LOI could partly be the result of significant proportions of magmatic hydrous and carbonate phases in TAC samples (Sokół et al., 2018).

Although the lower $\delta^{11}B$ samples have higher LOI (Fig. 4.4), alteration would be expected to increase the $\delta^{11}B$ of volcanic rocks if boron was transferred from the fluid to the rock, given the heavy $\delta^{11}B$ of surface water (Tonarini et al., 2003). There is also no increase in [B] with LOI, as would be expected from

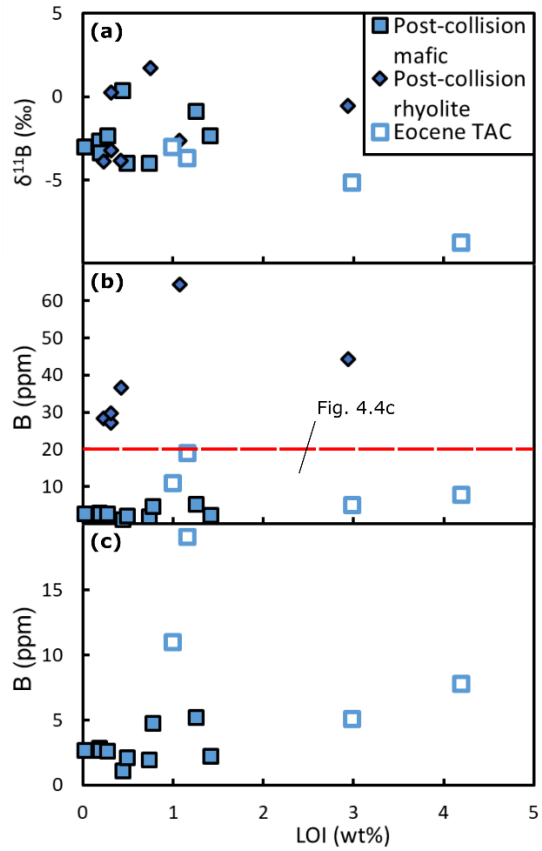

Figure 4.4 Variation in $\delta^{11}B$ and [B] with Loss on Ignition (LOI)

Showing the lack of correlation between $\delta^{11}B$ (a) and LOI and [B] and LOI (b,c). (c) shows the part of (b) below the dashed line. Some of the TAC samples have higher LOI, however it is argued the data they provide is still valuable given evidence from Sr isotopes and [B] (b,c) for these samples still being relatively unalatered. Alteration should increase [B], yet the high LOI samples have lower [B].

alteration. The variability in initial $^{87}Sr/^{86}Sr$ for TAC samples (0.7040-0.7052) may also be a reflection of alteration given the consistent $^{143}Nd/^{144}Nd$ (0.51274-0.51283; Sokół *et al.*, 2018). The low initial $^{87}Sr/^{86}Sr$ (<0.7042) in all TAC samples analysed for B is testament to their unaltered nature.

4.3 Analytical Methods

Most of the samples were prepared for boron isotope analysis at the IGG-CNR Pisa, Italy; ~0.2 g of sample powder was fused with K_2CO_3 in platinum crucibles with a 4:1 flux to sample ratio (Tonarini et al., 1997). Boron was then extracted from the fusion cakes by repeated crushing and centrifuging of the cakes in B-free water. The K flux gives the water a high pH (~10) as required for the column chemistry (Tonarini et al., 1997). It was further purified by passing the solution through anion and cation exchange columns. Anion columns were packed with Amberlite IRA-743 boron-specific anion exchange resin, while cation-exchange columns were packed

with AG 50W-X8 resin. The procedure used an anion column step, followed by a cation column step and then a final (repeat) anion column step to produce the final purified boron solution, as described by Tonarini *et al.* (1997). Of those samples prepared at IGG-CNR Pisa, the B isotope composition of nearly all of the mafic-intermediate Plio-Pleistocene post-collisional samples were measured on a Thermo Scientific^{TM} Neptune series multi-collector (MC)-ICP-MS in Pisa, specially tuned for $^{11}B/^{10}B$ analysis (following Foster, 2008). Samples were diluted to contain ~20 ppb B and were then bracketed with NBS 951 boric acid standard solution of the same concentration, to correct for machine induced mass fractionation. The boron concentrations of these purified boron solutions were measured together with $\delta^{11}B$ at IGG-CNR-Pisa, and converted to sample concentrations using accurate measurements of sample weights and the precisely known reagent volumes.

Within run errors are between 0.04 and 0.11‰ (all errors reported in this section are at the 2σ uncertainty interval). Several samples were re-prepared and re-analysed, reproducing the original value to within 1‰ or better. The accuracy of the measurement was monitored as follows: 28 replicate analyses of NBS 951 gave an average $\delta^{11}B$ of +0.01 ±0.41‰, 7 replicate analyses of the IAEA standard B1 (seawater) gave an average $\delta^{11}B$ of +39.38 ±0.27‰ (accepted value ~+39 ‰; Tonarini et al., 2003), and 3 replicate analyses of the JB2 (basalt) gave an average $\delta^{11}B$ of +7.25 ±0.57‰ (accepted value +7.33 ±0.37‰; Tonarini et al., 2003).

The Eocene TAC samples, as well as the one mafic sample from the Gegham volcanic highland (9.31B.04, Fig. 4.1) were prepared in the same way as the Plio-Pleistocene samples. However, analysis was by thermal ionisation mass spectrometry (TIMS) using a VG Isomass 54E mass spectrometer at IGG-CNR Pisa following the methods outlined in Tonarini et al. (2001). The accuracy of these measurements was monitored by analysis of the SRM-951 boric acid standard. Uncertainties on measurements are 0.4 to 0.6‰.

Boron isotope analyses of Plio-Pleistocene obsidians from the Gegham volcanic highland (Fig. 4.1) were made using multiple multiplier laser ablation inductively-coupled plasma mass spectrometry (MM-LA-ICP-MS) at the Department of Terrestrial Magnetism (DTM) of the Carnegie Institution of Washington. For the full method description see Savov et al. (2009) and references therein. The accuracy of these measurements was monitored by repeated analyses of

NBS 610, 612 and 614 glasses, as well as in-house produced (at 4 GPa) homogeneous glass of B-5 (Mt. Etna volcano basalt) and B-6 (Lipari obsidian) standards which yielded an average $\delta^{11}B$ (± 1‰) of -3.59‰ and -0.95‰ respectively. This can be compared to respective accepted values of -3.95‰ and -1.6‰ (Tonarini et al., 2003), suggesting reproducibility is better than 1‰, while within run uncertainties were < 1‰.

Boron concentrations for TAC and Gegham rhyolite samples were measured on a Perkin Elmer Optima 2000 DV inductively coupled Plasma-Optical Emission Spectrometer (ICP-OES) at the School of Geosciences of the University of South Florida. Samples were fluxed with Na_2CO_3 in platinum crucibles with lids using a furnace at 1400°C in a boron-free clean lab environment. Sample preparation techniques followed the methods outlined in Snyder et al. (2005). The analytical blank was measured as 1.5 ppm. The blank-corrected concentration of the JB-3 (basalt) external standard was correct to within 1 ppm (18.8 ppm, *vs.* accepted value 18 ppm).

All measurements of boron and its isotopes were made using the same sample powders as were used to measure the major and trace element concentrations, and Sr-Nd isotope ratios (Tables 4.1 and 4.2; methods in Sugden et al., 2019).

4.4 Results

All [B] and $\delta^{11}B$ values are shown in Table 4.2; $\delta^{11}B$ ranges from -5 to +2‰ (Fig. 4.5), consistently heavier than mid-ocean ridge basalts (MORB; -7.1 ±0.9‰; Marschall et al., 2017). There is no consistent variation with geographic position in the post-collision samples: samples from Aragats (-5 to 0‰), Vardenis (-3 to 0‰) and Syunik (-4 to +1‰) all show a similar $\delta^{11}B$ range (Table 4.2), confirming previous observations that despite changes in lithospheric thickness, the slab contribution is uniform across the Lesser Caucasus (Sugden et al., 2019). The B/Nb in mafic samples varies from 0.03 to 0.25, i.e. lower than in any modern volcanic arc (Fig. 4.5; De Hoog and Savov, 2018), and in fact overlapping with the range of MORB (0.15-1.05; Marschall et al., 2017). This suggests a fluid-mobile element (FME) depleted source when compared to the sources of arc volcanism, although

Table 4.2 [B] and $\delta^{11}B$ presented in this Thesis.

Sr-Nd isotope composition: (Connor et al., 2011; Sokół et al., 2018; Sugden et al., 2019).

Label	Volcano/ Volcanic highland	Rock type	$^{87}Sr/^{86}Sr$	$^{143}Nd/^{144}Nd$	B (ppm)	Nb (ppm)	B/Nb	$\delta^{11}B$ (‰)
Plio-Pleistocene post-collision								
4.20.04	Gegham	Rhyolite	0.70479	0.51275	64.4	45.0	1.4	-2.7
6.26.04	Gegham	Rhyolite	0.70416	0.51285	29.8	36.4	0.82	+0.3
8.29B.04	Gegham	Rhyolite	0.70493	0.51279	N.D.†	N.D.	N.D.	+1.7
8.30A.04	Gegham	Rhyolite	0.70421	0.51281	36.7	50.8	0.72	-3.8
9.31A.04	Gegham	Rhyolite	0.70422	0.51282	27.2	22.8	1.2	-3.2
9.31B.04	Gegham	Trachybasaltic andesite	0.70439	0.51281	N.D.	15.7	N.D.	-1.8
9.31D.04	Gegham	Rhyolite	0.70422	0.51282	28.4	21.5	1.3	-3.9
2.7.08	Syunik	Phonotephrite	0.70444	0.51280	2.7	30.3	0.090	-2.9
2.10.08	Syunik	Basalt	0.70440	0.51283	2.1	9.4	0.23	-1.9
6.26.08	Syunik	Trachyandesite	0.70427	0.51279	3.0	37.7	0.080	-2.1
8.3.15	Syunik	Trachybasaltic andesite	0.70444	0.51279	2.3	43.0	0.053	-2.4
8.5.15	Syunik	Trachybasaltic andesite	0.70462	0.51278	2.0	24.1	0.082	-4.0
9.1.15	Syunik	Trachybasaltic andesite	0.70444	0.51280	2.1	31.3	0.068	-4.0
10.2.15	Syunik	Trachybasaltic andesite	0.70426	0.51286	2.8	19.4	0.15	-2.7
11.1.15	Syunik	Trachybasaltic andesite	0.70438	0.51281	2.7	25.6	0.10	-3.0
11.4.15	Syunik	Tephrite	0.70428	0.51280	1.1	32.6	0.033	+0.4
6.2.17	Syunik	Trachybasaltic andesite	0.70433	0.51279	2.7	29.6	0.092	-3.3
11.35A.04	Aragats*	Rhyolite	0.70471	0.51286	n.d.	38.7	n.d.	-0.5
NPP 11	Aragats	Trachybasalt	0.70429	0.51281	1.7	16.6	0.10	-3.8
NPP 241	Aragats	Trachybasaltic andesite	0.70436	0.51282	3.2	15.3	0.21	-4.5
5.3.15	Vardenis	Trachyandesite	0.70446	0.51280	5.2	21.0	0.25	-0.9
6.3.15	Vardenis	Trachybasaltic andesite	0.70443	0.51280	2.6	25.8	0.10	-2.3
Eocene alkaline igneous rocks								
10.43.09	Tezhsar	Tephri-phonolite	0.70397	0.51283 *	7.8	10.5	0.74	-8.7
10.45.08	Tezhsar	Phonolite	0.70397	0.51282	11.0	55.0	0.20	-3.0
2.11.09	Tezhsar	Phonolite	0.70410	0.51274	5.1	19.2	0.27	-5.1
3.3.09	Tezhsar	Phonolite	0.70424	0.51281	19.1	24.0	0.80	-3.7

* Arteni complex, 45 km SW of Aragats summit

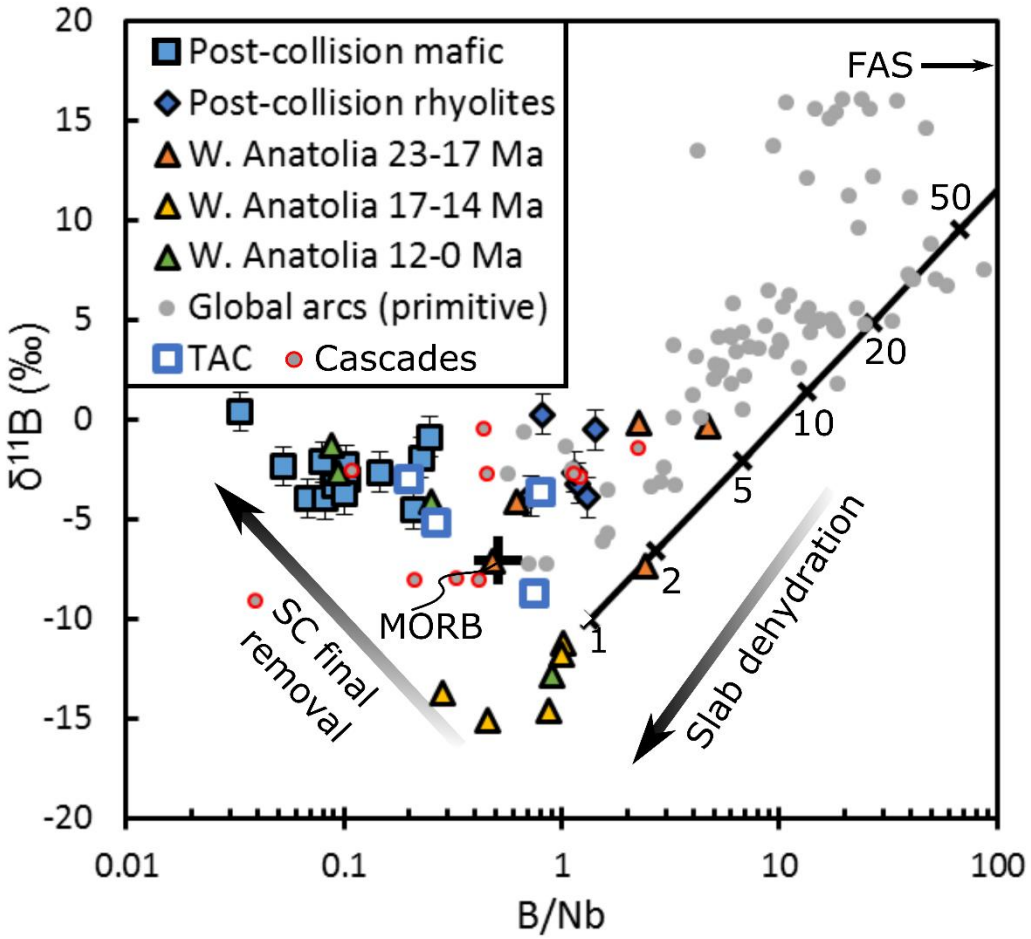

Figure 4.5 $\delta^{11}B$ *vs* B/Nb for arc and collision zone volcanic rocks.

B/Nb is used because both elements have similar compatibilities during mantle melting, but while B is a type FME, Nb is immobile, such that the ratio is a proxy of fluid enrichment. Post-collisional samples are filled blue symbols; mafic samples are squares, with the rhyolites as diamonds. Maximum error bars of 1‰ are shown for $\delta^{11}B$ of samples analysed for this study. TAC errors are smaller than the size of the symbols. The arrows denote the processes occurring in W. Anatolia during slab dehydration and transition to a slab-free geodynamic setting. The black curve is a simple Rayleigh fractionation model for dehydrating serpentinite assuming fluid/residue $\alpha = 1.005$, based on modelled differences between slab and wedge serpentinite $\delta^{11}B$ at depth (Konrad-Schmolke and Halama, 2014). Numbers refer to % of original boron remaining in the residue. FAS- fore-arc serpentinite end-member of Rayleigh fractionation model (De Hoog and Savov, 2018). West Anatolian data from Tonarini et al. (2005); arc data from De Hoog and Savov (2018); MORB data from Marschall et al. (2017).

there is some very modest enrichment in [B] for post-collision samples (1-5 ppm)compared to MORB, showing that the subduction component did impart a small budget of B in the source. The $\delta^{11}B$ of the studied rocks are similar to those from hot arcs such as the Cascades (arc samples which are circled red in Fig. 4.5), or the intraplate volcanoes of the Snake River Plain-Yellowstone region (Leeman et al., 2004; Savov et al., 2009), both shown to represent melting of fluid-starved sources.

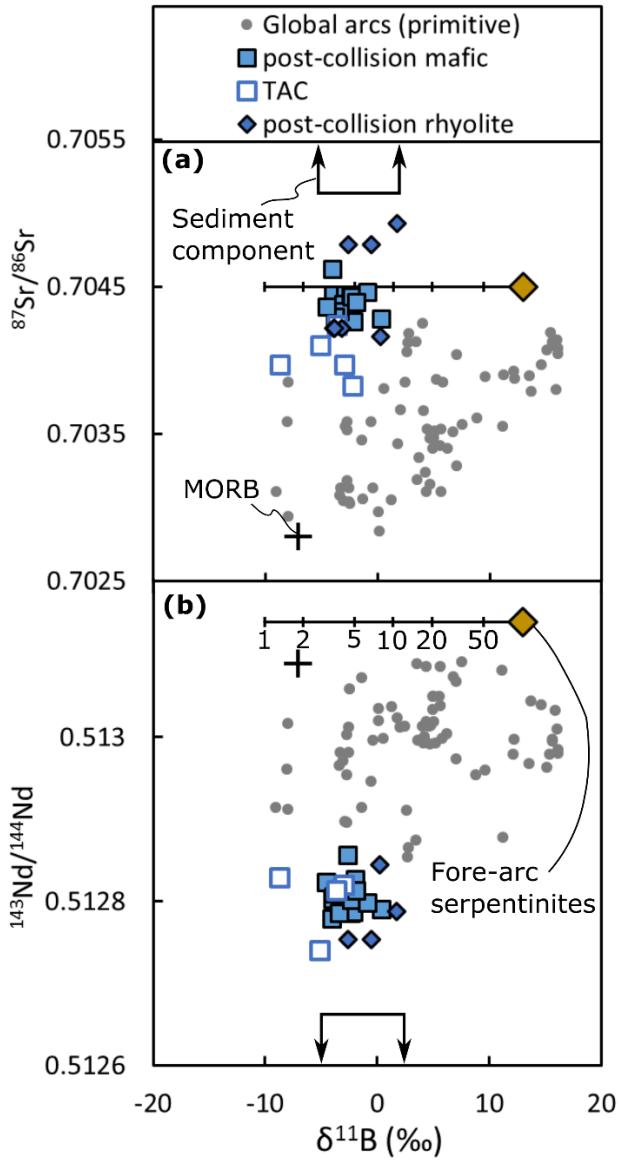

Figure 4.6 $^{87}Sr/^{86}Sr$ (a) and $^{143}Nd/^{144}Nd$ (b) *vs.* $\delta^{11}B$ for arc and collision zone volcanic rocks

Average mid-ocean ridge basalts (MORB; Marschall et al., 2017; White and Hofmann, 1982) shown for reference. $^{87}Sr/^{86}Sr$ and $^{143}Nd/^{144}Nd$ are initial values for TAC samples (Sokół et al., 2018). Other data sources are as in Fig. 4.2. Fore-arc serpentinites are shown as a proxy for the composition of slab derived fluids (De Hoog and Savov, 2018). Serpentinite dehydration line, with % B remaining in residual serpentinite as in Fig. 4.2. Here, $^{87}Sr/^{86}Sr$ and $^{143}Nd/^{144}Nd$ are assumed to not vary during dehydration. The bold double arrow lines in each figure point towards the likely B isotope composition of a sediment component.

B/Nb ratios are higher in the rhyolite samples by an order of magnitude (0.75-1.5; Fig. 4.5), but the $\delta^{11}B$ of the rhyolites is comparable (-4 to +2‰ *vs* -5 to +1‰ for mafic samples; Fig. 4.5).

The TAC rocks have a similar $\delta^{11}B$ to the post-collisional rocks, with one exception of a lighter $\delta^{11}B$ of -8.7‰ (Figs 4.5 and 4.6; Table 4.2). TAC samples have higher B concentrations (4-20 ppm) and B/Nb ratios (0.2-0.8) than the post-

collision samples, although B/Nb is still at the lower end for arcs generally (Fig. 4.5). Surprisingly, magma sources tapped at 41 Ma and <1.5 Ma have comparable Sr-Nd-B isotopic characteristics (Fig. 4.6)- with closely overlapping $^{143}Nd/^{144}Nd$ (0.51275-0.51286), and only slightly lower $^{87}Sr/^{86}Sr$ in TAC samples (initial values 0.7040-0.7042 *vs* 0.7042-0.7049). This latter discrepancy is removed when one considers that TAC samples not analysed for B have $^{87}Sr/^{86}Sr_{(i)}$ as high as 0.7052, although the extent to which these higher values reflect alteration is uncertain (see Section 4.2). The lower B/Nb and $^{143}Nd/^{144}Nd$; and higher $^{87}Sr/^{86}Sr$ of these collision-related magmas when compared to arc rocks, means they define a geochemical reservoir distinct to volcanic rocks from both arcs and oceanic ridges/islands.

4.5 Discussion

4.5.1 Origin of the subduction component

Prior to this study, Western Anatolia was the only region in the world where young (17-0 Ma) volcanic rocks, which erupted after continuous subduction ceased had been studied for [B] and $\delta^{11}B$. Western Anatolia has experienced rapid geodynamic changes over the past 25 Myr, from subduction to an extensional setting (Tonarini et al., 2005), which although not a continental collision, does provide an analogue of what happens when subduction ends. Here, 23-17 Ma calc-alkaline rocks have $\delta^{11}B$ (-7.1 to -0.1‰) and B/Nb which extend from MORB to heavier, more arc-like values (Fig. 4.5), reflecting their formation during subduction. However, 17-14 Ma ultra-potassic rocks have very light $\delta^{11}B$ (-15.0 to -11.2‰), interpreted to reflect the progressive dehydration of a stalled slab (Agostini et al., 2008), which is also shown by the gradual reduction in B/Nb (Fig. 4.5; Tonarini et al., 2005). The dehydration preferentially removes ^{11}B, giving the residual slab an increasingly light $\delta^{11}B$ (Konrad-Schmolke and Halama, 2014). These samples provide a useful comparison for the likely effects of a stalled slab on $\delta^{11}B$ and B/Nb with the Lesser Caucasus samples presented in this study. There is subsequently a rebound to heavier $\delta^{11}B$ (-4.1 to -0.8‰), but lower B/Nb in the 12-0 Ma volcanic rocks (Fig. 4.5), which has been argued to reflect the end of the influence of any contemporary subducting slab (Agostini et al., 2008). Despite the similar $\delta^{11}B$ and B/Nb of young volcanic rocks

from Western Anatolia and the Lesser Caucasus (Fig. 4.5), the magmas likely arrive at this composition through different mechanisms, given the intraplate-type trace element composition of the West Anatolian rocks, which contrasts with the arc-type geochemistry of the Lesser Caucasus volcanic rocks (Fig. 4.2).

The $\delta^{11}B$ of post-collisional volcanic rocks from the Lesser Caucasus is not consistent with a model in which a stalled slab progressively dehydrates during slab break-off associated with collision, a process which is likely to produce the very light $\delta^{11}B$ observed in the 17-14 Ma W. Anatolia samples (Fig. 4.5). Instead, in the Lesser Caucasus $\delta^{11}B$ has only exhibited modest variability over the past 41 Myr, on the basis of the post-collisional and TAC samples. Mixing with an intraplate mantle source (average OIB~ -10‰; Walowski et al., 2019), which had previously been underneath (and therefore unaffected by) a subducting slab, would produce a lighter $\delta^{11}B$ in the post-collisional volcanic rocks. Both mixing with intraplate magmas and dehydration of a stalled slab would also result in more variable trace element and Sr-Nd isotope compositions, which are not observed. While slab break-off is not considered a prominent process under the Lesser Caucasus, it could well be an important process elsewhere in the collision zone. This is particularly the case in the Lake Van region of E. Anatolia, where alkaline magma compositions are observed, suggesting an intraplate (below the slab) type mantle contributing to the magma source (Pearce et al., 1990; Keskin, 2003).

It seems most likely that the subduction signature observed in the post-collisional and TAC samples, has been stored for at least 41 Myr, to be inherited during later melting events. The subduction component is most likely to have been stored in the lithospheric mantle, where cooler temperatures (due to a conductive geotherm) stabilise metasomatic minerals able to store the subduction component long after subduction has ceased (Mandler and Grove, 2016). Amphibole, rather than phlogopite, is the most likely such mineral to break down during melting, based on the high Ba/Rb (20-40) and low Rb/Sr (0.01-0.04) ratios of the post-collisional volcanic rocks (Sugden et al., 2019)- Rb is an order of magnitude more compatible in phlogopite compared to amphibole (LaTourrette et al., 1995). This would require storage of the subduction component at temperatures of < 1100°C to stabilise pargasitic amphibole (Mandler and Grove, 2016).

Amphibole is supported by the positive correlation between Dy/Dy* and

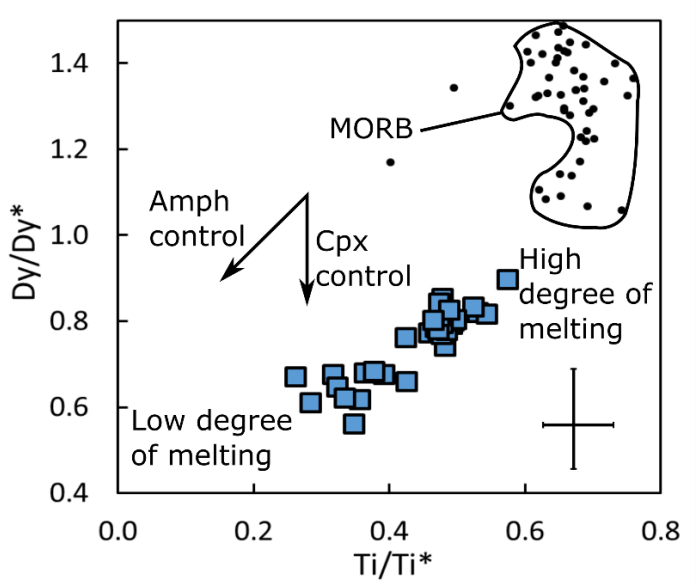

Figure 4.7 Dy/Dy* *vs.* Ti/Ti* for the most mafic post-collision samples from the Lesser Caucasus All samples have > 6 wt % MgO. Data from Neill et al. (2015) and Sugden et al. (2019). Also shown is the MORB field with higher Dy/Dy* and Ti/Ti* (after Davidson et al., 2013 and references therein). Dy/Dy* is a measure of the curvature of a rare-earth element profile, whereas Ti/Ti* is a measure of the size of the Ti anomaly on a mantle-normalised trace element pattern (Davidson et al., 2013). The error bar is indicative of the uncertainties associated with the trace element concentration analysis as described for Fig 3.11.

Ti/Ti* (Fig. 4.7; Davidson et al., 2013). Only amphibole and clinopyroxene preferentially partition the middle REE, decreasing the Dy/Dy* ratio of any melt equilibrating with these phases. The positive correlation with Ti/Ti* confirms that amphibole must be a residual phase in the source of the post-collisional magmas because Ti is an order of magnitude more compatible in amphibole than in pyroxene (Davidson et al. 2013). Thus, amphibole is able to store a subduction component (including slab-derived boron) for > 41 Myr, soaking up metasomatic components to be released during later melting caused by partial breakdown of amphibole (Sugden et al., 2019).

The low [B] of post-collisional volcanic rocks (1-5 ppm) relative to arc volcanic rocks are consistent with the low [B] observed in vein amphiboles within mantle xenoliths from the Kamchatka arc (0.2-3 ppm; Tomanikova et al., 2019). An amphibole source would be expected to produce magmas low in B given low experimental partition coefficients for boron in amphibole (Brenan et al., 1998), explaining its low capacity for concentrating boron in its structure during the storage of a subduction component. The $\delta^{11}B$ of the Lesser Caucasus volcanic rocks does

fall within the range observed for the Kamchatka xenolith vein amphiboles (average ~ -5‰; Tomanikova et al., 2019), suggesting it is a viable reservoir.

This stored subduction component is reminiscent of the "amphibole sponge" concept of Davidson et al. (2007), but instead of residing in lower crustal cumulates, the amphibole is stored in the mantle lithosphere. This is consistent with suggestions that an amphibole-bearing magma source is present in the post-collisional mantle lithosphere under the Lesser Caucasus (Sugden et al., 2019).

4.5.1.1 High boron concentrations in TAC and rhyolite samples and the origin of their subduction component

The higher B/Nb of two TAC samples (Fig. 4.5), and the lower $\delta^{11}B$ of one TAC sample (-8.7‰; Fig. 4.5) are similar to the volcanic rocks from "hot" subduction zones (Fig. 4.5; Leeman et al., 2004; Savov et al., 2009). This could suggest the subduction signature in the TAC samples is a mixture of the component observed in the post-collision samples, and a component derived from contemporaneous addition of material from a partially dehydrated slab.

Despite the higher B/Nb of the rhyolite post-collision samples, the matching Sr-Nd-B isotope characteristics of mafic and felsic samples shows that the magma source of the parental magma to these rhyolites is the same long-lived subduction-modified mantle source which supplied the mafic magmas. These isotope characteristics also confirm that crustal contamination did not play a role in the petrogenesis of the rhyolites, meaning B/Nb varies with the extent of crystal fractionation. [Nb] is invariant during fractional crystallisation, whereas [B] increases by an order of magnitude (Table 1). Nb must partition into a crystallising phase, while B remains in the magma. The reduction in Nb/Ta with SiO_2 content in these magmas (not shown) provides a potential explanation for the behaviour of Nb. A reduction in Nb/Ta during crystal fractionation reflects rutile fractionation in the middle to lower crust (Tang et al., 2019), suggesting Nb may be sequestered in rutile.

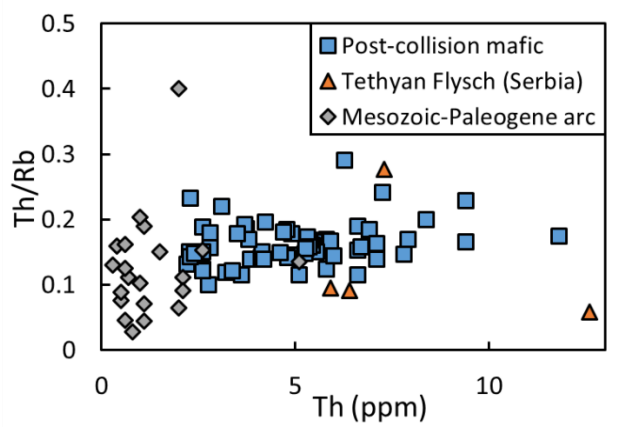

Figure 4.8 Th/Rb vs Th for post-collisional mafic volcanic rocks, subducted sediments and arc volcanic rocks

Subducted sediments are representative Tethyan flysch from Serbia (Prelević et al., 2008). Post-collisional samples are all those samples with > 4 wt% MgO and < 54 wt% SiO_2 from Syunik and Vardenis volcanic highlands (Chapter 3), Gegham volcanic highland (Savov, unpublished), Aragats volcano (Connor et al., 2011), and the northern Lesser Caucasus (Neill et al., 2015). Also shown are Mesozoic-Paleogene arc samples from the Pontides of Eastern Turkey (Aydinçakir and Sen, 2013) and the Kapan Zone of South Armenia (Mederer et al., 2013). These samples overlap with the post-collision samples in Th/Rb but extend to lower values, likely to reflect greater fluid input to the mantle source. Six arc samples which have very high Th/Rb of up to 2.5 are not shown on this figure, because they are interpreted to reflect post-emplacement alteration and leaching of Rb (Aydinçakir and Sen, 2013).

4.5.2 Nature of the subduction component

The subduction component is generally imparted by aqueous fluids, melts or supercritical fluids liberated from a subducting slab and overlying sediments. Here, melts and supercritical fluids will be treated as interchangeable, given the similar trace element partitioning behaviour of the two (Kessel et al., 2005).

The [B] and $\delta^{11}B$ of most arc rocks is dominated by aqueous fluids derived from dehydration of dominantly fore-arc serpentinite melanges (De Hoog and Savov, 2018, and references therein). Given the heavy $\delta^{11}B$ of fore-arc serpentinites (avg. ~+13 ‰ (Fig. 4.6), ranging from +5 to +25‰; De Hoog and Savov, 2018), the light $\delta^{11}B$ in the Lesser Caucasus rocks means that a source for the subduction component would have already lost a significant amount of fluid (and hence heavy B) prior to contributing to the post-collisional mantle source (Konrad-Schmolke and Halama, 2014). A simple Rayleigh fractionation model of fluid depletion of fore-arc serpentinite (assuming 5‰ fluid-residue fractionation) shows that the $\delta^{11}B$ and B/Nb of arc rocks (but not the post-collisional volcanic rocks), can be explained by mixing between MORB-source mantle and variably dehydrated serpentinite fluids (Fig.

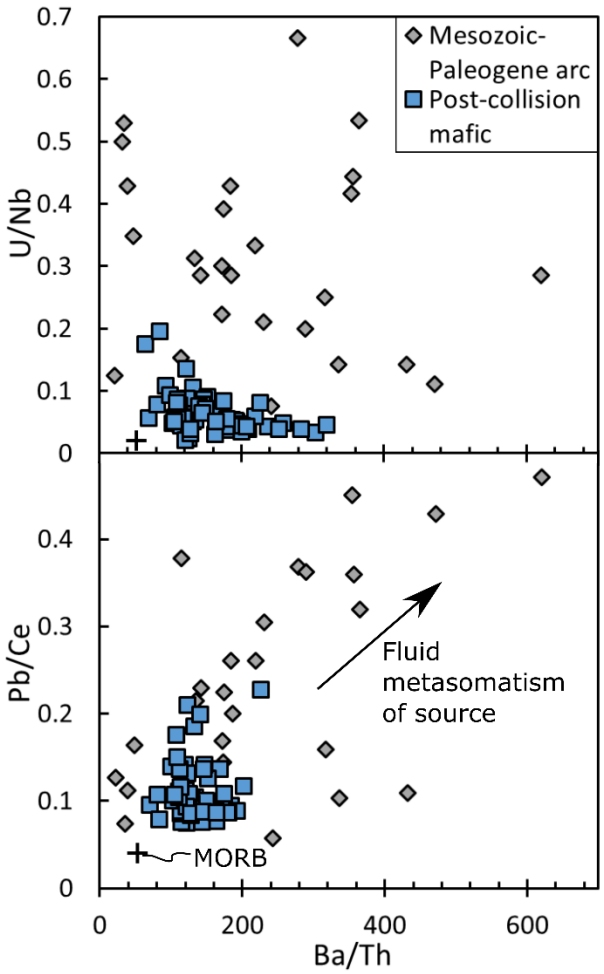

Figure 4.9 U/Nb, Pb/Ce and Ba/Th in mafic post-collisional and arc rocks.

Arc rocks are Mesozoic-Paleogene in age and are from the Lesser Caucasus and the Pontides to the west. Data is sourced and filtered as in Fig. 4.8. MORB values after Sun and McDonough (1989).

4.5). $^{87}Sr/^{86}Sr$ and $^{143}Nd/^{144}Nd$ would not vary during dehydration (horizontal trajectories in Fig. 4.6). Such a depleted fluid could explain the Sr-B isotope composition of the post-collisional magmas (Fig. 4.6a), but not the lower $^{143}Nd/^{144}Nd$ (Fig. 4.6b).

The subduction component must instead be a melt or supercritical fluid derived from subducted sediments or oceanic crust, in order to mobilise Nd and modify the $^{143}Nd/^{144}Nd$ of the mantle source. Adakites are thought to be geochemically characterised by a melt derived from oceanic crust. They have MORB-like Sr-Nd isotope ratios, rather than the high $^{87}Sr/^{86}Sr$ and low $^{143}Nd/^{144}Nd$ in the post-collisional rocks (Fig. 4.6). Moreover, although the post-collisional magmas do have the high Sr/Y ratios (15-130) of adakites, they lack the high primary SiO_2 contents, and have higher Y and Yb contents (Castillo, 2012).

This leaves a sediment melt as the carrier of the subduction component in the post-collisional rocks, supported by their low $^{143}Nd/^{144}Nd$. A sediment melt is also supported by the similar Th/Rb (Fig. 4.8) in the volcanic rocks (average for mafic samples~ 0.16 ±0.06 (2 SD)) and Tethyan flysch (avg. 0.13 ±0.2; Prelević et al., 2008). For Th/Rb to reflect local subducted flysch, the subduction component must be: a) derived from the sediment, and b), must be a melt or supercritical fluid for Th and Rb to partition similarly between the mobile and the residual phases given that Th is fluid-immobile (Johnson and Plank, 2000). In addition, given the relatively low Th content of the oceanic crust (Kelley et al., 2003), the high Th contents of post collisional samples (comparable to the Tethyan sediments) suggest derivation of the component from the slab sediments (Fig. 4.8).

The $\delta^{11}B$ of this sedimentary component is likely to be in the range of -5 to +2‰ (Fig. 4.6) based on the $\delta^{11}B$ of the TAC and post-collision samples. This can be compared to the $\delta^{11}B$ of tourmalines (one of the major carriers of B past the fore-arc) in metasediments. Tourmalines from metamorphosed terrigenous sediments have much lighter $\delta^{11}B$ than the Lesser Caucasus volcanic rocks (-7 to -15‰; Bebout and Nakamura, 2003). However, tourmaline prograde mantles (formed at peak metamorphic conditions) from Syros, Greece, have comparable $\delta^{11}B$ to the Lesser Caucasus samples (-1.6 to + 0.9‰; Marschall et al., 2008). The heavier $\delta^{11}B$ in Syros is likely a result of a mixture of marine-derived as well as terrigenous sediment in the protolith. It is probably the case that there is no $\delta^{11}B$ fractionation during separation of a melt phase from the residual sediment, given the tetrahedral co-ordination of B in both magma and most silicate minerals (Maner and London, 2018). A melt of the mixed marine-terrigenous metasediment could produce the subduction component observed in the Lesser Caucasus post-collisional magmas. Release of a supercritical fluid could involve none or only limited isotope fractionation given the likely high temperatures (Konrad-Schmolke and Halama, 2014). If instead separation of a supercritical fluid did involve isotope fractionation, then the isotopically lighter, dominantly terrigenous-derived sediment could be a more viable source for the subduction component.

Ratios such as Ba/Th, Pb/Ce and U/Nb (FME/immobile element of similar compatibility during melting) are higher and more variable in Mesozoic-Paleogene arc rocks from the Lesser Caucasus and Eastern Anatolia (Fig. 4.9; Aydinçakir and Sen, 2013; Mederer et al., 2013) compared to the relatively young post-collision

rocks investigated in this study. This indicates that a fluid component was present during subduction, but was not inherited by magmas formed after continental collision. This points to the sediment melt being much more long-lasting in the mantle, whereas the aqueous fluid component is transitory. Indeed, studies of U-Th series isotopes in Kamchatka suggest the fluid component can travel from slab to surface in 1-300 kyr, whereas a sediment component can take 350 kyr- 4 Myr to make the same journey (Turner et al., 2000). It could be the case that once the slab stalls the fluids are quickly removed, such that the subsequent subduction component is dominated by sediment melts.

4.6 Concluding remarks

Despite evidence that the source of Mesozoic-Paleogene Tethyan arc magmas was modified by aqueous fluids, the light $\delta^{11}B$ of post-collisional volcanic rocks indicates derivation from a mantle source modified by a fluid-starved subduction component. There is also no evidence for continued dehydration of a stalled slab following collision, which would be expected to produce the even lighter $\delta^{11}B$, as observed in the 16-17 Ma samples from Western Anatolia. Instead the similar $\delta^{11}B$ and Sr-Nd isotopes of post-collision and TAC samples indicate that the subduction component was inherited from preceding subduction, with the lack of the heavy $\delta^{11}B$ signature of aqueous fluids being a result of them being transitory and not surviving to impart their signature on post-collisional mantle sources. For this subduction component to be inherited, it needs to be stored since at least the 41 Ma TAC volcanism. The low [B] is consistent with trace element evidence that amphibole in the mantle source is the storage repository for the subduction component, given the low storage capacity for B in amphibole. Higher B/Nb in TAC samples (comparable with B/Nb in “hot” arcs) and overlapping $\delta^{11}B$ may suggest that an inherited subduction component, similar to that observed in post-collision samples was mixed with a component derived from a contemporaneously subducting slab. The more clustered Sr-Nd-B isotope compositions of the post-collisional samples suggests that by the Plio-Pleistocene only the inherited component remains. The sediment melt (or supercritical fluid) origin of the subduction component suggested on the basis of trace elements and Sr-Nd isotopes may be consistent with post-collisional volcanic

rock $\delta^{11}B$, given similar values for some dehydrated metasediments of mixed marine-terrigenous origin.

The lower $^{143}Nd/^{144}Nd$ in arc rocks compared to fore-arc serpentinites (Fig. 4.6) is perhaps a “smoking gun” for the presence of this sediment melt component in all arc rocks, but their heavy $\delta^{11}B$ is testament to it being obscured by a dominant, serpentinite-derived fluid component. As a setting in which only sediment melts metasomatise the mantle source, volcanism in continent-continent collision zones is an ideal setting to separate the effects of slab-derived sediment melt and aqueous fluids in subduction zones.

5. Post-collisional shift from central to distributed volcanism revealved by new Ar-Ar ages in the southern Lesser Caucasus volcanic field

5.1 Introduction

Volcanic eruptions through a central conduit of a long-lived polygenetic volcano (formed over multiple eruptive cycles) are by far the most studied style of volcanism. However distributed volcanism, whereby over time a volcanic field of numerous monogenetic (formed in a single eruptive episode) volcanoes is formed is equally, if not more, widespread (Valentine and Connor, 2015). Volcanic fields are found at every plate boundary and intraplate setting at which polygenetic volcanoes form (Smith and Németh, 2017). There are two main candidates for what might cause volcanic activity to produce monogenetic volcanoes instead of polygenetic ones: a low magma supply rate or a high rate of crustal extension (Connor and Conway, 2000). In any locality, a polygenetic volcano may be impossible to sustain due to either or both of these factors (Fedotov, 1981; Hasebe et al., 2001; Bucchi et al., 2015).

A polygenetic volcano needs magma to be repeatedly supplied to the base of the edifice, which requires a stable magma plumbing system. A low rate of magma supply will mean that magma ascends through both the crust and mantle as discrete batches with no connection to the mantle source or the surface, and hence no plumbing system (Fedotov, 1981). As an example, monogenetic volcanoes of the Sredinny ridge in the south of the Kamchatka peninsula have lower magma supply rates than the large polygenetic volcanoes on the peninsula (Fedotov, 1981).

High rates of extension are another possible way to prevent the formation of a large edifice. Magma focusing in plumbing systems may occur though dyke coalescence which allows different magma batches to be mixed together (Takada, 1994a). This coalescence is retarded in regions of high extension as dykes ascend parallel to each other (Takada, 1994b). An example of where extension may play an important role is the Carrán-Los Venados volcanic field in the southern Andes, where there is almost sufficient magma supply to establish a stable conduit. The nearby polygenetic volcano Puyehue-Cordón Caulle has a similar long term magma supply (although the short term supply during its most active periods may be

higher), but is in a compressional stress regime. In contrast the volcanic field is undergoing extension which could be preventing a polygenetic volcano from forming (Bucchi et al., 2015).

The Lesser Caucasus is another region host to both polygenetic and monogenetic volcanoes. Polygenetic volcanoes include Aragats (> 3 km tall with a 70 km basal diameter; Connor et al., 2011, 2012; Gevorgyan et al., 2018), Ararat (see Fig. 1.2a), Tskhouk and Ishkhanasar (Fig. 5.1; see chapters 1 and 2). There are > 500 mapped monogenetic volcanoes in the Lesser Caucasus, located on the flanks of Aragats and across the Gegham, Vardenis and Syunik volcanic highlands (Chapter 2; Fig. 5.1; Weller et al., 2018).

Both types of volcano present their own distinct hazard to local populations and infrastructure. Polygenetic volcanoes have the potential to produce the larger, more explosive eruptions, whose effects will cover the widest areas. The high altitude of these volcanoes means they are generally remote from human populations, such that a smaller eruption might have little effect, whereas a large eruption could be devastating. Monogenetic volcanoes are smaller and lava flows are the most common eruptive product (see Chapter 2). Their eruptions are likely to affect a smaller area, but are much more unpredictable in terms of their location, such that if they erupt in the wrong place the impact could be substantial. For example the Armenian Nuclear Power plant is surrounded by small monogenetic volcanoes but is also on the lower distal slopes of Aragats polygenetic volcano (Karakhanian et al., 2003; Connor et al., 2011; Connor et al., 2012; Aspinall et al., 2016; Weller et al., 2018). Yerevan, 30 km to the east of the power plant is a city with a population > 1 million people. Polygenetic volcanism from Aragats 50 km to the NW, and monogenetic volcanism extending from the city limits to Gegham ridge 40 km to the east could both effect the city. The former has the potential to produce ignimbrites similar to previous events which formed the deposit the city is built on (Gevorgyan et al., 2018). Meanwhile lava flows are exposed in the Hrazdan gorge which rings the city centre, and may well have erupted from a nearby monogenetic volcano (Lebedev et al., 2013). The U2 highway is the main road link with Iran and is a vital trade link for Armenia. This road crosses the lower slopes of Tskhouk and Ishkhanasar, while Holocene lava flows came within 5 km of the current road (Karakhanian et al., 2002; Sugden et al., 2019). The different hazards that a future

polygenetic or monogenetic eruption might pose mean that it is important for scientists to try and understand what sort of eruption is likely in the future.

The polygenetic volcanoes appear to be inactive, while the youngest Holocene eruptions in the Lesser Caucasus have been exclusively monogenetic (Karakhanian et al., 2002). This leads one to the hypothesis that rather than the two modes being contemporaneous, as was observed in the southern Andes (Bucchi et al., 2015), there has been a shift over time from polygenetic to monogenetic volcanism, and that a monogenetic eruption is more likely in the future than a polygenetic one.

This hypothesis is tested by presenting a new set of high quality Ar-Ar ages for key volcanic units from the southern Lesser Caucasus. These ages are used in conjunction with previous K-Ar (Philip et al., 2001; Karapetian et al., 2001; Ollivier et al., 2010; Lebedev et al., 2013), Ar-Ar (Joannin et al., 2010), apatite fission track (Karapetian et al., 2001) and archaeologically determined (Karakhanian et al., 2002) ages to assess the longevity of volcanism, to make some conservative estimates of the recurrence interval of eruptions, and to assess the precise timing of any polygenetic to monogenetic transition. The geographical extent of this transition is also investigated—that is whether a transition occurs in Syunik, in Vardenis, or in Gegham, or across the region. Furthermore, is this transition contemporaneous or diachronous across the Lesser Caucasus?

The age data are combined with geochemical data presented in Chapters 3 and 4 to investigate the origin of a possible polygenetic to monogenetic transition. As discussed above, it could either be a decreasing magma supply or an increasing rate of extension. The working hypothesis here is that the transition is a result of a decreasing magma supply, specifically as a consequence of the exhaustion of subduction components in the mantle source. This can be thought of as the "death of a subduction zone", where following collision and the end of continuous subduction of oceanic lithosphere, slab-derived components are progressively removed from the mantle source during post-collisional magmatism. Removal of these subduction components should remove fusible phases from the mantle source, so that less magma can be produced over time. Samples were selected for Ar-Ar dating so that they can be compared with the $\delta^{11}B$ data in Chapter 4 as a test of whether subduction components are being exhausted over time. If no correlation (positive or

negative) can be observed, then some other process must have driven the poly- to monogenetic transition.

5.2 Previous age constraints

Although sparse, there are several studies which have provided geochronological constraints on the history of post-collisional volcanism across the southern Lesser Caucasus volcanic field (Fig. 5.1). This volcanic field consists of the Syunik, Vardenis and Gegham volcanic highlands referred to in previous chapters, which in reality are a region of volcanic activity without distinct breaks in between them (see Chapter 2). As well as introducing the previous age constraints within the volcanic field, ages from the neighbouring Aragats volcano are also discussed. The literature data presented here are listed in Appendix C.

5.2.1 Aragats volcano

Aragats is the largest volcano in the Lesser Caucasus, with an area of >5000 km^2 and a volcanic sequence up to 3 km thick (Jrbashyan et al., 2012). Aragats erupted lavas and pyroclastic material between 2.5 and 0.5 Ma (Chernyshev et al., 2002). The complex is composed of a central summit which is the polygenetic volcanic centre, and numerous monogenetic centres (> 93) on the flanks of the volcano (Connor et al., 2011). Effusive eruptions produced large areas of lava flows, with individual flows as large as 18 km^3 (Connor et al., 2011). Explosive eruptions have produced numerous small scoria cones, six large ignimbrite sheets and three tephra fallout deposits (Gevorgyan et al., 2018). Eruptive products range in composition between trachybasalts and trachytes (Connor et al., 2011). Most of the age data presented here come from the youngest 500 kyr of deposits (Karakhanian et al., 2003; Connor et al., 2011; Gevorgyan et al., 2018).

Dating of monogenetic centres on the flanks of the volcano give ages of 1.3-0.5 Ma (Fig. 5.1b), and includes mafic scoria cones, mafic and intermediate lava flows and a pyroclastic deposit formed from the Irind flank vent (Chernyshev et al., 2002; Connor et al., 2011). The ignimbrite sheets must have been erupted from the polygenetic Aragats volcano because they form as a result of caldera collapse-requiring a volcano with a mature magma plumbing system and a large magma chamber (Hildreth, 1981). The ignimbrites have an age range of 1.8-0.65 Ma

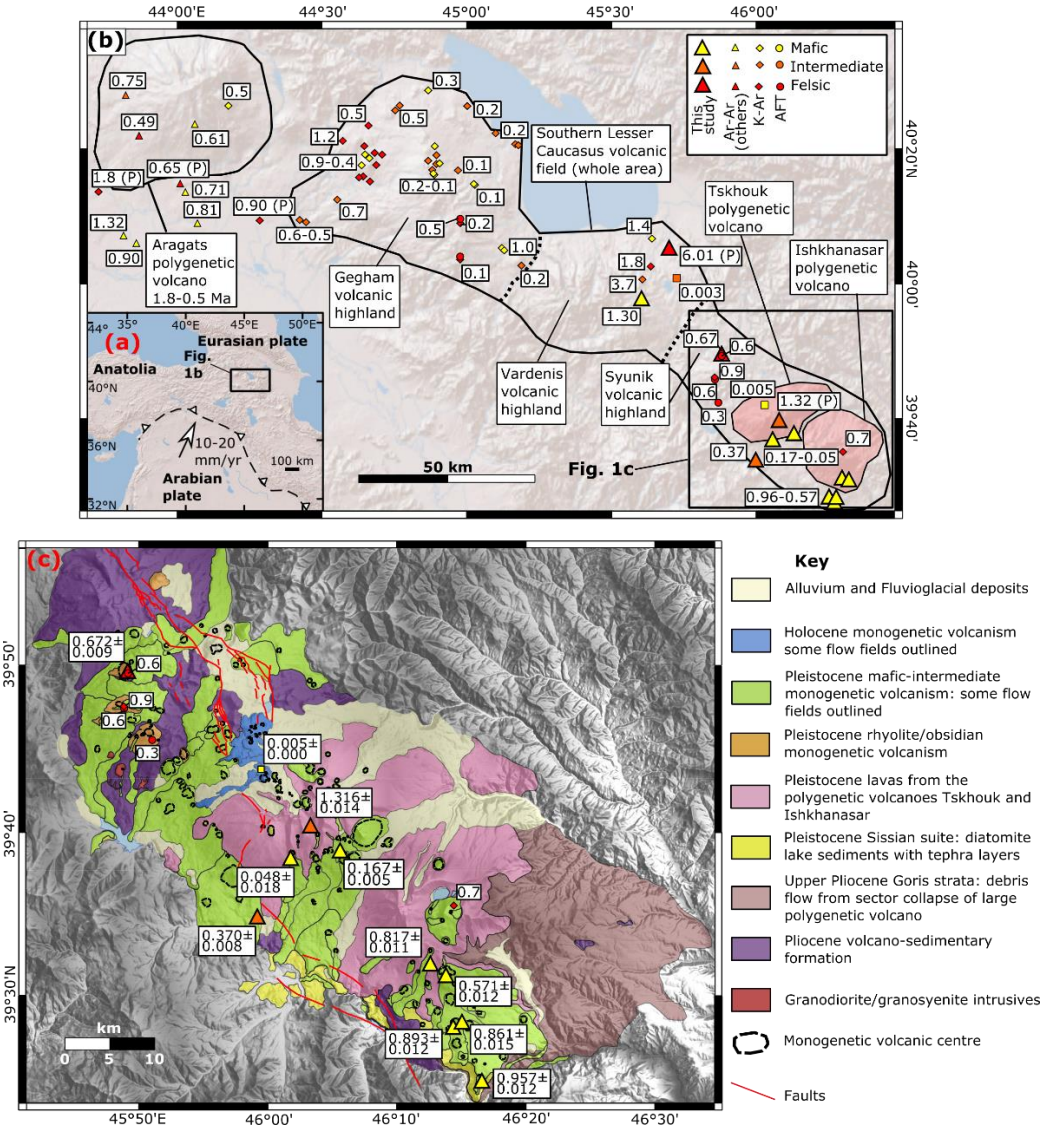

Figure 5.1 Maps of age constraints on southern Lesser Caucasus volcanic rocks

(a) Location of the Lesser Caucasus mountains within the Arabia-Eurasia collision zone at the northern edge of the Turkish-Iranian plateau. Plate velocity estimates after Reilinger et al. (2006). (b) Location map for samples with known age in the Southern Lesser Caucasus volcanic field, as well as the neighbouring Aragats volcano. Here the whole of the Southern Lesser Caucasus volcanic field is shown by the solid line, with the location of each of the three volcanic highlands referred to in previous chapters separated by dotted lines. These three highlands from NW to SE are Gegham, Vardenis and Syunik. The age range for the Aragats polygenetic volcano is from Gevorgyan et al. (2018), with individual K-Ar and Ar-Ar ages also shown (Ghukasyan, 1985; Mitchell and Westaway, 1999; Chernyshev et al., 2002; Connor et al., 2011; Gevorgyan et al., 2018). Samples are colour coded according to their composition and the shapes denote the method by which an age was obtained: Ar-Ar, K-Ar or apatite fission tracks (AFT). Within the volcanic field all the new ages and previously published ages considered in this chapter are shown (Karapetian et al., 2001; Philip et al., 2001; Karakhanian et al., 2002; Lebedev et al., 2013), with the exception of K-Ar and Ar-Ar ages of lava flows and tuff layers in lake sediments, which would all be located under the "0.96-0.57" Ma box. These ages are shown in Fig. 5.4, and are discussed in the text. The age (or range of ages for samples which are very close together) is shown by the boxed number next to the samples. Where a sample has been produced from an eruption from a polygenetic volcano the age is labelled "(P)". (c) Geological map of the Syunik volcanic highland, with the area of the map shown in Fig. 5.1b. Map modified from that shown in Sugden et al. (2019). Ar-Ar age determinations for this study are shown by the large triangles with 2σ error. Also note the Sissian suite of sediments shown in yellow, within which 2 tephra layers have been dated (1.24 and 1.16 Ma; Joannin et al., 2010), with several of the lava flows capping the sediment sequence also being dated (1-0.1 Ma; Ollivier et al., 2010).

(labelled P in Fig. 5.1b), showing broad overlap with the age range of the monogenetic centres (Ghukasyan, 1985; Mitchell and Westaway, 1999; Connor et al., 2011; Gevorgyan et al., 2018). Contemporaneous monogenetic and polygenetic volcanism suggests Aragats must have a magma supply close to the minimum required to sustain a polygenetic volcano (Bucchi et al., 2015). As such magmatism in the region might be susceptible to a polygenetic-monogenetic transition. However, the available evidence does not suggest that any temporal shift occurred at this volcano.

5.2.2 Gegham volcanic highland

Gegham forms the northern part of the Southern Lesser Caucasus volcanic field (Fig. 5.1). Eruptive products have bimodal compositions with mafic-intermediate lavas and rhyolites, but relatively few trachydacites (Fig. 3.3, see Chapter 3). Although there are rhyolite domes as large as Spitaksar and Geghasar (5 km diameter), there is no definitive evidence to show they are polygenetic. Monogenetic volcanic centres are widespread across the region, with numerous cones of both Pliocene and Pleistocene age (Lebedev et al., 2013). In general lavas on the lower western slopes appear to be older, while many of the youngest eruptions have focussed along the central axis of the Gegham ridge (Fig. 5.1b), which hosts a series of pull-apart structures (Karakhanian et al., 2003; Lebedev et al., 2013).

Although the K-Ar ages are of lower precision when compared with the Ar-Ar technique, Lebedev et al. (2013) provide the largest dataset of Quaternary ages (n=42) for monogenetic volcanoes of both mafic and felsic compositions in the southern Lesser Caucasus volcanic field (Fig. 5.1b). This large number of ages can be combined with ages from Vardenis and Syunik to provide a useful timeline of volcanic events during the Quaternary, including intervals of quiescence and more intense volcanic activity; as well as episodes of predominantly mafic *vs* felsic volcanism (see section 5.6). Karapetian et al. (2001) provided apatite fission track ages (AFT; Fig. 5.1) for two of the rhyolites also dated by Lebedev et al. (2013). The 0.1 Ma ages for Geghasar are in good agreement between both techniques, while the 0.5 Ma AFT age for Spitaksar is substantially older than the 0.2 Ma from K-Ar (Fig. 5.1b).

The evidence suggests this region has been dominated by monogenetic volcanism for at least the last 2 Myr, if not longer. There may be some isolated evidence for polygenetic volcanism at the Spitaksar rhyolite dome which is in a Pliocene caldera called Pich, the latter of which may be the remnants of a polygenetic volcano (Lebedev et al., 2013). However, the overall evidence of numerous Pliocene monogenetic cones does not suggest a polygenetic to monogenetic transition occurred here.

5.2.3 Vardenis volcanic highland

Based on fieldwork conducted during the preparation of this thesis, large ignimbrites form the base of the volcanic sequence (Fig. 2.3e), attesting to the presence of large caldera-forming volcanoes early in the volcanic history of the region. Above the ignimbrites are a succession of lava flow units which were mafic at the base, but grade into trachydacites up-section. One of these trachydacite volcanoes (Sandukhansar) has a K-Ar age of 2.3 Ma (Karapetian et al., 2001). It is unclear whether these lavas are the result of polygenetic or monogenetic volcanic eruptions, however the substantial size of these edifices (up to 10 km across, 3400m above sea level) might suggest they were polygenetic volcanoes.

All of the Pleistocene volcanism is monogenetic. The Choraphor rhyolite volcano is a small dome (~2 km diameter) on the northern slopes of the Vardenis ridge, and has a K-Ar age of 1.75 Ma (Fig. 5.1b; Karapetian et al., 2001). While investigating the long term slip rate on the Pambak-Sevan-Syunik strike-slip fault, Philip et al. (2001) measured the age of the Khonarhasar scoria cone as 1.4 Ma using the K-Ar technique (Fig. 5.1b). Khonarhasar is dissected by the fault, leading to one half of the cone being offset along the fault from the other. To the south of Khonarhasar, Porak volcano (Fig. 2.3c) has been interpreted as a Holocene monogenetic volcano based on archaeological and historical evidence, with documents suggesting the eruption occurred between 782 and 773 BC (Karakhanian et al., 2002).

The evidence available from previous studies suggests that while early volcanism in Vardenis produced caldera-collapse ignimbrite forming eruptions from polygenetic volcanoes, Pleistocene volcanism has largely seen the formation of

monogenetic volcanoes. This suggests a polygenetic to monogenetic transition did occur, probably sometime before 1.5 Ma, but the exact timing is uncertain.

5.2.4 Syunik volcanic highland

The evidence for a polygenetic to monogenetic transition is substantially clearer in Syunik when compared to the other regions. Geological mapping has generally indicated that the polygenetic volcanoes are older than the monogenetic volcanoes (Fig. 5.1c). Close to the base of the section is the Goris strata debris avalanche volcaniclastic deposit, which formed due to the collapse of a large (likely polygenetic) volcanic edifice. It is thought to be upper Pliocene in age given that it lies directly below the lower Pleistocene Sissian sediments (Fig. 5.1c). It is also stratigraphically below the lava flows from monogenetic volcanoes in the large gorge in the south of the map area (Fig. 5.1c). Two polygenetic edifices are still observable in Syunik: Ishkhanasar (in the SE) and Tskhouk (to the NW; Fig. 2.3a). The lava flows which are associated with the polygenetic volcanoes are sometimes covered by the volcanic deposits of monogenetic volcanoes. For example, the Sherepasar monogenetic volcano clearly formed on top of the pre-existing lava flows from Tskhouk polygenetic volcano (Fig. 2.3h).

Ar-Ar ages of 1.16 and 1.24 Ma have been obtained for volcanic tephra layers interbedded with diatomite sediments in the Sissian suite sediments (Joannin et al., 2010). The large clast size (described as “conglomeritic” with cm-sized pumice clasts) and the thickness of these deposits (1-2.5m), suggests the volcanic material could be derived from a proximal source (Joannin et al., 2010). A significant magma chamber, with a sufficient magma volume to force a mass eruption rate high enough to drive a Plinian eruption might require a local polygenetic volcano to erupt this tephra deposit.

Ages from monogenetic volcanoes in Syunik are exclusively younger than 1 Ma. Several lava flows from monogenetic volcanoes which cap these sedimentary sequences have all been dated as < 1 Ma using the K-Ar technique (Ollivier et al., 2010). Several monogenetic rhyolite domes have been dated to 0.9-0.3 Ma using AFT and K-Ar methods (Karapetian et al., 2001). Archaeological evidence suggests the youngest lava flows from monogenetic volcanoes were emplaced roughly 5000-4500 years BP using the ages of burial cairns and petroglyphs (Karakhanian et al.,

2002). The evidence suggests that in Syunik there was a transition from polygenetic to monogenetic volcanism, which might have occurred around 1 Ma.

5.3 Sample Selection

Sample selection focussed predominantly on the Syunik volcanic highland for several reasons: (i) the evidence that this is a region where a transition from polygenetic to monogenetic volcanism occurred; (ii) the large number of mafic eruptive centres, which when age constrained can be used to look at the potential exhaustion of fusible components in the mantle source over time (and hence a waning magma supply as a potential cause of the transition); (iii) the detailed geological map which allows Ar-Ar ages to be related to the number of mapped monogenetic centres, such that recurrence intervals of volcanism can be investigated; and (iv) the relative paucity of age data when compared to the Gegham highland allowing better age coverage across the southern Lesser Caucasus volcanic field. Two samples from the Vardenis highland were also dated, as this region represents a gap in geochronological constraints across the field, and because there is some indication here of a poly- to monogenetic transition.

In Vardenis, one basaltic trachyandesite lava (sample 6.3.15) and one ignimbrite (sample 5.1.15) were selected for dating. The lava is a small volume mafic eruption which lies directly on top of the 2.3 Ma massive trachydacite lavas (see Fig. 2.3g in Chapter 2). If this mafic lava is much younger than the trachydacites underneath it, then it is likely to be monogenetic. If it formed at a similar time to the dacites then the case for a polygenetic volcanic system (capable of erupting several batches of magma of different compositions) at this time would be strengthened. The precise age could further constrain the timing of the poly- to monogenetic shift. The large ignimbrite unit at the base of the volcanic section provides an age for the basement on which all younger lava flows must have been built, and an age at which volcanic activity must have included polygenetic activity.

In Syunik, one sample is from a lava flow coming off the Tskhouk polygenetic volcano (sample 5.5.12), while the other nine samples come from monogenetic centres. The age of Tskhouk will show definitively when the polygenetic volcano must have been active. If the age is similar to the tephra layers

in the diatomite sediments this would support the view that these tephra came from a local stratovolcano. It would also show that the polygenetic to monogenetic transition occurred later here than to the north.

The bulk of new ages presented in this chapter are for monogenetic volcanoes in Syunik. Most of the samples chosen have mafic compositions and have also been analysed for Sr-Nd-B isotopes. This means the ages can be used to look at how the magma source may have changed over time, and whether there are any signs of it being depleted. These samples will be the main source of evidence on what might have caused the poly- to monogenetic transition in Syunik.

5.4 Analytical Methods

The groundmass fraction of most samples was used for Ar-Ar analysis to avoid inherited argon and maximise the K content. Samples were prepared for irradiation at the Scottish Universities Environmental Research Centre (SUERC) by Patrick Sugden. Following irradiation, argon isotope analysis on gas flux mass spectrometers was carried out by Dan Barfod and co-workers.

Sample preparation followed a rigorous procedure, whereby samples were crushed to the 250μm size fraction; after which these grains were passed through a barrier-type Franz magnetic separator to remove phenocrysts and altered groundmass. Finally hand-picking removed any residual phenocrysts and altered groundmass to give 400 mg groundmass samples.

For the ignimbrite sample 5.1.15, sanidine phenocrysts were used instead to obtain an age via total fusions of a population of single grains. Sanidine crystals were processed by crushing and magnetic separation, in the same way as for the groundmass samples. Sanidine was then separated using heavy liquid density separation, followed by a final magnetic separation to minimise the presence of inclusions. The sanidine crystals were leached in dilute HF to remove any pumice glass coating the grains. Hand picking was then used to select the most appropriate phenocrysts for analysis.

Samples and neutron flux monitors were packaged in copper foil and stacked in quartz tubes with the relative positions of packets precisely measured for later reconstruction of neutron flux gradients. The sample package was irradiated in the

Oregon State University reactor, Cd-shielded facility. Alder Creek sanidine (1.1891±0.0008 (1σ) Ma; Niespolo et al., 2017) was used to monitor ^{39}Ar production and establish neutron flux values (J) for the samples. Gas was extracted from samples via step-heating using a mid-infrared (10.6 μm) CO_2 laser with a non-gaussian, uniform energy profile and a 3.5 mm beam diameter rastered over a sample well. The samples were housed in a doubly-pumped ZnS-window laser cell and loaded into a copper planchette containing four square wells (1.6 cm^2). Liberated argon was purified of active gases, e.g., CO_2, H_2O, H_2, N_2, CH_4, using three Zr-Al getters; one at 16°C and two at 400°C. Data for 9 groundmass samples were collected on a GVi instruments ARGUS V multi-collector mass spectrometer using a variable sensitivity faraday collector array in static collection (non-peak hopping) mode (Mark et al., 2009; Sparks et al., 2008). Data for samples 10.2.15 and 11.1.15 were collected on a Mass Analyser Products MAP-215-50 single-collector mass spectrometer using an electron multiplier collector in dynamic collection (peak hopping) mode. Time-intensity data are regressed to inlet time with second-order polynomial fits to the data. The average total system blank for laser extractions, measured between each sample run, was 1.4 ± 1.7 $\times 10^{-15}$ mol ^{40}Ar, 2.8±3.5$\times 10^{-17}$ mol ^{39}Ar, 9.0±7.4$\times 10^{-18}$ mol ^{36}Ar (2.75 ± 0.09 x10^{-15}, 3.0 ± 0.5 x10^{-17} and 0.12 ± 0.02 x10^{-18} respectively for samples 10.2.15 and 11.1.15). Mass discrimination was monitored on a daily basis, between and within sample runs by analysis of an air standard aliquot delivered by an automated pipette system (see raw data for D values applied to individual steps). All blank, interference and mass discrimination calculations were performed with the MassSpec software package (MassSpec, version 8.058, authored by Al Deino, Berkeley Geochronology Center). Inverse-variance-weighted plateau ages, or composite plateau ages for replicated samples, are chosen as the best estimates of the emplacement ages. Plateau ages were defined following these criteria:

1) Steps overlap in age within 2σ uncertainty.

2) Minimum ^{39}Ar content for a step is ≥0.1% of total ^{39}Ar release.

3) Minimum of three contiguous steps.

4) Minimum of 50% of ^{39}Ar in the chosen steps.

5) The inverse isochron formed by the plateau steps yields an age indistinguishable from the plateau age at 2σ uncertainty.

6) The trapped component composition, derived from this inverse isochron, is indistinguishable from the composition of air at the 2σ uncertainty level.

7) Age and uncertainty were calculated using the mean weighted by the inverse variance of each step.

Sanidine sample irradiation followed the same procedure as groundmass samples. Step-heated gas extraction used a narrower CO_2 laser beam with a 1.5 mm diameter. The samples were housed in a doubly-pumped ZnS-window laser cell and loaded into a stainless steel planchette containing 208 2.0mm diameter round wells. Data were collected on a Mass Analyser Products MAP-215-50 single-collector mass spectrometer using an electron multiplier collector in dynamic collection (peak hopping) mode. The average total system blank for laser extractions, measured between each sample run, was $9.4\pm0.4\times10^{-16}$ mol ^{40}Ar, $9.6\pm2.6\times10^{-18}$ mol ^{39}Ar, $7.3\pm2.0\times10^{-18}$ mol ^{36}Ar. Other aspects of analysis were identical to those of the groundmass samples.

5.5 New ^{40}Ar-^{39}Ar ages

The full Ar isotope dataset is displayed in Appendix D. A summary of this data is shown in Table 5.1, with the associated isochron, step-heating plateau and population distribution (in the case of the sanidine phenocrysts) diagrams shown in Figs 5.2 and 5.3. Fig. 5.2 shows the results of total fusion analyses of individual sanidine phenocrysts from an ignimbrite which forms the basement of the Southern Lesser Caucasus volcanic field in the Vardenis highland. Its age of 6.014 ± 0.067 Ma provides a maximum time frame over which most of the remainder of the southern Lesser Caucasus volcanic field was built. All the other new ages (Fig. 5.3) are less than 1.5 Ma, as reported in Table 5.1. This is in agreement with other previous age constraints (Joannin et al., 2010; Ollivier et al., 2010; Lebedev et al., 2013), which suggest that the surface exposure of lava flows and un-eroded scoria cones in the Southern Lesser Caucasus volcanic field largely represents a Quaternary pulse in volcanism. However, some of the volcanic units exposed in Gegham and Vardenis are of Pliocene age (Karapetian et al., 2001; Lebedev et al., 2013).

Sample 6-3-15 in Fig. 5.3 is the small mafic dome which overlies the

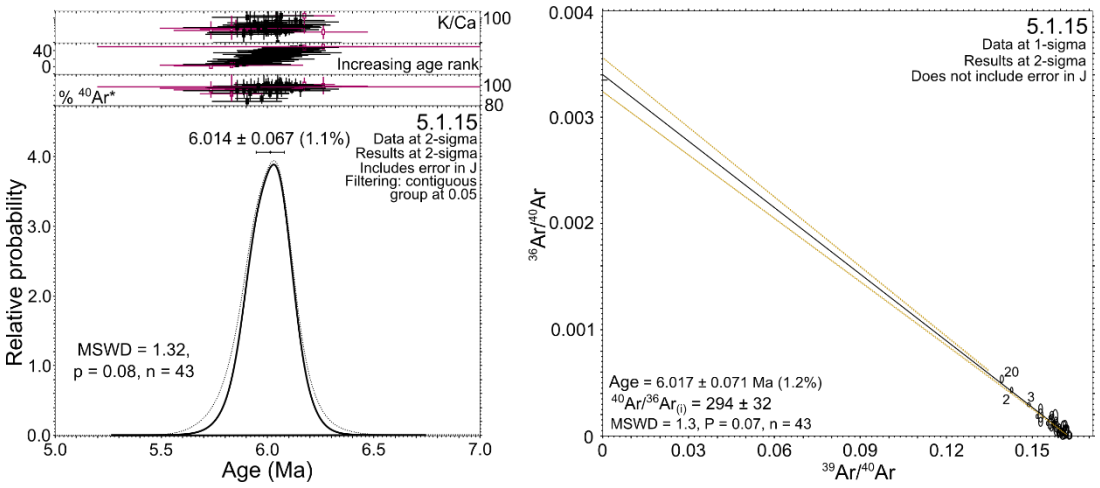

Figure 5.2 Population distribution and inverse isochron diagram for ignimbrite sample from the base of the Vardenis volcanic highland.

massive trachydacite units and has a plateau age of 1.301 ±0.014 Ma. This is a full 1 Myr younger than the dacites underneath. Such a time gap is comparable to the range of ages for erupted products from the modern Aragats volcanic edifice (1.3Myr; Connor et al., 2011; Gevorgyan et al., 2018), or of the lifespan of Neo-Sabalan volcano in NW Iran (0.4 Myr; Ghalamghash et al., 2016). As such this mafic unit is considered a separate monogenetic volcano to the dacites underneath. This lends further support to the notion that unlike in Syunik, volcanism was already monogenetic in Vardenis prior to 1 Ma.

In contrast the age of the lava flow on Tskhouk polygenetic volcano in Syunik is 1.316 ±0.014 Ma, providing the first direct geochronological evidence that polygenetic volcanoes were active in Syunik within the past 1.5 Ma. At the same time as volcanism in Vardenis was producing monogenetic volcanoes, volcanism in Syunik still took the form of polygenetic volcanoes.

All nine of the monogenetic volcano ages in Syunik are younger than 1 Ma (Figs 5.1 and 5.3). There is a cluster of four ages between 0.8 and 0.96 Ma (Fig. 5.3). The other five ages are younger than this, with the most recent cone forming at 0.048 ±0.024 Ma (sample 11.3.15; Fig. 5.3). The rhyolite obsidian sample (4.15.08) has an age of 0.674 ±0.01 Ma, in good agreement with an apatite fission track age of 0.61 Ma (Karapetian et al., 2001). The ages of the mafic-intermediate volcanoes show a vent migration with time, becoming younger to the north (Fig. 5.1).

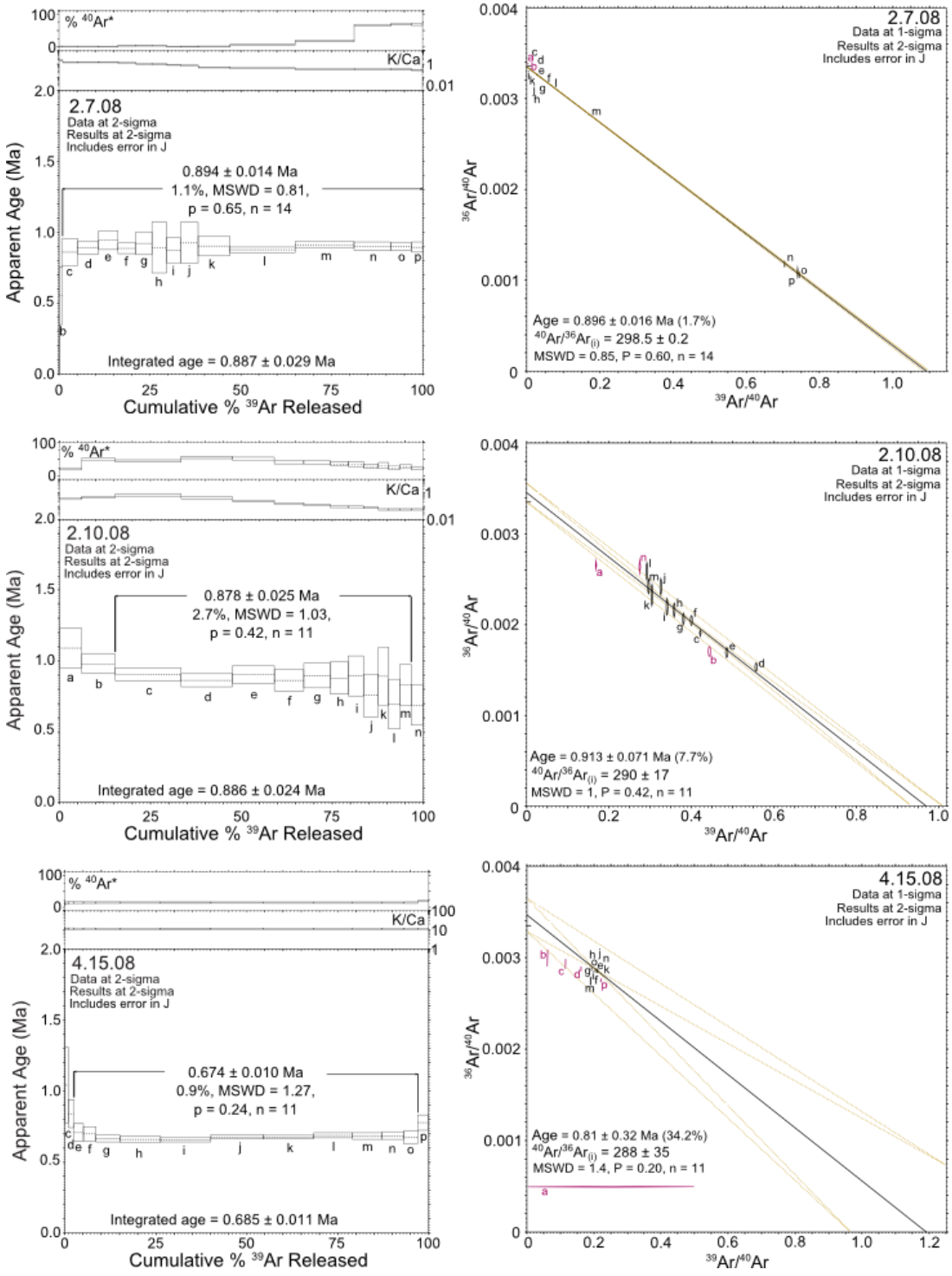

Figure 5.3 Plateau and isochron diagrams for ^{40}Ar-^{39}Ar step-heating experiments on groundmass samples

Sample 4.15.08 is obsidian glass. 5 samples (2.7.08, 2.10.08, 4.15.08, 10.2.15 and 11.3.15) had their step heating experiments repeated. This figure shows the first step heating experiment. The age reported in other figures is the inverse-variance-weighted composite age as shown in Table 5.1.

Figure 5.3 continued.

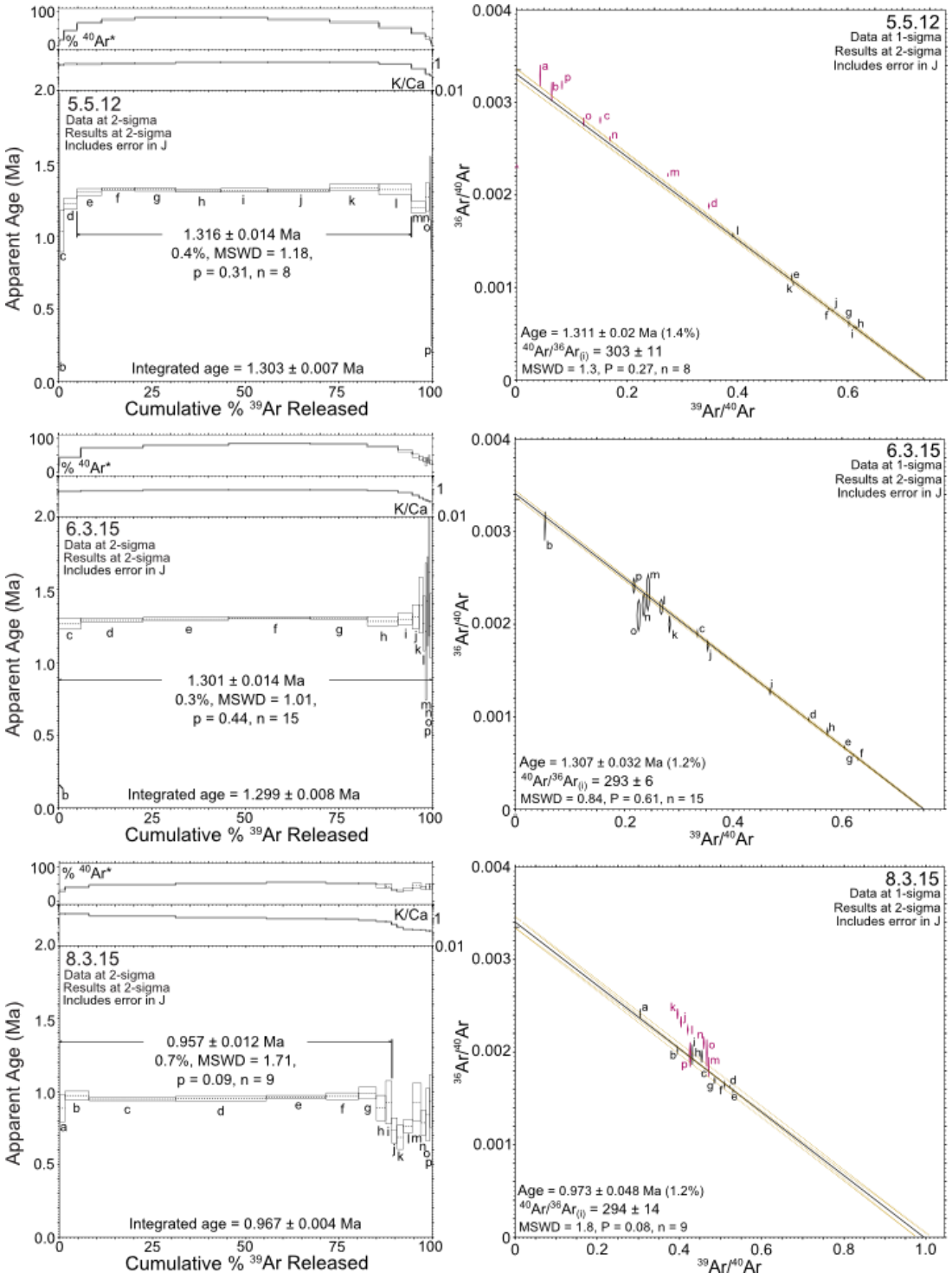

5.6 Volcanic history of the Lesser Caucasus

The late Miocene age for the Vardenis ignimbrite correlates with a second pulse of post-collisional rhyolite volcanism across Armenia (7-5-4.5 Ma), with an earlier one occurring 17-10 Ma (Karapetian et al., 2001). It also correlates with the end of the early stage of bimodal volcanism on the Erzurum-Kars plateau in neighbouring

Figure 5.3 continued.

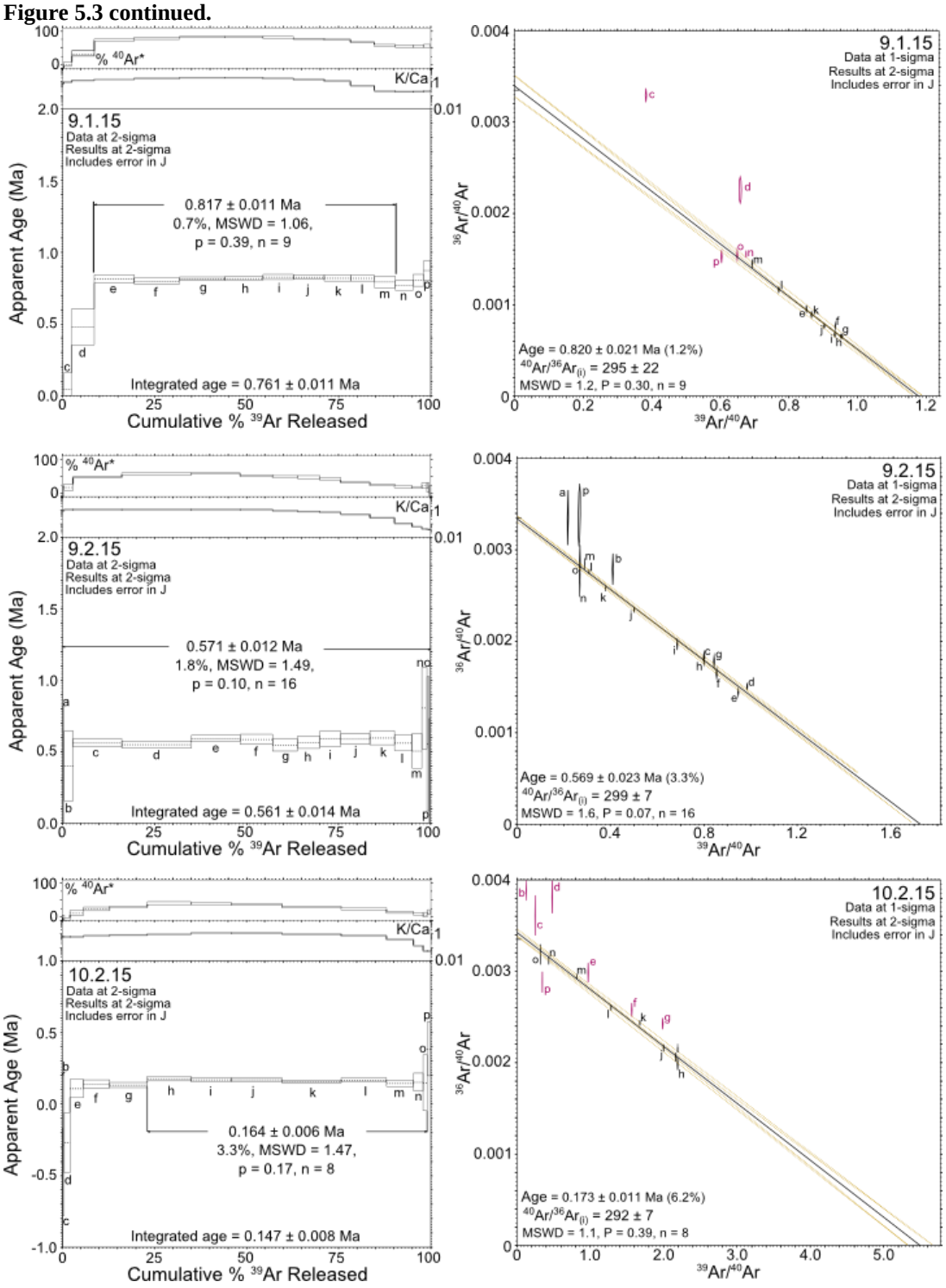

eastern Anatolia to the west, which included the production of felsic pyroclastic rocks (Keskin et al., 1998). This ignimbrite may have been part of a regional pulse of explosive felsic volcanic activity at this time.

Figure 5.3 continued.

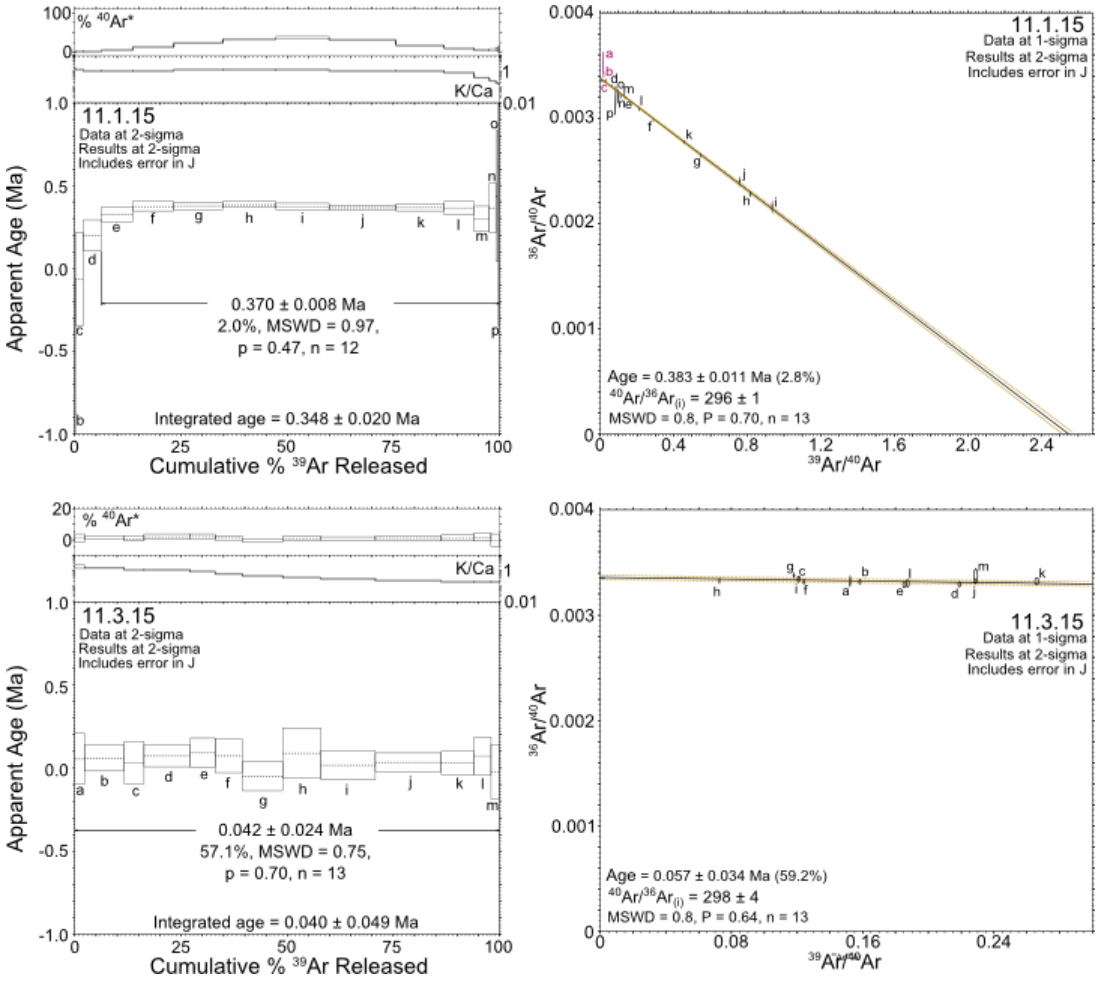

The stratigraphic position of this ignimbrite at the base of the volcanic sequence in Vardenis suggests most of the Southern Lesser Caucasus volcanic field must be Plio-Pleistocene in age. In the early phase of this period a large volcanic edifice was present in the Syunik region until it collapsed to form the Pliocene Goris strata. To the north in Vardenis massive dacite lava flows erupted, with monogenetic volcanoes forming in Gegham. Volcanic units of this age from Aragats have mostly been buried by younger eruptions, although Pliocene rocks are still exposed in some river gorges and as the neighbouring Arailer volcanic complex (Connor et al., 2011).

The vast majority of age constraints from the Southern Lesser Caucasus volcanic field are for Quaternary volcanic rocks, and are summarised in Fig. 5.4. On this basis, some tentative suggestions for episodes of volcanism within the field during this period can be made. As in any geochronological study, these suggestions should be treated with caution. This is because of the unavoidable potential of

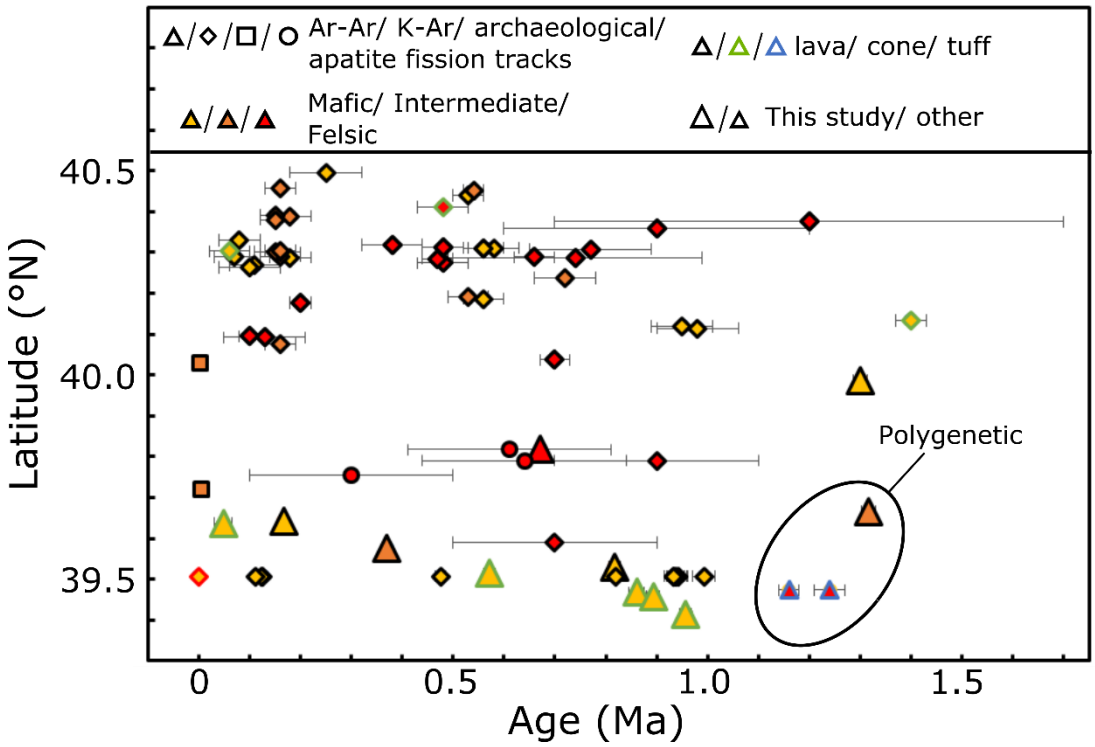

Figure 5.4 Summary of new ages alongside ages from the literature for Quaternary volcanism in the southern Lesser Caucasus volcanic field.

The ages of radiometrically dated samples from both this study and others are shown above *vs* the latitude of the sample. Error bars represent 2σ uncertainties. The shape of the symbol denotes the method of dating- triangles for Ar-Ar, diamonds for K-Ar etc. The fill colour of the symbols gives the sample composition: yellow for mafic, orange for intermediate, red for felsic. The border colour shows the sample type- is it from a lava flow, scoria cone or pumice/tuff layer? Symbols for samples dated in this study are larger than literature data. The area circled as polygenetic shows the ages thought to be associated with eruptions of a polygenetic volcano. The orange triangle is the age of the lava from Tskhouk dated for this study. The two smaller triangles are pumice layers in diatomite sediments (Joannin et al., 2010). Data sources are the same as for Fig. 5.1.

sampling bias given the relatively large number of volcanic centres compared to ages (183 centres *vs* 27 ages in Syunik for example).

- Stage 1 (before 1 Ma): eruptions from polygenetic volcanoes in Syunik. These eruptions produced intermediate lava flows, and possibly more felsic explosive eruptions (Joannin et al., 2010). To the north monogenetic volcanism was already underway in Vardenis producing both mafic and felsic volcanic rocks here. None of the volcanoes which have been dated in Gegham fall into this time period, potentially suggesting there was a period of quiescence in the north.
- Stage 2 (1-0.8 Ma): pulse of mostly mafic magmatism producing lava flows and scoria cones in both Syunik and Gegham

Table 5.1 ^{40}Ar-^{39}Ar age determination

Errors include J parameter. MSWD = mean square rooted deviation

Sample cone/ lava/ tuff	Volcano	No. of steps	$^{40}Ar/^{39}Ar$ total gas age (ka)	$^{40}Ar/^{39}Ar$ weighted mean plateau age				$^{40}Ar/^{39}Ar$ isochron age			
				Age (ka) ± 2σ	% ^{39}Ar	No. of steps	MSWD	Age (ka) ± 2σ	No. of steps	MSWD	$^{40}Ar/^{36}Ar$ (atm)
		16	887	894 ± 14	99	14	0.8	896 ± 16	14	0.85	298.5 ± 0.2
2.7.08 cone	Yerakov Blur (mafic)	15	883	892 ± 15	100	15	1.0	901 ± 18	15	0.86	298.4 ± 0.2
		29	895	**893 ± 12**	100	29	0.9	898 ± 14	29	0.83	298.5 ± 0.1
		14	886	878 ± 25	81.4	11	1.0	913 ± 71	11	1.02	289.6 ± 17.2
2.10.08 cone	Barurtumb (mafic)	14	857	853 ± 18	80.7	11	1.3	878 ± 36	11	1.09	289.9 ± 10.8
		22	861	**861 ± 15**	100	22	1.2	878 ± 34	22	1.21	293.4 ± 9.4
		15	685	674 ± 10	94.5	11	1.3	807 ± 322	11	1.37	288.4 ± 30.2
4.15.08 cone	Mets Satanakar (felsic)	15	669	670 ± 10	99.4	13	1.5	780 ± 221	13	1.56	290.5 ± 19.3
		24	672	**672 ± 9**	100	24	1.4	780 ± 140	24	1.34	290.5 ± 12
5.5.12 lava	Tskhouk (intermed-iate)	15	1303	**1316 ± 14**	89.6	8	1.2	1311 ± 20	8	1.27	302.5 ± 11
6.3.15 lava	Torgomayr (mafic)	15	1299	**1301 ± 14**	100	15	1.0	1307 ± 32	15	0.84	293.3 ± 5.8
8.3.15 cone	Verjiblur (mafic)	16	937	**957 ± 12**	89.1	9	1.0	973 ± 48	9	1.84	293.7 ± 14.2
9.1.15 lava	Spiovblur (mafic)	15	761	**817 ± 11**	81.7	9	1.1	820 ± 21	9	1.20	293.7 ± 14.2
9.2.15 cone	Chobanasar (mafic)	16	561	**571 ± 12**	100	16	1.5	569 ± 23	16	1.59	299.4 ± 6.9
		15	147	164 ± 6	75.9	8	1.5	173 ± 11	8	1.06	292 ± 6.4
10.2.15 lava	Kyorpasar (mafic)	15	140	175 ± 10	86.1	13	1.6	157 ± 22	13	1.45	304.6 ± 7.1
		21	154	**167 ± 5**	100	21	1.6	164 ± 11	21	1.68	300.3 ± 5.2
11.1.15 lava	Unknown (intermedia-te)	15	348	**370 ± 8**	93.7	12	1.0	383 ± 11	13	0.75	296 ± 1.3
		13	40	42 ± 24	100	13	0.8	57 ± 34	13	0.81	297.7 ± 3.9
11.3.15 cone	Sherepasar (mafic)	17	67	55 ± 25	100	17	1.0	26 ± 13	17	1.01	300.4 ± 3.7
		30	57	**48 ± 18**	100	30	0.9	41 ± 15	30	0.92	299.0 ± 2.7
				Single grain population age							
		No. grains				No. of grains			No. of grains		
5.1.15 tuff	Surakan ignimbrite (felsic)	50		**6014 ± 67**		43	1.3	6017 ± 30	43	1.34	294 ± 32

- Stage 3 (0.8-0.65 Ma): pulse of predominantly rhyolite volcanism, seen in both the north and south of the volcanic field
- Stage 4 (0.58-0.25 Ma): volcanism continuing, but possibly with a lower recurrence rate. There may also be some hiatus in volcanism around 0.3-0.2 Ma
- Stage 5 (0.2-0 Ma): most recent pulse of predominantly (although not exclusively) mafic-intermediate volcanism

5.7 Rates and repose intervals of volcanic activity

For this section, the Syunik volcanic highland is focused on as an area for which there is good geological information in terms of the number of vents and mapped volcanic units (Sugden et al., 2019). The simplest model for the rate of volcanic eruptions assumes a constant repose interval, and can be written as:

$$\lambda_t = \frac{N-1}{t_0 - t_y}$$

where λ_t is the number of eruptions per year, N is the total number of eruptions, t_0 is the age of the first eruption, and t_y the age of the most recent. If it is assumed that each eruption forms a new vent, the number of eruptions can be estimated as being the number of monogenetic vents present in Syunik (183 have been mapped). It is assumed that all monogenetic volcanoes in Syunik are between 1 and 0 Ma in age on the basis of the available age constraints. As such, taking the oldest lava thought to come from a monogenetic vent in Syunik (0.993 Ma; Ollivier et al., 2010) gives a reasonable estimate for t_0. The youngest eruption has been established as 0.005 Ma on the basis of archaeological evidence (Karakhanian et al., 2002). This calculation suggests 1.8 $x10^{-4}$ eruptions/year, which is within the range of volcanic fields globally (the Michoacán-Guanajuato field has a rate of 2 $x10^{-3}$ eruptions/year over the last 40 kyr; Valentine and Connor, 2015), meaning the estimate is a sensible one. However the Syunik rate is at the upper end of the range for most volcanic fields (10^{-5} to 10^{-4} eruptions per year). For example in the Southwest Nevada volcanic field the rate is just 8 $x10^{-6}$ eruptions/year (Valentine and Connor, 2015). The rate in Syunik is sufficiently low to allow volcanism to be monogenetic, however this could be a volcanic field where high rates of extension are also required to prevent a polygenetic volcano from forming.

The Syunik rate also equates to one eruption every ~ 5500 years, similar to the time since the last eruptive event which formed the Kharkar group Holocene volcanoes (Karakhanian et al., 2002). However, before too hastily suggesting another eruption is imminent, it is worth noting that the last eruption involved the formation of multiple vents closely spaced in time. The most recent lava generations of the Holocene lava flow field (Fig. 5.1c) appear to have been fed by five vents. All of these lavas are thought to have formed over the course of a few hundred years

(Karakhanian et al., 2002), such that they can be treated as one eruptive event. If one eruptive event can form 5 vents, this could suggest eruptions every ~ 27000 years.

The assumption of a constant rate of eruptive activity may well be incorrect, as has been seen in other volcanic fields, such as Auckland, New Zealand (Leonard et al., 2017). Based on the current age data it is not possible to rule out episodic pulses of more intense volcanic activity. If this is the case, given the higher number of ages from the last 0.175 Ma (Fig. 5.4), and the presence of 8 vents from the Holocene alone, Syunik may now be in a phase of more frequent eruptions, and 5500 years could be an overestimate of the modern repose interval.

While the precise timing of a future eruption is uncertain, the region is still demonstrably volcanically active. On 4th March, 2016 there was a swarm of 40 earthquakes at depths of 7 to 16 km under some late Pleistocene monogenetic volcanoes on the Gegham ridge (Sargsyan et al., 2018). The earthquakes have been interpreted as being of volcanic origin suggesting magma is currently present under the volcanic field, and could produce an eruption in Gegham, Vardenis or Syunik in the future.

5.8 Origin of the transition from polygenetic to monogenetic volcanism

The new $^{40}Ar/^{39}Ar$ ages obtained as part of this study confirm that there was a temporal shift from polygenetic to monogenetic volcanism in Syunik. The age of Tskhouk lavas (1.316 ± 0.014 Ma- sample 5.5.12; Fig. 5.3; Table 5.1) suggests the volcano could have still been active when the tephra layers were deposited in the diatomite sediments (Section 5.2.4). These tephra layers could then have been derived from local Plinian eruptions, and may in fact be the youngest marker of polygenetic volcanism in Syunik (Fig. 5.5). All the ages for monogenetic volcanic centres in Syunik are younger than 1 Ma (Table 5.1), in agreement with all previous ages (Karapetian et al., 2001; Karakhanian et al., 2002; Ollivier et al., 2010). After 1 Ma the polygenetic edifices were covered by a younger generation of monogenetic volcanoes and their associated lava flow fields (Fig. 5.5).

The age of the mafic summit of Torgomayr (Fig. 2.3g; sample 6.3.15) as 1.301 ± 0.014 Ma (Fig. 5.3; Table 5.1) supports the interpretation in Section 5.2.3

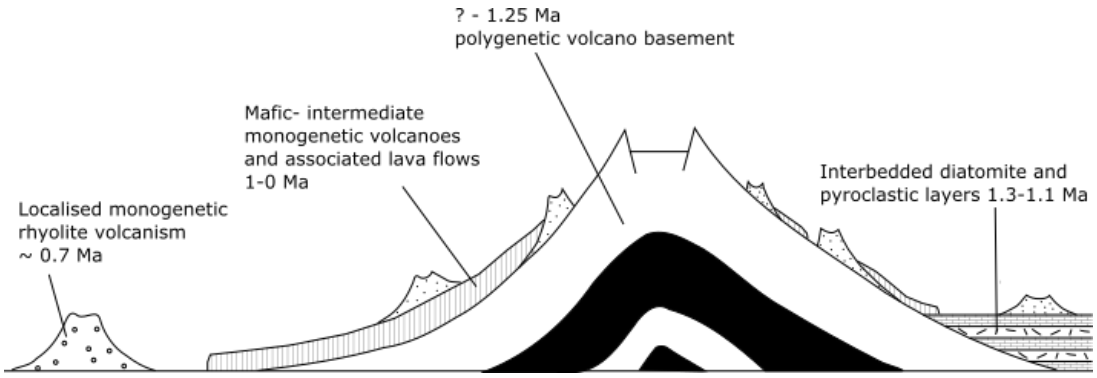

Figure 5.5 Cartoon stratigraphy of the Syunik volcanic highland.

Volcanism prior to 1 Ma was dominated by large polygenetic volcanoes, of which there were at least 2, possibly of multiple generations. Towards the end of the lifetime of these large volcanoes diatomite sediments were deposited in lakes on their lower slopes. Tephra layers were interbedded with these sediments. These layers were possibly associated with plinian eruptions during the later stages of polygenetic volcanism. Mafic-intermediate monogenetic volcanism younger than 1 Ma overlies both the polygenetic volcanoes and lake sediments. Individual scoria cones may be associated with lava flow fields of variable sizes. Monogenetic felsic volcanism also occurred in the last 1 Myr, but was localized in the north of the Syunik volcanic highland (see Fig. 5.1).

that by this time (1.5 - 1 Ma), Vardenis was already a region of monogenetic volcanism while volcanoes in Syunik were still polygenetic. Unfortunately, the age of the ignimbrite (Fig. 5.2; Table 5.1- sample 5.1.15) at 6.014 ± 0.067 Ma does not provide much further constraint on how recently volcanism was definitely polygenetic. All that can be said is that at some point between 6 and 1.5 Ma a shift does seem to have occurred.

The question then arises, why is volcanism in Syunik now monogenetic, while the large polygenetic volcanoes are now dormant or extinct? Monogenetic volcanism requires the absence of a long lived magma-plumbing system (Connor and Conway, 2000). A reduced magma supply could be the result of the exhaustion in subduction components in the mantle source, while increased rates of extension would have implications for the tectonic history of the region. Both of these possibilities and their implications are now discussed.

5.8.1 Decreased magma supply?

A reduction in magma flux to the crust would ultimately be a reflection of reduced magma production rates at depth. This could be the result of a reduced degree of partial melting in the mantle- the crust does not contribute to magma production (see Sr-Nd isotope data in Chapter 3). Reducing the degree of melting would be expected

to increase the concentration of the most incompatible trace elements. Using concentration data is greatly complicated by the fact that such elements are also influenced by the degree of crystal fractionation the magma has experienced. Yet even if mafic samples which have experienced similar (small) degrees of fractionation are compared, there is no coherent trend with age (not shown here).

A decrease in the degree of melting could be the result of fertile components in the mantle source becoming exhausted, such that the mantle source would be expected to become depleted. This can be thought of as the "death of a subduction zone", whereby subduction components are progressively removed from the mantle source during melting events following the end of continuous subduction. Removal of subduction components would force $^{87}Sr/^{86}Sr$ and $^{143}Nd/^{144}Nd$ to more mantle-like values (less radiogenic and more radiogenic respectively). As the subduction component is inherited from previous subduction (see Chapter 4), then if it were removed, $\delta^{11}B$ would be expected to approach mantle values (-7.1‰; Marschall et al., 2017). There are no systematic trends in $^{143}Nd/^{144}Nd$ or $\delta^{11}B$ with age (Fig. 5.6). A long-lived mantle source appears to be being tapped and continuously supplying magma. Although $^{87}Sr/^{86}Sr$ is lower in some of the most recent samples (Fig. 5.6), one of the samples (from Porak in Vardenis) has a similar value to the older monogenetic volcanoes. Given that the other isotopes don't show any similar variation, and all the younger volcanoes with lower $^{87}Sr/^{86}Sr$ occur within 12 km of each other, the variation may simply reflect small scale heterogeneity in the mantle source on the scale of 10s of km.

Even if the degree of partial melting has remained the same, the rate of magma supply could be reduced if the volume of mantle being partially melted reduced over time. This could occur without any shift in the measured isotopic compositions of magmas. However, there are a couple of other observations which suggest the magma supply has not reduced to a lower level over the past 1 Ma. Firstly, as was previously mentioned (sections 2.2.1, 3.4.1, 3.4.2, 5.2), this volcanic field is host to mafic, intermediate and felsic volcanoes. Some of the most recent Holocene eruptions from monogenetic volcanoes are andesites, while rhyolite domes have erupted over the last 1 Ma (Fig. 5.6). The production of evolved magmas requires a thermal anomaly in the crust substantial enough to allow magmas to stall and fractionate while retaining a sufficient melt fraction to remain "eruptible" (Sparks et al., 2019). As such, evolved compositions are thought to be associated

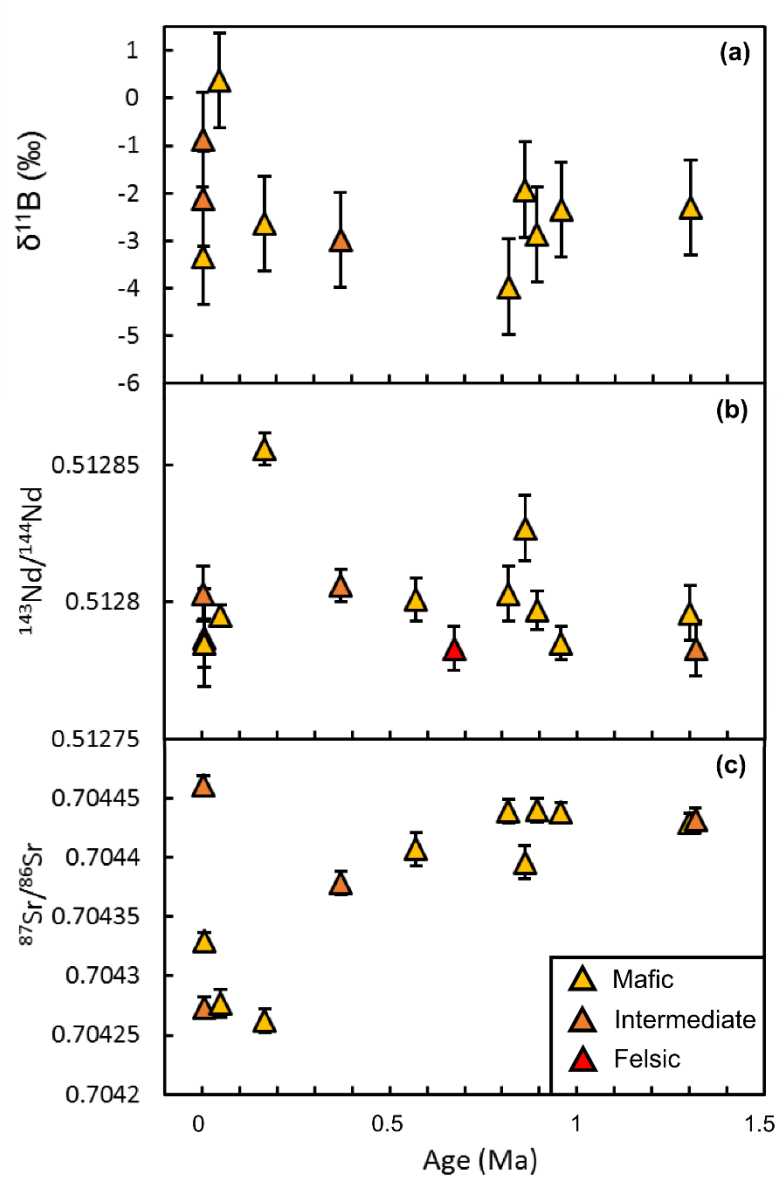

Figure 5.6 $\delta^{11}B$, $^{143}Nd/^{144}Nd$ and $^{87}Sr/^{86}Sr$ *vs* age.

The isotope data is from that presented in Chapters 3 and 4. While $\delta^{11}B$ (a) and $^{143}Nd/^{144}Nd$ (b) show no correlation with age, some of the younger samples have lower $^{87}Sr/^{86}Sr$ (c). Error bars for $\delta^{11}B$ are given as 1‰, on the basis of the reproducibility from duplicate analyses (see Chapter 4). Error bars for $^{143}Nd/^{144}Nd$ and $^{87}Sr/^{86}Sr$ are 2σ analytical uncertainties.

with volcanic fields with a relatively high rate of magma supply (Smith and Németh, 2017). This suggests that in Syunik it is unlikely to be magma supply which is preventing a polygenetic volcano from forming.

Secondly, on the basis of geological mapping (Fig. 5.1) there is no evidence that the rate of lava flow emplacement is decreasing- at least in terms of areal coverage. The area covered by Holocene lavas (blue in Fig. 5.1c) is 27 km^2, while the total area covered by monogenetic lavas since 1 Ma is 679 km^2. This gives an

emplacement rate over the last 10000 years of 2.7 $x10^{-3}$ km^2/yr compared with an average rate of 6.8 $x10^{-4}$ km^2/yr over the last 1 Ma. The average rate is likely to be an underestimate because older monogenetic lava flows may be covered by younger ones. However, there is no evidence for the rate of lava flow emplacement decreasing with time.

It is also worth noting that the shift from polygenetic to monogenetic volcanism is specific to the Syunik volcanic highland, or at least the southern Lesser Caucasus volcanic field (Fig. 5.1). Polygenetic volcanism has continued unabated to the west in eastern Anatolia (Yilmaz et al., 1998), and to the south in Iran (Davidson et al., 2004; Ghalamghash et al., 2016). It seems unlikely for magma fluxes to be reduced in one particular locality while many surrounding locations continue to produce the same volumes of magma. On the basis of this discussion, it is possible to suggest that a reduced magma flux is highly unlikely to be the cause of the poly- to monogenetic transition in Syunik. As such this transition does not reflect the removal of subduction components from the mantle source following continental collision, and is instead more likely the result of local tectonic changes. The final part of this discussion explores these potential tectonic changes.

5.8.2 Increased rate of extension?

Many of the youngest generation of volcanoes (Holocene) form small clusters which are located in modern pull apart basins, including several of the youngest cones in the Gegham highland (found on the central ridge axis), at Porak in Vardenis (0.003 Ma in Fig. 5.1b), and the Karckar group of lava flows and scoria cones in Syunik (Fig. 5.1; Karakhanian et al., 2002; Sargsyan et al., 2018). These pull-aparts are stepping structures in the Pambak-Sevan-Syunik strike-slip fault system. There are several other clusters of monogenetic volcanic centres in the Syunik volcanic highland (Fig. 5.1c). Although it has been suggested such clusters could form over enriched domains in a heterogeneous mantle (Valentine and Connor, 2015), the similar age of vents within each cluster suggests they may have also formed in similar pull-apart basin settings in the past (Fig. 5.1c).

Observations from other volcanic fields suggest that these fault structures influence magma ascent pathways (Valentine and Connor, 2015). In the absence of pre-existing weaknesses in the crust, magmas would ascend through dykes

perpendicular to the principal stress component. Dykes can deviate from this orientation if pre-existing faults provide an easier ascent route for the magma. In this way eruptions will be focused close to fault structures, as this is where the most favourable ascent routes for magma will be.

There is a migration of volcanoes with time roughly parallel with the local orientation of the Pambak-Sevan-Syunik strike slip fault system (Fig. 5.1c). This vent migration is most clearly seen by looking at mafic-intermediate cones (Fig. 5.7). The felsic samples from the north of Syunik do not fit the trend (Fig. 5.7), showing that it probably only applies to the southern part of Syunik. At 4.5 cm/yr the vent migration is too fast and in the wrong direction for it to be plate motion over a hotspot-style stationary source (Reilinger et al., 2006). It is possible to speculate that this vent migration represents repeated formation of clusters of volcanoes in pull-apart basins along the fault. Normal faulting and dyke injection are both ways of accommodating crustal extension, the former by displacement, the latter by filling the space created by extension with magma. When a pull-apart basin forms, extension will be accommodated via normal faulting, but as volcanoes erupt the extension will instead be accommodated by dyking, "healing" the normal faults. A new pull-apart basin then forms, and the volcanism follows the new extensional structures.

Given the associations of volcanoes with pull-apart basins (Karakhanian et al., 2002; Sargsyan et al., 2018), extension structures have clearly interacted with magmatism in the Lesser Caucasus. The question is then how does this extension relate to the polygenetic to monogenetic transition at 1 Ma. The most obvious model would be for the rate of motion (and hence extension) on the Pambak-Sevan-Syunik fault system to have increased at that time. However, the rate of motion on the major strike slip fault has been constant over the past 1.4 Myr at 1 mm/yr, at least on the southern branch close to the volcanoes in Syunik (Karakhanyan et al., 2013). Hence, on the basis of strike-slip motion there is no evidence for increasing deformation rates across the time interval of the polygenetic to monogenetic transition.

It is worth re-iterating that the polygenetic to monogenetic transition occurred latest in the Syunik highland. Syunik is currently at the southern end of the Pambak-Sevan-Syunik strike-slip fault system (Karakhanyan et al., 2013). It is known that faults propogate radially and increase in length during their history, either by

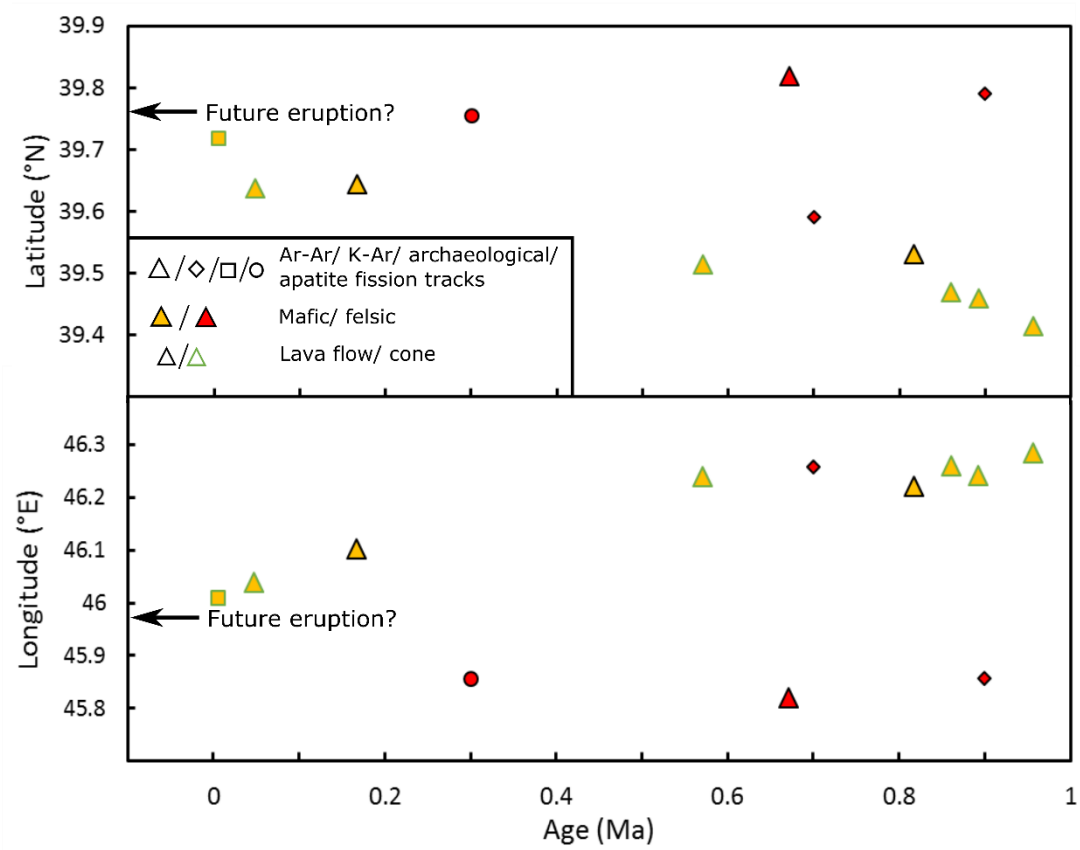

Figure 5.7 Illustrating vent migration in the Syunik volcanic highland.

A northwestward migration with time in the location of mafic monogenetic vents. This migration suggests a future eruption would be likely to be closest to the most recent eruption (shown by the arrow). The felsic samples in red do not fit the trend observed for mafic samples. Sample 11.1.15 (0.37 Ma) was removed from the plot as the location of the vent the sample is associated with is uncertain.

growing at the tips or by smaller segments coalescing (Cladouhos and Marrett, 1996). It is suggested that in the case of the Lesser Caucasus, 1 Ma was the time at which the Pambak-Sevan-Syunik strike-slip fault system lengthened sufficiently to encompass the Syunik highland. Only once this had occurred was Syunik subject to similar levels of extension as the northern part of southern Lesser Caucasus volcanic field, where volcanism had already been monogenetic for some time. This polygenetic to monogenetic transition in Syunik may be acting as a tape recorder of the lengthening of the Pambak-Sevan-Syunik strike-slip fault system.

5.9 Conclusion

A new set of ^{40}Ar-^{39}Ar ages confirm that a transition from polygenetic to monogenetic volcanism occurred at 1 Ma in the Syunik highland. Two new ages

suggest a transition could have occurred in the Vardenis highland to the north, but that by 1.5 Ma volcanism was already monogenetic meaning that the transition would have occurred earlier. Some clustering of age data suggests volcanism over the past 1 Ma was episodic, with some periods of dominantly felsic volcanism, notably 0.8-0.65 Ma. With an average rate of 2 $x10^{-4}$ eruptions/year in Syunik, the frequency of volcanic eruptions is at the upper end of the observed range for volcanic fields, and there is no sign that activity is waning. Given the north-westward migration of eruptive centres, a future eruption may be particularly likely close to or NW of the recent Holocene eruptions in Syunik. The main road from Iran to the Caucasus region passes within 5 km of the most recent lava flows and is a key trade link in the region. A future eruption could not only pose a significant hazard to local populations, but also have important geopolitical implications were the road to be blocked during an eruption. There is a lack of geochemical variation with time, which suggests a long-lived magma source is continuing to supply magma at a constant rate and degree of melting. As such, despite being in a post-collisional setting, there is no evidence for the exhaustion of the fusible slab component. Rather than a reduction in magma supply, the polygenetic to monogenetic transition is a product of an increased rate of crustal extension at 1 Ma. This is argued to be the result of the Pambak-Sevan-Syunik strike-slip fault lengthening sufficiently to encompass Syunik, and increase extension rates in Syunik to the rates seen in the rest of the southern Lesser Caucasus volcanic field. Syunik represents an important case study of a region where the monogenetic character of volcanism can not simply be explained by a low magma supply, but requires a high rate of extension.

6. Conditions of magma storage from amphibole and clinopyroxene geothermobarometry

6.1 Introduction

The preceding 3 chapters have explored how post-collisional magmas are able to form and erupt, whereas this chapter reviews the amphibole and clinopyroxene geothermobarometry and hygrometry of southern Lesser Caucasus volcanic rocks. In other words, what happens between melt formation and ultimate eruption? Specifically, what can be ascertained regarding a magma's evolution and storage during its ascent through the crust? This chapter constrains the conditions (pressure and temperature) of crystal fractionation, which occurred during periods of magma storage in the crust prior to final ascent and eruption at the surface. It will also try to constrain H_2O content and oxygen fugacity of the magmas, in order to better understand the effects of mantle metasomatism, and to use geothermobarometers calibrated for hydrous magmas. It will then be possible to critically evaluate some of the conclusions from previous chapters. Are the calculated magmatic temperatures consistent with the melting mechanism as proposed in Chapter 3? Is the oxygen fugacity and H_2O content of magmas consistent with their derivation from a subduction-modified mantle source? Are those values consistent with the H_2O content and $Fe^{3+}/\Sigma Fe$ used in modelling mantle melting in Chapter 3? Is the conclusion from Chapter 5 that magma supply remains constant during the recent history of volcanism supported by uniform magmatic temperatures and H_2O contents?

The mafic minerals amphibole (Ridolfi and Renzulli, 2012; Putirka, 2016) and clinopyroxene (Nimis, 1995; Putirka, 2008) are often used to estimate the pressure-temperature (*P-T)* conditions (geothermobarometry) of magma storage and crystallisation. As shown in Fig. 6.1, most of the southern Lesser Caucasus eruptives are not glassy, nor are there abundant melt inclusions. Estimates of the melt composition are therefore lacking, and it is only possible to use models which rely on the mineral compositions alone. The more common occurrence of amphibole in the southern Lesser Caucasus compared to the volcanoes to the north makes this a particularly good region in which to use this approach. This chapter presents the major element composition of amphibole and clinopyroxene, before detailing the

method used in calculating *P-T* conditions. Finally, the implications of these estimates for the other conclusions in this thesis are discussed.

6.2 Amphibole and clinopyroxene occurrence and textures

The samples for which amphibole and clinopyroxene compositions were analysed have mafic-intermediate compositions. Six samples are trachybasaltic andesite (7.5.15, 2.5.08, 2.6.08, 8.3.15, 9.1.15, 10.2.15), while there is one phonotephrite (2.7.08), one tephrite (11.3.15), one trachybasalt (9.2.15) and one trachyandesite (7.4.15). Samples have MgO of 3.7- 6.3 wt % and SiO_2 of 47-58 wt %. Clearly, both amphibole and clinopyroxene occur in some of the most mafic magmas in the region, and as such offer the potential to provide insights on the physical-chemical properties of mantle-derived magmas which have experienced only limited degrees of crystal fractionation.

The petrography of the studied samples (n=10) is detailed in Section 3.3. However a few salient points are worth re-iterating here. Fig. 6.1 shows photomicrographs and back-scattered electron (BSE) images that are examples of the phenocrysts analysed for this chapter. Amphiboles exhibit a wide range of crystal sizes (200μm-2 mm in Fig. 6.1). Some amphibole crystals appear to exhibit subtle zonation (Fig. 6.1c, i) between the core and rim. Commonly amphibole phenocrysts do not exhibit euhedral crystal faces, and instead have corroded rims (Fig. 6.1a, e, i, m), which suggests they were out of equilibrium with the final melt. At greater degrees of disequilibrium, amphibole crystals form reaction rims, which can be macro- (Fig. 6.1c, j) or microcrystalline (Fig. 6.1g, h). In extreme cases large parts of the original phenocryst have reacted to form an oxide-clinopyroxene-plagioclase- apatite symplectite (Fig. 6.1f). For several samples (n=4) it is only possible to estimate the conditions under which the amphibole cores formed. The extent to which this issue is problematic depends on the degree of mineral zonation.

Clinopyroxenes are common and occur as phenocrysts (up to 2.5 mm; Fig. 6.1b, d), and also as glomerocrysts (Fig. 6.1i, j, l, n). Crystals often show normal zonation, and in the case of the glomerocrysts exhibit several Mg-rich cores and a single Fe-rich rim (Fig. 6.1l).

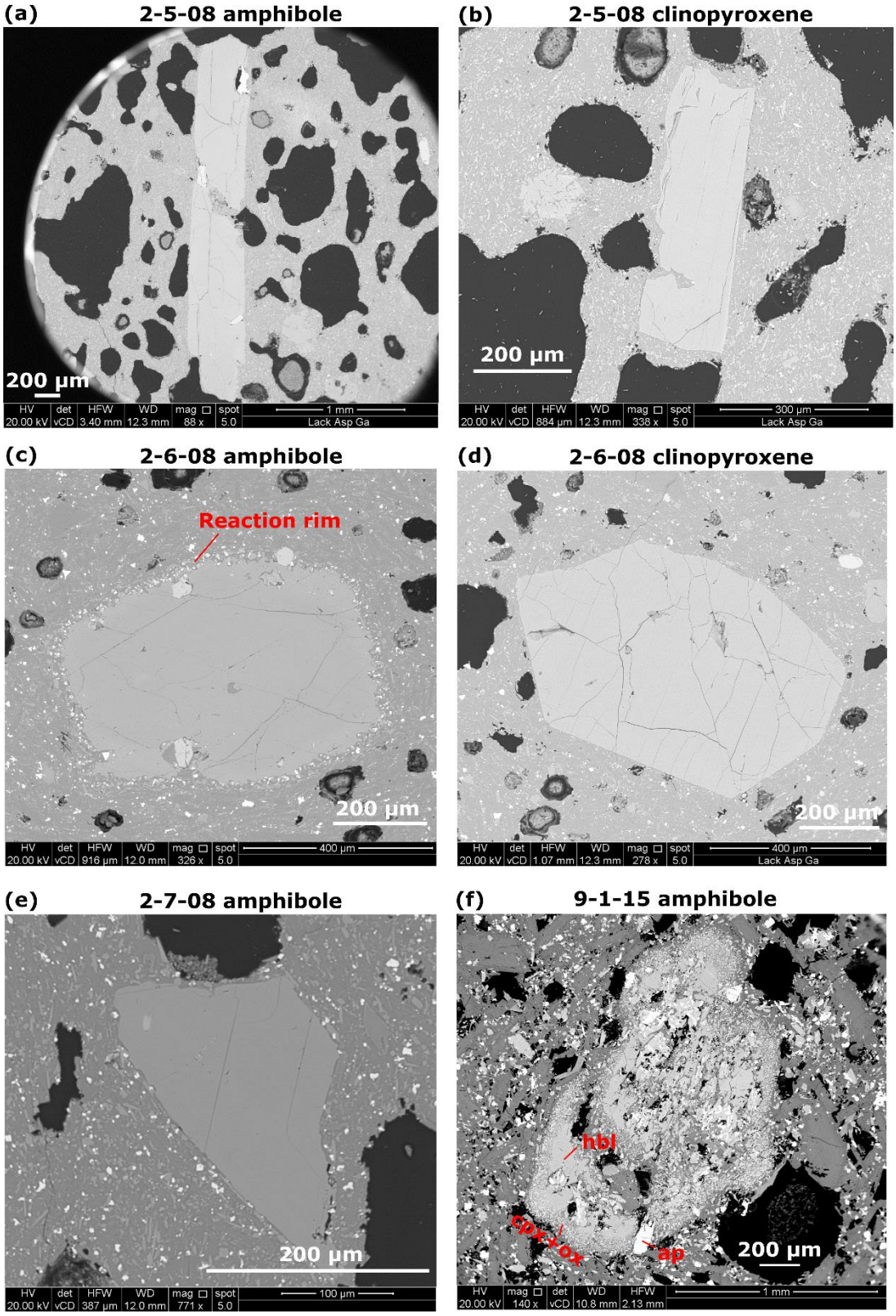
(a) 2-5-08 amphibole
200 µm
HV 20.00 kV | det vCD | HFW 3.40 mm | WD 12.3 mm | mag 88 x | spot 5.0 | 1 mm | Lack Asp Ga
(b) 2-5-08 clinopyroxene
200 µm
HV 20.00 kV | det vCD | HFW 884 µm | WD 12.3 mm | mag 338 x | spot 5.0 | 300 µm | Lack Asp Ga
(c) 2-6-08 amphibole
Reaction rim
200 µm
HV 20.00 kV | det vCD | HFW 916 µm | WD 12.0 mm | mag 326 x | spot 5.0 | 400 µm
(d) 2-6-08 clinopyroxene
200 µm
HV 20.00 kV | det vCD | HFW 1.07 mm | WD 12.3 mm | mag 278 x | spot 5.0 | 400 µm | Lack Asp Ga
(e) 2-7-08 amphibole
200 µm
HV 20.00 kV | det vCD | HFW 387 µm | WD 12.0 mm | mag 771 x | spot 5.0 | 100 µm
(f) 9-1-15 amphibole
hbl
cpx + ox
ap
200 µm
HV 20.00 kV | mag 140 x | det vCD | WD 10.8 mm | HFW 2.13 mm | 1 mm

(g) 7-4-15 amphibole

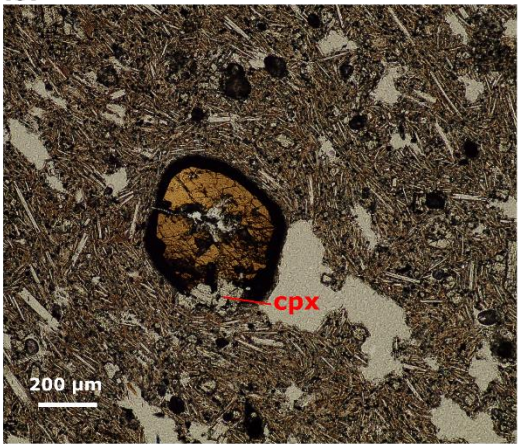

(h) 7-5-15 amphibole

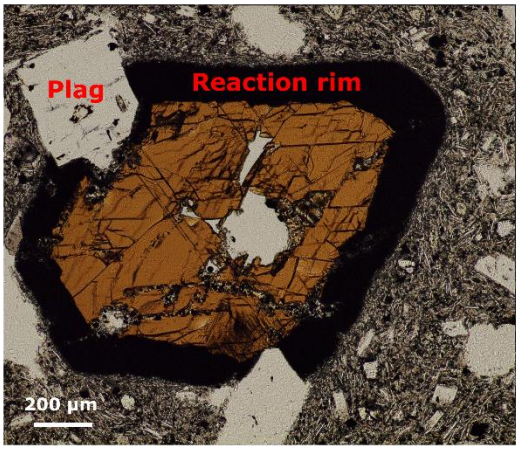

(i)8-3-15 amphibole & clinopyroxene

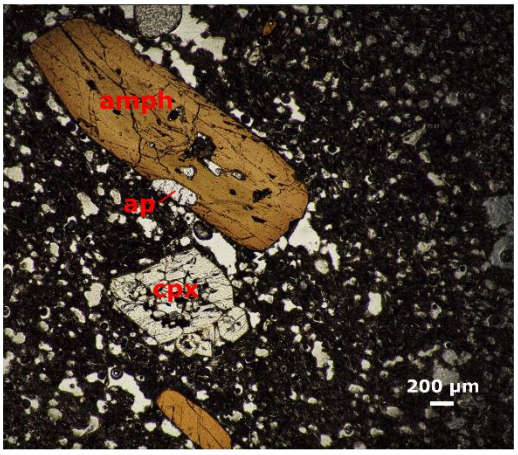

(j) 9-2-15 amphibole & clinopyroxene

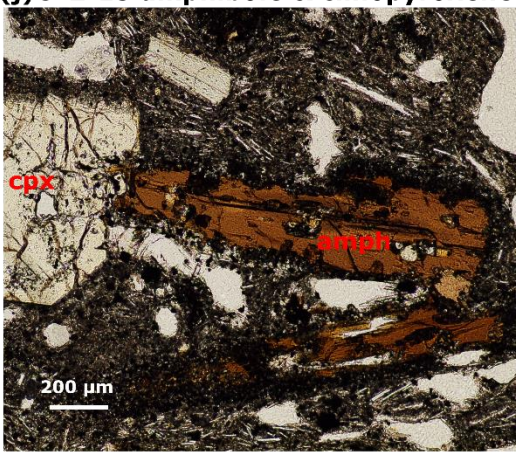

(k) 8-3-15 amphibole

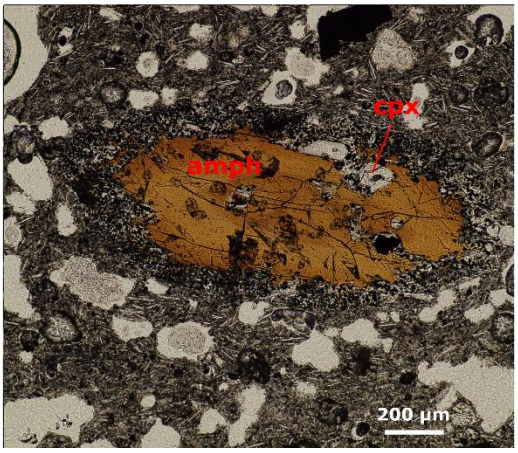

(l) Poikilitic texture

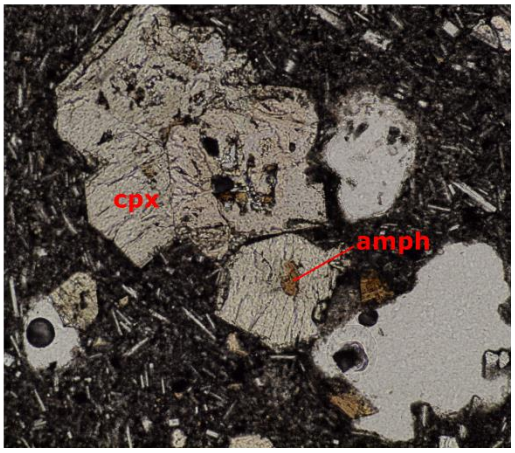

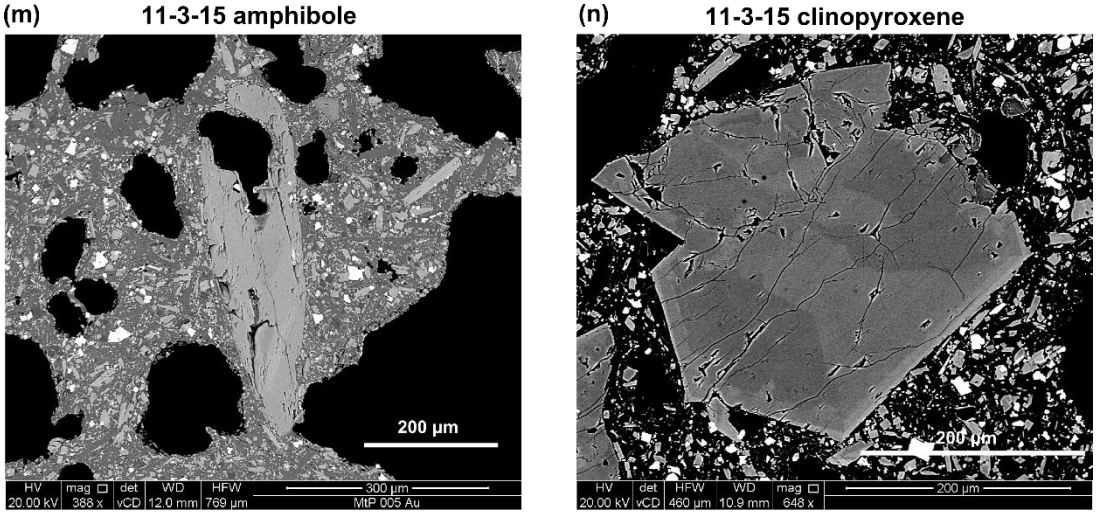

Figure 6.1 SEM images and photomicrographs of amphibole and clinopyroxene crystals and their sample number.

(a) Large euhedral amphibole phenocryst; (b) euhedral clinopyroxene phenocryst; (c) amphibole phenocryst with thin macrocrystalline reaction rim; (d) large clinopyroxene phenocryst; (e) amphibole microphenocryst with corroded rims, no zonation or reaction textures; (f) pseudomorph of former amphibole phenocryst which has reacted extensively with the magma such that only remnants of the original crystal remain (labelled amph). The reaction rim is made of clinopyroxene and Fe-Ti oxide microcrystals (cpx + ox), but also apatite crystals (labelled ap); (g) Amphibole phenocryst with microcrystalline symplectite rim. Clinopyroxene is seen to be overgrowning amphibole phenocryst. Groundmass texture is pilotaxitic; (h) as (g) with a larger phenocryst and wider reaction rim. Also overgrown by plagioclase phenocryst (Plag); (i) amphibole phenocryst (amph) with corroded rim and apatite crystal on rim (ap) and clinopyroxene glomerocryst (cpx); (j) amphibole (amph) overgrowing clinopyroxene (cpx), yet amphibole has reaction rims while clinopyroxene appears in equilibrium with the melt; (k) Poikilitic amphibole with reaction rim. Inclusion of clinopyroxene; (l) poikilitic texture from sample 1.4C.08 (no EPMA data for this sample) of a clinopyroxene glomerocryst with amphibole inclusions; (m) Corroded amphibole phenocryst; (n) clinopyroxene glomerocryst showing Mg-rich cores (darker) and more Fe rich rims (brighter).

Amphibole and clinopyroxene crystals often occur in close proximity to each other (Fig. 6.1i, j). Euhedral clinopyroxene crystal faces and the lack thereof for amphibole suggests that only clinopyroxene is likely to be in equilibrium with the final melt. Poikilitic textures are not uncommon, with both amphibole included in clinopyroxene (Fig. 6.1j, l) and clinopyroxene included in amphibole (Fig. 6.1g, k). It is likely therefore that both minerals formed under similar conditions, and the *P-T* conditions calculated from the two minerals can be expected to match.

6.3 Electron probe micro-analysis (EPMA) analytical methods

In situ major element amphibole and clinopyroxene compositions were determined on a JEOL8230 electron microprobe at the University of Leeds. Analysis was performed using a focussed beam, with an acceleration voltage of 20 keV. Major elements were analysed for 30 sec. on peak and with a beam current of 30 nA. Minor elements in olivine and amphibole were run for 80 to 120 sec. on peak with a beam current of 100 nA.

The main secondary standards used were the Smithsonian Kakanui hornblende and the GEO2 diopside (Jarosewich et al., 1980). Spot analyses of these standards are given in Appendix E. GEO2 diopside analyses reproduced expected oxide abundances to within 0.25 wt % on average. Calculated cation sums for unknown samples were close to 4 (~4.02), suggesting the analyses were good. Analyses of Kakanui hornblende gave systematic errors in some oxides, notably Al_2O_3 (1.5 wt % offset on average). Analyses of unknown samples were corrected accordingly (Jarosewich et al., 1980). Amphibole may contain up to 2 wt % H_2O, such that totals should be between 98-100 wt %. Applying the Kakanui hornblende normalisation to the data from unknown samples improves the totals (from ~96 wt % to ~99 wt %, see Appendix E), justifying the approach. The standard error of the mean for the spot analyses on each sample is < 0.1 wt %, which gives a *P-T* sensitivity of ~5˚C and 15 MPa- i.e. negligible relative to the uncertainty on the geothermobarometric models used.

6.4 Amphibole and clinopyroxene compositions

Major element spot analyses of amphibole and clinopyroxene from 9 samples is given in Appendix E. Spot analyses for several phenocrysts were averaged to give a single core and rim composition for amphibole and clinopyroxene for each sample (Table 6.1).

Amphiboles are either magnesiohastingsites or pargasites (Fig. 6.2a-c). These calcic amphiboles are typical of amphiboles found in alkaline volcanic rocks such as those in the southern Lesser Caucasus (Ridolfi and Renzulli, 2012; Sugden et al., 2019). There is generally little distinction between the cores and rims of

Table 6.1 Major element oxide (wt %) composition of amphibole and clinopyroxene

Averaged for all crystal core and crystal rim measurements in each southern Lesser Caucasus volcanic rock sample

	SiO_2	TiO_2	Al_2O_3	FeO	MnO	MgO	CaO	Na_2O	K_2O	Total
Amphibole										
2-5-08 core	40.33	3.54	13.83	11.74	0.15	13.38	11.86	2.42	1.56	98.81
2-5-08 rim	40.48	3.40	13.80	11.61	0.13	13.51	11.88	2.58	1.42	98.80
2.6.08 core	40.68	3.53	13.69	11.23	0.14	14.06	11.63	2.65	1.11	98.70
2-6-08 rim	40.53	3.20	13.81	12.04	0.18	13.64	11.44	2.69	1.13	98.66
2-7-08 core	40.43	3.69	13.82	10.77	0.11	14.23	11.91	2.50	1.28	98.73
2-7-08 rim	40.39	3.56	13.78	11.38	0.12	13.82	11.86	2.53	1.27	98.71
8-3-15 core	40.50	3.64	13.66	11.96	0.17	14.00	11.81	2.60	1.13	99.46
8-3-15 rims	40.65	3.56	13.59	11.20	0.13	14.18	11.77	2.58	1.18	98.85
11-3-15 core	40.50	3.61	13.66	11.28	0.11	14.31	11.53	2.56	1.31	98.87
11-3-15 rims	40.58	3.76	13.50	12.00	0.14	13.78	11.42	2.52	1.32	99.03
9-1-15 core	40.65	3.70	13.69	11.18	0.12	14.45	11.64	2.68	1.13	99.25
7-4-15 core	42.20	3.11	13.27	10.69	0.12	14.76	11.81	2.56	0.79	99.32
9-2-15 core	40.79	3.75	13.90	11.14	0.11	14.20	11.68	2.59	0.93	99.08
7-5-15 core	40.91	3.98	13.33	11.65	0.13	13.79	11.28	2.49	1.00	98.56
Clinopyroxene										
2-5-08 core	51.23	0.51	3.38	7.51	0.32	13.81	22.21	0.80		99.87
2-5-08 rim	49.31	1.11	5.04	7.43	0.19	13.50	22.16	0.67		99.46
2-6-08 core	49.89	0.93	4.95	6.59	0.15	14.56	21.41	0.66		99.46
2-6-08 rim	51.06	0.80	4.05	6.99	0.18	14.90	21.09	0.61		99.86
8-3-15 core	50.53	0.78	4.34	6.44	0.13	14.84	21.45	0.64	0.00	99.35
8-3-15 rim	48.92	1.25	5.33	7.41	0.15	14.01	21.37	0.55	0.01	99.17
11-3-15 core	50.70	0.88	4.47	6.98	0.14	14.82	20.63	0.96	0.01	99.77
11-3-15 rim	49.05	1.42	4.85	7.32	0.13	13.91	22.15	0.64	0.01	99.55
9-1-15 core	50.82	0.70	3.52	7.25	0.20	15.38	20.57	0.51	0.00	99.11
9-2-15 core	51.02	0.76	3.42	7.27	0.27	14.32	21.63	0.69	0.00	99.54

amphibole phenocrysts, with the Mg# (Mg/Mg+Fe) varying only between 0.67 and 0.71 (Fig. 6.2). Amphiboles appear to be in equilibrium with a magma more evolved than the bulk rock (Fig. 6.2d). This is to be expected given that amphiboles occur in association with clinopyroxene and sometimes olivine phenocrysts, but (at least for the Syunik samples) no plagioclase phenocrysts. Amphibole could instead be in equilibrium with the matrix composition. Amphiboles have a uniform composition in the studied samples, irrespective of the whole-rock composition, suggesting they may all have formed from a compositionally similar magma reservoir. Given this reservoir is seen in even the most mafic samples, it is likely the *P-T* calculations will

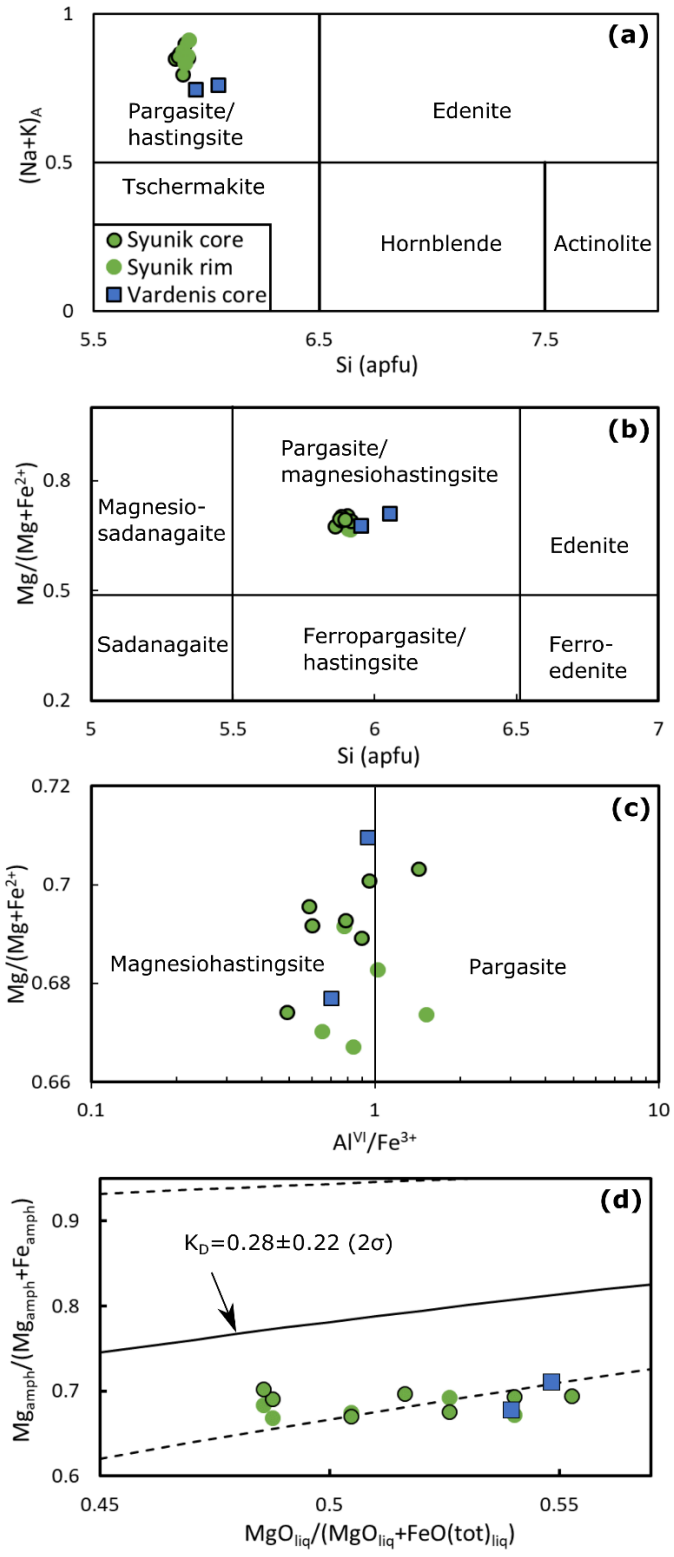

Figure 6.2 Major element composition of amphiboles in southern Lesser Caucasus volcanic rocks.

Amphibole cations are calculated on a 23 oxygen basis (Leake et al., 1997). (a-c) show the classification of amphiboles (Leake et al., 1997). All amphiboles are calcic (Ca_B>1.5), with Ti<0.5. Estimates of Al^{VI} and Fe^{3+} are purely stoichiometric, based on the major element oxides alone using the methods suggested by Leake et al. (1997). (d) The Mg# for both amphiboles and the host rock is a molar ratio, calculated on the basis of 100% Fe hosted as Fe^{2+} (see text). Fe-Mg exchange equilibrium is given with 2 standard deviation upper and lower bounds as dashed lines (Putirka, 2016).

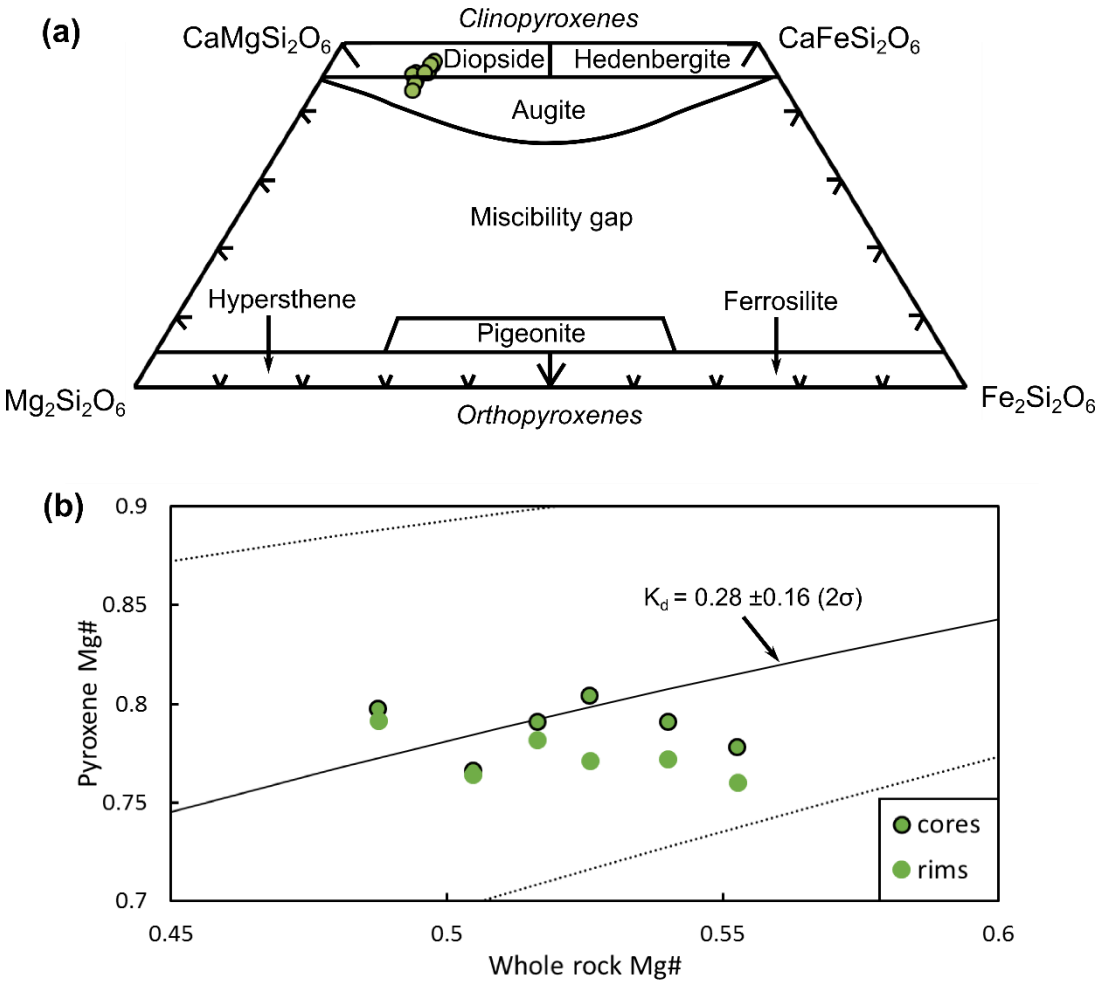

Figure 6.3 Major element composition of amphiboles in southern Lesser Caucasus volcanic rocks. Clinopyroxene components are calculated as described in Putirka (2008). (a) Classification of clinopyroxene phenocrysts. (b) Mg# (Mg/Mg+Fe molar ratio) of clinopyroxenes and the host bulk rock. Fe is assumed to be hosted exclusively as Fe^{2+} in both the mineral and magma. Fe-Mg exchange equilibrium is given with 2 standard deviation upper and lower bounds as dotted lines (Putirka, 2008).

relate to a magma reservoir which has only experienced limited crystal fractionation since extraction from the mantle source.

For six of the samples for which amphibole compositions were determined, clinopyroxene was also analysed. Clinopyroxenes have transitional diopside to augite compositions (Fig. 6.3a). As suggested by BSE images (Fig. 6.1l), many clinopyroxene phenocrysts and glomerocrysts seem to exhibit normal zonation, with average crystal rims having a lower Mg# ($X^{Mg}/(X^{Mg}+X^{Fe}_{\text{all ferrous}})$ when compared with the cores (Fig. 6.3b).

Clinopyroxene phenocrysts are within error of Fe-Mg exchange equilibrium with the composition of their respective bulk rocks (Fig. 6.3b; Putirka, 2008). This

could suggest that clinopyroxene crystallised earlier and from a less evolved magma than amphibole. However both Figs 6.2d and 6.3b are based on the probably erroneous assumptions that Fe in both the minerals and magma is exclusively Fe^{2+}. The amphibole stoichiometry suggests that significant amounts of Fe are hosted as Fe^{3+} (Fig. 6.2c), although the exact proportions are uncertain and depend on which method is used to calculate Fe^{3+} (Leake et al., 1997). There are also likely to be significant amounts of Fe^{3+} in the host magma given its arc-type geochemistry (Brounce et al., 2014). These large uncertainties hamper constraints being placed on Fe-Mg exchange, as well as the significant uncertainties in the exchange coefficient (Figs 6.2d, 6.3b). As such it is still quite possible that clinopyroxene and amphibole were at times in equilibrium with each other and the same magma, as suggested by the petrography (Fig. 6.1).

6.5 Geothermobarometric calculations

Amphibole and clinopyroxene compositions can be used to calculate the magmatic *P-T* conditions in the absence of any estimate of the composition of the equilibrated melt phase (Nimis, 1995; Ridolfi and Renzulli, 2012).

The approach taken in this chapter is to calculate a range of possible values for P and T. This involves taking the combined standard errors of estimates (1σ) of both amphibole and clinopyroxene thermobarometers to give a ~90% confidence interval of pressures and temperatures (Fig. 6.4). One pitfall of this approach is that it assumes that estimates derived from amphibole and clinopyroxene compositions will be independent of each other, but the pressures, temperatures and H_2O contents input in the clinopyroxene equations are derived from the amphibole thermobarometry, as is explained below. Estimates of error are taken from the regressions of the large datasets Putirka (2016) for amphibole, and Putirka (2008) for clinopyroxene. Where possible, a regression of data not used in model calibration is used.

The first step of the calculation is to get an initial estimate of the likely range of possible crystallisation temperatures from amphibole alone (Fig. 6.4a). The Ridolfi and Renzulli (2012) thermometer is:

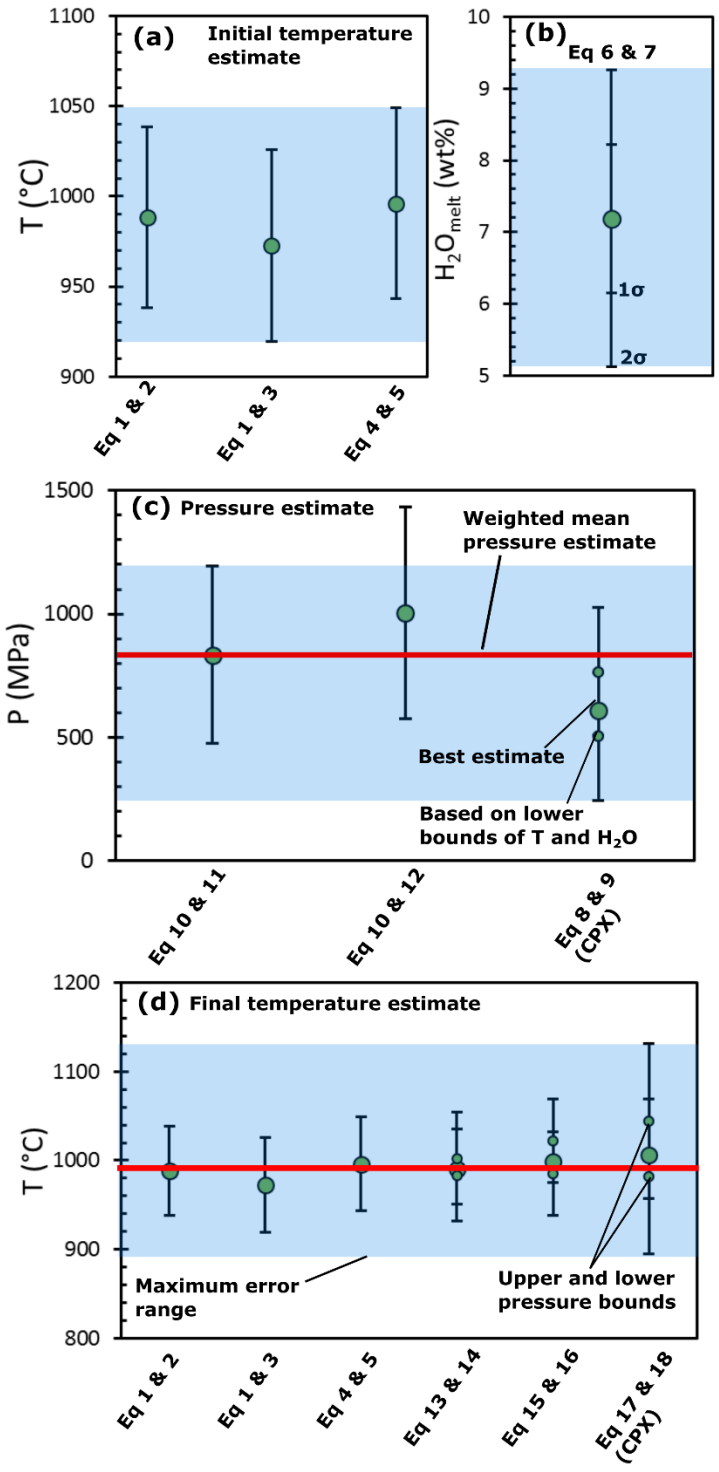

Figure 6.4 Sequence of equations used to calculate P-T conditions

Error propagation and the method used to get to the final P-T estimates and uncertainty ranges are shown **(a)** A range of initial temperature estimates from amphibole alone. Error bars are the standard error of each estimate (1σ, SEE). The total range of errors represented by the blue box is propagated through to the clinopyroxene pressure estimate in (c). **(b)** An estimate of melt H_2O content. The SEE is doubled for the clinopyroxene pressure estimate as only one equation is used here. **(c)** P is calculated by combining constraints from amphibole and clinopyroxene. A best clinopyroxene estimate is made on the basis of the average temperature and H_2O contents. Upper and lower bounds (shown by the small green circles) of this pressure estimate are made based on the limits of the blue error envelopes in (a) and (b). A final pressure estimate is shown by the red line which is the weighted mean of the three estimates shown. The blue box shows the likely pressure range. **(d)** The pressure estimate and range are used to make a final temperature estimate, with error range.

$$T(℃) = 17098 - 1322.3[Si^{amph}] - 1035.1[Ti^{amph}] - 1208.2[Al^{amph}] - 1230.4[Fe^{amph}] - 1152.9[Mg^{amph}] - 130.4[Ca^{amph}] + 200.54[Na^{amph}] + 29.408[K^{amph}] + 24.41\ln(P) \quad (6.1)$$

The pressure term is calculated as the P-statistic described in Ridolfi and Renzulli (2012), itself derived only from amphibole. The terms Si^{amph} etc represent the number of atoms per formula unit on a 23 O basis. Regression of this equation for the datasets in Putirka (2016) gave:

$$T(℃)_{obs} = 0.9T_{calc} + 79 \quad SEE = 50℃ \quad (6.2)$$

$$T(℃)_{obs} = 0.74T_{calc} + 225 \quad SEE = 53℃ \quad (6.3)$$

Equation 6.4 of (Putirka, 2016) also requires no independent estimate of pressure:

$$T(℃) = 1781 - 132.74[Si^{amph}] + 116.6[Ti^{amph}] - 69.41[Fe^{amph}] + 101.62[Na^{amph}] \quad (6.4)$$

A regression of the test dataset gave (Putirka, 2016):

$$T(℃)_{obs} = 0.89T_{calc} + 98 \quad SEE = 53℃ \quad (6.5)$$

Magmatic pressures are calculated using both amphibole and clinopyroxene geobarometers. A pressure estimate on the basis of clinopyroxene composition requires magmatic temperature and H_2O content to be constrained. The temperature range is estimated on the basis of the maximum and minimum values derived from Eqs 6.2, 6.3 and 6.5 (blue box in Fig. 6.4a). H_2O content is calculated following the algorithm of Ridolfi and Renzulli (2012):

$$\ln(H_2O_{melt}(wt\%)) = -65.907 + 5.0981[Si^{amph}] + 3.1308[Ti^{amph}] + 4.9211[Al^{amph}] + 4.9744[Fe^{amph}] + 4.6536[Mg^{amph}] + 1.0018[Ca^{amph}] - 0.7890[Na^{amph}] - 0.539[K^{amph}] + 0.4642\ln(P) \quad (6.6)$$

As in Eq. 6.1, P is calculated solely from the amphibole composition. The only error estimate for this equation was based on the limited dataset of Ridolfi and Renzulli (2012):

$$H_2O(wt\%)_{obs} = 0.963H_2O_{calc} + 0.225 \quad SEE = 14.4\% \quad (6.7)$$

As well as the limited dataset, another drawback for this equation is that most experimental igneous amphiboles are formed under H_2O saturated conditions, limiting the experimental range, and reducing leverage for model calibration (Putirka, 2016). This H_2O content estimate is a key weakness of the approach in this chapter, which is why a 2σ error range is used for the clinopyroxene equation (Fig. 6.4b).

A clinopyroxene based pressure estimate is given as (Putirka, 2008):

$$P(kbar) = 1458 + 0.197T(°K) - 241\ln(T(°K) + 0.453H_2O_{melt}(wt\%) + 55.5X^{cpx}_{Al(VI)} + 8.05[Fe^{cpx}] - 277[K^{cpx}] + 18X^{cpx}_{Jd} + 44.1X^{cpx}_{DiHd} + 2.2\ln\left(X^{cpx}_{Jd}\right) - 17.7[Al^{cpx}]^2 + 97.3(X^{cpx}_{Fe(M2)})^2 + 30.7(X^{cpx}_{Mg(M2)})^2 - 27.6(X^{cpx}_{DiHd})^2 \quad (6.8)$$

$$P(kbar)_{obs} = P_{calc} \quad SEE = 260\ MPa \quad (6.9)$$

The X^{cpx} terms are calculated as described in Putirka (2008) and represent (in order of appearance in the equation): the number of 6 co-ordinated Al atoms per formula unit; the proportion of the jadeite end-member in the natural clinopyroxene; the proportion of diopside/hedenbergite end member, the number of Fe atoms per formula unit in the M2 site, the number of Mg atoms per formula unit in the M2 site. The partitioning of Fe and Mg between M1 and M2 sites is calculated as described in Nimis (1995). Terms such as $[Fe^{cpx}]$ are atoms per formula unit. An amphibole pressure estimate can also be made using a barometer from Ridolfi and Renzulli (2012) and regression of the two datasets after Putirka (2016):

$$\text{P (MPa)} = 26106 - 1991.9[Si^{amph}] - 3035[Ti^{amph}] - 1472.2[Al^{amph}] - 2454.8[Fe^{amph}] - 2125.8[Mg^{amph}] - 830.64[Ca^{amph}] + 2708.8[Na^{amph}] + 2204.1[K^{amph}] \quad (10)$$

$$P(MPa)_{obs} = 0.65P_{calc} + 200 \quad SEE = 360\ MPa \quad (6.11)$$

$$P(MPa)_{obs} = 0.64P_{calc} + 380 \quad SEE = 430\ MPa \quad (6.12)$$

Pressure ranges from equations 6.9, 6.11 and 6.12 (using the propagated uncertainties of T and H_2O for clinopyroxene) can be used to constrain the likely range of pressure conditions (Fig. 6.4c). This range utilises the range from clinopyroxene as well as one of the amphibole error ranges- whichever is closer to the clinopyroxene estimate. This gives two independent constraints at 1σ and

therefore a 90% confidence in this range. A best estimate of pressure can be made by taking the weighted mean from Eqs 6.9, 6.11 and 6.12 (Fig. 6.4c), where the weighting is inversely proportional to the error on Eqs 6.9, 6.11 and 6.12, plus propagated errors in the case of clinopyroxene.

This pressure range can then be used to provide additional constraints on temperature (Fig. 6.4d), using the maximum and minimum pressures already calculated for the following amphibole based equations (Putirka, 2016):

$$T(\text{°C}) = 1687 - 118.7[Si^{amph}] + 131.56[Ti^{amph}] - 71.41[Fe^{amph}] + 86.13[Na^{amph}] + 22.44P(GPa) \quad (6.13)$$

$$T(\text{°C})_{obs} = 0.89T_{calc} + 97 \quad SEE = 52\text{°C} \quad (6.14)$$

As well as:

$$T(\text{°C}) = 1201.4 - 97.93[Si^{amph}] + 201.82[Ti^{amph}] + 72.85[Mg^{amph}] + 88.9[Na^{amph}] + 40.65P(GPa) \quad (6.15)$$

$$T(\text{°C})_{obs} = 0.96T_{calc} + 40 \quad SEE = 47\text{°C} \quad (6.16)$$

And the following clinopyroxene based equation:

$$T(°K) = \frac{93100 + 544P(kbar)}{61.1 + 36.6[Ti^{cpx}] + 10.9[Fe^{cpx}] - 0.95([Al^{cpx}] + [Cr^{cpx}] - [Na^{cpx}] - [K^{cpx}]) + 0.395(\ln(a_{en}^{cpx}))^2} \quad (6.17)$$

$$T(\text{°C})_{obs} = 0.82(T_{calc}(°K) - 273.15) + 61 \quad SEE = 87\text{°C} \quad (6.18)$$

These equations can then be used to calculate a final weighted mean temperature estimate in the same manner as for pressure (Fig. 6.4d). The final temperature range is taken from Eq. 6.18, as this encompasses the temperatures from clinopyroxene and amphibole. A smaller range is also shown in Fig. 6.5 (labelled A), which is the range from amphibole alone. These average *P-T* conditions are consistent with the experimental range of amphibole stability (Fig. 6.5; Ridolfi et al., 2010; Ridolfi and Renzulli, 2012). The variation in calculated *P-T* conditions for each sample is very small, suggesting they all formed under similar conditions, from a magma with a consistent composition. The calculated pressures and temperatures with upper and lower bounds are given in Table 6.2.

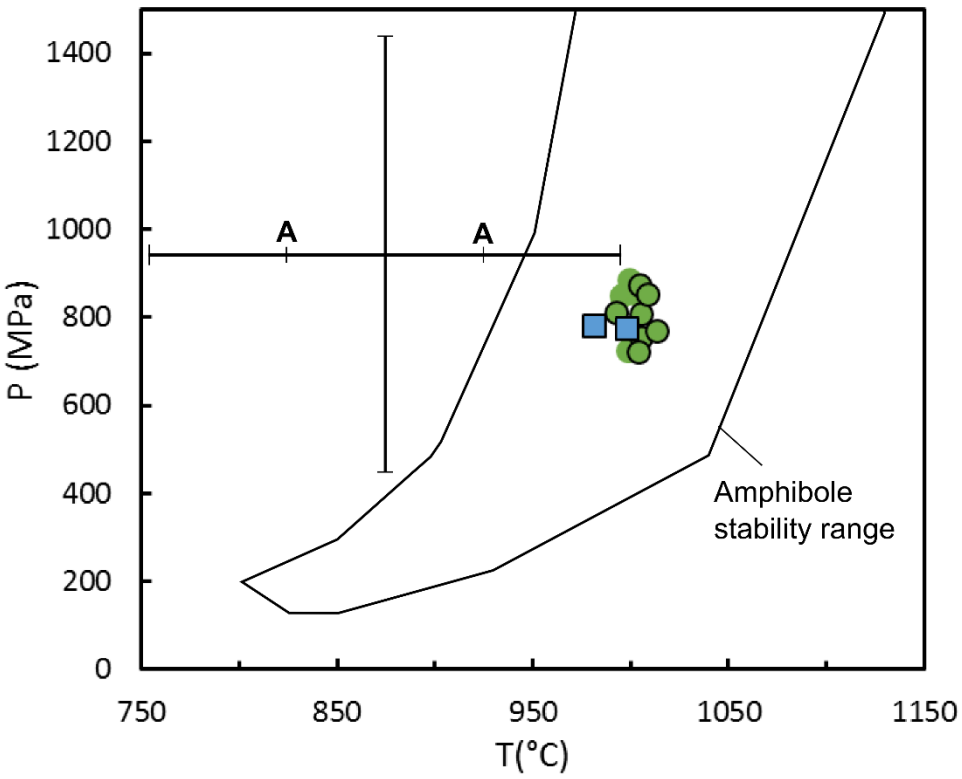

Figure 6.5 *P-T* estimates for southern Lesser Caucasus volcanic rocks

Pressures and temperatures (the horizontal (red) lines in Fig. 6.4) are plotted for all the samples in Figs 6.2 and 6.3. For those samples without clinopyroxene analyses, the pressure and temperature estimates and ranges are derived from amphibole alone. Horizontal error bar is 1σ error for the clinopyroxene estimate (full range) and the amphibole estimate (labelled A). Vertical error bar is the combined 1σ errors from both the amphibole and clinopyroxene estimates. These ranges are explained in more detail in Fig. 6.4 and section 6.5. All samples plot within the amphibole stability field and the *P-T* range of the experimental dataset used for model calibration (Ridolfi and Renzulli, 2012). Symbols for each sample are as in Fig. 6.2.

6.6 Discussion

The substantial errors on estimates of pressure (Figs 6.4 and 6.5) limit the meaningful conclusions one can draw with regard to the absolute depths of crystal fractionation. Estimates of crustal thickness from Sr/Y and La/Yb ratios (see Chapter 3; Hu et al., 2017) suggest the crust below the study area is around 60 km thick. The upper pressure limit in Table 6.2 varies from 1110-1260 MPa, equating to 40-45 km depth, showing that all magmas must stall and fractionate in the crust, rather than stalling below the Moho and fractionating before rapid ascent to the surface. This is unsurprising given that the southern Lesser Caucasus are host to both mafic and felsic igneous rocks. Magmas would not be able to evolve to felsic compositions in the mantle as buoyancy forces would cause magma to ascend into the crust before such a felsic composition was produced (Cox, 1993), or else the

Table 6.2 Calculated pressures (and equivalent depths), temperatures and melt H_2O contents of clinopyroxene and amphibole crystallisation

	Pressure (MPa)	Pressure range	Temperature (°C)	Temperature range	Depth (km)	Depth range	H_2O_{melt} (wt %)*
Amphibole and clinopyroxene							
2-5-08 core	811	244-1194	992	895-1132	29	9-43	7.2
2-5-08 rim	850	247-1242	995	888-1128	31	9-45	8.0
2.6.08 core	810	213-1203	1005	912-1152	29	8-43	6.7
2-6-08 rim	855	219-1261	1002	919-1164	31	8-45	7.2
8-3-15 core	754	183-1137	1005	914-1152	27	7-41	6.4
8-3-15 rim	758	135-1169	1002	896-1139	27	5-42	6.7
11-3-15 core	852	352-1198	1009	924-1154	31	13-43	6.5
11-3-15 rim	725	60-1161	998	874-1120	26	2-42	6.2
9-1-15 core	771	96-1199	1013	916-1164	28	3-43	6.3
9-2-15 core	723	153-1109	1004	902-1140	26	6-40	6.3
Amphibole only							
2-7-08 core	873	435-1396	1005	929-1095	31	16-50	6.7
2-7-08 rim	887	448-1409	999	926-1087	32	16-51	7.0
7-4-15 core	782	343-1306	981	911-1067	28	12-47	7.0
7-5-15 core	776	338-1300	998	930-1084	28	12-47	5.6

*± 14.4% (1σ)

magma would stall and crystallise completely under batch processes.

The minimum pressure estimates are 50-350 MPa, equating to 2-13 km depth. This means that the geobarometry techniques presented here do little more than constrain the depth of magma storage to somewhere within the crust. However, the pressure estimates shown in Fig. 6.5 give the most likely depths of crystal fractionation- probably somewhere in the mid-crust (15-40 km). While it is difficult to constrain the absolute pressures, given that all samples are treated the same, it is worth looking at the relative pressure differences between samples. The difference in pressure estimates between all samples is only around 130 MPa, or around 5 km. This suggests that magma storage occurs in a relatively narrow lens in the mid-crust.

The mean temperature of crystallisation is within error, but slightly lower (~100˚C) than the upper stability limit of amphibole in the mantle (Mandler and Grove, 2016). Given magma generation is occurring in the lithosphere (Neill et al., 2015; Sugden et al., 2019), the magmas may only have to travel a few 10s of km from the mantle source to the location of magma storage. Samples 11-3-15 and 9-2-15 (Tables 6.1 and 6.2) have some of the most mafic bulk rock compositions of any volcanic rocks in the region, with SiO_2 of 47 wt % and MgO of 6 wt %. Such magmas can only have experienced limited fractionation since their formation in the mantle. Magmas ascending from the mantle source will cool adiabatically, and possibly suffer contamination by cool mantle lithosphere domains (Kavanagh and Sparks, 2009), which could explain the small discrepancy between the temperatures calculated here and the amphibole dehydration solidus in the mantle. The temperatures calculated for even the most mafic magmas are sufficiently hot to be consistent with amphibole breakdown melting in the mantle.

As an analogue example, the ascent of kimberlite magmas over 200-400 km may only give a temperature decrease of ~100˚C, even with additional cooling mechanisms such as gas exsolution (Kavanagh and Sparks, 2009). As such the temperatures calculated here for mafic magmas are too low to be explained by melt extraction from the convecting mantle at temperatures of 1300-1400˚C (Priestley et al., 2006). Thus, the *P-T* conditions are consistent with the magma petrogenesis model presented in Chapter 3, whereby magmas are formed within the lithosphere.

The estimated melt H_2O contents (Table 6.2) are 6-8 wt %, which puts them at the upper end of the range typical for arcs (3.5-9 wt %; Ridolfi et al., 2010). This is consistent with the widely observed arc-like bulk-rock geochemistry of Lesser Caucasus volcanic rocks (Neill et al., 2013; Neill et al., 2015; Sugden et al., 2019). That the estimate is towards the upper end of arc rocks may be testament to the low degree of melting modelled for these rocks (see Chapter 3). This is because H_2O is likely to act as an incompatible element (with a similar bulk partition coefficient during mantle melting to Ce; Dixon et al., 2002), such that it will increase in concentration at lower degrees of melting. H_2O/Ce ratios of 300-800 are above the range for MORB (100-300; Dixon et al., 2002), confirming that water was added to the mantle source during a metasomatic event. These H_2O contents are in good agreement with the H_2O content used for the basalt geothermobarometry calculations in Chapter 3 (7 wt %).

The H_2O estimates are substantially higher that the < 2 wt % H_2O contents of olivine-hosted melt inclusions from the Gegham highland (Savov, personal communication). This discrepancy could in part be due to the lower partial melt fraction in the southern Lesser Caucasus, as revealed by the higher concentration of immobile incompatible trace elements such as Nb (Chapter 3). It might also be related to additional metasomatism in the thicker lithosphere below the southern Lesser Caucasus. Geochemical traces of metasomatic apatite in the mantle source are only seen in the south (Chapter 3), and this metasomatism could have added more H_2O (apatite contains OH groups in its structure). It is also possible that the melt inclusions have lost volatiles post-entrapment as can occur even for texturally pristine inclusions (e.g. Wallace et al., 2015).

Five of the samples for which amphibole and clinopyroxene data have been collected, have also had Ar-Ar ages determined (see Chapter 5). A reduced magma flux could reduce the temperature of magmas if any thermal anomaly in the crust derived from magmatism becomes weaker. If there are fewer melt lenses in the crust, magma may ascend more rapidly and stall in different places, giving some pressure variations. A reduced degree of melting might be expected to increase H_2O in the youngest magmas. As can be seen in Fig. 6.6, none of this is observed, suggesting a constant supply rate of hydrous magma throughout the period, consistent with the interpretations in Chapter 5.

6.6.1 Magmatic oxygen fugacity (fO_2) and $Fe^{3+}/\Sigma Fe$

Ridolfi and Renzulli (2012) also calibrated an oxybarometer dependent on amphibole components alone:

$$\begin{aligned}\Delta NNO = {} & 214.39 - 17.042[Si^{amph}] - 26.08[Ti^{amph}] - 16.389[Al^{amph}] \\ & - 18.397[Fe^{amph}] - 15.152[Mg^{amph}] + 0.2162[Ca^{amph}] \\ & + 6.1987[Na^{amph}] + 14.389[K^{amph}] \quad SEE \\ & = 0.37 \log units \quad (6.19)\end{aligned}$$

Oxygen fugacities calculated from this equation range from +1.7 to +3.6 ΔNNO. The bulk of amphibole-based oxygen fugacity estimates from subduction zone volcanoes are between 0 and +2 ΔNNO (Ridolfi et al., 2010). Southern Lesser Caucasus volcanic rocks appear to be highly oxidised, even when compared to arc rocks.

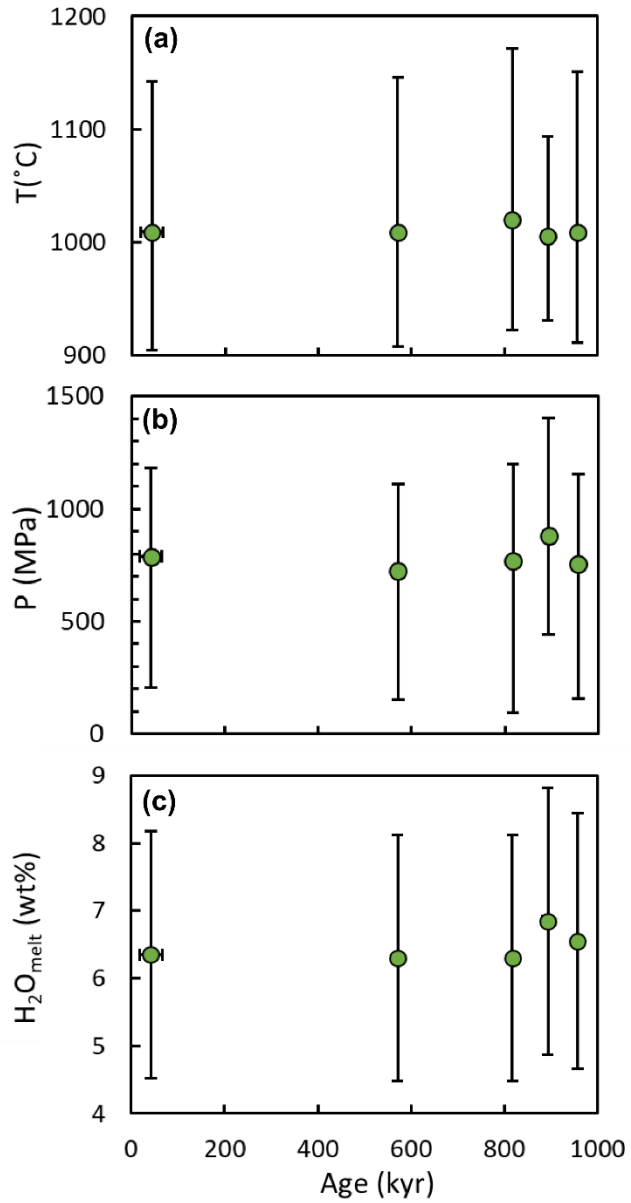

Figure 6.6 Pressure temperature and melt H_2O content *vs* age

5 of the samples in Tables 6.1 and 6.2 also had ages determined, which from left to right are 11-3-15, 9-2-15, 9-1-15, 2-7-08 and 8-3-15. Where age error bars are not visible, they are smaller than the symbol. Values and errors for T, P and H_2O_{melt} are from Table 6.2.

The calculated P-T conditions (Table 6.2; Fig. 6.5) give fO_2 between 6.4 x10^{-9} and 4.7 x10^{-7} bars. The higher ΔNNO estimates give fO_2 values higher than those for the most oxidised experiment used in calibration of Eq. 6.19. The *P-T* conditions given in Table 6.2 are outside the calibration range of the experimental data used for Eq. 6.19, with the data presented here indicating pressures above the maximum pressure. These two issues mean that the ΔNNO estimates for the southern Lesser Caucasus volcanic rocks are an extrapolation of the calibration of Eq. 6.19 and in the words of Ridolfi and Renzulli (2012) "uncertainties of the equations may be higher

(to an unpredictable degree) and we therefore recommend caution in the interpretation of the amphibole crystallisation data." For these reasons the oxybarometry results are not presented in detail.

In Chapter 3, when calculating the *P-T* conditions of magma generation in the mantle, the $Fe^{3+}/\Sigma Fe$ ratio was assumed to be 0.25. It is possible to calculate the likely $Fe^{3+}/\Sigma Fe$ ratio from the output of Eq. 6.19 using the formulations of Kress and Carmichael (1991). This requires an estimate of the melt composition in equilibrium with the amphibole. Using an equation which relates amphibole composition and magma temperature to SiO_2 content (Putirka, 2016) provides an initial constraint. Harker diagrams of southern Lesser Caucasus volcanic rocks are used to constrain the other major elements, in a similar manner to that in Appendix B, but for a specific SiO_2 rather than MgO content. This rough melt composition estimate introduces further uncertainties into the $Fe^{3+}/\Sigma Fe$ calculation.

This calculation suggests $Fe^{3+}/\Sigma Fe$ could range from 0.36 to 0.56. The 0.25 estimate used in Chapter 3 is likely to have been an underestimate. If a value of 0.46 is taken, calculated *P-T* conditions of magma generation (see Chapter 3; Plank and Forsyth, 2016) are 1.9 GPa (~70 km depth) and 1155˚C. The underestimate of $Fe^{3+}/\Sigma Fe$ only effects the depth of melting estimate by 5-10 km. The temperature is close to the upper stability limit of amphibole in the mantle (Mandler and Grove, 2016). The slightly shallow depth of melting is still within ~ 5 km of the spinel-garnet transition (Robinson and Wood, 1998), consistent with trace element evidence.

Highly oxidised magmas are consistent with the subduction-modified mantle source clearly identified in Chapters 3 and 4 (Brounce et al., 2014). The high oxygen fugacity is comparable to low volume alkaline magmas from the Western Mexico volcanic belt and may be a result of the metasomatic phases which contribute to magma generation (Carmichael et al., 1996). Both Western Mexico and the Southern Lesser Caucasus have an unusually wide range of fO_2, perhaps reflective of small-scale heterogeneity in the mantle source.

6.7 Conclusions

The depth of magma fractionation is relatively poorly explained but is most likely to occur in the mid-crust (15-40 km) depth. The homogeneity of amphibole and clinopyroxene phenocrysts between samples suggests that melt lenses will have occupied a narrow depth interval of perhaps only 5 km somewhere in this range. Temperatures are much better constrained as being close to 1000°C, which is consistent with the model presented in Chapter 3 of amphibole dehydration melting in the lithosphere forming these magmas. Melt H_2O contents are consistent with a subduction-modified mantle source, and also potentially with the low degree of melting suggested by non-modal batch melting modelling. The very high oxygen fugacity suggests an oxidised mantle source which is consistent with subduction modification and the presence of metasomatic minerals such as amphibole in the source.

7. Discussion and Conclusions

7.1 A holistic model of volcanism in the southern Lesser Caucasus

The southern Lesser Caucasus is a region which has not seen subduction of an oceanic slab since at least 25 Ma (Okay et al., 2010; Rolland et al., 2012). In the introduction to this thesis a central question was posed: why are there such numerous volcanoes in the southern Lesser Caucasus? Synthesising the results and interpretations presented in Chapters 3 to 6 makes it possible to answer that question. The holistic model of volcanism presented here (Figs 7.1 and 7.2) threads a geological history from mantle metasomatism to the volcanic eruptions at the surface. As well as explaining how magma is generated, the model explores why the volcanoes are so numerous- why do we observe lots of monogenetic centres (183 in Syunik volcanic highland alone) rather than a few polygenetic ones? Figures 7.1 and 7.2 present the model in two stages. The first stage (Fig. 7.1) shows how a subduction signature is imparted during oceanic subduction and then stored in metasomatic amphibole in the lithosphere. The second stage (Fig. 7.2) is the currently operating post-collision episode and concerns how and where magma is generated, how it evolves during storage in the crust, and how it interacts with tectonic forces and structures in the upper crust to produce the southern Lesser Caucasus volcanic phenomena.

The 6-8 wt % water in magmas- calculated using amphibole hygrometry (Chapter 6), show that the post-collisional mantle source is hydrated and must have been metasomatised. The volcanic rocks have an arc-type geochemistry, with enrichments in large-ion lithophile elements (LILE) and light rare earth elements (LREE) and depletions in high field strength elements (HFSE) giving positive spikes in Ba, K, Pb and Sr, and negative Nb-Ta and Ti anomalies on MORB normalised incompatible trace element diagrams (Fig. 3.5). These geochemical signatures suggest the metasomatising agent was a subduction component. The heavier $\delta^{11}B$ signature when compared to ultra-potassic volcanic rocks from Western Anatolia (Fig. 4.5), as well as the similar Sr-Nd-B isotope composition of post-collisional volcanic rocks and 41 Ma samples from the nearby Tezhsar alkaline complex (Fig. 4.6), suggests that this subduction component is inherited from previous subduction which occurred at least 40 Myr ago. There is no evidence for a stalled slab releasing

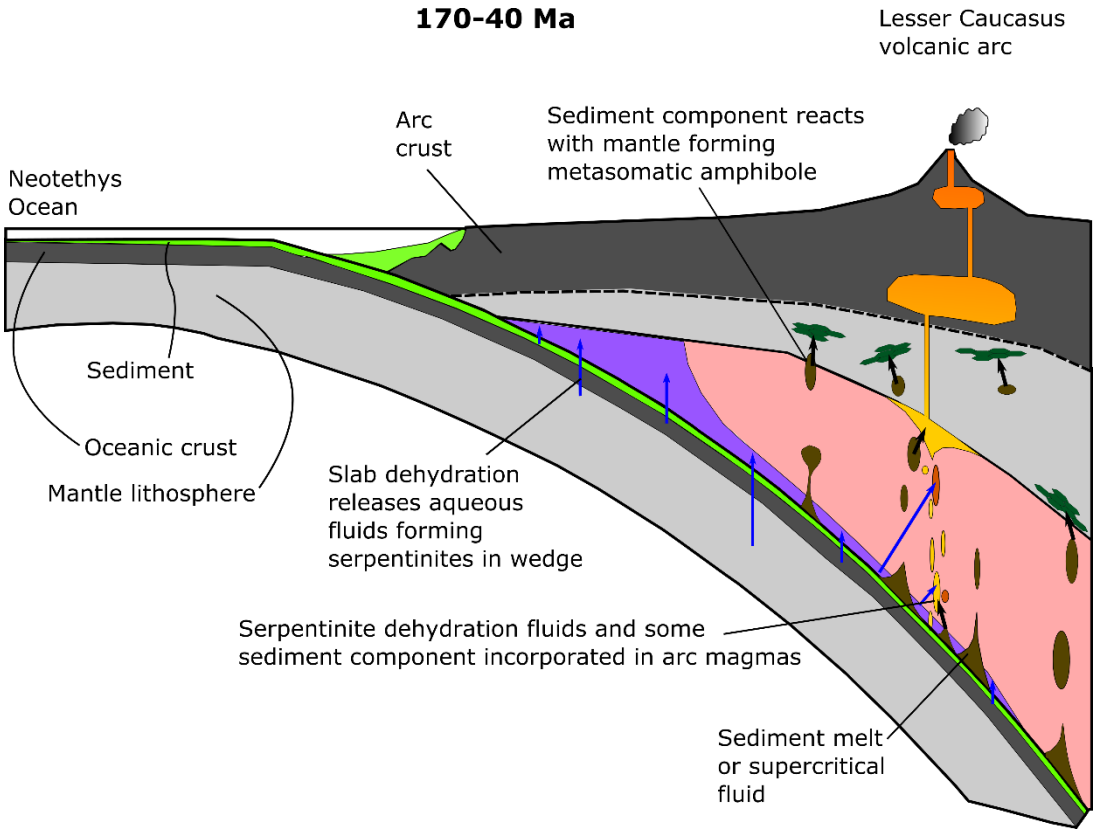

Figure 7.1 First stage of the holistic model for volcanism in the southern Lesser Caucasus (pre-collision)

The first stage is pre-collision (subduction) when the mantle source is metasomatised to reduce its melting temperature. Blue arrows show the transfer of aqueous fluid from altered oceanic crust and sediments to serpentinites and then arc magmas. The brown diapirs (labelled sediment melts or supercritical fluids) are the second slab component, some of which enter arc magmas, and some of which metasomatise the lithosphere of the overriding plate. The sediment melts/supercritical fluids are incorporated into metasomatic amphibole as shown by the black arrows and green crystals.

increasingly refractory components to the mantle source after the end of subduction, as has been suggested in Western Anatolia, resulting in the very light $\delta^{11}B$ observed there (Tonarini et al., 2005; Agostini et al., 2008).

Prior to the continent-continent collision between Arabia and Eurasia, the two continents were separated by the Neotethys Ocean (Rolland, 2017). The Neotethys oceanic lithosphere and accompanying sediments constituted a subduction package that was consumed along a series of trenches that delineated (mostly north dipping) subduction zones (see Chapter 2). The presence of Mesozoic and Paleogene arc-related volcanic rocks confirms that the Lesser Caucasus itself was previously a region of active subduction (Mederer et al., 2013). Figure 7.1 shows how Tethyan subduction imparted a slab signature which is inherited by post-

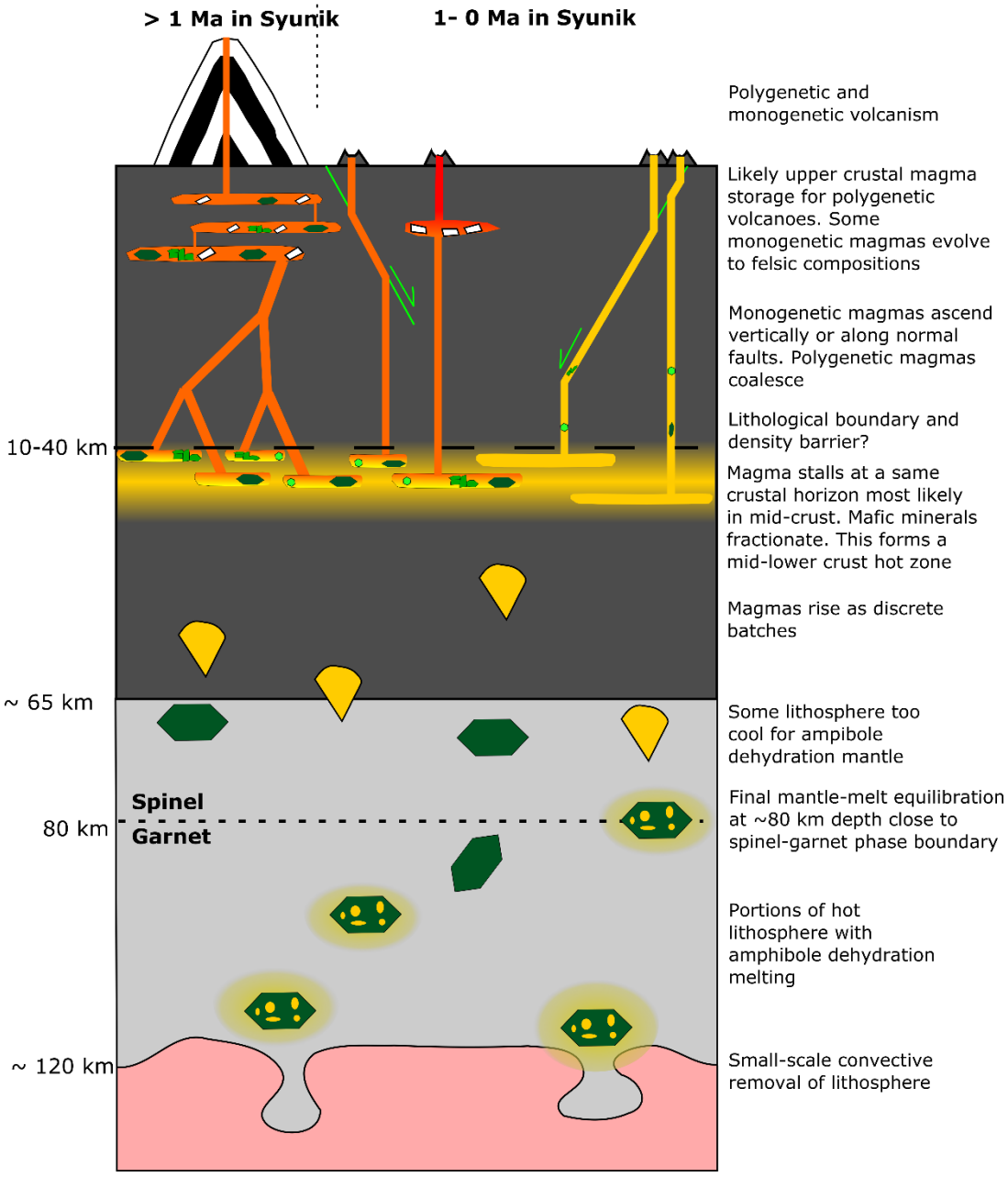

Figure 7.2 Second stage of the holistic model for volcanism in the southern Lesser Caucasus (post-collision)

The second stage is post-collision and involves magma generation, crystal fractionation and volcanic eruptions. Amphibole dehydration melting occurs in the lithosphere and is represented here by the green crystals with pockets of melt forming. This melting occurs in response to heating of the lithosphere either by convective removal of its base or in hot zones in the interior of the lithosphere generated by relaxation of non-linear geothermal gradients (Sugden et al., 2019; see also Chapter 3). Magmas then ascend into the crust until they stall at a regular horizon, which is probably a lithological boundary somewhere in the mid-crust (as shown by amphibole/clinopyroxene barometry). Here the mafic minerals amphibole, clinopyroxene and probably olivine fractionate. On the left the polygenetic case of volcanism is shown with magmas ascending from the mid-crust and dyke coalescence and upper crustal magma storage. The monogenetic volcanoes on the right are fed by vertical dykes, as well as dykes which follow normal faults. These faults can form clusters of volcanoes by focussing magma close to the fault's surface outcrop. Some monogenetic magmas probably stall in the upper crust to further fractionate and eventually evolve to more felsic compositions. Here, plagioclase feldspar also fractionates.

collisional volcanoes.

For the subduction component to be stored for millions of years after the end of subduction, it must have resided in the mantle lithosphere below the Lesser Caucasus, which at that time was part of the overriding plate of this convergent margin (Fig. 7.1). The higher temperatures of the convecting mantle would have led to melting and removal of this subduction component (Pearce, 1982; Pearce and Peate, 1995; Grove et al., 2012). The lower temperatures in the lithospheric mantle stabilise metasomatic minerals which can store the subduction component. Given the high water contents of southern Lesser Caucasus magmas, this mineral is likely to be hydrous with possibilities including amphibole, apatite and phlogopite. An inherited subduction component in some of the Western Mexico volcanoes is predominantly stored in phlogopite for example (Carmichael et al., 1996).

In the southern Lesser Caucasus this mineral appears to be predominantly amphibole, on the basis of the low Rb/Sr (Fig. 3.18) and Dy/Dy* (Fig. 4.7) in post-collisional volcanic rocks. The heavy $\delta^{11}B$ signature of both arc magmas and aqueous fluids in subduction zones are not observed in the post-collisional volcanic rocks (see Chapter 4). Aqueous fluids (blue arrows in Fig. 7.1) are transitory and do not contribute to the subduction component of the post-collisional mantle source. Southern Lesser Caucasus samples are marked by low $^{143}Nd/^{144}Nd$, despite Nd being a relatively immobile element- evidence of a melt or supercritical fluid transporting the subduction component from a radiogenic source (i.e. sediment).

To summarise this first stage of the model, sediment melts (or supercritical fluids) react with the mantle lithosphere precipitating metasomatic amphibole which is able to store a subduction component. This all occurred at least 40 Myr ago - at some point during the Mesozoic-Paleogene subduction of the Neotethys Ocean along a volcanic arc in the Lesser Caucasus.

Following continent-continent collision, heating-induced amphibole breakdown leads to dehydration melting in the mantle lithosphere (Fig. 7.2). Trace element modelling is consistent with amphibole being a residual phase during magma generation (Chapter 3). Magmatic amphibole crystallisation temperatures are just 100°C below the amphibole stability limit for some of the most mafic samples (see Chapter 6). The mechanism of heating is thought to be small-scale convective removal at the lithosphere-asthenosphere boundary and/or relaxation of

non-linear geothermal gradients in the interior of the mantle lithosphere (Sugden et al., 2019). In Chapter 3, it was argued that the non-linear geothermal gradient resulted from underthrusting of the Arabian lithosphere. However, as Chapter 4 and Fig. 7.1 illustrate, the subduction component must have been stored in the Eurasian mantle lithosphere. We are likely looking at a section of Eurasian lithosphere which during convergence and thickening has developed a complex geotherm. It could also be a simpler case that initial collision buried colder lithospheric mantle to greater depths, where heating to amphibole breakdown temperatures releases water and triggers melting. 1% partial melting of a mixed spinel-garnet peridotite source occurs at around 75 km depth. It is unclear whether this depth represents polybaric magma-mantle separation between the base of the lithosphere and the Moho, or whether it represents the final mantle-melt equilibration depth.

Low degrees of melting may mean that it takes a substantial amount of time for small pockets of magma to coalesce into a body of sufficient volume to be buoyant and eventually ascend through the crust (Fig. 7.2). The low frequency of eruptions (in Syunik there is one eruption roughly every 5500 years, see Chapter 5) suggests that there is unlikely to be continuous magma connectivity between the surface and the zone of mantle melting (Fedotov, 1981; Smith and Németh, 2017). Instead magma is likely to ascend through the crust as discrete batches (Fig. 7.2). The small volume of these magma batches is probably consistent with the Sr-Nd isotope evidence for the lack of assimilation of continental crust (Chapter 3). It is also possible that other post-collisional magmas which solidified at depth have provided an “armour” for newly ascending magmas, such that they do not come into contact with crustal rocks of distinct isotope compositions.

During their ascent, the magmas stall and fractionate mafic minerals including amphibole and clinopyroxene (Fig. 7.2). The very similar pressures calculated for amphibole and clinopyroxene crystallisation in different samples suggests that all magmas stall at a similar depth interval (see Chapter 6). This interval could be controlled by a density or rheological interface due to a change in lithology, which initially prevents magmas ascending further. Unfortunately, due to the large errors involved in the amphibole and clinopyroxene geobarometry it is not possible to constrain this depth accurately, but it is most likely to be in the mid-crust (10-40 km).

The ascent of magmas from this storage depth to the surface has varied during the Quaternary evolution of the southern Lesser Caucasus. In Syunik prior to 1 Ma, volcanic eruptions produced large polygenetic edifices. Magmas did not ascend vertically, such that dykes coalesced, probably forming an upper crustal hot zone (Annen et al., 2015) and a stable magma plumbing system (Fig. 7.2). Ar-Ar ages show that in Vardenis and Syunik volcanic highlands after 1 Ma, volcanism was exclusively monogenetic. In Chapter 5, it was argued that this is a result of local extension of the crust. Extension is likely to lead to dykes forming vertically, all else being equal (Takada, 1994a; Takada, 1994b). Some magmas encounter normal faults and ascend along these planes instead. This latter ascent path will cluster volcanoes close to the surface expression of faults, as seen by the association of monogenetic volcanoes with pull-apart basins.

Many magmas ascend rapidly to the surface, erupting mafic compositions. Some of the monogenetic volcanoes also have felsic compositions, which probably requires further magma fractionation given the lack of Sr-Nd isotope evidence for crustal contamination. It is assumed that the magmas which supplied those volcanoes must have stalled in the upper crust and fractionated further (Fig. 7.2). Such fractionation would produce a very large volume of cumulates. The presence of granitic xenoliths in one of the scoria cones (see Chapter 3) shows there is a plutonic complement to volcanism, and that a substantial amount of storage and fractionation of magma is occurring in the crust below the Lesser Caucasus. It is also possible that these rhyolites represent partial melts of basalts and andesites which previously froze before erupting in the crust.

To summarise, the southern Lesser Caucasus magma source was metasomatised at >40 Ma during oceanic subduction which preceded the Arabia-Eurasia collision. Sediment melts or supercritical fluids were the metasomatic agent which reacted with peridotite in the mantle lithosphere to form zones enriched in amphibole. These amphiboles stored a subduction component until heating of the lithosphere after continental collision led to amphibole dehydration, and as a consequence low degree (~1%) partial melting at ~ 75 km depth. The magmas generated then accumulated into bodies which were able to ascend into the crust, where they stalled at a lithological barrier. Fractionation of olivine, clinopyroxene and amphibole was followed by further magma ascent and eruption at the surface.

Volcanism has predominantly taken the form of large numbers of monogenetic volcanoes (n=183 in Syunik) because localised extension has prevented dyke coalescence and allowed each eruption to form a new vent.

7.2 Comparison with magmatism elsewhere in the Arabia-Eurasia collision zone

This section will explore how the holistic model of volcanism in the southern Lesser Caucasus fits into the overall picture of magmatism across the Turkish-Iranian Plateau. As described in the Introduction, to the west of the Lesser Caucasus are the volcanoes of eastern Anatolia, which formed above a thin lithospheric lid (Şengör et al., 2003; Al-Lazki, 2003). To the south-east are the Zagros mountains and NW Iran, a region of more sporadic volcanism over a very thick lithosphere (Priestley et al., 2012).

Evidence for crustal contamination of mantle-derived magmas shows an east-west split across the plateau. The mantle-like radiogenic isotope ratios of Sr and Nd reported in this thesis (Chapter 3) match the compositions observed in the northern Lesser Caucasus and NW Iran (Neill et al., 2013; Allen et al., 2013; Neill et al., 2015). However, to the west in eastern Anatolia, there is widespread isotopic evidence for crustal contamination playing a major role in petrogenesis (Pearce et al., 1990; Buket and Temel, 1998; Şen et al., 2004; Keskin et al., 2006). Eastern Anatolia is also distinct as the only region which hosts OIB-type alkaline igneous rocks, with no subduction signature. Such rocks are largely found in south-eastern Anatolia in the Lake Van region (Pearce et al., 1990; Keskin, 2003; Di Giuseppe et al., 2017).

Both the OIB-type magmas and the increased role for crustal contamination in eastern Anatolia can be explained by the region's thin lithosphere. The East Anatolian Accretionary Complex crust sits almost directly on convecting mantle (Keskin, 2003; Keskin, 2007), and can be expected to have a higher heat flow and steeper geotherm. The higher temperatures expected will help ascending magmas to melt and assimilate portions of the crust during their ascent. With regard to the subduction signatures observed in the southern Lesser Caucasus and elsewhere in the collision zone (Pearce et al., 1990; Keskin et al., 1998; Allen et al., 2013; Neill et

al., 2013; Neill et al., 2015; Ghalamghash et al., 2016), they might only be found in magmas derived from the lithospheric mantle. Here, lower temperatures stabilise metasomatic phases such as amphibole, which are able to store a component from earlier oceanic subduction that is inherited by the post-collisional magmas. Continuous convection and high temperatures will make such long term storage impossible in the asthenosphere. In the Lake Van region, where the mantle lithosphere is thought to be very thin, the convecting mantle may be able to upwell to sufficiently shallow depths that it can undergo low degree decompression melting, producing OIB-type magmas. Where the lithosphere is thicker, this is not possible, and magmas are derived from the lithosphere instead, producing magmas containing a subduction signature.

In some cases where the lithosphere is thin, but a mantle lithosphere is still retained, magmas may originate in both the asthenosphere and the lithosphere. Initial magmas generated by decompression melting may be contaminated by lithospheric melts on their ascent to the crust. This might be the case for some lavas to the north of Lake Van, which have muted slab signatures (Oyan et al., 2017).

The predominantly monogenetic character of recent volcanism in the southern Lesser Caucasus contrasts with the large polygenetic volcanoes of Nemrut, Süphan, Tendürek and Ararat in eastern Anatolia. This difference in style of volcanic activity appears to have more to do with a greater degree of localised extension in the Lesser Caucasus than a lower magma supply. That said, monogenetic volcanism in NW Iran is not associated with any local pull-apart structures (Allen et al., 2013). In this region of thickest lithosphere (>200 km; Priestley et al., 2012), magma supply is probably the limiting factor. In the Lesser Caucasus, a decrease in the degree of melting accompanies an increase in lithospheric thickness from north to south (Chapter 3; Sugden et al., 2019). As such, although a low shear wave velocity is observed at ~ 100 km depth across the Plateau (Maggi and Priestley, 2005), the volumes of magma produced are likely to reduce as lithosphere thickness increases.

The Arabia-Eurasia collision zone provides a unique opportunity to investigate post-collisional magmatism. Their Quaternary age allows volcanic rocks to be contextualised in terms of the lithosphere structure in the region of magma genesis. Thinner lithosphere in the west results in a greater amount of crustal

contamination, a higher rate of magma production, more OIB-type, and less arc-type volcanic rocks.

7.3 Suggestions for further study

Interpretations of where magma was generated in Chapter 3 were hampered by the resolution of the geophysical observations. Previous geophysical studies show a relatively low density of seismic stations in the vicinity of the southern Lesser Caucasus (e.g. Gök et al., 2011). Future studies of magma generation processes in the Lesser Caucasus would be helped by a higher spatial resolution tomography and/or receiver function study of the local crustal and lithospheric structure using a denser seismic station array. The Armenian National Academy of Sciences has already deployed such an array. The results of that study will provide important constraints to test the melting model as presented in Chapter 3. If the depths of the lithosphere-asthenosphere boundary, Moho, and melt generation can all be constrained more precisely than has hitherto been achieved, then it would be possible to say with more confidence whether magma formed at the base of the lithosphere, in the middle of the mantle lithosphere or at the base of the crust. Such geophysical constraints would also help to better constrain the meaning of the melting depth calculated from basalt geothermobarometry. Does it represent the average depth of polybaric melting, or the final depth of mantle-melt equilibration?

The understanding of the boron isotope composition of post-collisional volcanic rocks (Chapter 4) would be improved by analysing Mesozoic-Paleogene arc rocks as a comparison. If there is only a fluid component in the arc rocks, and not the post-collisional samples, then it might be expected we would see a heavier $\delta^{11}B$ signature and higher [B] in the arc samples.

A good check on the argument presented in this thesis that the subduction component in the southern Lesser Caucasus is inherited from oceanic subduction would be to measure the activity ratios of U-Th series isotopes. Any deviation from secular equilibrium (activity ratios of 1), as has been observed in volcanic arcs (Turner et al., 2000), would suggest the subduction component is much younger and cannot have been inherited from oceanic subduction > 40 Myr ago.

As discussed in Section 7.2, this subduction component is likely to be inherited widely across the collision zone. An exception is likely to be the Lake Van region where OIB-type alkaline lavas are erupted. If alkaline magmas have really not been influenced by subduction processes they should have $\delta^{11}B$ similar to MORB or OIB (-10 to -7‰; Marschall et al., 2017; Walowski et al., 2019). It would also be interesting to select samples of various ages from the region and look at the evolution of boron isotopes over time as evidence of slab break-off. Would the very light $\delta^{11}B$ seen in Western Anatolia volcanic rocks (Tonarini et al., 2005) be observed in the Lake Van region?

In Chapter 5, the transition from polygenetic to monogenetic volcanism in the Syunik volcanic highland was argued to be the result of increased rates of crustal extension. A key point of the discussion was that the magma supply appears to have been consistent across the transition. This argument could be strengthened by estimating the volumes of lava flows in Syunik over time using the geological map shown in Chapters 2 and 5 and a high resolution digital elevation model. This would show whether the eruptive flux, and thus the magma supply has changed with time.

The Holocene volcanoes in Syunik are being investigated as a site with geothermal energy potential. A better understanding of the subsurface structure of the southern Lesser Caucasus volcanic field would help us to understand more about magma plumbing systems in this region. Understanding magma storage in the Lesser Caucasus could help determine whether this and other young volcanoes in the region offer potential as geothermal energy sites, and how best to exploit this potential. Geothermobarometry using amphibole, clinopyroxene and plagioclase could be used to establish how hot the magma was and the depths at which it was stored. Diffusion modelling could also be used to look at the timescales of magma storage. A longer period of magma storage of several years might be more likely to have a cumulate or plutonic reservoir associated with it, which is still supplying heat to the surrounding crust today.

The diverse range of young and well preserved volcanic structures, and high-quality geochemical data have made the southern Lesser Caucasus an exceptional natural laboratory for improving our understanding of volcanism in post-collisional settings. This thesis has provided a foundational understanding of various aspects of magmatism, from evolution of the magma source, to the formation of monogenetic

volcanoes. Even so, the southern Lesser Caucasus remain exceptionally fertile ground for future research into many aspects of contemporary magma petrogenesis and volcanology in an active continent-continent collision.

The case for further research is not merely scientific; there is also a strong impetus with regards to the socio-economic impacts of any future eruption. Over 1 million people living in the city of Yerevan, just 50 km from the southern Lesser Caucasus. The road to Armenia's southern border with Iran represents a vital trade link for the country, but it passes right through both the Syunik and Vardenis highlands, within a few kilometres of Holocene lava flows. Were this road to be blocked by lava flows, or closed due to a nearby eruption, the impact on the Armenian economy could be substantial. It is vital that researchers continue to improve our understanding of post-collisional volcanism in the region, so that the risk it poses to both the local population and economy can be assessed as well as possible.

List of References

Agostini, S., Ryan, J.G., Tonarini, S. and Innocenti, F. 2008. Drying and dying of a subducted slab : Coupled Li and B isotope variations in Western Anatolia Cenozoic Volcanism. *Earth and Planetary Science Letters*. **272**, pp.139–147.

Al-Lazki, A.I. 2003. Tomographic Pn velocity and anisotropy structure beneath the Anatolian plateau (eastern Turkey) and the surrounding regions. *Geophysical Research Letters*. **30**(24), pp.4–7.

Allen, M.B., Kheirkhah, M., Neill, I., Emami, M.H. and McLeod, C.L. 2013. Generation of arc andwithin-plate chemical signatures in collision zone magmatism: Quaternary lavas from kurdistan province, Iran. *Journal of Petrology*. **54**(5), pp.887–911.

Angus, D.A., Wilson, D.C., Sandvol, E. and Ni, J.F. 2006. Lithospheric structure of the Arabian and Eurasian collision zone in eastern Turkey from S-wave receiver functions. *Geophysical Journal International*. **166**(3), pp.1335–1346.

Annen, C., Blundy, J.D., Leuthold, J. and Sparks, R.S.J. 2015. Construction and evolution of igneous bodies: Towards an integrated perspective of crustal magmatism. *Lithos*. **230**, pp.206–221.

Arutyunyan, E. V., Lebedev, V.A., Chernyshev, I. V. and Sagatelyan, A.K. 2007. Geochronology of Neogene-Quaternary volcanism of the Geghama Highland (Lesser Caucasus, Armenia). *Doklady Earth Sciences*. **416**(1), pp.1042–1046.

Aspinall, W., Charbonnier, S., Connor, C.B., Connor, L.J., Costa, A., Courtland, L., Delgado Granados, H., Hibino, K., Hill, B., Komorowski, J.C., McNutt, S., Meliksetian, K., Nakada, S., Newhall, C., Samaddar, S., Savov, I.P., Self, S., Uchiyamer, Y., Wilson, T. and Yamamoto, T. 2016. *Volcanic Hazard Assessment for Nuclear Installations: Methods and Examples in Site Evaluation.* International Atomic Energy Agency TECDOC series, 1795.

Aydinçakir, E. and Sen, C. 2013. Petrogenesis of the post-collisional volcanic rocks from the Borçka (Artvin) area: Implications for the evolution of the Eocene magmatism in the Eastern Pontides (NE Turkey). *Lithos*. **172**, pp.98–117.

Baghdasaryan, G.P. and Ghukasyan, R.K. 1985. *Geochrnology of magmatic, metamorphic and ore formations of Armenian SSR*. Yerevan: Academy of Sciences of Armenian soviet socialist republic.

Le Bas, M.J., Le Maitre, R.W., Streckeisen, A. and Zanettin, B. 1986. A chemical classification of volcanic rocks based on the total alkali-silica diagram. *Journal of Petrology*. **27**(3), pp.745–750.

Bebout, G.E. and Nakamura, E. 2003. Record in metamorphic tourmalines of subduction-zone devolatilization and boron cycling. *Geology*. **31**(5), pp.407–410.

Brenan, J.M., Neroda, E., Lundstrom, C.C., Shaw, H.F., Rverson, F.J. and Phinney, D.L. 1998. Behaviour of boron, beryllium, and lithium during melting and crystallization: constraints from mineral-melt partitioning experiments. *Geochimica et Cosmochimica Acta*. **62**(12), pp.2129–2141.

Brounce, M.N., Kelley, K.A. and Cottrell, E. 2014. Variations in Fe3+/∑Fe of Mariana Arc Basalts and MantleWedge fO2. *Journal of Petrology*. **55**(12), pp.2513–2536.

Bucchi, F., Lara, L.E. and Gutiérrez, F. 2015. The Carrán-Los Venados volcanic field and its relationship with coeval and nearby polygenetic volcanism in an intra-arc setting. *Journal of Volcanology and Geothermal Research*. **308**, pp.70–81.

Buket, E. and Temel, A. 1998. Major-element, trace-element, and Sr-Nd isotopic geochemistry and genesis of Varto (Mus) volcanic rocks, Eastern Turkey. *Journal of Volcanology and Geothermal Research*. **85**, pp.405–422.

Bürgmann, R. and Dresen, G. 2008. Rheology of the Lower Crust and Upper Mantle: Evidence from Rock Mechanics, Geodesy, and Field Observations. *Annual Review of Earth and Planetary Sciences*. **36**, pp.531–567.

Carmichael, I.S.E., Lange, R.A. and Luhr, J.F. 1996. Quaternary minettes and associated volcanic rocks of Mascota, western Mexico: A consequence of plate extension above a subduction modified mantle wedge. *Contributions to Mineralogy and Petrology*. **124**(3–4), pp.302–333.

Carmichael, I.S.E., Nicholls, J. and Smith, A.L. 1970. Silica activity in igneous rocks. *American Mineralogist*. **55**(1–2), pp.246–263.

Castillo, P.R. 2012. Adakite petrogenesis. *Lithos*. **134**, pp.304–316.

Chernyshev, I. V., Lebedev, V.A., Arakelyants, R.T., Jrbashian, R.T. and Ghukasyan, Y. 2002. Geochronology of the Aragats volcanic centre, Armenia: evidence from K-Ar dating. *Doklady Earth Sciences*. **384**, pp.393–398.

Chiaradia, M., Müntener, O., Beate, B. and Fontignie, D. 2009. Adakite-like volcanism of Ecuador: Lower crust magmatic evolution and recycling. *Contributions to Mineralogy and Petrology*. **158**(5), pp.563–588.

Cladouhos, T.T. and Marrett, R. 1996. Are fault growth and linkage models consistent with power-law distributions of fault lengths? *Journal of Structural Geology*. **18**(2–3), pp.281–293.

Connor, C.B., Connor, L., Halama, R., Meliksetian, K. and Savov, I. 2011. *Volcanic Hazard Assessment of the Armenia Nuclear Power Plant Site , Final Report*. Tampa, FL, USA; Leeds, UK; Yerevan, Armenia.

Connor, C.B. and Conway, F.M. 2000. Basaltic Volcanic Fields *In*: H. Sigurdsson, B. Houghton, S. R. McNutt, H. Rymer and J. Stix, eds. *Encyclopedia of Volcanoes*. San Diego, USA; Waltham, USA: Academic Press, pp.331–343.

Connor, L.J., Connor, C.B., Meliksetian, K. and Savov, I. 2012. Probabilistic approach to modeling lava flow inundation: a lava flow hazard assessment for a nuclear facility in Armenia. *Journal of Applied Volcanology*. **1**(1), p.3.

Cottrell, E. and Kelley, K.A. 2011. The oxidation state of Fe in MORB glasses and the oxygen fugacity of the upper mantle. *Earth and Planetary Science Letters*. **305**, pp.270–282.

Cox, K.G. 1993. Continental Magmatic Underplating. *Philosophical Transactions of the Royal Society A: Mathematical, Physical and Engineering Sciences*. **342**(1663), pp.155–166.

Davidson, J., Hassanzadeh, J., Berzins, R., Stockli, D.F., Bashukooh, B., Turrin, B. and Pandamouz, A. 2004. The geology of Damavand volcano, Alborz Mountains, northern Iran. *Bulletin of the Geological Society of America*. **116**(1–2), pp.16–29.

Davidson, J., Turner, S., Handley, H., Macpherson, C. and Dosseto, A. 2007. Amphibole 'sponge' in arc crust? *Geology*. **35**, pp.787–790.

Davidson, J., Turner, S. and Plank, T. 2013. Dy / Dy *: Variations Arising from Mantle Sources and Petrogenetic Processes. *Journal of Petrology*. **54**(3), pp.525–537.

Defant, M.J. and Drummond, M.S. 1990. Derivation of some modern arc magmas by melting of young subducted lithosphere. *Nature*. **347**(6294), pp.662–665.

Dewey, J.F., Hempton, M.R., Kidd, W.S.F., Saroglu, F. and Sengor, a. M.C. 1986. Shortening of continental lithosphere: the neotectonics of Eastern Anatolia -- a young collision zone. *Geological Society, London, Special Publications*. **19**(1), pp.1–36.

Dixon, J.E., Leist, L., Langmuir, C. and Schilling, J.G. 2002. Recycled dehydrated lithosphere observed in plume-influenced mid-ocean-ridge basalt. *Nature*. **420**(6914), pp.385–389.

Ercan, T., Fujitami, T., Madsuda, J.-I., Notsu, K. and Ui, T. 1990. Doğu ve Güneydoğu Anadolu Neojen-Kuvaterner volkanitlerine ilişkin yeni jeokjmyasal, radyometrik ve izotopik verilerin yorumu. *Maden Tetkik ve Arama Dergisi*. **110**.

Ershov, A. V and Nikishin, A.M. 2004. Recent geodynamics of the Caucasus-Arabia-East Africa region. *Geotectonics*. **38**(2), pp.123–136.

Fedotov, S.A. 1981. Magma rates in feeding conduits of different volcanic centres. *Journal of Volcanology and Geothermal Research*. **9**, pp.379–394.

Foster, G.L. 2008. Seawater pH, pCO2 and [CO2-3] variations in the Caribbean Sea over the last 130 kyr: A boron isotope and B/Ca study of planktic foraminifera.

Earth and Planetary Science Letters. **271**(1–4), pp.254–266.

Frost, D.J. 2006. The stability of hydrous mantle phases *In*: H. Keppler and J. R. Smyth, eds. *Reviews in Mineralogy and Geochemistry vol. 62: 'Water in Nominally Anhydrous Minerals'*. Chelsea, USA: Geochemical Society and the Mineralogical Society of America, pp.243–271.

Furman, T. and Graham, D. 1999. Erosion of lithospheric mantle beneath the East African Rift system: Geochemical evidence from the Kivu volcanic province *In*: *Developments in Geotectonics*. Elsevier, pp.237–262.

Galoyan, G., Rolland, Y., Sosson, M., Corsini, M., Billo, S., Verati, C. and Melkonyan, R. 2009. Geology, geochemistry and Ar/Ar dating of Sevan ophiolites (Lesser Caucasus, Armenia): evidence for Jurassic back-arc opening and hot spot event between the South Armenian Block and Eurasia. *Journal of Asian Earth Sciences*. **34**, pp.135–153.

Garbe-Schönberg, C. 1993. Simultaneous determination of thirty-seven trace elements in twenty-eight international rock standards by ICP-MS. *Geostandards Newsletter*. **17**, pp.81–97.

Gevorgyan, H., Repstock, A., Schulz, B., Meliksetian, K., Breitkreuz, C. and Israyelyan, A. 2018. Decoding a post-collisional multistage magma system: The Quaternary ignimbrites of Aragats stratovolcano, western Armenia. *Lithos*. **318**, pp.267–282.

Ghalamghash, J., Mousavi, S.Z., Hassanzadeh, J. and Schmitt, A.K. 2016. Geology, zircon geochronology, and petrogenesis of Sabalan volcano (northwestern Iran). *Journal of Volcanology and Geothermal Research*. **327**, pp.192–207.

Ghalamghash, J., Schmitt, A.K. and Chaharlang, R. 2019. Age and compositional evolution of Sahand volcano in the context of post-collisional magmatism in northwestern Iran: Evidence for time-transgressive magmatism away from the collisional suture. *Lithos*. **344**–**345**, pp.265–279.

Ghukasyan, Y. 1985. *Petrography, Mineralogical-Geochemical Characteristics and the History of the Forming of Aragats Volcanic Complex*. Academy of Sciences, Yereven, Armenian SSR.

Di Giuseppe, P., Agostini, S., Lustrino, M., Karaoglu, Ö., Savaşçin, M.Y., Manetti, P. and Ersoy, Y. 2017. Transition from compression to strike-slip tectonics revealed by miocene-pleistocene volcanism west of the karliova triple junction (east anatolia). *Journal of Petrology*. **58**(10), pp.2055–2087.

Gök, R., Mellors, R.J., Sandvol, E., Pasyanos, M., Hauk, T., Takedatsu, R., Yetirmishli, G., Teoman, U., Turkelli, N., Godoladze, T. and Javakishvirli, Z. 2011. Lithospheric velocity structure of the Anatolian plateau - Caucasus - Caspian region. *Journal of Geophysical Research: Solid Earth*. **116**(B5), pp.1–14.

Gök, R., Türkelli, N., Sandvol, E., Seber, D. and Barazangi, M. 2000. Regional wave propagation in Turkey and surrounding regions. *Geophysical Research Letters*. **27**(3), pp.429–432.

Green, D.H. and Falloon, T.J. 2005. Primary magmas at mid-ocean ridges, 'hotspots' and other intraplate settings: Constraints on mantle potential temperature *In*: G. R. Foulger, J. H. Natland, D. C. Presnall and D. L. Anderson, eds. *Plates, plumes and Paradigms*. Geological Society of America Special Papers, pp.217–248.

Green, T.H., Blundy, J.D., Adam, J. and Yaxley, G.M. 2000. SIMS determination of trace element partition coefficients between garnet, clinopyroxene and hydrous basaltic liquids at 2-7.5 GPa and 1080-1200°C. *Lithos*. **53**(3–4), pp.165–187.

Grove, T.L., Till, C.B. and Krawczynski, M.J. 2012. The Role of H2O in Subduction Zone Magmatism. *Annual Review of Earth and Planetary Sciences*. **40**, pp.413–439.

Hasebe, N., Fukutani, A., Sudo, M. and Tagami, T. 2001. Transition of eruptive style in an arc-arc collision zone: K-Ar dating of Quaternary monogenetic and polygenetic volcanoes in the Higashi-Izu region, Izu peninsula, Japan. *Bulletin of Volcanology*. **63**(6), pp.377–386.

Hässig, M., Rolland, Y., Sahakyan, L., Sosson, M., Galoyan, G., Avagyan, A., Bosch, D. and Müller, C. 2015. Multi-stage metamorphism in the South Armenian Block during the Late Jurassic to Early Cretaceous: Tectonics over south-dipping subduction of Northern branch of Neotethys. *Journal of Asian Earth Sciences*. **102**, pp.4–23.

Hässig, M., Rolland, Y., Sosson, M., Galoyan, G., Müller, C., Avagyan, A. and Sahakyan, L. 2013. New structural and petrological data on the Amasia ophiolites (NW Sevan-Akera suture zone, Lesser Caucasus): Insights for a large-scale obduction in Armenia and NE Turkey. *Tectonophysics*. **588**, pp.135–153.

Hildreth, W. 1981. Gradients in silicic magma chambers: implications for lithospheric magmatism. *Journal of Geophysical Research*. **86**(B11), pp.10153–10192.

Hofmann, A.W. 2003. Sampling Mantle Heterogeneity through Oceanic Basalts : Isotopes and Trace Elements *In*: R. W. Carlson, ed. *Treatise on Geochemistry*. Oxford, UK: Elsevier-Pergamon, pp.61–101.

De Hoog, J.C.M. and Savov, I.P. 2018. Boron Isotopes as a Tracer of Subduction Zone Processes *In*: H. Marschall and G. Foster, eds. *Boron Isotopes: The Fifth Element* [Online]. Springer International Publishing AG, pp.217–247. Available from: http://link.springer.com/10.1007/978-3-319-64666-4_9.

Hu, F., Ducea, M.N., Liu, S. and Chapman, J.B. 2017. Quantifying Crustal Thickness in Continental Collisional Belts: Global Perspective and a Geologic Application. *Scientific Reports*. **7**(1), p.7058.

Innocenti, F., Mazzuoli, R., Pasquare', G., Serri, G. and Villari, L. 1980. Geology of the volcanic area north of Lake Van (Turkey). *Geologische Rundschau*.

Innocenti, F., Mazzuoli, R., Pasquarè, G., Radicati Di Brozolo, F. and Villari, L. 1982. Tertiary and quaternary volcanism of the Erzurumkars area (Eastern Turkey): Geochronological data and geodynamic evolution. *Journal of Volcanology and Geothermal Research*. **13**, pp.223–240.

Ionov, D.A., Bodinier, J.-L., Mukasa, S.B. and Zanetti, A. 2002. Mechanisms and Sources of Mantle Metasomatism: Major and Trace Element Compositions of Peridotite Xenoliths from Spitsbergen in the Context of Numerical Modelling. *Journal of Petrology*. **43**(12), pp.2219–2259.

Ionov, D.A. and Hofmann, A.W. 1995. Nb-Ta-rich mantle amphiboles and micas: Implications for subduction-related metasomatic trace element fractionations.

Earth and Planetary Science Letters. **131**, pp.341–356.

Jacobsen, S.B. and Wasserburg, G.J. 1980. Sm-Nd isotopic evolution of chondrites. *Earth and Planetary Science Letters*. **50**(1), pp.139–155.

Jagoutz, O. and Schmidt, M.W. 2013. The composition of the foundered complement to the continental crust and a re-evaluation of fluxes in arcs. *Earth and Planetary Science Letters*. **371**, pp.177–190.

Jarosewich, E., Nelen, J.A. and Norberg, J.A. 1980. Reference Samples for Electron Microprobe Analysis. *Geostandards Newsletter*. **4**(1), pp.43–47.

Joannin, S., Cornée, J.-J., Münch, P., Fornari, M., Vasiliev, I., Krijgsman, W., Nahapetyan, S., Gabrielyan, I., Ollivier, V., Roiron, P. and Chataigner, C. 2010. Early Pleistocene climate cycles in continental deposits of the Lesser Caucasus of Armenia inferred from palynology, magnetostratigraphy, and 40Ar/39Ar dating. *Earth and Planetary Science Letters*. **291**(1–4), pp.149–158.

Johnson, M.C. and Plank, T. 2000. Dehydration and melting experiments constrain the fate of subducted sediments. *Geochemistry, Geophysics, Geosystems*. **1**(12).

Jrbashian, R.T. and Gukasyan, Y.G. 2002. Geochronology of the Aragats volcanic centre, Armenia: evidence from K/Ar dating. *Doklady Earth Sciences2*. **384**(4), pp.393–398.

Jrbashyan, R.T., Ghukasyan, Y.G., Karapetyan, S.G. and Mnatsakanyan, A.Kh. Navasardyan, G.Kh. Gevorgyan, H.P. 2012. Types of volcanic eruptions and forms of manifestation of the late-collision on-land volcanism in Armenia. *Arm. Natl. Acad. Sci. Inst. Geol. Sci. Earth Sciences,*. **3**, pp.3-20 (in Russian).

Kaislaniemi, L., van Hunen, J., Allen, M.B. and Neill, I. 2014. Sublithospheric small-scale convection--A mechanism for collision zone magmatism. *Geology*. **42**(4), pp.291–294.

Kakihana, H., Kotaka, M., Satoh, S., Nomura, M. and Okamoto, M. 1977. Fundamental Studies on the Ion-Exchange Separation of Boron Isotopes. *Bulletin of the Chemical Society of Japan*. **50**(1), pp.158–163.

Karakhanian, A., Djrbashian, R., Trifonov, V., Philip, H., Arakelian, S. and Avagian, A. 2002. Holocene-historical volcanism and active faults as natural risk factors for Armenia and adjacent countries. *Journal of Volcanology and Geothermal Research*. **113**(1–2), pp.319–344.

Karakhanian, A., Jrbashyan, R., Trifonov, V., Philip, H., Arakelian, S., Avagyan, A., Baghdassaryan, H., Davtian, V. and Ghoukassyan, Y. 2003. Volcanic hazards in the region of the Armenian Nuclear Power Plant. *Journal of Volcanology and Geothermal Research*. **126**(1–2), pp.31–62.

Karakhanyan, A., Vernant, P., Doerflinger, E., Avagyan, A., Philip, H., Aslanyan, R., Champollion, C., Arakelyan, S., Collard, P., Baghdasaryan, H., Peyret, M., Davtyan, V., Calais, E. and Masson, F. 2013. GPS constraints on continental deformation in the Armenian region and Lesser Caucasus. *Tectonophysics*. **592**, pp.39–45.

Karaoğlan, F., Parlak, O., Hejl, E., Neubauer, F. and Kloetzli, U. 2016. The temporal evolution of the active margin along the South-east Anatolian Orogenic Belt (SE Turkey): evidence from U–Pb, Ar–Ar and fission track chronology. *Gondwana Research*. **33**, pp.190–208.

Karaoğlan, F., Parlak, O., Robertson, A., Thöni, M., Klötzli, U., Koller, F. and Okay, A.I. 2013. Evidence of Eocene high-temperature/high-pressure metamorphism of ophiolitic rocks and granitoid intrusion related to Neotethyan subduction processes (Doğanşehir area, SE Anatolia). *Geological Society, London, Special Publications*. **372**(1), pp.249–272.

Karapetian, S.G., Jrbashian, R.T. and Mnatsakanian, A.K. 2001. Late collision rhyolitic volcanism in the north-eastern part of the Armenian highland. *Journal of Volcanology and Geothermal Research*. **112**(1–4), pp.189–220.

Kavanagh, J.L. and Sparks, R.S.J. 2009. Temperature changes in ascending kimberlite magma. *Earth and Planetary Science Letters*. **286**, pp.404–413.

Kelemen, P.B., Hanghøj, K. and Greene, A.R. 2003. One View of the Geochemistry of Subduction-related Magmatic Arcs , with an Emphasis on Primitive Andesite and Lower Crust. *Treatise on Geochemistry*. **3**, pp.593–659.

Kelley, K.A., Plank, T., Ludden, J. and Staudigel, H. 2003. Composition of altered oceanic crust at ODP Sites 801 and 1149. *Geochemistry, Geophysics, Geosystems*. **4**(6), p.8910.

Keskin, M. 2007. Eastern Anatolia: a hot spot in a collision zone without a mantle plume *In*: G. R. Foulger and D. M. Jurdy, eds. *Plates, plumes and planetray processes*. Geological Society of America Special Paper, pp.693–722.

Keskin, M. 2003. Magma generation by slab steepening and breakoff beneath a subduction-accretion complex: An alternative model for collision-related volcanism in Eastern Anatolia, Turkey. *Geophysical Research Letters*. **30**(24), p.8046.

Keskin, M., Pearce, J.A. and Mitchell, J.G. 1998. Volcano-stratigraphy and geochemistry of collision-related volcanism on the Erzurum-Kars Plateau, northeastern Turkey. *Journal of Volcanology and Geothermal Research*. **85**, pp.355–404.

Keskin, M., Pearce, J.A., Pavlides, S., Greenwood, P., Kempton, P.D. and Dilek, Y. 2006. Magma-crust interactions and magma plumbing in a postcollisional setting: Geochemical evidence from the Erzurum-Kars volcanic plateau, eastern Turkey. *Geological Society of America Special Papers*. **409**, pp.475–505.

Kessel, R., Schmidt, M.W., Ulmer, P. and Pettke, T. 2005. Trace element signature of subduction-zone fluids, melts and supercritical liquids at 120-180 km depth. *Nature*. **437**(7059), pp.724–727.

Kharazyan, E.D. 2005. Geological map of Republic of Armenia. , p.1.

Konrad-Schmolke, M. and Halama, R. 2014. Combined thermodynamic-geochemical modeling in metamorphic geology: Boron as tracer of fluid-rock interaction. *Lithos*. **208**, pp.393–414.

Koulakov, I., Zabelina, I., Amanatashvili, I. and Meskhia, V. 2012. Nature of orogenesis and volcanism in the Caucasus region based on results of regional tomography. *Solid Earth*. **3**(2), pp.327–337.

Kress, V.C. and Carmichael, I.S.E. 1991. The compressibility of silicate liquids containing Fe2O3 and the effect of composition, temperature, oxygen fugacity and pressure on their redox states. *Contributions to Mineralogy and Petrology*. **108**(1–2), pp.82–92.

Langmuir, C.H. and Forsyth, D.W. 2000. Mantle Melting Beneath Mid-Ocean ridges. *Oceanography*. **20**(1), pp.78–89.

LaTourrette, T., Hervig, R.L. and Holloway, J.R. 1995. Trace element partitioning between amphibole, phlogopite, and basanite melt. *Earth and Planetary Science Letters*. **135**, pp.13–30.

Leake, B.E., Woolley, A.R., Arps, C.E.S., Birch, W.D., Gilbert, M.C., Grice, J.D., Hawthorne, F.C., Kato, A., Kisch, H.J., Krivovichev, V.G., Linthout, K., Laird, J., Mandarino, J.A., Maresch, W. V., Nickel, E.H., Rock, N.M.S., Schumacher, J.C., Smith, D.C., Stephenson, N.C.N., Ungaretti, L., Whittaker, E.J.W. and Youzhi, G. 1997. Nomenclature of amphiboles: Report of the subcommittee on amphiboles of the international mineralogical association, commission on new minerals and mineral names. *American Mineralogist*. **35**(1), pp.219–246.

Lebedev, V.A., Chernyshev, I. V., Shatagin, K.N., Bubnov, S.N. and Yakushev, A.I. 2013. The quaternary volcanic rocks of the Geghama highland, Lesser Caucasus, Armenia: Geochronology, isotopic Sr-Nd characteristics, and origin. *Journal of Volcanology and Seismology*. **7**, pp.204–229.

Lee, C.T.A., Luffi, P., Plank, T., Dalton, H. and Leeman, W.P. 2009. Constraints on the depths and temperatures of basaltic magma generation on Earth and other terrestrial planets using new thermobarometers for mafic magmas. *Earth and Planetary Science Letters*. **279**(1–2), pp.20–33.

Leeman, W.P., Tonarini, S., Chan, L.H. and Borg, L.E. 2004. Boron and lithium isotopic variations in a hot subduction zone - The southern Washington Cascades. *Chemical Geology*. **212**(1), pp.101–124.

Leonard, G.S., Calvert, A.T., Hopkins, J.L., Wilson, C.J.N., Smid, E.R., Lindsay, J.M. and Champion, D.E. 2017. High-precision 40Ar/39Ar dating of Quaternary basalts from Auckland Volcanic Field, New Zealand, with implications for eruption rates and paleomagnetic correlations. *Journal of Volcanology and Geothermal Research*. **343**, pp.60–74.

Li, Z.H., Xu, Z.Q. and Gerya, T. V. 2011. Flat versus steep subduction: Contrasting modes for the formation and exhumation of high- to ultrahigh-pressure rocks in continental collision zones. *Earth and Planetary Science Letters*. **301**(1–2), pp.65–77.

Luth, R.W. 2003. Mantle Volatiles-Distribution and Consequences *In*: R. Carlson, H. D. Holland and K. Turekian, Karl, eds. *Treatise on Geochemistry*. Elsevier, pp.319–361.

Maggi, A. and Priestley, K. 2005. Surface waveform tomography of the Turkish-Iranian plateau. *Geophysical Journal International*. **125**, pp.729–742.

Mandler, B.E. and Grove, T.L. 2016. Controls on the stability and composition of amphibole in the Earth ’s mantle. *Contributions to Mineralogy and Petrology*. **171**(8), pp.1–20.

Maner, J.L. and London, D. 2018. Fractionation of the isotopes of boron between granitic melt and aqueous solution at 700 °C and 800 °C (200 MPa). *Chemical Geology*. **489**, pp.16–27.

Mark, D.F., Barfod, D., Stuart, F.M. and Imlach, J. 2009. The ARGUS multicollector noble gas mass spectrometer: Performance for 40Ar/39Ar geochronology. *Geochemistry, Geophysics, Geosystems*. **10**(2), Q0AA02.

Marschall, H.R., Altherr, R., Kalt, A. and Ludwig, T. 2008. Detrital, metamorphic and metasomatic tourmaline in high-pressure metasediments from Syros (Greece): Intra-grain boron isotope patterns determined by secondary-ion mass spectrometry. *Contributions to Mineralogy and Petrology*. **155**(6), pp.703–717.

Marschall, H.R., Wanless, V.D., Shimizu, N., Pogge von Strandmann, P.A.E., Elliott, T. and Monteleone, B.D. 2017. The boron and lithium isotopic composition of mid-ocean ridge basalts and the mantle. *Geochimica et Cosmochimica Acta*. **207**, pp.102–138.

Mather, K.A., Pearson, D.G., McKenzie, D., Kjarsgaard, B.A. and Priestley, K. 2011. Constraints on the depth and thermal history of cratonic lithosphere from peridotite xenoliths, xenocrysts and seismology. *Lithos*. **125**(1–2), pp.729–742.

McKenzie, D.M. and O'Nions, R.K. 1991. Partial melt distributions from inversion of rare earth element concentrations. *Journal of Petrology*. **32**(5), pp.1021–1091.

McKenzie, D.M. and Priestley, K. 2008. The influence of lithospheric thickness variations on continental evolution. *Lithos*. **102**, pp.1–11.

McNab, F., Ball, P.W., Hoggard, M.J. and White, N.J. 2018. Neogene Uplift and Magmatism of Anatolia: Insights From Drainage Analysis and Basaltic Geochemistry. *Geochemistry, Geophysics, Geosystems*. **19**(1), pp.175–213.

Mederer, J., Moritz, R., Ulianov, A. and Chiaradia, M. 2013. Middle Jurassic to Cenozoic evolution of arc magmatism during Neotethys subduction and arc-continent collision in the Kapan Zone , southern Armenia. *Lithos*. **177**, pp.61–78.

Meliksetian, K. 2013. Pliocene-Quaternary volcanism of the Syunik upland. *Archaologie in Armenian II*. **67**, pp.247–258.

Mitchell, J. and Westaway, R. 1999. Chronology of Neogene and Quaternary uplift and magmatism in the Caucasus: constraints from K-Ar dating of volcanism in Armenia. *Tectonophysics*. **304**(3), pp.157–186.

Morgan, W.J. 1971. Convection plumes in the lower mantle. *Nature*. **230**, pp.42–43.

Muttik, N., Kirsimäe, K., Newsom, H.E. and Williams, L.B. 2011. Boron isotope composition of secondary smectite in suevites at the Ries crater, Germany: Boron fractionation in weathering and hydrothermal processes. *Earth and Planetary Science Letters*. **310**(3–4), pp.244–251.

Neill, I., Kheirkhah, M., Survey, G., Meliksetian, K. and Academy, N. 2014. Four flavours of orogenic plateau magmatism : what's melting beneath the Turkish-Iranian Plateau ? *In*: *EGU General Assembly Conference abstracts Vol. 16.*, pp.EGU2014-6400.

Neill, I., Meliksetian, K., Allen, M.B., Navarsardyan, G. and Karapetyan, S. 2013. Pliocene-Quaternary volcanic rocks of NW Armenia: Magmatism and

lithospheric dynamics within an active orogenic plateau. *Lithos*. **180**, pp.200–215.

Neill, I., Meliksetian, K., Allen, M.B., Navasardyan, G. and Kuiper, K. 2015. Petrogenesis of mafic collision zone magmatism: The Armenian sector of the Turkish–Iranian Plateau. *Chemical Geology*. **403**, pp.24–41.

Niespolo, E.M., Rutte, D., Deino, A.L. and Renne, P.R. 2017. Intercalibration and age of the Alder Creek sanidine 40Ar/39Ar standard. *Quaternary Geochronology*. **39**, pp.205–213.

Nimis, P. 1995. A clinopyroxene geobarometer for basaltic systems based on crystal-structure modeling. *Contributions to Mineralogy and Petrology*. **121**, pp.115–125.

Niu, Y., Zhao, Z., Zhu, D.C. and Mo, X. 2013. Continental collision zones are primary sites for net continental crust growth - A testable hypothesis. *Earth-Science Reviews*. **127**, pp.96–110.

Okay, A.I., Zattin, M. and Cavazza, W. 2010. Apatite fission-track data for the Miocene Arabia-Eurasia collision. *Geology*.

Ollivier, V., Nahapetyan, S., Roiron, P., Gabrielyan, I., Gasparyan, B., Chataigner, C., Joannin, S., Cornée, J.J., Guillou, H., Scaillet, S., Munch, P. and Krijgsman, W. 2010. Quaternary volcano-lacustrine patterns and palaeobotanical data in southern Armenia. *Quaternary International*. **223**, pp.312–326.

Oswalt, F. 1912. *Armenian. Handbuch der regionalen Geologie. H. 10*. Heidelberg.

Oyan, V., Keskin, M., Lebedev, V.A., Chugaev, A. V., Sharkov, E. V. and Ünal, E. 2017. Petrology and geochemistry of the quaternary mafic volcanism to the NE of Lake Van, Eastern Anatolian collision zone, Turkey. *Journal of Petrology*. **58**(9), pp.1701–1728.

Özdemir, Y., Karaoğlu, Ö., Tolluoğlu, A.Ü. and Güleç, N. 2006. Volcanostratigraphy and petrogenesis of the Nemrut stratovolcano (East Anatolian High Plateau): The most recent post-collisional volcanism in Turkey.

Chemical Geology. **226**, pp.189–211.

Pang, K.N., Chung, S.L., Zarrinkoub, M.H., Lin, Y.C., Lee, H.Y., Lo, C.H. and Khatib, M.M. 2013. Iranian ultrapotassic volcanism at ~11 Ma signifies the initiation of post-collisional magmatism in the Arabia-Eurasia collision zone. *Terra Nova*. **25**(5), pp.405–413.

Paul, A., Hatzfeld, D., Kaviani, A., Tatar, M. and Péquegnat, C. 2010. Seismic imaging of the lithospheric structure of the Zagros mountain belt (Iran). *Geological Society, London, Special Publications*. **330**(1), pp.5–18.

Peacock, S.M. and Hervig, R.L. 1999. Boron isotopic composition of subduction-zone metamorphic rocks. *Chemical Geology*. **160**(4), pp.281–290.

Pearce, J.A. 1983. Role of the sub-continental lithosphere in magma genesis at active continental margins *In*: C. J. Hawkesworth and M. J. Norry, eds. *Continental basalts and mantle xenoliths*. Nantwich, UK: Shiva Publications, pp.230–249.

Pearce, J.A. 1982. Trace element characteristics of lavas from destructive plate boundaries. *In*: R. S. Thorpe, ed. *Andesites: Orogenic Andesites and Related Rocks*. Chichester, UK: John Wiley and Sons, pp.528–548.

Pearce, J.A., Bender, J.F., De Long, S.E., Kidd, W.S.F., Low, P.J., Güner, Y., Saroglu, F., Yilmaz, Y., Moorbath, S. and Mitchell, J.G. 1990. Genesis of collision volcanism in Eastern Anatolia, Turkey. *Journal of Volcanology and Geothermal Research*. **44**(1–2), pp.189–229.

Pearce, J.A. and Peate, D.W. 1995. Tectonic Implications of the Composition of Volcanic Arc Magmas. *Annual Review of Earth and Planetary Sciences*. **23**, pp.251–285.

Philip, H., Avagyan, A., Karakhanian, A., Ritz, J.F. and Rebai, S. 2001. Estimating slip rates and recurrence intervals for strong earthquakes along an intracontinental fault: Example of the Pambak-Sevan-Sunik fault (Armenia). *Tectonophysics*. **343**(3–4), pp.205–232.

Plank, T. and Forsyth, D.W. 2016. Thermal structure and melting conditions in the mantle beneath the Basin and Range province from seismology and petrology. *Geochemistry, Geophysics, Geosystems*. **17**(4), pp.1312–1338.

Prelević, D., Akal, C., Romer, R.L., Mertz-Kraus, R. and Helvaci, C. 2015. Magmatic Response to Slab Tearing : Constraints from the Afyon Alkaline Volcanic Complex , Western Turkey. *Journal of Petrology*. **56**(3), pp.527–562.

Prelević, D., Foley, S.F., Romer, R. and Conticelli, S. 2008. Mediterranean tertiary lamproites derived from multiple source components in postcollisional geodynamics. *Geochimica et Cosmochimica Acta*. **72**(8), pp.2125–2156.

Priestley, K. and McKenzie, D. 2013. The relationship between shear wave velocity, temperature, attenuation and viscosity in the shallow part of the mantle. *Earth and Planetary Science Letters*. **381**, pp.78–91.

Priestley, K. and McKenzie, D. 2006. The thermal structure of the lithosphere from shear wave velocities. *Earth and Planetary Science Letters*. **244**, pp.285–301.

Priestley, K., McKenzie, D., Barron, J., Tatar, M. and Debayle, E. 2012. The Zagros core: Deformation of the continental lithospheric mantle. *Geochemistry, Geophysics, Geosystems*. **13**, pp.1–21.

Priestley, K., McKenzie, D. and Debayle, E. 2006. The state of the upper mantle beneath southern Africa. *Tectonophysics*. **416**(1–4), pp.101–112.

Putirka, K.D. 2016. Amphibole thermometers and barometers for igneous systems and some implications for eruption mechanisms of felsic magmas at arc volcanoes. *American Mineralogist*. **101**, pp.841–858.

Putirka, K.D. 2008. Thermometers and Barometers for Volcanic Systems *In*: K. D. Purtika and F. J. I. Tepley, eds. *Minerals, inclusions and volcanic processes*. Reviews in mineralogy and geochemistry, pp.61–120.

Reilinger, R., McClusky, S., Vernant, P., Lawrence, S., Ergintav, S., Cakmak, R., Ozener, H., Kadirov, F., Guliev, I., Stepanyan, R., Nadariya, M., Hahubia, G., Mahmoud, S., Sakr, K., ArRajehi, A., Paradissis, D., Al-Aydrus, A., Prilepin,

M., Guseva, T., Evren, E., Dmitrotsa, A., Filikov, S. V., Gomez, F., Al-Ghazzi, R. and Karam, G. 2006. GPS constraints on continental deformation in the Africa-Arabia-Eurasia continental collision zone and implications for the dynamics of plate interactions. *Journal of Geophysical Research: Solid Earth*. **11**, p.B05411.

Ridolfi, F. and Renzulli, A. 2012. Calcic amphiboles in calc-alkaline and alkaline magmas : thermobarometric and chemometric empirical equations valid up to 1 , 130 ° C and 2 . 2 GPa. *Contributions to Mineralogy and Petrology*. **163**(5), pp.877–895.

Ridolfi, F., Renzulli, A. and Puerini, M. 2010. Stability and chemical equilibrium of amphibole in calc-alkaline magmas: An overview, new thermobarometric formulations and application to subduction-related volcanoes. *Contributions to Mineralogy and Petrology*. **160**, pp.45–66.

Robinson, J.A.C. and Wood, B.J. 1998. The depth of the spinel to garnet transition at the peridotite solidus. *Earth and Planetary Science Letters*. **164**(1–2), pp.277–284.

Roeder, P.L. and Emslie, R.F. 1970. Olivine-liquid equilibrium. *Contributions to Mineralogy and Petrology*. **29**(4), pp.275–289.

Rolland, Y. 2017. Caucasus collisional history: Review of data from East Anatolia to West Iran. *Gondwana Research*. **49**, pp.130–146.

Rolland, Y., Galoyan, G., Sosson, M., Melkonyan, R. and Avagyan, A. 2010. The Armenian Ophiolite: insights for Jurassic back-arc formation, Lower Cretaceous hot spot magmatism and Upper Cretaceous obduction over the South Armenian Block. *Geological Society, London, Special Publications*. **340**, pp.353–382.

Rolland, Y., Hässig, M., Bosch, D., Meijers, M.J.M., Sosson, M., Bruguier, O., Adamia, S. and Sadradze, N. 2016. A review of the plate convergence history of the East Anatolia-Transcaucasus region during the Variscan: Insights from the Georgian basement and its connection to the Eastern Pontides. *Journal of Geodynamics*. **96**, pp.131–145.

Rolland, Y., Perincek, D., Kaymakci, N., Sosson, M., Barrier, E. and Avagyan, A. 2012. Evidence for ~80-75Ma subduction jump during Anatolide-Tauride-Armenian block accretion and ~48Ma Arabia-Eurasia collision in Lesser Caucasus-East Anatolia. *Journal of Geodynamics*. **56**, pp.76–85.

Rollinson, H.R. 1993. *Using Geochemical data: Evaluation, presentation, interpretation.* 1st ed. Oxford, UK: Pearson Education Ltd.

Rotstein, Y. and Kafka, A.L. 1982. Seismotectonics of the southern boundary of Anatolia, eastern Mediterranean region: Subduction, collision, and arc jumping. *Journal of Geophysical Research*. **87**(B9), p.7694.

Rudnick, R.L. and Gao, S. 2014. Composition of the Continental Crust *In*: H. D. Holland and K. K. Turekian, eds. *Treatise on Geochemistry*. Elsevier, pp.659–723.

Sargsyan, L., Meliksetian, K., Metaxian, J.-P., Levonyan, A., Karakhanyan, A., Demirchyan, H., Navasardyan, G., Margaryan, S., Gevorgyan, M. and Babayan, H. 2018. Preliminary results of analysis of earthquake swarms in Gegham volcanic ridge *In*: *EGU General Assembly Conference abstracts Vol. 20*. Vienna: EGU, p.417.

Savov, I.P., Leeman, W.P., Lee, C.T.A. and Shirey, S.B. 2009. Boron isotopic variations in NW USA rhyolites: Yellowstone, Snake River Plain, Eastern Oregon. *Journal of Volcanology and Geothermal Research*. **188**(1), pp.162–172.

Şen, P.A., Temel, A. and Gourgaud, A. 2004. Petrogenetic modelling of Quaternary post-collisional volcanism: a case study of central and eastern Anatolia. *Geological Magazine*. **141**(1), pp.81–98.

Sengor, A.M.. 1984. The Cimmeride Orogenic System and the Tectonics of Eurasia. *Geological Society of America Special Papers*. **195**, pp.1–76.

Şengör, A.M.C., Özeren, M.S., Keskin, M., Sakinç, M., Özbakir, A.D. and Kayan, I. 2008. Eastern Turkish high plateau as a small Turkic-type orogen: Implications for post-collisional crust-forming processes in Turkic-type orogens. *Earth-Science Reviews*. **90**(1–2), pp.1–48.

Şengör, A.M.C., Özeren, S., Genç, T. and Zor, E. 2003. East Anatolian High Plateau as a mantle-supported, north-south shortened domal structure. *Geophysical Research Letters*. **30**(24), p.8045.

Shaw, D.M. 2006. *Trace elements in Magmas: a Theoretical Treatment* (S. R. Taylor, ed.). Cambridge, UK.: Cambridge University Press.

Sheth, H., Meliksetian, K., Gevorgyan, H., Israyelyan, A. and Navasardyan, G. 2015. Intracanyon basalt lavas of the Debed River (northern Armenia), part of a Pliocene–Pleistocene continental flood basalt province in the South Caucasus. *Journal of Volcanology and Geothermal Research*. **295**, pp.1–15.

Smith, I.E.M. and Németh, K. 2017. Source to surface model of monogenetic volcanism: a critical review *In*: K. Németh, G. Carrasco-Núñez, J. J. Aranda-Gómez and I. E. M. Smith, eds. *Monogenetic volcanism*. London: Geological Society, London, Special Publications, pp.1–28.

Snyder, G.T., Savov, I.P. and Muramatsu, Y. 2005. Iodine and boron in Mariana serpentinite mud volcanoes (ODP Legs 125 and 195): Implications for forearc processes and subduction recycling *In*: M. Shinohara, M. H. Salisbury and C. Richter, eds. *Proceedings of the ocean drilling program, Scientific results. Vol. 195*., pp.1–18.

Sobolev, A. V., Hofmann, A.W., Sobolev, S. V. and Nikogosian, I.K. 2005. An olivine-free mantle source of Hawaiian shield basalts. *Nature*. **434**(7033), pp.590–597.

Sokół, K., Halama, R., Meliksetian, K., Savov, I.P., Navasardyan, G. and Sudo, M. 2018. Alkaline magmas in zones of continental convergence: The Tezhsar volcano-intrusive ring complex, Armenia. *Lithos*. **321**, pp.172–191.

Sosson, M., Rolland, Y., Müller, C., Danelian, T., Melkonyan, R., Kekelia, S., Adamia, S., Babazadeh, V., Kangarli, T., Avagyan, A., Galoyan, G. and Mosar, J. 2010. Subductions, obduction and collision in the Lesser Caucasus (Armenia, Azerbaijan, Georgia), new insights. *Geological Society, London, Special Publications*. **340**(1), pp.329–352.

Sparks, R.S.J., Annen, C., Blundy, J.D., Cashman, K. V., Rust, A.C. and Jackson,

M.D. 2019. Formation and dynamics of magma reservoirs. *Philosophical Transactions of the Royal Society A: Mathematical, Physical and Engineering Sciences*. **377**, p.20180019.

Sparks, R.S.J., Folkes, C.B., Humphreys, M.C.S., Barfod, D.N., Clavero, J., Sunagua, M.C., McNutt, S.R. and Pritchard, M.E. 2008. Uturuncu volcano, Bolivia: Volcanic unrest due to mid-crustal magma intrusion. *American Journal of Science*. **308**(6), pp.727–769.

Stampfli, G.M., Hochard, C., Vérard, C., Wilhem, C. and VonRaumer, J. 2013. The formation of Pangea. *Tectonophysics*. **593**, pp.1–19.

Sugden, P.J., Savov, I.P., Wilson, M., Meliksetian, K., Navasardyan, G. and Halama, R. 2019. The Thickness of the Mantle Lithosphere and Collision-related Volcanism in the Lesser Caucasus. *Journal of Petrology*. **60**(2), pp.199–230.

Sun, S. and McDonough, W.F. 1989. Chemical and isotopic systematics of oceanic basalts: implications for mantle composition and processes *In*: A. D. Saunders and M. J. Norry, eds. *Magmatism in the Ocean Basins*. London: Geological Society Special Publication, pp.313–345.

Takada, A. 1994a. Development of a subvolcanic structure by the interaction of liquid-filled cracks. *Journal of Volcanology and Geothermal Research*. **62**, pp.207–224.

Takada, A. 1994b. The influence of regional stress and magmatic input on styles of monogenetic and polygenetic volcanism. *Journal of Geophysical Research: Solid Earth*. **99**(B7), pp.13563–13573.

Tang, M., Lee, C.T.A., Chen, K., Erdman, M., Costin, G. and Jiang, H. 2019. Nb/Ta systematics in arc magma differentiation and the role of arclogites in continent formation. *Nature Communications*. **10**(1), p.235.

Thirlwall, M.F., Upton, B.G.J. and Jenkins, C. 1994. Interaction between continental lithosphere and the Iceland plume-sr-nd-pb isotope geochemistry of tertiary basalts, ne Greenland. *Journal of Petrology*. **35**(3), pp.839–879.

Tomanikova, L., Savov, I.P., Harvey, J., Hoog, J.C.M. De, Churikova, T.G., Gordeychik, B. and Yogodzinski, G.M. 2019. A limited role for metasomatized subarc mantle in the generation of Boron Isotope Signatures of Arc Volcanic Rocks. *Geology*. **47**(6), pp.517–521.

Tonarini, S., Agostini, S., Innocenti, F. and Manetti, P. 2005. δ11B as tracer of slab dehydration and mantle evolution in Western Anatolia Cenozoic Magmatism. *Terra Nova*. **17**(3), pp.259–264.

Tonarini, S., Armienti, P., D'Orazio, M. and Innocenti, F. 2001. Subduction-like fluids in the genesis of Mt. Etna magmas: Evidence from boron isotopes and fluid mobile elements. *Earth and Planetary Science Letters*.

Tonarini, S., Pennisi, M., Adorni-Braccesi, A., Dini, A., Ferrara, G., Gonfiantini, R., Wiedenbeck, M. and Gröning, M. 2003. Intercomparison of boron isotope and concentration measurements. Part I: Selection, preparation and homogeneity tests of the intercomparison materials. *Geostandards Newsletter*. **27**(1), pp.21–39.

Tonarini, S., Pennisi, M. and Leeman, W.P. 1997. Precise boron isotopic analysis of complex silicate (rock) samples using alkali carbonate fusion and ion-exchange separation. *Chemical Geology*. **142**(1–2), pp.129–137.

Topuz, G., Çelik, Ö.F., Şengör, A.M.C., Altintaş, I.E., Zack, T., Rolland, Y. and Barth, M. 2013a. Jurassic ophiolite formation and emplacement as backstop to a subduction-accretion complex in northeast Turkey, the refahiye ophiolite, and relation to the Balkan ophiolites. *American Journal of Science*. **313**(10), pp.1054–1087.

Topuz, G., Göçmengil, G., Rolland, Y., Faruk Çelik, O., Zack, T. and Schmitt, A.K. 2013b. Jurassic accretionary complex and ophiolite from northeast Turkey: No evidence for the Cimmerian continental ribbon. *Geology*. **41**(2), pp.255–258.

Topuz, G., Okay, A.I., Altherr, R., Schwarz, W.H., Sunal, G. and Altinkaynak, L. 2014. Triassic warm subduction in northeast Turkey: Evidence from the Ağvanis metamorphic rocks. *Island Arc*. **23**(3), pp.181–205.

Toussaint, G., Burov, E. and Avouac, J.P. 2004. Tectonic evolution of a continental

collision zone: A thermomechanical numerical model. *Tectonics*. **23**(6), pp.1–24.

Turner, S.J., Langmuir, C.H., Dungan, M.A. and Escrig, S. 2017. The importance of mantle wedge heterogeneity to subduction zone magmatism and the origin of EM1. *Earth and Planetary Science Letters*. **472**, pp.216–228.

Turner, S.P., George, R.M.M., Evans, P.J., Hawkesworth, C.J. and Zellmer, G.F. 2000. Time-scales of magma formation, ascent and storage beneath subduction-zone volcanoes. *Philosophical Transactions of the Royal Society A: Mathematical, Physical and Engineering Sciences*. **358**(1770), pp.1443–1464.

Valentine, G.A. and Connor, C.B. 2015. Basaltic Volcanic Fields *In*: H. Sigurdsson, ed. *The Encyclopedia of Volcanoes*. San Diego, USA; Waltham, USA: Academic Press, pp.423–439.

Villaseca, C., Orejana, D., Paterson, B.A., Billstrom, K. and Pé rez-Soba, C. 2007. Metaluminous pyroxene-bearing granulite xenoliths from the lower continental crust in central Spain: their role in the genesis of Hercynian I-type granites. *European Journal of Mineralogy*. **19**(4), pp.463–477.

Wallace, P.J., Kamenetsky, V.S. and Cervantes, P. 2015. Melt inclusion CO2 contents, pressures of olivine crystallization, and the problem of shrinkage bubbles. *American Mineralogist*. **100**(4), pp.787–794.

Walowski, K.J., Kirstein, L.A., De Hoog, J.C.M., Elliott, T.R., Savov, I.P. and Jones, R.E. 2019. Investigating ocean island mantle source heterogeneity with boron isotopes in melt inclusions. *Earth and Planetary Science Letters*. **508**, pp.97–108.

Walsh, J.N., Buckley, F. and Barker, J. 1981. The simultaneous determination of the rare-earth elements in rocks using inductively coupled plasma source spectrometry. *Chemical Geology*. **33**, pp.141–153.

Watson, E.B. 1980. Apatite and phosphorus in mantle source regions: An experimental study of apatite/melt equilibria at pressures to 25 kbar. *Earth and Planetary Science Letters*. **51**, pp.322–335.

Weaver, B.L. and Tarney, J. 1984. Empirical approach to estimating the composition of the continental crust. *Nature*. **310**(5978), pp.575–577.

Weis, D., Kieffer, B., Maerschalk, C., Barling, J., De Jong, J., Williams, G.A., Hanano, D., Pretorius, W., Mattielli, N., Scoates, J.S., Goolaerts, A., Friedman, R.M. and Mahoney, J.B. 2006. High-precision isotopic characterization of USGS reference materials by TIMS and MC-ICP-MS. *Geochemistry, Geophysics, Geosystems*. **7**(8), p.Q08006.

Weller, J.N., Martin, A.J., Connor, C.B., Connor, L.J. and Karakhanian, A. 2018. Modelling the spatial distribution of volcanoes: an example from Armenia *In*: H. M. Mader, S. G. Coles, C. B. Connor and L. J. Connor, eds. *Statistics in Volcanology*. Bath, UK: Special Publications of IAVCEI, 1. Geological Society, London, pp.77–88.

White, W.M. and Hofmann, A.W. 1982. Sr and Nd isotope geochemistry of oceanic basalts and mantle evolution. *Nature*. **296**(5860), pp.821–825.

Willett, S., Beaumont, C. and Fullsack, P. 1993. Mechanical model for the tectonics of doubly vergent compressional orogens. *Geology*. **21**(4), pp.371–374.

Yilmaz, A., Adamia, S., Chabukiani, A., Chkhotua, T., ErdoĞan, K., Tuzcu, S. and KarabiyikoĞlu, M. 2000. Structural Correlation of the Southern Transcaucasus (Georgia)-Eastern Pontides (Turkey). *Geological Society, London, Special Publications*. **173**(1), pp.171–182.

Yilmaz, Y., Güner, Y. and Şaroglu, F. 1998. Geology of the quaternary volcanic centres of the east Anatolia. *Journal of Volcanology and Geothermal Research*. **85**, pp.173–210.

Zhang, G.L. and Smith-Duque, C. 2014. Seafloor basalt alteration and chemical change in the ultra thinly sedimented South Pacific. *Geochemistry, Geophysics, Geosystems*. **15**, pp.3066–3080.

Zhu, B.Q., Mao, C.X., Lugmair, G.W. and Macdougall, J.D. 1983. Isotopic and geochemical evidence for the origin of Plio-Pleistocene volcanic rocks near the Indo-Eurasian collisional margin at Tengchong, China. *Earth and Planetary Science Letters*. **65**(2), pp.263–275.

Zor, E. 2008. Tomographic evidence of slab detachment beneath eastern Turkey and the Caucasus. *Geophysical Journal International*. **175**(3), pp.1273–1282.

Zor, E., Sandvol, E., Gürbüz, C., Türkelli, N., Seber, D. and Barazangi, M. 2003. The crustal structure of the East Anatolian plateau (Turkey) from receiver functions. *Geophysical Research Letters*. **30**(24), p.8044.

List of Abbreviations

#Mg- Mg number (molar ratio MgO/(MgO+FeO)

AFT- Apatite fission track dating

Amph- amphibole

Ap- apatite

BSE- Back-scattered electron

BP- years before present

Cpx- Clinopyroxene

DMM- Depleted MORB mantle

EKP- Erzurum-Kars Plateau

FAS- fore-arc serpentinite

FME- fluid-mobile element

Fo- Forsterite (Mg end-member in olivine solid solution) content of olivine phenocryst

HFSE- High field strength elements

HREE- Heavy rare earth elements

ICP-OES- Inductively coupled plasma optical emission spectroscopy

ICP-MS- Inductively coupled plasma mass spectrometry

ka- age in thousands of years

LCC- Lower Continental Crust

LILE- Large Ion Lithophile Elements

LOI- Loss on Ignition

LREE- Light Rare Earth elements

Ma- age in millions of years

Myr- time interval in million years

NLC- Northern Lesser Caucasus

N-MORB- “Normal” Mid-ocean ridge basalt

NW- north-west

OIB- Ocean Island Basalt

Ol- Olivine

Plag- Plagioclase feldspar

ppm- parts per million

REE- Rare earth element

RH- Royal Holloway University

SAB- South Armenian Block

SC- Subduction Component

SE- south-east

SLC- Southern Lesser Caucasus

TAC- Tezhsar alkaline complex

TIMS- Thermal Ionisation Mass Spectrometry

TIP- Turkish-Iranian Plateau

T_p- Mantle potential temperature

wt %- Weight per cent concentration

Appendices

A. Major and Trace elements

This Appendix gives the full data tables for major and trace element concentrations used in this thesis, as well as providing details on the analyses of standard materials.

A.1 Bulk rock geochemical data

Location and geochemical data for collision related volcanic rocks from the southern Lesser Caucasus.

Table A.1 Full major and trace element dataset for Syunik volcanic highland

a- Sample 1-4B-08 is a granitic crustal xenolith
b- Samples analysed at Royal Holloway report Fe as FeO (tot); Samples analysed at ACME labs, Vancouver report Fe as Fe_2O_3 (tot)
c- Major elements analysed by x-ray fluorescence (XRF) at Royal Holloway or inductively coupled plasma atomic emission spectra (ICP-AES) at ACME labs, Vancouver
d- Samples listed in order of date of collection
e- Trace elements run by ICP-AES after HF digestions at Royal Holloway or by ICP- mass spectrometry (ICP-MS) at ACME labs, Vancouver
f- Trace elements run by ICP-AES after fusions at Royal Holloway or by ICP-MS at ACME labs
g- Run by ICP-MS
h- Obsidian samples, where major elements were analysed by electron probe microanalysis
i- Lab where sample was run- Royal Holloway (RH) or ACME labs, Vancouver

Table A.1

Sample[d]	1.1.08	1.2.08	1.3.08	1.4A.08	1.4B.08[a]	2.5.08	2.6.08	2.7.08
Latitude	39.59280	39.61808	39.55255	39.04413	39.04413	39.43065	39.48285	39.45870
Longitude	46.06533	46.07458	46.08887	46.08888	46.08888	46.31612	46.26930	46.24037
Lab	RH	RH	RH	RH	RH	RH	RH	RH
SiO_2[c]	56.15	56.19	52.28	50.52	76.29	49.69	53.23	50.44
TiO_2	1.02	1.02	1.10	1.43	0.07	1.34	1.12	1.32
Al_2O_3	16.70	16.87	15.89	16.31	13.24	16.65	17.11	16.82
Fe_2O_3 (tot)[b]								
FeO (tot)[b]	7.32	7.44	7.71	8.97	0.72	8.51	7.78	8.38
Cr_2O_3	0.01	0.01	0.01	0.01	0.00	0.01	0.01	0.01
MnO	0.12	0.12	0.13	0.14	0.01	0.14	0.13	0.14
MgO	3.62	3.72	3.91	5.20	0.09	4.87	4.15	4.44
CaO	6.62	6.77	8.25	8.74	0.89	8.47	6.87	8.16
Na_2O	4.60	4.56	4.77	4.36	3.62	4.57	5.03	5.12
K_2O	2.82	2.81	2.94	2.73	5.23	2.82	3.20	3.25
P_2O_5	0.71	0.72	0.96	1.02	0.01	0.99	0.96	1.12
LOI								
Total	99.68	100.22	97.93	99.40	100.17	98.05	99.59	99.20
Mg#	0.47	0.47	0.47	0.51	0.18	0.50	0.49	0.49
Li[e]	16.8	16.3	18.7	13.0	2.9	13.0	16.8	14.2
Be[g]	2.1	2.1	2.0	2.0	1.1	2.1	2.9	2.3
Sc[e]	12.6	13.2	12.0	15.5	0.0	13.0	10.6	11.0
V[e]	140.5	143.4	137.6	185.9	6.9	155.9	141.4	158.4
Co[e]	19.4	19.6	19.8	26.5	1.1	24.8	20.6	23.7
Ni[e]	28.4	29.2	28.4	49.9	0.3	51.8	52.4	45.0
Cu[e]	55.8	59.1	52.7	80.4	3.2	53.2	46.5	64.2
Zn[f]	90.8	107.0	100.0	144.5	57.4	105.4	124.5	111.0
Ga[g]								
Rb[g]								
Sr[f]	1125	1131	1689	2003	591	2070	1722	2531
Y[f]	23.1	22.6	22.5	23.3	4.1	24.0	23.4	24.1
Zr[f]	213	221	179	199	49	212	234	224
Nb[g]								
Mo[g]								
Cs[g]	0.7	0.8	0.9	0.6	0.8	0.7	0.9	0.8
Ba[f]	968	958	1123	1109	809	1051	1057	1220
La[g]	67.6	68.8	72.4	88.9	21.7	80.7	95.4	98.7
Ce[g]	117.5	119.0	129.4	169.7	29.8	152.5	172.2	193.2
Pr[g]	12.4	12.4	13.8	18.8	3.0	16.9	18.0	21.4
Nd[g]	46.0	47.3	53.2	73.3	9.2	65.8	66.5	83.6
Sm[g]	7.6	7.6	8.2	11.3	1.2	10.5	10.3	12.7
Eu[g]	2.1	2.1	2.3	2.9	0.5	2.8	2.7	3.3
Gd[g]	5.6	5.7	6.3	8.0	1.0	7.4	7.5	8.7
Tb[g]	0.9	0.9	0.9	1.1	0.2	1.1	1.0	1.2
Dy[g]	3.8	3.8	3.8	4.3	0.8	4.3	4.0	4.3
Ho[g]	0.7	0.7	0.7	0.8	0.2	0.8	0.7	0.8
Er[g]	1.9	1.9	1.9	2.0	0.6	2.0	2.0	2.0
Tm[g]	0.3	0.3	0.3	0.3	0.1	0.3	0.3	0.3
Yb[g]	2.0	1.9	2.0	2.0	0.5	2.0	2.0	2.0
Lu[g]	0.3	0.3	0.3	0.3	0.1	0.3	0.3	0.3
Hf[g]	4.8	4.9	4.0	4.5	1.9	4.6	5.1	4.9
Ta[g]	1.2	1.2	1.3	1.6	1.2	1.5	1.8	1.7
Tl[g]	0.0	0.1	0.0	0.1	0.2	0.0	0.0	0.0
Pb[g]	16.0	15.2	14.1	15.2	19.9	14.4	18.0	16.7
Th[g]	7.2	7.0	7.2	6.5	43.1	5.7	8.2	6.8
U[g]	1.6	1.6	2.0	1.4	5.9	1.3	1.7	1.5

Table A.1 continued

Sample[d]	2.8.08	2.9.08	2.10.08	2.11A.08	2.11B.08	3.12A.08	3.12B.08	3.12C.08
Latitude	39.46010	39.48452	39.46787	39.50280	39.50280	39.77477	39.77477	39.77477
Longitude	46.26768	46.21770	46.25762	46.18945	46.18945	45.79218	45.79218	45.79218
Lab	RH	RH	RH	RH	RH	RH	RH	RH
SiO_2[c]	51.74	51.58	47.08	60.38	52.74	77.95	58.80	77.91
TiO_2	1.14	1.07	1.31	0.61	1.27	0.10	0.98	0.09
Al_2O_3	16.26	16.49	14.39	16.61	16.29	12.73	16.61	12.73
Fe_2O_3 (tot)[b]								
FeO (tot)[b]	7.87	7.61	10.31	4.20	7.13	0.73	6.77	0.76
Cr_2O_3	0.01	0.02	0.07	0.00	0.01	0.00	0.01	0.00
MnO	0.13	0.13	0.15	0.08	0.12	0.06	0.11	0.06
MgO	4.77	4.71	11.65	1.65	3.80	0.06	3.35	0.06
CaO	8.61	7.03	9.83	3.18	7.04	0.51	5.87	0.51
Na_2O	4.76	4.90	3.29	5.21	4.75	4.11	4.59	4.20
K_2O	2.89	3.33	1.19	4.38	3.90	4.65	2.97	4.69
P_2O_5	1.00	0.93	0.53	0.38	1.07	0.01	0.55	0.01
LOI								
Total	99.17	97.78	99.74	96.68	98.11	100.90	100.61	101.02
Mg#	0.52	0.52	0.67	0.41	0.49	0.13	0.47	0.12
Li[e]	15.0	16.9	8.1	24.6	16.7	56.4	19.8	58.5
Be[g]	2.5	2.6	1.2	3.7	2.8	4.2	2.1	4.3
Sc[e]	14.1	10.8	24.2	4.3	9.7	1.4	11.6	1.1
V[e]	145.8	130.2	154.6	76.3	158.9	1.6	111.9	1.3
Co[e]	22.3	21.2	39.7	10.3	21.7	1.0	17.8	0.9
Ni[e]	56.7	85.1	275.5	11.1	45.5	0.3	28.4	0.3
Cu[e]	61.2	56.0	64.9	20.1	73.2	1.6	33.6	0.8
Zn[f]	102.3	107.3	98.0	79.9	111.7	32.0	106.2	40.8
Ga[g]								
Rb[g]								
Sr[f]	1998	2050	1073	1084	2378	21	981	21
Y[f]	20.6	20.5	22.2	14.3	17.4	11.8	21.4	11.7
Zr[f]	246	220	126	308	233	98	184	94
Nb[g]								
Mo[g]								
Cs[g]	0.7	0.9	0.5	2.0	1.0	4.3	0.8	4.7
Ba[f]	1107	1192	430	1007	1254	62	779	58
La[g]	93.0	88.8	31.9	68.2	88.8	34.3	55.7	33.4
Ce[g]	174.5	158.8	65.6	117.4	170.2	52.8	95.2	51.7
Pr[g]	18.7	16.8	8.3	11.9	18.7	4.9	10.3	4.8
Nd[g]	72.1	62.7	34.3	42.2	70.1	14.2	38.5	13.4
Sm[g]	11.1	9.5	6.5	6.0	10.4	1.8	6.5	1.7
Eu[g]	2.9	2.6	1.8	1.5	2.6	0.2	1.7	0.2
Gd[g]	7.7	7.0	4.9	4.3	6.9	1.7	5.0	1.7
Tb[g]	1.1	1.0	0.9	0.6	0.9	0.3	0.8	0.3
Dy[g]	4.0	3.7	4.0	2.4	3.3	1.4	3.6	1.3
Ho[g]	0.7	0.7	0.8	0.4	0.6	0.3	0.7	0.3
Er[g]	1.9	1.8	2.1	1.3	1.5	1.1	1.9	1.1
Tm[g]	0.3	0.3	0.4	0.2	0.2	0.3	0.3	0.2
Yb[g]	1.9	1.9	2.2	1.4	1.4	1.6	2.0	1.4
Lu[g]	0.3	0.3	0.4	0.3	0.3	0.3	0.3	0.3
Hf[g]	5.4	4.7	3.0	7.1	5.5	5.0	4.4	4.0
Ta[g]	1.7	1.6	0.7	2.2	1.7	2.7	1.3	2.7
Tl[g]	0.0	0.0	0.1	0.2	0.0	0.5	0.0	0.6
Pb[g]	17.5	19.9	9.0	26.8	22.2	29.4	18.0	30.1
Th[g]	8.4	7.8	2.6	17.8	8.3	36.9	11.5	37.6
U[g]	1.5	1.7	0.7	3.9	1.8	9.3	2.6	9.7

Table A.1 continued.

Sample[d]	3.13.08	3.14A.08	3.14B.08	4.15A.08[h]	4.15B.08	4.16.08	4.17.08	4.18A.08[h]
Latitude	39.76002	39.59143	39.59143	39.81777	39.81777	39.81867	39.81867	39.79052
Longitude	45.77190	45.93635	45.93635	45.81843	45.81843	45.81397	45.81397	45.82100
Lab	RH	RH	RH	RH	RH	RH	RH	RH
SiO_2[c]	57.88	54.28	54.16	76.25	75.46	65.62	59.61	76.91
TiO_2	0.97	1.00	1.00	0.08	0.08	0.55	0.86	0.08
Al_2O_3	16.37	16.62	16.46	12.63	12.74	16.10	16.36	12.55
Fe_2O_3 (tot)[b]								
FeO (tot)[b]	6.71	7.56	7.53	0.47	0.70	4.13	6.03	0.48
Cr_2O_3	0.00	0.01	0.01	0.00	0.00	0.01	0.00	0.00
MnO	0.11	0.12	0.12	0.05	0.06	0.06	0.10	0.06
MgO	3.30	4.32	4.22	0.02	0.05	1.44	2.91	0.03
CaO	6.04	7.65	7.55	0.40	0.45	3.92	5.27	0.47
Na_2O	4.48	4.52	4.58	4.17	4.06	4.16	4.61	3.90
K_2O	2.85	2.83	2.80	4.63	4.50	3.33	3.22	4.81
P_2O_5	0.53	0.87	0.87	0.00	0.01	0.23	0.49	0.00
LOI								
Total	99.25	99.79	99.30	100.00	98.11	99.54	99.48	100.00
Mg#	0.47	0.50	0.50	0.07	0.11	0.38	0.46	0.11
Li[e]	19.6	14.6	14.2	71.7	66.4	20.0	16.5	61.2
Be[g]	2.3	2.2	2.0	4.9	4.9	2.0	2.1	4.2
Sc[e]	11.3	14.0	13.7	1.1	2.2	7.1	10.1	0.3
V[e]	106.6	138.9	145.6	1.0	1.2	74.7	98.7	1.2
Co[e]	18.0	20.1	20.2	0.8	1.0	11.2	15.9	0.8
Ni[e]	28.1	38.9	38.4	0.3	0.3	23.6	24.9	0.3
Cu[e]	39.8	48.7	43.7	1.0	0.8	31.0	32.5	1.9
Zn[f]	80.3	98.9	111.7	32.9	38.6	64.5	84.5	118.4
Ga[g]								
Rb[g]								
Sr[f]	964	1430	1450	10	10	592	992	20
Y[f]	20.3	20.6	21.9	11.1	10.8	15.0	20.1	11.8
Zr[f]	176	204	207	92	87	176	213	91
Nb[g]								
Mo[g]								
Cs[g]	1.2	0.6	0.7	5.4	5.3	1.8	0.7	4.5
Ba[f]	720	993	1015	26	27	769	980	50
La[g]	51.9	75.9	76.3	27.3	26.9	47.1	63.5	33.2
Ce[g]	90.6	134.1	136.1	42.4	42.2	66.6	105.6	50.5
Pr[g]	9.8	14.3	14.4	4.0	4.0	7.5	11.1	4.8
Nd[g]	36.8	53.5	54.4	10.7	10.9	27.1	40.0	13.5
Sm[g]	6.3	8.6	8.6	1.4	1.3	4.3	6.6	1.7
Eu[g]	1.7	2.3	2.3	0.1	0.1	1.3	1.8	0.2
Gd[g]	4.9	6.4	6.5	1.3	1.3	3.5	5.2	1.7
Tb[g]	0.8	0.9	0.9	0.3	0.3	0.6	0.8	0.3
Dy[g]	3.5	3.8	3.8	1.2	1.2	2.4	3.4	1.3
Ho[g]	0.6	0.7	0.7	0.3	0.3	0.5	0.6	0.3
Er[g]	1.8	1.8	1.8	1.0	1.0	1.4	1.7	1.0
Tm[g]	0.3	0.3	0.3	0.2	0.2	0.2	0.3	0.2
Yb[g]	2.0	1.8	1.9	1.6	1.6	1.4	1.9	1.6
Lu[g]	0.3	0.3	0.3	0.3	0.3	0.3	0.3	0.3
Hf[g]	4.3	4.4	4.4	4.1	4.1	4.5	4.9	4.0
Ta[g]	1.3	1.4	1.4	2.9	3.3	1.5	1.3	2.7
Tl[g]	0.0	0.0	0.0	0.7	0.7	0.1	0.1	0.6
Pb[g]	17.2	17.9	17.6	177.0	33.0	18.9	79.3	23.4
Th[g]	11.4	7.6	7.8	41.5	39.6	19.4	12.2	37.4
U[g]	2.6	1.6	1.6	11.2	10.7	4.8	2.4	9.7

Table A.1 continued.

Sample[d]	4.18B.08	4.19.08	5.20A.08	5.20B.08	5.21.08	5.22.08	5.23.08	6.24.08
Latitude	39.79052	39.79098	39.75548	39.75548	39.75548	39.74215	39.68235	39.68745
Longitude	45.82100	45.82100	45.82830	45.85745	45.85745	45.84407	45.88542	45.91403
Lab	RH	RH	RH	RH	RH	RH	RH	RH
SiO_2[c]	74.78	54.35	77.78	76.30	53.46	56.07	53.73	48.97
TiO_2	0.10	1.19	0.07	0.06	1.05	1.06	1.23	1.56
Al_2O_3	13.51	17.20	12.81	12.57	16.41	16.95	17.13	16.28
Fe_2O_3 (tot)[b]								
FeO (tot)[b]	0.77	7.91	0.65	0.68	7.75	7.46	8.16	9.06
Cr_2O_3	0.00	0.00	0.00	0.00	0.01	0.01	0.00	0.00
MnO	0.06	0.12	0.07	0.07	0.13	0.12	0.12	0.14
MgO	0.06	3.66	0.04	0.05	4.84	3.55	3.54	4.77
CaO	0.48	6.66	0.49	0.50	7.12	6.10	6.78	8.63
Na_2O	3.88	4.63	4.51	4.17	4.45	4.41	4.61	4.47
K_2O	4.30	2.92	4.46	4.36	3.02	2.87	3.14	3.03
P_2O_5	0.00	0.84	0.00	0.00	0.92	0.68	0.89	1.30
LOI								
Total	97.95	99.48	100.89	98.76	99.15	99.27	99.33	98.19
Mg#	0.12	0.45	0.11	0.12	0.53	0.46	0.44	0.48
Li[e]	65.0	15.1	69.0	64.8	16.1	17.8	15.2	13.5
Be[g]	4.9	2.1	5.3	5.1	1.9	2.2	2.3	2.3
Sc[e]	0.7	10.7	1.5	2.0	13.4	11.9	9.8	14.1
V[e]	1.5	144.6	0.5	0.6	143.5	144.2	169.8	202.2
Co[e]	1.2	21.3	0.8	0.7	22.4	20.5	22.1	27.2
Ni[e]	0.3	26.0	0.3	0.3	66.9	34.4	13.6	38.3
Cu[e]	1.7	34.8	0.9	0.8	39.5	53.0	32.1	71.9
Zn[f]	42.9	106.5	41.0	39.4	103.4	94.5	102.7	110.0
Ga[g]								
Rb[g]								
Sr[f]	57	1374	7	9	1585	1098	1973	2358
Y[f]	11.4	22.5	8.5	8.3	23.0	21.3	21.9	24.3
Zr[f]	99	223	94	84	192	204	209	197
Nb[g]								
Mo[g]								
Cs[g]	4.7	0.7	5.3	5.1	0.3	0.8	0.7	0.6
Ba[f]	41	961	15	14	1102	864	1119	1176
La[g]	31.5	75.6	18.3	17.9	85.3	63.5	94.3	97.1
Ce[g]	50.8	138.1	28.6	27.7	149.9	111.3	172.9	193.6
Pr[g]	4.7	15.2	2.8	2.7	15.9	12.0	19.0	21.8
Nd[g]	13.2	58.3	7.2	6.9	59.5	44.8	71.4	86.0
Sm[g]	1.6	9.6	0.7	0.8	9.4	7.4	11.0	13.2
Eu[g]	0.2	2.5	0.1	0.1	2.4	2.0	2.8	3.3
Gd[g]	1.6	6.9	0.8	0.9	7.0	5.7	7.5	8.9
Tb[g]	0.3	1.1	0.2	0.2	1.1	0.9	1.1	1.2
Dy[g]	1.3	4.2	0.9	0.9	4.1	3.8	4.0	4.5
Ho[g]	0.3	0.8	0.2	0.2	0.8	0.7	0.7	0.8
Er[g]	1.1	2.0	0.9	0.9	2.0	2.0	1.9	2.1
Tm[g]	0.2	0.3	0.2	0.2	0.3	0.3	0.3	0.3
Yb[g]	1.6	2.0	1.4	1.4	2.1	2.1	1.8	1.9
Lu[g]	0.3	0.3	0.3	0.3	0.4	0.3	0.3	0.3
Hf[g]	4.1	4.9	4.4	4.0	4.3	4.5	4.8	4.7
Ta[g]	3.0	1.6	2.9	2.8	1.3	1.3	1.6	1.7
Tl[g]	0.6	0.1	0.6	0.6	0.1	0.0	0.0	0.1
Pb[g]	31.0	15.7	32.7	32.6	15.7	16.2	16.6	17.2
Th[g]	41.0	7.4	39.7	38.1	8.3	8.1	7.6	6.1
U[g]	10.1	1.7	11.0	10.6	1.4	1.8	1.6	1.4

Table A.1 continued

Sample[d]	6.25.08	6.26.08	2.3.10	2.4.10	2.5.10	2.6.10	2.7.10	2.8.10
Latitude	39.68745	39.68872	39.78705	39.78315	39.77372	39.77243	39.82953	39.83390
Longitude	45.91403	45.91847	45.94045	45.94143	45.94703	45.94713	45.97773	45.99253
Lab	RH	RH	RH	RH	RH	RH	RH	RH
SiO_2[c]	48.91	55.45	69.07	54.21	55.06	54.25	54.65	54.10
TiO_2	1.60	1.08	0.45	1.22	0.88	1.19	1.10	1.00
Al_2O_3	16.37	16.97	16.11	17.08	17.52	17.09	17.08	16.77
Fe_2O_3 (tot)[b]								
FeO (tot)[b]	9.13	7.43	2.74	8.03	7.43	8.17	7.84	7.16
Cr_2O_3	0.00	0.00	0.00	0.01	0.01	0.01	0.00	0.01
MnO	0.14	0.12	0.02	0.12	0.11	0.12	0.11	0.11
MgO	4.66	3.62	0.67	4.16	3.38	4.13	3.27	3.85
CaO	8.81	6.68	0.69	7.27	7.31	7.07	7.39	8.06
Na_2O	4.02	4.70	4.91	4.80	4.23	4.72	4.40	4.46
K_2O	3.07	3.12	4.39	2.81	2.52	2.73	2.88	3.33
P_2O_5	1.36	0.91	0.06	0.75	0.64	0.71	0.74	0.91
LOI								
Total	98.05	100.07	99.09	100.44	99.07	100.18	99.47	99.76
Mg#	0.48	0.46	0.30	0.48	0.45	0.47	0.43	0.49
Li[e]	16.6	14.3	8.7	12.9	24.7	12.8		12.1
Be[g]	2.2	2.0						
Sc[e]	14.5	11.6	6.2	13.9	13.6	13.5		12.1
V[e]	157.0	146.8	62.6	151.6	176.2	148.8		137.4
Co[e]	27.4	19.6	7.2	24.1	20.5	23.4		19.9
Ni[e]	38.6	25.7	19.1	36.6	40.9	41.3		36.0
Cu[e]	68.2	45.5	15.1	47.3	28.1	41.1		72.5
Zn[f]	113.5	102.1	56.8	104.3	105.7	88.7	91.3	96.7
Ga[g]								
Rb[g]			103.4	38.1	41.1	39.2	44.7	47.2
Sr[f]	2576	1589	356	1472	1343	1254	1311	1931
Y[f]	23.5	20.3	24.9	23.8	20.1	25.3	24.1	22.2
Zr[f]	198	221	168	191	152	205	200	197
Nb[g]			21.4	23.2	21.4	25.3	29.6	27.4
Mo[g]			0.7	1.1	0.9	1.0	1.2	0.8
Cs[g]	0.6	0.6	0.6	0.3	0.6	0.3	0.6	0.4
Ba[f]	1211	1147	802	914	852	864	936	1189
La[g]	98.4	82.6	58.7	71.6	68.6	68.5	77.0	90.3
Ce[g]	198.0	149.8	91.3	131.7	123.4	123.5	141.6	167.5
Pr[g]	22.1	16.0	9.5	13.9	12.7	12.9	15.1	17.6
Nd[g]	86.8	60.2	34.4	52.1	46.4	48.3	56.4	65.0
Sm[g]	13.5	9.5	6.1	8.3	7.2	7.7	8.8	9.6
Eu[g]	3.4	2.5	1.8	2.2	2.0	2.2	2.3	2.5
Gd[g]	9.3	6.9	5.4	6.1	5.2	6.0	6.6	6.7
Tb[g]	1.3	1.0	0.8	0.8	0.7	0.9	0.9	0.8
Dy[g]	4.7	3.8	4.0	4.1	3.4	4.3	4.0	3.8
Ho[g]	0.8	0.7	0.8	0.8	0.7	0.9	0.8	0.7
Er[g]	2.1	1.8	2.0	2.2	1.8	2.4	2.1	2.0
Tm[g]	0.3	0.3	0.3	0.3	0.2	0.3	0.3	0.2
Yb[g]	2.0	1.7	1.6	1.7	1.6	2.0	1.7	1.5
Lu[g]	0.3	0.3	0.2	0.3	0.2	0.3	0.2	0.2
Hf[g]	4.6	4.8	4.2	4.1	3.5	4.5	4.3	4.4
Ta[g]	1.8	1.4	1.5	0.9	0.8	1.1	1.2	1.1
Tl[g]	0.1	0.0	0.5	0.2	0.2	0.2	0.1	0.2
Pb[g]	23.2	28.7						
Th[g]	6.0	7.3	20.1	5.8	7.7	6.7	7.2	7.1
U[g]	1.3	1.6	6.5	1.3	1.7	1.5	1.3	1.4

Table A.1 continued.

Sample[d]	2.9.10	3.10.10	3.11.10	3.12.10	3.13.10	3.14.10	3.15.10	4.16.10
Latitude	39.83062	39.79367	39.78590	39.78258	39.77927	39.58312	39.58832	39.56577
Longitude	45.98512	46.02328	46.01777	46.01837	46.00793	46.21038	46.21135	46.21687
Lab	RH	RH	RH	RH	RH	RH	RH	RH
SiO_2[c]	58.69	62.73	55.73	58.03	54.92	57.06	55.65	53.53
TiO_2	0.87	0.56	0.99	0.94	1.12	0.85	0.98	1.13
Al_2O_3	16.83	16.61	16.36	16.74	17.11	17.33	17.50	17.08
Fe_2O_3 (tot)[b]								
FeO (tot)[b]	6.63	4.57	6.95	6.60	7.48	6.25	7.03	7.63
Cr_2O_3	0.01	0.00	0.00	0.01	0.00	0.01	0.00	0.01
MnO	0.10	0.08	0.12	0.11	0.12	0.11	0.12	0.12
MgO	3.22	1.90	3.38	3.21	3.54	3.21	3.21	4.02
CaO	5.96	4.64	6.74	6.04	6.90	5.89	6.42	7.71
Na_2O	4.35	4.44	4.91	4.38	4.77	5.22	5.09	4.75
K_2O	3.17	3.44	3.80	3.07	3.31	3.51	3.51	3.20
P_2O_5	0.57	0.34	1.07	0.59	0.93	0.58	0.72	0.93
LOI								
Total	100.39	99.31	100.06	99.72	100.20	100.01	100.23	100.10
Mg#	0.46	0.43	0.46	0.46	0.46	0.48	0.45	0.48
Li[e]	17.0	15.7	20.0	16.7	12.0	15.8	13.7	12.5
Be[g]								
Sc[e]	11.2	7.7	10.6	12.0	12.0	10.0	12.1	14.2
V[e]	122.4	93.9	125.0	125.2	142.7	115.7	123.7	162.0
Co[e]	17.8	11.3	18.0	18.1	20.7	16.2	17.9	22.3
Ni[e]	27.4	18.2	27.3	27.6	28.2	37.6	28.3	37.5
Cu[e]	52.1	31.1	37.2	42.3	58.6	44.2	48.4	56.1
Zn[f]	71.0	63.6	79.2	74.0	83.4	75.2	85.2	81.8
Ga[g]								
Rb[g]	57.6	68.6	58.9	53.7	44.6	48.9	45.4	37.0
Sr[f]	962	903	1908	1022	1728	1395	1350	1827
Y[f]	22.4	16.7	24.4	22.5	22.8	20.8	23.1	23.6
Zr[f]	201	171	189	210	218	244	242	201
Nb[g]	25.4	20.6	29.6	23.2	30.5	33.3	28.9	24.5
Mo[g]	2.0	0.9	0.3	2.0	1.2	0.9	0.7	0.4
Cs[g]	0.8	1.0	0.6	0.8	0.5	0.4	0.2	0.2
Ba[f]	883	846	1379	903	1194	1022	1017	1152
La[g]	69.8	55.3	97.5	64.6	85.1	77.1	76.9	82.1
Ce[g]	120.5	96.0	169.9	113.3	158.1	136.2	137.5	151.9
Pr[g]	12.1	9.7	17.2	11.5	16.6	13.7	14.0	16.0
Nd[g]	43.3	34.3	62.3	41.9	60.9	48.3	50.1	60.2
Sm[g]	6.9	5.2	8.9	6.6	9.2	7.1	7.8	9.0
Eu[g]	2.2	1.4	2.5	1.9	2.4	1.9	2.1	2.4
Gd[g]	5.3	4.0	6.8	5.1	6.7	5.3	5.8	6.5
Tb[g]	0.8	0.5	0.9	0.7	0.8	0.7	0.8	0.8
Dy[g]	3.7	2.4	3.9	3.6	3.9	3.2	3.6	3.9
Ho[g]	0.8	0.5	0.8	0.7	0.8	0.7	0.7	0.8
Er[g]	2.1	1.5	2.2	2.1	2.0	1.9	2.1	2.1
Tm[g]	0.3	0.2	0.3	0.3	0.3	0.2	0.3	0.3
Yb[g]	1.9	1.2	1.8	1.7	1.6	1.5	1.7	1.6
Lu[g]	0.3	0.2	0.3	0.3	0.2	0.2	0.2	0.2
Hf[g]	6.5	4.1	4.2	4.6	4.5	5.4	5.1	4.3
Ta[g]	1.1	1.0	1.3	1.0	1.2	1.4	1.3	0.9
Tl[g]	0.3	0.4	0.2	0.3	0.1	0.2	0.1	0.1
Pb[g]								
Th[g]	9.6	12.1	11.4	8.9	6.4	9.7	8.1	5.5
U[g]	2.2	3.0	2.7	1.9	1.4	1.9	1.5	1.0

Table A.1 continued.

Sample[d]	4.17.10	4.18.10	4.19.10	5.1.12	5.2.12	5.3.12	5.4.12A	5.4.12B
Latitude	39.55612	39.58467	39.59172	39.68375	39.68428	39.68867	39.68077	39.68077
Longitude	46.21807	46.22022	46.24905	46.04950	46.04902	46.05203	46.04030	46.04030
Lab	RH	RH	RH	ACME	ACME	ACME	ACME	ACME
SiO_2[c]	58.73	56.29	60.46	57.44	55.30	54.57	56.34	55.81
TiO_2	0.79	0.99	0.59	0.86	1.03	1.04	1.01	0.97
Al_2O_3	17.54	17.40	17.14	17.74	17.25	17.03	18.86	17.08
Fe_2O_3 (tot)[b]				5.76	7.48	7.41	4.69	7.03
FeO (tot)[b]	5.52	6.89	4.44					
Cr_2O_3	0.00	0.00	0.00	<0.01	<0.01	<0.01	<0.01	<0.01
MnO	0.10	0.11	0.08	0.10	0.13	0.13	0.09	0.11
MgO	2.35	3.31	1.99	2.39	3.73	3.77	1.90	3.57
CaO	4.98	6.68	5.04	4.45	6.90	7.12	4.86	6.80
Na_2O	5.59	4.89	5.29	5.27	4.59	4.64	4.92	4.57
K_2O	4.08	3.17	3.38	4.61	2.85	2.78	4.76	2.80
P_2O_5	0.62	0.65	0.44	0.64	0.73	0.77	0.56	0.72
LOI								
Total	100.29	100.39	98.85	100.28	100.30	99.69	99.58	100.21
Mg#	0.43	0.46	0.44	0.45	0.50	0.50	0.45	0.50
Li[e]	20.4	14.8	16.7					
Be[g]				5.0	2.0	2.0	4.0	3.0
Sc[e]	7.5	11.9	6.1					
V[e]	102.1	135.3	70.1	126.0	155.0	151.0	239.0	145.0
Co[e]	14.4	17.9	10.7	16.7	22.6	23.2	12.0	20.7
Ni[e]	23.0	26.5	17.1	14.0	23.2	15.7	4.7	28.8
Cu[e]	22.9	36.8	43.9	45.0	49.3	14.0	95.2	48.1
Zn[f]	83.2	77.2	63.8	57.0	54.0	42.0	75.0	71.0
Ga[g]				18.6	17.9	17.9	17.8	16.7
Rb[g]	62.7	43.5	50.3	96.3	49.9	51.4	100.0	49.9
Sr[f]	1396	1226	1107	1561	1185	1284	1972	1207
Y[f]	20.2	21.9	15.6	24.3	20.5	20.3	15.8	19.0
Zr[f]	287	219	219	342	232	239	334	203
Nb[g]	39.9	25.9	26.6	40.2	22.6	21.4	43.0	23.5
Mo[g]	0.9	1.0	2.3	0.3	0.7	0.2	0.1	0.7
Cs[g]	0.8	0.3	1.0	1.6	0.5	0.4	2.0	0.8
Ba[f]	973	973	992	1143	1052	1070	1198	894
La[g]	84.7	66.5	66.1	99.3	74.2	72.6	91.1	69.7
Ce[g]	150.7	118.6	112.8	179.4	126.4	123.6	160.3	118.5
Pr[g]	15.0	12.1	11.1	20.6	13.4	13.2	17.6	12.9
Nd[g]	52.5	44.0	38.2	70.3	45.3	44.9	59.4	44.4
Sm[g]	7.4	7.1	5.6	10.2	7.2	7.0	7.6	6.4
Eu[g]	2.0	1.9	1.5	2.5	1.9	1.9	1.9	1.8
Gd[g]	5.6	5.3	4.1	7.7	5.6	5.8	5.0	5.3
Tb[g]	0.7	0.8	0.5	0.9	0.7	0.7	0.6	0.6
Dy[g]	3.3	3.6	2.3	4.6	4.0	3.8	3.1	3.6
Ho[g]	0.7	0.7	0.4	0.8	0.7	0.7	0.5	0.6
Er[g]	1.9	2.1	1.4	2.1	2.0	2.0	1.4	1.8
Tm[g]	0.2	0.3	0.1	0.3	0.3	0.3	0.2	0.3
Yb[g]	1.7	1.8	1.1	2.2	1.7	1.8	1.4	1.5
Lu[g]	0.2	0.2	0.1	0.3	0.3	0.3	0.2	0.2
Hf[g]	6.5	4.8	5.4	6.9	5.2	4.7	6.8	4.4
Ta[g]	1.9	1.0	1.2	1.8	1.0	1.1	1.8	1.0
Tl[g]	0.2	0.2	0.2	<0.1	<0.1	<0.1	<0.1	<0.1
Pb[g]								
Th[g]	13.9	7.6	10.0	17.7	7.9	6.8	20.1	8.5
U[g]	3.1	1.4	2.2	4.2	1.7	1.6	4.6	1.8

Table A.1 continued

Sample[d]	5.5.12	5.6.12	8.2.15	8.3.15	8.4.15	8.5.15	8.6.15	8.7.15b
Latitude	39.66542	39.63242	39.42896	39.41410	39.49615	39.49431	39.50412	39.50771
Longitude	46.06113	46.05875	46.27307	46.28308	46.24583	46.24621	46.20926	46.20948
Lab	ACME	ACME	ACME	ACME	ACME	ACME	ACME	ACME
SiO_2[c]	55.27	57.91	49.16	51.58	52.01	45.80	50.11	49.06
TiO_2	1.02	0.95	1.43	1.21	1.12	1.58	1.14	1.33
Al_2O_3	17.22	16.61	16.91	16.65	16.68	14.92	15.92	16.25
Fe_2O_3 (tot)[b]	7.14	6.42	9.03	7.66	7.26	9.56	7.28	7.94
FeO (tot)[b]								
Cr_2O_3	<0.01	<0.01	<0.01	<0.01	0.01	0.02	0.01	<0.01
MnO	0.12	0.11	0.14	0.13	0.13	0.16	0.13	0.13
MgO	3.60	3.14	5.37	4.29	4.54	7.77	4.44	4.48
CaO	6.74	5.89	8.66	8.01	7.23	10.02	8.60	8.70
Na_2O	4.79	4.52	4.23	4.48	4.31	4.30	4.78	4.75
K_2O	2.98	3.12	2.54	3.14	3.24	2.64	3.75	3.78
P_2O_5	0.71	0.62	1.24	1.06	0.98	1.27	1.18	1.24
LOI			0.98	1.41	1.92	0.73	0.88	1.07
Total	100.06	100.24	99.83	99.76	99.60	98.90	98.42	98.91
Mg#	0.50	0.49	0.54	0.53	0.55	0.62	0.55	0.53
Li[e]								
Be[g]	<1	3.0	2.0	3.0	2.0	1.0	2.0	4.0
Sc[e]								
V[e]	145.0	128.0	212.0	177.0	147.0	220.0	171.0	194.0
Co[e]	19.6	17.8	28.7	23.1	23.1	36.1	22.2	24.8
Ni[e]	23.9	12.0	66.3	25.0	66.3	117.1	19.9	28.4
Cu[e]	44.2	22.5	143.3	66.0	55.7	34.3	41.2	49.4
Zn[f]	34.0	51.0	92.0	75.0	82.0	81.0	58.0	65.0
Ga[g]	16.1	16.6	18.6	18.2	18.1	15.7	17.9	18.4
Rb[g]	52.0	56.9	34.9	43.0	46.7	31.3	53.3	46.7
Sr[f]	1229	1026	2150	2161	2198	2325	2812	2814
Y[f]	19.6	18.5	21.7	19.5	20.0	23.4	21.1	21.2
Zr[f]	227	209	204	217	244	166	236	214
Nb[g]	26.0	22.2	37.8	28.4	31.1	24.1	31.8	29.0
Mo[g]	0.9	0.1	0.8	0.7	0.7	1.1	1.4	0.9
Cs[g]	0.5	0.9	0.4	0.5	0.8	0.4	0.6	0.8
Ba[f]	888	881	1181	1180	1363	1093	1705	1496
La[g]	67.9	64.4	101.3	93.9	94.4	74.6	102.9	100.4
Ce[g]	120.9	111.9	197.3	174.6	177.1	158.1	190.1	191.8
Pr[g]	13.2	12.1	23.1	20.0	19.6	19.6	21.3	22.8
Nd[g]	44.8	41.0	80.8	70.7	67.5	74.8	75.7	80.1
Sm[g]	6.5	6.4	11.7	9.7	9.5	11.0	10.4	11.2
Eu[g]	1.7	1.7	3.1	2.6	2.5	3.0	2.8	3.0
Gd[g]	5.0	5.0	8.0	6.8	6.6	7.6	7.4	7.7
Tb[g]	0.7	0.7	0.9	0.8	0.7	0.9	0.9	0.9
Dy[g]	3.5	3.5	4.6	4.0	3.8	4.7	4.3	4.4
Ho[g]	0.7	0.6	0.7	0.7	0.7	0.8	0.7	0.7
Er[g]	1.8	1.8	1.9	1.7	1.8	2.1	1.9	1.8
Tm[g]	0.3	0.3	0.3	0.3	0.3	0.3	0.3	0.2
Yb[g]	1.7	1.7	1.7	1.7	1.6	1.9	1.7	1.7
Lu[g]	0.3	0.3	0.3	0.2	0.3	0.3	0.3	0.2
Hf[g]	4.9	4.5	4.5	4.5	4.6	3.7	4.7	4.5
Ta[g]	1.2	1.2	1.4	1.2	1.4	0.9	1.4	1.3
Tl[g]	<0.1	<0.1	<0.1	<0.1	0.2	<0.1	<0.1	<0.1
Pb[g]								
Th[g]	10.6	9.4	6.6	6.6	7.9	3.6	7.8	5.8
U[g]	2.6	2.4	1.4	1.2	1.5	0.8	1.9	1.4

Table A.1 continued.

Sample[d]	8.7.15s	9.1.15	9.2.15	9.3.15	10.1.15	10.2.15	10.3.15	10.4.15
Latitude	39.50771	39.53042	39.51419	39.50737	39.64401	39.64359	39.64130	39.65483
Longitude	46.20948	46.22106	46.23795	46.24666	46.10200	46.10184	46.10138	46.11162
Lab	ACME	ACME	ACME	ACME	ACME	ACME	ACME	ACME
SiO_2[c]	49.81	51.60	47.68	52.66	47.89	51.35	51.44	54.32
TiO_2	1.37	1.22	1.78	1.19	1.26	1.48	1.46	1.01
Al_2O_3	16.80	17.40	15.80	17.58	15.58	16.93	16.91	16.97
Fe_2O_3 (tot)[b]	8.15	8.20	10.07	7.25	8.14	8.96	8.92	7.31
FeO (tot)[b]								
Cr_2O_3	<0.01	<0.01	0.01	<0.01	<0.01	<0.01	<0.01	<0.01
MnO	0.13	0.13	0.15	0.13	0.14	0.14	0.14	0.12
MgO	4.55	4.42	6.28	3.25	4.45	4.78	4.79	4.28
CaO	8.29	7.51	9.54	7.25	9.64	8.23	8.07	7.60
Na_2O	4.62	4.50	4.24	4.68	4.47	4.85	4.81	4.60
K_2O	3.50	3.06	2.10	3.48	3.87	2.11	2.13	2.63
P_2O_5	1.17	1.26	1.14	0.90	1.54	0.81	0.82	0.74
LOI	1.32	0.49	0.77	1.26	0.55	0.18	0.29	0.77
Total	99.87	99.94	99.68	99.77	97.74	99.93	99.90	100.45
Mg#	0.53	0.52	0.55	0.47	0.52	0.51	0.52	0.54
Li[e]								
Be[g]	4.0	2.0	3.0	3.0	<1	3.0	4.0	3.0
Sc[e]								
V[e]	190.0	204.0	247.0	138.0	117.0	177.0	184.0	156.0
Co[e]	25.2	24.5	34.8	19.5	24.3	28.6	29.0	22.4
Ni[e]	29.6	41.6	60.8	5.1	12.1	34.0	35.8	35.7
Cu[e]	87.5	45.4	71.9	19.0	28.2	48.8	31.9	41.7
Zn[f]	80.0	88.0	82.0	27.0	57.0	71.0	59.0	65.0
Ga[g]	19.0	18.9	17.5	19.8	16.6	18.6	17.9	18.1
Rb[g]	44.2	41.5	26.9	46.9	51.2	34.0	33.7	42.3
Sr[f]	2504	2032	2128	2556	2889	1413	1363	1374
Y[f]	20.3	22.3	24.0	21.4	25.0	26.6	26.3	20.2
Zr[f]	210	218	177	267	202	240	235	202
Nb[g]	28.8	31.3	21.9	39.5	28.7	19.4	20.5	21.2
Mo[g]	0.8	0.5	1.0	0.2	1.5	1.1	0.4	0.3
Cs[g]	0.6	0.3	0.3	0.6	0.8	0.3	0.3	0.3
Ba[f]	1446	1201	1022	1287	1795	924	915	990
La[g]	97.6	103.6	75.1	113.5	102.4	61.3	63.6	67.5
Ce[g]	192.8	189.0	150.9	221.6	195.2	115.4	114.0	120.2
Pr[g]	22.7	21.2	18.0	25.8	22.9	12.9	13.0	12.9
Nd[g]	81.9	72.2	67.8	90.8	81.1	47.7	46.7	45.5
Sm[g]	11.7	10.1	10.4	12.5	11.6	8.0	7.6	6.8
Eu[g]	3.0	2.7	2.9	3.1	3.1	2.3	2.4	2.0
Gd[g]	7.6	7.7	8.1	8.2	8.6	6.9	7.1	5.8
Tb[g]	0.9	0.9	0.9	0.9	0.9	0.8	0.9	0.7
Dy[g]	4.6	4.8	4.9	4.4	4.8	5.0	4.9	3.8
Ho[g]	0.7	0.7	0.8	0.7	0.8	0.9	0.9	0.7
Er[g]	1.9	2.1	2.0	1.9	2.1	2.6	2.5	1.9
Tm[g]	0.3	0.3	0.3	0.3	0.3	0.4	0.4	0.3
Yb[g]	1.7	1.8	2.0	1.7	2.0	2.4	2.3	1.6
Lu[g]	0.2	0.3	0.3	0.3	0.3	0.4	0.4	0.3
Hf[g]	4.6	4.3	4.0	5.6	4.5	5.1	4.8	4.3
Ta[g]	1.2	1.2	0.9	1.8	1.1	0.8	0.8	0.9
Tl[g]	<0.1	<0.1	<0.1	<0.1	0.5	<0.1	<0.1	<0.1
Pb[g]								
Th[g]	5.1	6.0	3.2	8.8	7.1	4.8	4.9	6.5
U[g]	1.1	1.1	1.0	1.6	1.1	1.0	1.1	1.6

Table A.1 continued.

Sample[d]	10.5.15	10.6.15	11.1.15	11.2.15	11.3.15	11.4.15	11.5.15
Latitude	39.65203	39.63462	39.57705	39.62041	39.63605	39.63671	39.63842
Longitude	46.11353	46.11344	45.99658	46.02615	46.03841	46.04296	46.06461
Lab	ACME	ACME	ACME	ACME	ACME	ACME	ACME
SiO_2[c]	54.30	54.65	55.65	49.60	47.27	48.67	57.53
TiO_2	1.09	1.12	1.08	1.25	1.80	1.73	0.95
Al_2O_3	16.89	16.64	17.52	16.87	15.49	15.86	16.60
Fe_2O_3 (tot)[b]	7.44	7.35	7.38	8.49	10.07	9.77	6.50
FeO (tot)[b]							
Cr_2O_3	<0.01	<0.01	<0.01	<0.01	0.01	<0.01	<0.01
MnO	0.12	0.12	0.12	0.14	0.15	0.14	0.11
MgO	4.04	3.96	3.21	5.09	5.97	5.65	3.23
CaO	7.58	7.08	6.07	8.48	9.87	9.69	5.95
Na_2O	4.47	4.54	4.90	4.87	4.50	4.37	4.62
K_2O	2.73	2.52	3.12	2.75	2.52	2.49	3.01
P_2O_5	0.81	0.68	0.82	1.27	1.17	1.12	0.65
LOI	0.76	1.12	0.02	0.22	0.08	0.44	0.55
Total	100.35	99.89	100.01	99.19	99.04	100.06	99.83
Mg#	0.52	0.52	0.46	0.54	0.54	0.53	0.50
Li[e]							
Be[g]	<1	3.0	2.0	2.0	5.0	3.0	1.0
Sc[e]							
V[e]	176.0	149.0	142.0	167.0	266.0	240.0	135.0
Co[e]	22.0	23.8	19.1	26.9	33.5	31.6	18.3
Ni[e]	19.5	21.7	10.1	49.0	41.7	35.0	11.4
Cu[e]	36.6	12.3	24.9	52.6	70.4	77.7	28.6
Zn[f]	62.0	26.0	39.0	84.0	79.0	88.0	28.0
Ga[g]	18.4	17.6	18.3	17.8	17.6	17.5	17.3
Rb[g]	44.0	48.3	51.5	33.2	33.8	34.1	59.7
Sr[f]	1456	1206	1333	2185	2348	2131	1063
Y[f]	22.3	22.0	20.8	21.6	22.0	22.3	20.3
Zr[f]	220	244	239	169	190	186	224
Nb[g]	22.8	19.8	25.6	23.2	33.4	32.6	22.1
Mo[g]	0.3	0.3	0.3	1.3	0.9	1.2	<0.1
Cs[g]	0.4	0.6	0.4	0.6	0.3	0.4	1.0
Ba[f]	1112	967	1125	1301	1151	1105	954
La[g]	77.9	65.3	79.9	94.6	88.4	86.3	65.4
Ce[g]	140.9	114.1	138.4	175.4	187.1	174.6	116.2
Pr[g]	15.3	12.8	15.7	20.3	22.3	20.9	12.5
Nd[g]	52.0	46.0	55.8	70.7	81.5	76.4	44.2
Sm[g]	8.2	7.1	7.8	10.0	11.7	10.7	6.6
Eu[g]	2.3	2.0	2.2	2.7	3.1	2.9	1.8
Gd[g]	6.4	6.0	6.2	7.1	8.6	7.8	5.3
Tb[g]	0.8	0.7	0.7	0.8	0.9	0.9	0.7
Dy[g]	4.1	4.3	4.0	4.4	4.8	4.6	3.8
Ho[g]	0.7	0.8	0.7	0.7	0.7	0.8	0.6
Er[g]	2.0	2.1	2.1	1.8	2.0	1.9	1.9
Tm[g]	0.3	0.3	0.3	0.3	0.3	0.3	0.3
Yb[g]	1.8	2.0	1.9	1.7	1.7	1.7	1.8
Lu[g]	0.3	0.3	0.3	0.2	0.2	0.3	0.3
Hf[g]	4.7	5.3	5.1	3.9	3.9	4.0	4.7
Ta[g]	1.0	0.9	1.3	1.0	1.3	1.2	1.1
Tl[g]	<0.1	<0.1	<0.1	<0.1	<0.1	<0.1	<0.1
Pb[g]							
Th[g]	7.0	7.5	7.8	5.5	5.5	5.8	10.8
U[g]	1.4	1.8	1.5	1.0	1.3	1.2	2.5

Table A.2 Full Major and trace element dataset for Vardenis volcanic highland

a- Samples analysed at Royal Holloway report Fe as FeO (tot); Samples analysed at ACME labs, Vancouver report Fe as Fe_2O_3 (tot)
b- Major elements analysed by x-ray fluorescence (XRF) at Royal Holloway or inductively coupled plasma atomic emission spectra (ICP-AES) at ACME labs, Vancouver
c- Samples listed in order of date of collection
d- Trace elements run by ICP-AES after HF digestions at Royal Holloway or by ICP- mass spectrometry (ICP-MS) at ACME labs, Vancouver
e- Trace elements run by ICP-AES after fusions at Royal Holloway or by ICP-MS at ACME labs
f- Run by ICP-MS
g- Lab where sample was run- Royal Holloway (RH) or ACME labs, Vancouver

Table A.2

Sample[c]	6.27.08	7.28B.08	7.29.08	7.31.08	7.32.08	8.33.08	8.34.08	7.30.08
Latitude	40.09045	40.06415	40.14205	40.07710	40.07712	40.10300	40.11353	40.07680
Longitude	45.41402	45.63003	45.61920	45.52558	45.52560	45.50550	45.55378	45.51587
Lab[g]	RH	RH	RH	RH	RH	RH	RH	ACME
SiO_2[b]	51.62	76.02	50.94	68.48	52.87	58.53	54.85	53.96
TiO_2	1.20	0.10	1.34	0.34	1.23	1.13	1.03	1.01
Al_2O_3	16.31	12.38	16.37	14.73	16.93	16.65	16.47	16.47
Fe_2O_3 (tot)[a]								6.82
FeO (tot)[a]	8.65	0.72	8.72	2.87	8.54	7.23	7.48	
Cr_2O_3	0.02	0.00	0.01	0.00	0.01	0.01	0.01	0.01
MnO	0.13	0.05	0.14	0.07	0.14	0.12	0.12	0.12
MgO	6.23	0.12	6.36	1.15	4.40	3.85	5.04	4.08
CaO	8.54	0.55	8.43	2.44	7.93	6.28	7.08	7.97
Na_2O	3.93	3.66	4.54	4.00	4.61	4.35	4.24	4.36
K_2O	2.27	4.79	2.00	4.19	2.13	1.93	2.45	3.37
P_2O_5	0.52	0.01	0.72	0.19	0.77	0.39	0.58	0.61
LOI								0.59
Total	99.41	98.40	99.56	98.44	99.56	100.46	99.34	99.49
Mg#	0.56	0.23	0.57	0.42	0.48	0.49	0.55	0.54
Li[d]	12.2	52.3	12.1	35.7	14.3	15.5	11.9	
Be[f]	1.5	3.1	1.5	2.6	1.6	1.5	1.9	1.0
Sc[d]	17.7	0.0	17.8	3.9	15.7	13.9	15.0	
V[d]	163.4	1.5	130.2	49.4	151.5	107.5	123.4	112.0
Co[d]	27.5	1.2	27.6	6.1	24.0	21.3	22.9	19.4
Ni[d]	77.6	1.6	86.8	7.2	45.9	34.0	79.1	18.8
Cu[d]	54.9	1.8	47.7	6.8	44.7	25.6	41.9	12.9
Zn[e]	86.3	36.4	91.5	50.6	107.3	73.9	81.3	33.0
Ga[f]								14.8
Rb[f]								67.7
Sr[e]	1161	17	1217	468	1142	680	1036	845
Y[e]	19.4	12.5	24.9	13.2	26.8	23.5	20.9	19.9
Zr[e]	141	81	188	151	187	178	194	187
Nb[f]								18.9
Mo[f]								0.2
Cs[f]	0.8	5.2	0.5	4.4	0.4	1.2	0.7	1.1
Ba[e]	778	43	754	650	707	511	816	768
La[f]	39.2	27.8	56.9	45.4	57.5	39.5	55.6	52.0
Ce[f]	75.8	46.3	98.6	70.7	102.0	65.9	95.4	90.6
Pr[f]	9.0	4.9	10.8	7.1	11.0	7.6	10.3	9.9
Nd[f]	36.9	15.8	41.1	23.5	42.4	29.7	38.2	33.7
Sm[f]	6.6	2.5	7.3	3.4	7.6	5.5	6.5	5.5
Eu[f]	1.9	0.3	2.1	0.9	2.1	1.6	1.9	1.5
Gd[f]	5.0	2.1	5.8	2.8	5.9	4.5	5.1	4.5
Tb[f]	0.8	0.4	1.0	0.5	1.0	0.9	0.9	0.6
Dy[f]	3.6	1.9	4.3	2.1	4.7	4.1	3.6	3.7
Ho[f]	0.7	0.4	0.8	0.4	0.9	0.8	0.7	0.7
Er[f]	1.9	1.2	2.2	1.2	2.3	2.1	1.8	2.0
Tm[f]	0.3	0.2	0.4	0.2	0.4	0.4	0.3	0.3
Yb[f]	2.0	1.5	2.5	1.5	2.4	2.3	1.9	1.9
Lu[f]	0.3	0.3	0.4	0.3	0.4	0.4	0.3	0.3
Hf[f]	3.4	3.4	4.1	4.4	4.1	4.4	4.4	4.4
Ta[f]	1.1	2.5	1.1	1.9	1.0	1.0	1.1	0.9
Tl[f]	0.0	0.7	<0.1	0.4	<0.1	0.0	0.1	<0.1
Pb[f]	15.9	31.3	18.2	23.6	14.4	13.2	16.4	
Th[f]	6.3	42.9	5.7	27.2	5.9	10.3	7.7	11.8
U[f]	1.5	11.2	1.5	7.7	1.2	2.7	1.7	3.3

Table A.2 continued.

Sample[c]	Porak	Suratan	1.1.12	1.3.12	2.1.12	2.2A.12	2.2B.12	2.3.12
Latitude	40.03073	40.11460	39.99902	40.02615	40.10283	40.03612	40.03612	40.09402
Longitude	45.71282	45.68688	45.45092	45.45323	45.39072	45.42975	45.42975	45.46670
Lab[g]	RH	RH	ACME	ACME	ACME	ACME	ACME	ACME
SiO_2[b]	58.15	73.24	75.12	59.38	52.17	54.81	62.41	58.78
TiO_2	0.94	0.14	0.13	0.80	1.11	0.94	0.66	0.79
Al_2O_3	16.10	12.79	13.16	16.53	17.40	16.86	16.62	16.33
Fe_2O_3 (tot)[a]	6.44	0.94	0.90	5.94	7.77	6.78	4.68	5.88
FeO (tot)[a]								
Cr_2O_3	0.01	<0.01	<0.01	<0.01	<0.01	0.01	<0.01	<0.01
MnO	0.12	0.04	0.05	0.10	0.13	0.12	0.08	0.10
MgO	3.79	0.38	0.10	3.05	4.60	3.81	2.22	2.99
CaO	6.29	0.75	0.41	5.59	8.27	7.43	4.64	5.47
Na_2O	4.28	2.86	3.99	4.38	4.62	4.77	4.49	4.23
K_2O	2.94	5.44	4.82	3.35	2.76	3.18	3.37	3.35
P_2O_5	0.55	0.04	0.02	0.58	0.95	0.70	0.38	0.58
LOI	0.68	3.54	1.20	0.49	0.35	0.68	0.33	0.90
Total	100.38	100.22	99.93	100.31	100.25	100.22	99.99	99.52
Mg#	0.54	0.44	0.18	0.50	0.54	0.53	0.48	0.50
Li[d]								
Be[f]	<1	4.0	3.0	4.0	2.0	9.0	4.0	3.0
Sc[d]								
V[d]	<8	107.0	<8	135.0	177.0	160.0	87.0	128.0
Co[d]	0.6	22.8	0.7	17.3	25.7	21.2	13.1	17.3
Ni[d]	3.4	17.0	0.5	12.9	32.8	33.4	9.6	10.9
Cu[d]	5.1	19.3	2.0	49.1	52.5	64.5	19.2	16.4
Zn[e]	10.0	24.0	18.0	48.0	72.0	61.0	14.0	36.0
Ga[f]	10.9	15.7	14.2	19.0	19.4	19.3	19.1	19.0
Rb[f]	85.8	54.5	146.2	72.9	41.1	60.4	82.8	73.4
Sr[e]	91	1171	57	1048	1890	1523	949	1043
Y[e]	7.3	19.6	12.8	18.3	18.9	16.9	14.4	17.8
Zr[e]	119	200	128	218	195	205	186	213
Nb[f]	15.9	25.3	33.1	23.3	28.3	26.5	19.0	22.6
Mo[f]	0.1	0.1	0.3	0.4	1.2	0.9	0.2	0.2
Cs[f]	1.9	1.0	3.3	1.2	0.8	1.2	1.3	1.5
Ba[e]	366	882	219	998	1098	1101	1057	1006
La[f]	43.1	65.6	38.1	67.7	83.6	71.5	56.6	67.2
Ce[f]	66.5	117.9	67.4	114.3	148.3	124.7	94.3	114.1
Pr[f]	6.1	13.2	6.8	12.1	16.3	13.7	10.2	12.1
Nd[f]	17.4	46.4	20.0	40.4	56.6	46.1	35.2	40.2
Sm[f]	2.4	7.0	2.9	6.1	8.0	6.7	5.0	5.8
Eu[f]	0.3	1.8	0.4	1.6	2.2	1.9	1.4	1.6
Gd[f]	1.5	5.3	2.2	4.8	6.1	5.2	4.2	4.8
Tb[f]	0.2	0.7	0.3	0.6	0.7	0.6	0.5	0.6
Dy[f]	1.3	3.7	2.0	3.4	3.8	3.4	2.6	3.4
Ho[f]	0.3	0.7	0.4	0.6	0.7	0.6	0.5	0.6
Er[f]	0.7	1.9	1.3	1.7	1.7	1.6	1.3	1.7
Tm[f]	0.1	0.3	0.2	0.3	0.3	0.2	0.2	0.3
Yb[f]	0.8	1.7	1.3	1.6	1.6	1.6	1.3	1.6
Lu[f]	0.2	0.3	0.2	0.2	0.3	0.3	0.2	0.3
Hf[f]	3.4	4.5	4.5	4.6	4.3	4.7	4.8	4.7
Ta[f]	1.0	1.3	1.8	1.2	1.2	1.1	1.1	1.1
Tl[f]	<0.1	<0.1	<0.1	<0.1	<0.1	<0.1	<0.1	<0.1
Pb[f]								
Th[f]	19.9	9.9	29.4	11.8	9.4	12.5	16.3	11.8
U[f]	3.7	1.9	6.4	3.2	1.9	3.2	4.6	3.4

Table A.2 continued.

Sample[c]	2.4.12	3.1.12	3.3B.12	3.3D.12	3.4.12	3.5.12	4.1.12	1.1.13
Latitude	40.08937	40.03443	40.01627	40.01622	40.12277	40.11190	40.18002	40.02458
Longitude	45.46282	45.60598	45.60892	45.59918	45.60407	45.59078	45.64320	45.83628
Lab[g]	ACME	ACME	ACME	ACME	ACME	ACME	ACME	ACME
SiO_2[b]	65.38	55.93	64.57	63.57	59.95	54.77	74.48	51.71
TiO_2	0.49	0.93	0.53	0.55	0.75	1.03	0.10	1.39
Al_2O_3	15.44	16.87	16.18	16.25	16.02	17.09	12.57	17.31
Fe_2O_3 (tot)[a]	3.45	6.86	4.17	4.32	5.68	7.33	0.57	8.34
FeO (tot)[a]								
Cr_2O_3	<0.01	<0.01	<0.01	<0.01	<0.01	<0.01	<0.01	<0.01
MnO	0.07	0.13	0.07	0.08	0.10	0.12	0.04	0.13
MgO	1.56	3.99	1.96	2.22	3.55	3.96	0.06	4.15
CaO	3.45	6.73	4.17	4.46	5.72	7.16	0.65	7.34
Na_2O	4.23	4.39	4.35	4.28	4.29	4.74	3.64	4.52
K_2O	3.95	3.17	3.09	2.99	3.34	2.78	4.89	3.08
P_2O_5	0.31	0.74	0.27	0.28	0.55	0.84	<0.01	1.23
LOI	1.35	0.34	0.26	1.06	0.04	0.44	2.96	0.75
Total	99.76	100.20	99.71	100.14	100.12	100.39	99.98	100.09
Mg#	0.47	0.54	0.48	0.50	0.55	0.52	0.17	0.50
Li[d]								
Be[f]	3.0	3.0	4.0	2.0	2.0	4.0	4.0	3.0
Sc[d]								
V[d]	66.0	148.0	102.0	77.0	129.0	146.0	<8	128.0
Co[d]	9.0	23.1	12.0	13.1	19.0	21.0	0.6	17.8
Ni[d]	5.9	31.5	6.9	5.0	17.9	22.5	0.5	12.0
Cu[d]	5.2	49.9	19.5	12.5	14.2	27.6	2.4	22.5
Zn[e]	28.0	63.0	23.0	10.0	42.0	55.0	3.0	51.0
Ga[f]	16.4	17.4	17.0	16.3	17.8	17.3	13.3	16.6
Rb[f]	92.6	59.4	76.1	69.7	80.1	44.1	183.4	56.9
Sr[e]	725	1196	734	767	971	1375	52	1026
Y[e]	13.1	21.5	14.6	13.8	17.6	20.7	7.7	18.5
Zr[e]	177	215	154	155	203	216	70	209
Nb[f]	20.8	23.1	15.4	15.3	21.5	26.9	24.4	22.2
Mo[f]	<0.1	0.7	0.5	<0.1	1.1	0.6	1.3	0.1
Cs[f]	3.0	0.4	1.8	2.0	1.0	0.4	6.5	0.9
Ba[e]	877	1016	801	794	1001	952	106	881
La[f]	52.8	70.9	45.1	44.0	63.6	75.5	30.5	64.4
Ce[f]	84.5	125.3	72.7	73.1	108.3	135.3	46.2	111.9
Pr[f]	8.7	13.6	7.6	7.4	11.4	14.6	4.1	12.1
Nd[f]	27.6	46.1	26.3	25.9	38.8	51.1	11.1	41.0
Sm[f]	4.1	6.9	3.9	3.7	5.6	7.1	1.2	6.4
Eu[f]	1.0	1.9	1.1	1.1	1.6	2.0	0.2	1.7
Gd[f]	3.3	5.6	3.3	3.4	4.8	6.1	1.1	5.0
Tb[f]	0.4	0.7	0.4	0.4	0.6	0.7	0.2	0.7
Dy[f]	2.4	3.8	2.6	2.5	3.4	4.0	1.0	3.5
Ho[f]	0.4	0.7	0.5	0.5	0.6	0.8	0.2	0.6
Er[f]	1.2	1.8	1.4	1.3	1.7	2.0	0.7	1.8
Tm[f]	0.2	0.3	0.2	0.2	0.2	0.3	0.1	0.3
Yb[f]	1.3	1.7	1.3	1.3	1.8	1.8	1.0	1.7
Lu[f]	0.2	0.3	0.2	0.2	0.3	0.3	0.2	0.3
Hf[f]	4.2	4.8	3.7	3.7	4.8	4.5	2.7	4.5
Ta[f]	1.3	1.1	1.0	1.0	1.0	1.1	1.8	1.2
Tl[f]	<0.1	<0.1	<0.1	<0.1	<0.1	<0.1	<0.1	<0.1
Pb[f]								
Th[f]	19.4	10.0	14.3	13.7	12.3	7.8	38.5	9.4
U[f]	5.7	2.2	4.7	4.0	4.0	1.6	14.0	2.4

Table A.2 continued.

Sample[c]	1.2.13	3.1.13	3.2.13	3.3.13	4.1.13	4.2.13	5.1.13	5.2.13
Latitude	40.08497	40.04498	40.05927	40.07163	40.02044	40.00945	39.91519	39.74482
Longitude	45.83638	45.78986	45.79923	45.78805	45.29230	45.29599	45.39214	45.54521
Lab[g]	ACME	ACME	ACME	ACME	ACME	ACME	ACME	ACME
SiO_2[b]	51.93	61.52	52.81	51.60	58.08	58.33	57.50	59.00
TiO_2	1.38	0.46	1.29	1.37	0.98	0.96	0.88	0.93
Al_2O_3	17.39	15.64	16.42	17.23	17.22	17.19	16.91	16.34
Fe_2O_3 (tot)[a]	8.39	4.61	7.87	8.25	6.75	6.68	6.57	6.50
FeO (tot)[a]								
Cr_2O_3	<0.01	<0.01	<0.01	<0.01	<0.01	<0.01	<0.01	0.02
MnO	0.13	0.10	0.14	0.13	0.11	0.11	0.11	0.11
MgO	4.12	2.08	4.03	4.12	3.35	3.31	3.44	4.57
CaO	7.32	5.23	7.49	7.34	6.02	6.01	6.21	6.57
Na_2O	4.61	3.35	4.65	4.85	4.58	4.57	4.41	3.86
K_2O	3.08	2.57	3.11	3.13	2.65	2.70	3.05	2.49
P_2O_5	1.23	0.18	0.97	1.21	0.58	0.58	0.61	0.27
LOI	0.61	4.34	0.70	0.27	-0.07	-0.03	0.16	-0.10
Total	100.34	100.14	99.62	99.66	100.35	100.52	99.98	100.62
Mg#	0.49	0.47	0.50	0.50	0.50	0.50	0.51	0.58
Li[d]								
Be[f]	4.0	3.0	3.0	5.0	1.0	2.0	3.0	3.0
Sc[d]								
V[d]	188.0	187.0	117.0	135.0	186.0	138.0	137.0	134.0
Co[d]	23.1	24.3	11.8	22.0	24.8	19.0	20.0	20.9
Ni[d]	32.0	30.8	7.1	23.1	33.0	12.2	21.8	13.6
Cu[d]	38.8	53.8	20.2	46.8	61.5	26.7	4.2	38.6
Zn[e]	76.0	76.0	40.0	79.0	83.0	25.0	23.0	40.0
Ga[f]	16.5	17.0	13.7	16.2	17.7	17.6	18.3	18.1
Rb[f]	35.4	38.2	57.3	42.5	40.7	57.2	59.5	67.3
Sr[e]	2084	2150	495	1932	2186	978	976	1135
Y[e]	21.2	21.6	12.5	23.6	21.8	20.1	20.1	20.2
Zr[e]	213	219	114	210	222	237	237	225
Nb[f]	31.6	33.2	8.2	27.6	33.7	20.4	20.2	24.2
Mo[f]	0.4	0.5	0.5	0.4	1.4	0.2	<0.1	0.2
Cs[f]	0.4	0.5	1.6	0.4	0.5	0.8	0.9	0.9
Ba[e]	1184	1199	563	1162	1214	901	910	1041
La[f]	95.7	97.7	20.9	79.2	100.1	60.8	60.7	69.4
Ce[f]	179.5	184.2	34.9	151.2	193.3	104.9	105.9	125.8
Pr[f]	20.6	20.8	3.7	16.8	22.1	11.6	11.6	13.3
Nd[f]	72.5	73.6	13.1	59.4	77.9	39.3	40.3	46.6
Sm[f]	10.0	10.8	2.5	8.9	10.7	6.0	6.4	6.8
Eu[f]	2.6	2.7	0.8	2.4	2.9	1.8	1.8	2.0
Gd[f]	7.4	7.6	2.5	6.7	8.1	5.5	5.8	6.0
Tb[f]	0.8	0.9	0.4	0.8	0.9	0.7	0.7	0.7
Dy[f]	4.5	4.4	2.1	4.5	4.7	4.0	4.0	4.1
Ho[f]	0.7	0.7	0.4	0.8	0.8	0.7	0.7	0.7
Er[f]	1.9	2.0	1.3	2.3	2.0	2.0	2.1	2.1
Tm[f]	0.3	0.3	0.2	0.3	0.3	0.3	0.3	0.3
Yb[f]	1.7	1.9	1.2	2.1	1.9	1.9	1.9	1.8
Lu[f]	0.3	0.3	0.2	0.3	0.3	0.3	0.3	0.3
Hf[f]	4.6	4.7	2.8	4.4	5.1	5.3	5.5	5.3
Ta[f]	1.5	1.3	0.6	1.2	1.4	1.1	1.0	1.2
Tl[f]	<0.1	<0.1	<0.1	<0.1	<0.1	<0.1	<0.1	<0.1
Pb[f]								
Th[f]	5.9	5.9	6.6	6.9	6.5	8.6	8.9	11.4
U[f]	1.4	1.2	1.6	1.7	1.3	2.1	2.5	3.2

Table A.2 continued.

Sample[c]	6.1.13	6.2b.13	4.2.15	5.2.15	5.3.15	5.4.15	5.05.15	5.6.15
Latitude	39.84915	39.80887	40.17904	40.11460	40.03073	39.97251	39.96966	39.96908
Longitude	45.69122	45.69716	45.61860	45.68688	45.69655	45.69520	45.68228	45.68293
Lab[g]	ACME	ACME	ACME	ACME	ACME	ACME	ACME	ACME
SiO_2[b]	55.59	54.15	51.51	57.71	56.98	56.76	77.12	51.47
TiO_2	1.11	1.17	1.33	0.96	0.91	0.88	0.14	1.52
Al_2O_3	17.50	17.75	16.77	16.41	15.71	16.53	12.53	16.47
Fe_2O_3 (tot)[a]	7.38	7.63	8.57	6.58	6.30	6.32	0.93	8.60
FeO (tot)[a]								
Cr_2O_3	<0.01	<0.01	0.02	<0.01	0.01	<0.01	<0.01	<0.01
MnO	0.12	0.12	0.14	0.11	0.11	0.12	0.06	0.14
MgO	3.22	3.36	6.15	3.55	3.72	3.34	0.10	4.56
CaO	6.23	6.60	8.33	6.15	6.84	6.47	0.48	8.59
Na_2O	4.80	4.80	4.66	4.40	4.19	4.26	3.98	4.20
K_2O	2.96	3.18	2.04	3.12	2.88	3.19	4.69	2.26
P_2O_5	0.78	0.93	0.73	0.66	0.52	0.66	0.02	0.93
LOI	0.13	0.49	0.06	0.46	1.25	1.20	0.30	0.62
Total	99.93	100.33	100.41	100.24	99.53	99.85	100.37	99.46
Mg#	0.46	0.47	0.59	0.52	0.54	0.51	0.18	0.51
Li[d]								
Be[f]	2.0	<1	<1	1.0	1.0	1.0	5.0	<1
Sc[d]								
V[d]	134.0	154.0	160.0	139.0	127.0	132.0	<8	165.0
Co[d]	25.9	20.9	21.9	20.6	20.7	19.8	0.9	28.3
Ni[d]	25.7	15.8	16.3	20.6	18.4	19.7	2.4	18.8
Cu[d]	26.3	55.9	25.9	23.5	20.8	21.3	4.0	18.8
Zn[e]	25.0	67.0	73.0	54.0	37.0	48.0	25.0	28.0
Ga[f]	16.8	18.3	19.4	16.8	15.9	16.9	14.4	16.8
Rb[f]	75.4	50.0	47.9	80.1	72.2	71.3	180.2	37.4
Sr[e]	546	1390	1899	1216	955	1278	55	1537
Y[e]	21.5	22.4	21.9	19.7	21.2	19.0	9.9	25.0
Zr[e]	170	244	245	201	208	205	112	202
Nb[f]	14.0	25.4	28.3	23.1	21.0	22.6	32.8	20.0
Mo[f]	1.1	0.3	0.3	0.3	0.3	0.2	0.6	0.3
Cs[f]	1.5	0.6	0.4	1.7	1.3	1.3	6.4	0.3
Ba[e]	568	1001	1171	968	819	1024	91	947
La[f]	36.8	74.6	88.6	67.8	56.6	69.9	48.2	75.4
Ce[f]	64.6	135.7	166.6	124.1	99.5	122.9	68.3	137.8
Pr[f]	7.1	15.0	19.4	13.6	10.8	13.4	5.8	15.7
Nd[f]	25.1	52.7	67.7	46.0	37.4	46.2	15.2	57.5
Sm[f]	4.5	8.0	9.9	7.1	6.0	6.8	1.8	8.6
Eu[f]	1.4	2.2	2.7	1.9	1.6	1.9	0.2	2.4
Gd[f]	4.8	6.9	7.7	5.8	5.3	5.6	1.6	7.1
Tb[f]	0.7	0.8	0.9	0.7	0.7	0.7	0.2	0.8
Dy[f]	4.0	4.5	4.6	3.8	4.3	3.9	1.3	4.6
Ho[f]	0.8	0.8	0.7	0.7	0.8	0.7	0.3	0.9
Er[f]	2.4	2.1	2.1	1.9	2.3	1.9	1.1	2.4
Tm[f]	0.3	0.3	0.3	0.3	0.3	0.3	0.2	0.3
Yb[f]	2.3	2.0	2.0	1.9	2.1	1.7	1.4	2.1
Lu[f]	0.4	0.3	0.3	0.3	0.3	0.3	0.3	0.3
Hf[f]	4.4	5.4	5.5	4.9	4.7	4.6	4.0	4.5
Ta[f]	1.0	1.2	1.2	1.3	1.0	1.2	2.4	1.0
Tl[f]	<0.1	<0.1	<0.1	<0.1	<0.1	<0.1	<0.1	<0.1
Pb[f]								
Th[f]	14.4	9.4	7.1	13.1	12.6	12.0	39.3	6.9
U[f]	4.3	2.2	1.6	4.3	4.0	3.5	12.1	1.5

Table A.2 continued.

Sample[c]	5.7.15	5.8.15	5.9.15	6.2.15	6.3.15	6.4.15	7.1.15	7.2.15
Latitude	39.97775	39.98943	40.01611	39.98949	39.98746	40.00154	39.93198	39.93311
Longitude	45.67582	45.67303	45.69622	45.62366	45.61326	45.63467	45.50536	45.50792
Lab[g]	ACME	ACME	ACME	ACME	ACME	ACME	ACME	ACME
SiO_2[b]	66.10	69.96	65.99	67.66	53.73	55.14	55.46	73.92
TiO_2	0.39	0.30	0.37	0.41	1.08	1.02	1.01	0.20
Al_2O_3	15.47	15.51	17.21	15.61	17.09	16.92	17.17	13.98
Fe_2O_3 (tot)[a]	2.88	2.19	2.65	3.05	7.60	7.30	7.20	0.99
FeO (tot)[a]								
Cr_2O_3	<0.01	<0.01	<0.01	<0.01	<0.01	0.02	<0.01	<0.01
MnO	0.06	0.05	0.09	0.07	0.13	0.12	0.12	0.01
MgO	1.20	0.74	0.56	1.32	4.06	4.60	3.74	0.17
CaO	3.00	2.92	1.72	3.04	7.24	6.73	6.66	0.83
Na_2O	4.32	4.39	5.63	4.45	4.79	4.62	4.56	3.66
K_2O	3.78	3.26	5.05	3.76	2.75	2.76	2.88	4.80
P_2O_5	0.23	0.12	0.14	0.22	0.90	0.67	0.74	0.07
LOI	2.24	0.45	0.57	0.35	0.27	0.03	0.15	1.27
Total	99.78	99.99	100.15	100.04	99.78	100.02	99.82	99.95
Mg#	0.45	0.40	0.30	0.46	0.51	0.56	0.51	0.25
Li[d]								
Be[f]	3.0	2.0	5.0	4.0	1.0	2.0	1.0	<1
Sc[d]								
V[d]	67.0	35.0	30.0	48.0	162.0	153.0	161.0	31.0
Co[d]	6.3	4.1	2.6	7.2	21.4	23.6	20.4	1.9
Ni[d]	4.2	1.0	5.5	2.6	23.7	48.7	21.9	0.9
Cu[d]	9.6	5.0	2.3	6.2	27.8	52.8	25.6	4.3
Zn[e]	18.0	6.0	17.0	11.0	69.0	53.0	66.0	24.0
Ga[f]	16.3	17.1	17.0	15.3	17.3	17.4	16.9	14.7
Rb[f]	94.7	85.0	108.4	95.4	43.4	47.7	43.3	160.1
Sr[e]	691	522	506	643	1411	1106	1238	254
Y[e]	11.3	11.7	16.9	12.5	21.4	18.7	21.5	12.0
Zr[e]	153	159	294	151	215	214	195	177
Nb[f]	17.4	13.4	32.4	17.5	25.8	22.1	23.1	27.7
Mo[f]	0.3	<0.1	0.1	0.2	0.3	0.9	0.7	0.3
Cs[f]	3.0	1.5	2.0	2.6	0.3	0.3	0.5	4.9
Ba[e]	869	872	1271	837	962	885	967	458
La[f]	44.0	37.1	77.1	43.7	75.4	64.5	66.2	51.2
Ce[f]	73.1	61.7	128.3	70.4	132.1	109.9	117.3	78.4
Pr[f]	7.3	6.1	13.0	7.4	14.5	12.0	13.1	7.6
Nd[f]	23.8	19.4	40.5	23.9	50.0	41.7	44.3	22.8
Sm[f]	3.4	3.2	5.6	3.4	8.0	6.3	6.9	2.9
Eu[f]	0.9	0.7	1.1	0.9	2.0	1.8	1.8	0.5
Gd[f]	2.6	2.4	4.0	2.7	5.8	5.1	5.3	2.3
Tb[f]	0.4	0.3	0.5	0.4	0.7	0.6	0.7	0.3
Dy[f]	2.0	1.9	3.0	1.9	3.8	3.6	3.8	1.8
Ho[f]	0.4	0.4	0.6	0.4	0.7	0.6	0.7	0.3
Er[f]	1.2	1.1	1.8	1.3	2.0	1.8	2.0	1.1
Tm[f]	0.2	0.2	0.3	0.2	0.3	0.3	0.3	0.2
Yb[f]	1.1	1.2	1.8	1.3	1.8	1.7	1.8	1.3
Lu[f]	0.2	0.2	0.3	0.2	0.3	0.2	0.3	0.2
Hf[f]	3.9	4.1	6.4	3.6	4.3	4.3	4.4	4.6
Ta[f]	1.2	0.9	1.7	1.2	1.0	1.0	1.0	2.0
Tl[f]	<0.1	<0.1	<0.1	<0.1	<0.1	<0.1	<0.1	<0.1
Pb[f]								
Th[f]	17.8	14.7	21.0	18.5	7.1	7.8	8.7	31.6
U[f]	5.3	3.7	6.2	5.8	1.4	1.6	2.3	8.3

Table A.2 continued.

Sample[c]	7.3.15	7.4.15	7.5.15
Latitude	39.91637	39.91637	39.92848
Longitude	45.50962	45.50962	45.51638
Lab[g]	ACME	ACME	ACME
SiO_2[b]	57.53	57.44	54.64
TiO_2	0.80	0.79	1.09
Al_2O_3	16.30	16.20	16.72
Fe_2O_3 (tot)[a]	6.01	5.99	7.32
FeO (tot)[a]			
Cr_2O_3	<0.01	0.01	<0.01
MnO	0.10	0.10	0.12
MgO	3.66	3.67	4.33
CaO	6.28	6.25	7.30
Na_2O	4.50	4.31	4.61
K_2O	2.96	3.06	2.94
P_2O_5	0.61	0.61	0.76
LOI	0.21	1.01	0.11
Total	99.07	99.53	100.08
Mg#	0.55	0.55	0.54
Li[d]			
Be[f]	3.0	2.0	3.0
Sc[d]			
V[d]	126.0	135.0	159.0
Co[d]	19.3	17.9	23.3
Ni[d]	7.3	21.4	31.4
Cu[d]	8.3	21.9	33.3
Zn[e]	13.0	50.0	71.0
Ga[f]	17.2	16.4	17.4
Rb[f]	62.8	64.2	51.3
Sr[e]	1161	1113	1493
Y[e]	16.6	17.6	19.7
Zr[e]	186	186	191
Nb[f]	20.0	20.1	19.9
Mo[f]	0.5	0.1	0.7
Cs[f]	1.0	1.1	0.6
Ba[e]	966	972	1039
La[f]	63.9	63.1	65.1
Ce[f]	107.0	108.4	120.1
Pr[f]	11.7	11.4	13.5
Nd[f]	41.0	39.4	46.4
Sm[f]	5.8	5.6	7.3
Eu[f]	1.6	1.7	2.0
Gd[f]	4.7	4.7	5.7
Tb[f]	0.6	0.6	0.7
Dy[f]	3.2	3.1	3.9
Ho[f]	0.6	0.6	0.7
Er[f]	1.6	1.6	1.9
Tm[f]	0.2	0.2	0.3
Yb[f]	1.5	1.4	1.8
Lu[f]	0.2	0.2	0.3
Hf[f]	4.1	4.1	4.2
Ta[f]	0.8	1.0	0.9
Tl[f]	<0.1	<0.1	<0.1
Pb[f]			
Th[f]	9.9	10.1	8.7
U[f]	2.2	2.5	2.0

A.2 Standard data

This section shows the monitoring of data quality through the analysis of major and trace element standards. Tables A.3 and A.4 deal with the ACME lab standards for major and trace elements respectively. Tables A.5 and A.6 deal with the Royal Holloway standards.

Table A.3 Major element composition of standard materials at ACME labs

	STD OREAS72B				**Expected value**	STD SY-4(D)				**Expected value**
SiO_2	51.64	51.35	51.33	51.18	**51.17**	50.04	49.98	49.78	49.9	**49.90**
TiO_2	0.35	0.35	0.34	0.35	**0.36**	0.29	0.28	0.29	0.29	**0.29**
Al_2O_3	9.03	8.99	8.96	8.97	**8.97**	20.77	20.76	20.67	20.77	**20.69**
Fe_2O_3	9.8	9.74	9.74	9.74	**9.72**	6.18	6.17	6.13	6.16	**6.21**
Cr_2O_3	0.15	0.14	0.15	0.15	**0.15**	<0.01	<0.01	<0.01	<0.01	**0.00**
MnO	0.13	0.13	0.13	0.13	**0.13**	0.1	0.11	0.1	0.11	**0.11**
MgO	16.1	16.04	16.11	16.08	**16.22**	0.53	0.52	0.52	0.52	**0.54**
CaO	3.95	3.94	3.93	3.94	**3.96**	7.97	7.96	7.95	7.96	**8.05**
Na_2O	1.32	1.28	1.3	1.3	**1.29**	7.26	7.27	7.27	7.32	**7.10**
K_2O	1.35	1.33	1.34	1.34	**1.33**	1.68	1.69	1.69	1.67	**1.68**
P_2O_5	0.05	0.06	0.06	0.06	**0.06**	0.12	0.13	0.13	0.13	**0.13**
LOI	5.21	5.32	5.32	5.3	**5.14**	4.56	4.56	4.56	4.56	**4.56**
Total	99.13	98.71	98.74	98.58	**98.49**	99.56	99.48	99.13	99.43	**99.26**

Table A.4 Trace element composition of standard materials at ACME labs

			STD SO-18			Expected value			STD SO-19			Expected Value
Be	2	1	<1	<1	2	**1**	19	15	20	21	19	**20**
V	207	200	208	204	202	**200**	179	164	176	174	163	**165**
Co	27.7	26.7	27.4	27	26.2	**26.2**	25.4	22.7	24.2	25	23.7	**24**
Ga	18.5	17	17.4	18	17.5	**17.6**	18.1	16	16.7	18.5	16.7	**17.5**
Rb	29.6	28.7	28.6	28.1	27.4	**28.7**	21.2	19.7	20.9	21.5	19.4	**19.5**
Sr	416.8	410.8	401.9	418	410	**407.4**	340.3	323.5	337.1	354.1	336.2	**317.1**
Y	32.6	31.2	31.9	30.9	29.6	**29**	39.7	34.4	37.7	37.6	35.7	**35.5**
Zr	311.2	315.4	302.3	298.4	289.2	**290**	114.6	112	116.8	115.7	111	**112**
Nb	20.8	20.3	20.1	20.2	19.7	**19.3**	73.4	70.6	74.6	72.9	69.4	**68.5**
Cs	7.1	6.9	7.1	7.3	6.7	**7.1**	4.5	4.2	4.6	4.4	4.5	**4.5**
Ba	544	546	535	539	529	**514**	516	500	519	506	499	**486**
La	12.7	12.7	12.3	12.2	12.5	**12.3**	69.4	68.9	72.9	71.2	67.8	**71.3**
Ce	28.3	26.9	26.6	25.6	26.5	**27.1**	161.9	155	164.1	158.3	152.4	**161**
Pr	3.49	3.4	3.46	3.4	3.21	**3.45**	20.03	19.16	20.77	20.14	18.62	**19.4**
Nd	14.7	13.8	13.9	13.7	13.2	**14**	79.4	75	80.4	78.1	72.9	**75.7**
Sm	3.16	2.75	2.95	2.91	2.79	**3**	13.76	12.56	14.21	12.96	12.99	**13.7**
Eu	0.89	0.88	0.9	0.88	0.82	**0.89**	3.94	3.56	3.91	3.7	3.54	**3.81**
Gd	3.23	3.11	3.3	3.08	2.96	**2.93**	11.09	10.2	11.4	11.36	10.07	**10.53**
Tb	0.48	0.48	0.47	0.48	0.45	**0.53**	1.35	1.28	1.39	1.37	1.33	**1.41**
Dy	3.06	3.06	3.14	2.92	2.93	**3**	7.61	7.2	7.83	7.39	7.06	**7.5**
Ho	0.63	0.6	0.61	0.59	0.59	**0.62**	1.35	1.33	1.33	1.34	1.32	**1.39**
Er	1.76	1.82	1.85	1.91	1.73	**1.84**	3.88	3.65	3.7	3.75	3.55	**3.78**
Tm	0.27	0.26	0.27	0.27	0.28	**0.27**	0.51	0.5	0.54	0.55	0.51	**0.55**
Yb	1.78	1.7	1.66	1.68	1.65	**1.79**	3.47	3.11	3.48	3.4	3.35	**3.55**
Lu	0.28	0.27	0.27	0.27	0.27	**0.27**	0.56	0.49	0.52	0.52	0.48	**0.53**
Hf	9.5	9.4	9.8	9.7	9.1	**9.8**	3.2	3	3.2	3.1	3	**3.1**
Ta	6.8	7.1	6.8	6.8	6.3	**7.4**	4.6	4.4	5	5.2	5	**4.9**
Th	11.2	9.9	10	10.1	9.7	**9.9**	14.1	13.1	13.9	13.5	12.2	**13**
U	16.6	16.3	16	16.3	16.6	**16.4**	19.5	19.8	20.5	19.8	20.9	**19.4**
			STD DS-10						STD OREAS4EA			
Ni	72.3	75.1	76	75.8		**74.6**	364.6	363.1	401.9	395.9		**381**
Cu	152.5	161.1	155.1	151.5		**154.6**	666.9	676.5	721.1	692.4		**709**
Zn	374	360	370	380		**370**	31	30	32	33		**31.4**
Mo	11.5	12.3	14.8	12.5		**13.6**	1.5	1.7	1.5	1.6		**1.6**
Pb	144.1	150.3	154.1	153.6		**150.55**	13.3	13.7	15.8	15.3		**14.3**

Table A.5 Analyses of the major element composition of standard materials at Royal Holloway

2 sets of standard analyses (both internal and external) accompany the unknown samples. One accompanies the samples whose number ends -10, the other accompanies samples whose number ends -08

	Internal standards 2010							
	KC-10		KC-11		KC-12		KC-14	
	Measured	Expected	Measured	Expected	Measured	Expected	Measured	Expected
SiO_2	48.01	**48.00**	55.00	**55.55**	69.40	**69.00**	77.48	**77.20**
TiO_2	0.83	**0.84**	1.11	**1.10**	0.34	**0.35**	0.12	**0.13**
Al_2O_3	17.94	**17.40**	16.39	**16.51**	15.27	**15.20**	11.63	**11.60**
FeO	9.94	**9.90**	8.57	**8.71**	3.60	**3.99**	1.86	**1.68**
Cr_2O_3	0.05	**0.05**	0.02	**0.02**	0.00	**0.00**	0.00	**<0.0015**
MnO	0.13	**0.13**	0.14	**0.14**	0.04	**0.05**	0.03	**0.02**
MgO	7.79	**7.70**	3.95	**3.99**	1.25	**1.20**	0.02	**0.01**
CaO	11.80	**11.90**	6.89	**6.86**	1.87	**1.80**	0.23	**0.21**
Na_2O	2.55	**2.40**	3.31	**3.30**	4.11	**4.20**	3.80	**3.78**
K_2O	0.23	**0.20**	2.20	**2.15**	4.16	**4.30**	4.87	**4.78**
P_2O_5	0.05	**0.09**	0.35	**0.32**	0.11	**0.12**	0.00	**0.00**
Total	99.27	**98.56**	97.90	**98.63**	100.16	**100.21**	100.03	**99.41**

Table A.5 continued.

	Internal standards 2010		**External standards 2010**					
	RH-21		NIM-G		NIM-L		BHVO-1	
	Measured	Expected	Measured	Expected	Measured	Expected	Measured	Expected
SiO_2	53.53	**53.70**	76.28	**75.70**	51.85	**52.40**	50.09	**49.94**
TiO_2	1.13	**1.14**	0.09	**0.09**	0.49	**0.48**	2.69	**2.71**
Al_2O_3	17.89	**17.90**	12.12	**12.08**	13.52	**13.64**	13.92	**13.80**
FeO	9.63	**9.70**	2.03	**1.90**	9.82	**9.91**	11.83	**11.40**
Cr_2O_3	0.03	**0.03**	0.00	**0.00**	0.00	**0.00**	0.04	**0.04**
MnO	0.16	**0.16**	0.02	**0.02**	0.75	**0.77**	0.17	**0.17**
MgO	4.00	**4.06**	0.09	**0.06**	0.25	**0.28**	7.37	**7.23**
CaO	5.68	**5.65**	0.79	**0.78**	3.14	**3.22**	11.38	**11.40**
Na_2O	2.37	**2.33**	3.30	**3.36**	8.72	**8.37**	2.23	**2.26**
K_2O	3.16	**3.18**	5.21	**4.99**	6.08	**5.51**	0.28	**0.52**
P_2O_5	0.43	**0.40**	0.00	**0.01**	0.03	**0.06**	0.29	**0.27**
Total	97.98	**98.22**	99.9	**99.0**	94.7	**94.6**	100.2	**99.7**

Table A.5 continued.

	External standards 2010							
	RGM-1		STM-1		AGV-1		PCC-1	
	Measured	Expected	Measured	Expected	Measured	Expected	Measured	Expected
SiO_2	73.68	**73.45**	59.75	**59.64**	59.04	**59.25**	41.94	**41.88**
TiO_2	0.28	**0.27**	0.13	**0.14**	1.10	**1.06**	0.00	**0.01**
Al_2O_3	13.78	**13.72**	18.46	**18.39**	17.24	**17.15**	0.57	**0.74**
FeO	1.87	**1.77**	5.19	**4.96**	6.87	**6.76**	8.11	**8.26**
Cr_2O_3	0.00	**0.00**	0.00	**0.00**				
MnO	0.04	**0.04**	0.21	**0.22**	0.10	**0.10**	0.12	**0.12**
MgO	0.28	**0.28**	0.11	**0.10**	1.51	**1.53**	43.52	**43.23**
CaO	1.20	**1.15**	1.15	**1.09**	4.99	**4.94**	0.51	**0.52**
Na_2O	4.28	**4.07**	8.60	**8.94**	4.31	**4.25**	0.02	**0.03**
K_2O	4.58	**4.30**	4.35	**4.28**	2.99	**2.90**	0.00	**0.01**
P_2O_5	0.04	**0.05**	0.15	**0.16**	0.49	**0.48**	0.00	**0.00**
Total	100.0	**99.1**	98.1	**97.9**	98.6	**98.4**	94.8	**94.8**

Table A.5 continued.

	Internal standards 2008							
	KC-10		KC-11		KC-12		KC-14	
	Measured	Expected	Measured	Expected	Measured	Expected	Measured	Expected
SiO_2	48.14	**48.00**	55.86	**55.55**	70.09	**69.00**	78.67	**77.20**
TiO_2	0.84	**0.84**	1.09	**1.10**	0.35	**0.35**	0.13	**0.13**
Al_2O_3	17.75	**17.40**	16.35	**16.51**	15.06	**15.20**	11.52	**11.60**
FeO	10.04	**9.90**	8.65	**8.71**	3.08	**3.99**	1.89	**1.68**
Cr_2O_3	0.05	**0.05**	0.01	**0.02**	0.00	**0.00**	0.00	**<0.0015**
MnO	0.14	**0.13**	0.14	**0.14**	0.04	**0.05**	0.03	**0.02**
MgO	7.82	**7.70**	3.96	**3.99**	1.24	**1.20**	0.01	**0.01**
CaO	11.42	**11.90**	6.79	**6.86**	1.82	**1.80**	0.22	**0.21**
Na_2O	2.52	**2.40**	3.28	**3.30**	4.04	**4.20**	3.80	**3.78**
K_2O	0.23	**0.20**	2.13	**2.15**	4.05	**4.30**	4.76	**4.78**
P_2O_5	0.05	**0.09**	0.31	**0.32**	0.12	**0.12**	0.01	**0.00**
Total	98.95	**98.56**	98.56	**98.63**	99.90	**100.21**	101.04	**99.41**

Table A.5 continued.

	Internal standards 2008		External standards 2008					
	RH-21		NIM-G		NIM-L		BHVO-1	
	Measured	Expected	Measured	Expected	Measured	Expected	Measured	Expected
SiO_2	54.21	**53.70**	76.90	**75.70**	52.80	**52.40**	50.52	**49.94**
TiO_2	1.13	**1.14**	0.09		0.46	**0.48**	2.67	**2.71**
Al_2O_3	17.73	**17.90**	12.08	**12.08**	13.40	**13.64**	13.60	**13.80**
FeO	9.56	**9.70**	2.00	**1.90**	10.03	**9.91**	12.25	**11.40**
Cr_2O_3	0.03	**0.03**	0.00	**0.00**	0.00	**0.00**	0.04	**0.04**
MnO	0.16	**0.16**	0.02	**0.02**	0.70	**0.77**	0.17	**0.17**
MgO	4.06	**4.06**	0.04	**0.06**	0.25	**0.28**	7.24	**7.23**
CaO	5.61	**5.65**	0.78	**0.78**	3.08	**3.22**	11.05	**11.40**
Na_2O	2.34	**2.33**	3.32	**3.36**	8.01	**8.37**	2.23	**2.26**
K_2O	3.11	**3.18**	5.01	**4.99**	5.18	**5.51**	0.55	**0.52**
P_2O_5	0.46	**0.40**	0.00	**0.01**	0.04	**0.06**	0.25	**0.27**
Total	98.37	**98.22**	100.24	**98.90**	93.95	**94.64**	100.52	**99.70**

Table A.5 continued.

	External standards 2008			
	RGM-1		STM-1	
	Measured	Expected	Measured	Expected
SiO_2	74.30	**73.45**	60.63	**59.64**
TiO_2	0.26	**0.27**	0.13	**0.14**
Al_2O_3	13.71	**13.72**	18.33	**18.39**
FeO	1.87	**1.77**	5.30	**4.96**
Cr_2O_3	0.00	**0.00**	0.00	**0.00**
MnO	0.03	**0.04**	0.22	**0.22**
MgO	0.28	**0.28**	0.10	**0.10**
CaO	1.18	**1.15**	1.13	**1.09**
Na_2O	4.06	**4.07**	8.81	**8.94**
K_2O	4.33	**4.30**	4.24	**4.28**
P_2O_5	0.04	**0.05**	0.15	**0.16**
Total	100.07	**99.09**	99.04	**97.91**

Table A.6 Trace element composition of standard materials at Royal Holloway

2 sets of standard analyses (both internal and external) accompany the unknown samples. One accompanies the samples whose number ends -10, the other accompanies samples whose number ends -08

	Internal standards 2010							
	KC-10		KC-11		KC-12		KC-14	
	Measured	Expected	Measured	Expected	Measured	Expected	Measured	Expected
Li	4.1	*6.0*	391.3	*380.0*	6.7	*8.0*	31.2	*38.0*
Be								
Sc	34.9	*33.0*	24.0	*24.0*	4.3	*4.0*	0.6	*<1*
V	219.2	*220.0*	211.4	*210.0*	35.9	*30.0*	2.0	*<5*
Co	38.6	*45.0*	27.8	*27.0*	7.8	*8.0*	4.0	*<2*
Ni	101.1	*104.0*	280.7	*280.0*	14.4	*15.0*	4.5	*<5*
Cu	163.2	*170.0*	108.0	*108.0*	24.3	*27.0*	4.4	*2.0*
Zn	64.5	*60.0*	122.7	*119.0*	42.9	*42.0*	108.7	*90.0*
Rb	3.6	*4.0*			61.1	*61.0*	299.1	*292.0*
Sr	364.9	*360.0*	373.7	*370.0*	457.7	*460.0*	6.8	*8.0*
Y	13.4	*13.0*	27.3	*28.0*	6.2	*6.0*	121.9	*120.0*
Zr	37.7	*38.0*	143.9	*145.0*	160.6	*160.0*	452.4	*420.0*
Nb	1.8	*2.3*			2.5	*3.5*	33.8	*30.0*
Mo	0.0	*bd*			0.0	*bd*	1.4	*bd*
Cs	0.1	*0.2*			0.3	*0.4*	7.0	*7.0*
Ba	134.2	*126.0*	498.5	*491.0*	1622.4	*1600.0*	80.5	*112.0*
La	3.8	*4.3*			36.7	*37.0*	56.5	*59.0*
Ce	9.0	*9.2*			66.8	*70.0*	120.2	*120.0*
Pr	1.2	*1.6*			6.9	*7.2*	13.0	*13.0*
Nd	6.1	*6.8*			24.9	*27.0*	53.0	*58.0*
Sm	1.7	*1.7*			3.6	*3.3*	12.9	*14.0*
Eu	0.8	*0.8*			1.3	*1.1*	0.4	*0.6*
Gd	1.6	*1.9*			2.4	*2.1*	12.6	*15.0*
Tb	0.3	*bd*			0.3	*bd*	2.8	*bd*
Dy	2.0	*2.0*			1.1	*1.2*	18.3	*18.0*
Ho	0.5	*0.4*			0.2	*0.3*	4.4	*4.0*
Er	1.3	*1.3*			0.7	*0.8*	11.6	*11.8*
Tm	0.2	*bd*			0.1	*bd*	2.0	*bd*
Yb	1.0	*1.1*			0.4	*0.5*	12.9	*11.2*
Lu	0.1	*0.2*			0.1	*0.1*	1.7	*1.5*
Hf	1.1	*1.4*			3.4	*3.5*	18.8	*19.0*
Ta	0.0	*<0.1*			0.0	*<0.1*	3.5	*3.3*
Tl	0.1	*0.2*			0.4	*0.5*	1.4	*1.6*
Pb								
Th	0.2	*<0.1*			17.1	*14.0*	26.1	*26.0*
U	0.1	*0.2*			0.2	*0.3*	6.7	*6.6*

Table A.6 continued.

	Internal standards 2010		External standards 2010					
	RH-21		NIM-G		NIM-L		BHVO-1	
	Measured	Expected	Measured	Expected	Measured	Expected	Measured	Expected
Li	33.8	*40.0*	11.8	*12.0*	42.8	*48.0*	3.3	*4.6*
Be								
Sc	24.4	*24.0*	0.8	*0.9*	0.6	*0.3*	30.4	*31.8*
V	192.5	*187.0*	2.4	*2.0*	88.1	*81.0*	303.5	*317.0*
Co	27.4	*26.0*	0.6	*0.4*	4.5	*8.0*	48.6	*45.0*
Ni	579.2	*578.0*	4.6	*8.0*	8.9	*11.0*	115.6	*121.0*
Cu	77.0	*75.0*	11.9	*12.0*	26.4	*13.0*	137.6	*136.0*
Zn	101.4	*98.0*	52.6	*50.0*	403.2	*400.0*	101.9	*105.0*
Rb	105.4	*105.0*					11.1	*11.0*
Sr	301.0	*303.0*	11.7	*10.0*	4662.9	*4600.0*	394.0	*403.0*
Y	30.7	*30.0*	133.5	*143.0*	23.7	*22.0*	29.0	*27.6*
Zr	147.7	*144.0*	285.3	*300.0*	11563.7	*11000.0*	176.4	*179.0*
Nb	12.6	*12.0*					18.9	*19.0*
Mo	0.4	*bd*					1.1	*1.0*
Cs	3.9	*3.7*					0.1	*0.1*
Ba	753.2	*754.0*	113.6	*120.0*	423.2	*450.0*	131.9	*139.0*
La	14.3	*13.0*					15.8	*15.8*
Ce	38.3	*33.0*					38.9	*39.0*
Pr	4.0	*3.6*					5.3	*5.7*
Nd	17.5	*18.0*					25.4	*25.2*
Sm	3.8	*3.3*					6.4	*6.2*
Eu	1.2	*1.6*					2.1	*2.1*
Gd	3.4	*3.2*					5.8	*6.4*
Tb	0.6	*bd*					1.0	*1.0*
Dy	4.4	*4.6*					5.4	*5.2*
Ho	1.2	*1.0*					1.1	*1.0*
Er	3.4	*2.5*					2.7	*2.4*
Tm	0.5	*bd*					0.3	*0.3*
Yb	3.4	*3.3*					2.0	*2.0*
Lu	0.5	*0.4*					0.3	*0.3*
Hf	3.5	*2.3*					4.2	*4.4*
Ta	0.7	*0.6*					1.2	*1.2*
Tl	0.8	*0.9*					0.1	*0.1*
Pb								
Th	10.5	*9.5*					1.2	*1.1*
U	2.3	*2.2*					0.7	*0.4*

Table A.6 continued.

	External standards 2010							
	RGM-1		STM-1		AGV-1		PCC-1	
	Measured	Expected	Measured	Expected	Measured	Expected	Measured	Expected
Li	66.0	*57.0*	37.7	*32.0*				
Be								
Sc	4.5	*4.4*	0.9	*0.6*				
V	12.2	*13.0*	7.9	*8.7*				
Co	3.3	*2.0*	1.3	*0.9*				
Ni	5.9	*4.4*	3.2	*3.0*				
Cu	11.8	*11.6*	6.2	*4.6*				
Zn	32.2	*32.0*	226.6	*235.0*	84.5	*88.0*	48.4	*42.0*
Rb	149.7	*149.0*	115.7	*118.0*				
Sr	113.1	*108.0*	667.2	*700.0*	689.7	*662.0*	0.6	*0.4*
Y	24.6	*25.0*	43.4	*46.0*	21.4	*21.0*	0.0	*bd*
Zr	231.1	*219.0*	1173.2	*1210.0*	228.6	*225.0*	0.9	*0.3*
Nb	8.9	*8.9*	265.9	*268.0*				
Mo	2.5	*2.3*	4.8	*5.2*				
Cs	9.9	*9.6*	1.5	*1.5*				
Ba	941.9	*807.0*	552.4	*560.0*	1265.7	*1221.0*	0.8	*1.2*
La	24.0	*24.0*	151.0	*150.0*				
Ce	47.2	*47.0*	267.6	*259.0*				
Pr	5.2	*4.7*	24.7	*19.0*				
Nd	19.7	*19.0*	81.4	*79.0*				
Sm	4.2	*4.3*	12.6	*12.6*				
Eu	0.7	*0.7*	3.5	*3.6*				
Gd	3.6	*3.7*	10.2	*9.5*				
Tb	0.7	*0.7*	1.5	*1.6*				
Dy	3.8	*4.1*	8.1	*8.1*				
Ho	0.9	*1.0*	1.7	*1.9*				
Er	2.5	*2.6*	4.4	*4.2*				
Tm	0.4	*0.4*	0.7	*0.7*				
Yb	2.6	*2.6*	4.3	*4.4*				
Lu	0.4	*0.4*	0.6	*0.6*				
Hf	6.3	*6.2*	28.2	*28.0*				
Ta	0.9	*1.0*	19.8	*18.6*				
Tl	1.0	*0.9*	0.3	*0.3*				
Pb								
Th	14.3	*15.1*	30.2	*31.0*				
U	5.6	*5.8*	8.1	*9.1*				

Table A.6 continued.

	Internal standards 2008							
	KC-10		KC-11		KC-12		KC-14	
	Measured	Expected	Measured	Expected	Measured	Expected	Measured	Expected
Li	6.9	*6.0*	433.9	*380.0*	8.2	*8.0*	34.6	*38.0*
Be	0.5		7.4		1.2		8.8	
Sc	34.5	*33.0*	23.2	*24.0*	4.3	*4.0*	0.0	*<1*
V	238.2	*220.0*	212.4	*210.0*	36.4	*30.0*	1.6	*<5*
Co	40.8	*45.0*	26.9	*27.0*	7.4	*8.0*	4.3	*<2*
Ni	106.7	*104.0*	282.7	*280.0*	12.1	*15.0*	1.0	*<5*
Cu	180.1	*170.0*	108.3	*108.0*	23.5	*27.0*	4.7	*2.0*
Zn	73.7	*60.0*	120.9	*119.0*	51.7	*42.0*	112.2	*90.0*
Rb	3.2	*4.0*	235.0	*270.0*	49.9	*61.0*	246.7	*292.0*
Sr	345.0	*360.0*	370.0	*370.0*	441.8	*460.0*	7.8	*8.0*
Y	12.9	*13.0*	27.2	*28.0*	5.5	*6.0*	128.6	*120.0*
Zr	34.1	*38.0*	149.0	*145.0*	153.9	*160.0*	531.2	*420.0*
Nb	0.8	*2.3*	8.3	*12.0*	0.8	*3.5*	29.4	*30.0*
Mo								
Cs	0.3	*0.2*	47.4	*47.0*	0.5	*0.4*	7.2	*7.0*
Ba	146.9	*126.0*	501.7	*491.0*	1633.0	*1600.0*	90.9	*112.0*
La	5.5	*4.3*	24.5	*23.0*	36.9	*37.0*	55.3	*59.0*
Ce	9.7	*9.2*	49.3	*49.0*	64.6	*70.0*	117.9	*120.0*
Pr	1.7	*1.6*	6.3	*5.9*	7.2	*7.2*	13.1	*13.0*
Nd	7.4	*6.8*	26.7	*26.5*	26.0	*27.0*	53.3	*58.0*
Sm	1.7	*1.7*	5.5	*5.2*	3.6	*3.3*	14.0	*14.0*
Eu	0.8	*0.8*	1.5	*1.4*	1.3	*1.1*	0.5	*0.6*
Gd	1.6	*1.9*	4.7	*5.0*	2.7	*2.1*	12.5	*15.0*
Tb	0.4	-	0.9	-	0.4	-	3.1	-
Dy	2.0	*2.0*	4.4	*4.5*	1.2	*1.2*	17.5	*18.0*
Ho	0.4	*0.4*	0.9	*1.0*	0.2	*0.3*	3.7	*4.0*
Er	1.2	*1.3*	2.3	*2.7*	0.7	*0.8*	10.6	*11.8*
Tm	0.2	-	0.4	-	0.1	-	2.0	-
Yb	1.2	*1.1*	2.5	*2.2*	0.5	*0.5*	14.3	*11.2*
Lu	0.2	*0.2*	0.4	*0.3*	0.1	*0.1*	2.0	*1.5*
Hf	1.1	*1.4*	4.0	*3.3*	4.3	*3.5*	21.8	*19.0*
Ta	0.0	*<0.1*	7.5	*5.0*	0.1	*<0.1*	4.0	*3.3*
Tl	-0.1	*0.2*	1.2	*1.5*	0.2	*0.5*	1.1	*1.6*
Pb	5.3	*1.0*	12.4	*8.0*	14.8	*10.0*	32.2	*26.0*
Th	0.0	*<0.1*	2.9	*2.4*	24.6	*14.0*	31.7	*26.0*
U	0.2	*0.2*	2.1	*1.8*	0.5	*0.3*	7.4	*6.6*

Table A.6 continued.

	Internal standards 2008		External standards 2008					
	RH-21		NIM-G		NIM-L		BHVO-1	
	Measured	Expected	Measured	Expected	Measured	Expected	Measured	Expected
Li	38.1	*40.0*	13.4	*12.0*	49.9	*48.0*	6.5	*4.6*
Be	1.8		7.6	*7.8*	29.1	*29.5*	0.8	*1.1*
Sc	23.9	*24.0*	0.5	*0.9*	0.4	*0.5*	31.7	*31.8*
V	190.8	*187.0*	1.3	*2.0*	96.4	*81.0*	307.0	*317.0*
Co	25.5	*26.0*	1.0	*0.4*	4.7	*2.4*	45.0	*45.0*
Ni	571.3	*578.0*	2.5	*8.0*	0.3	*2.2*	111.8	*121.0*
Cu	77.9	*75.0*	10.0	*12.0*	23.7	*13.0*	133.7	*136.0*
Zn	106.0	*98.0*	49.3	*50.0*	372.4	*395.0*	104.0	*105.0*
Rb	83.4	*105.0*	242.7	*325.0*	139.2	*190.0*	6.8	*11.0*
Sr	300.3	*303.0*	13.2	*10.0*	4392.1	*4600.0*	386.3	*403.0*
Y	30.9	*30.0*	145.7	*143.0*	22.9	*22.0*	28.2	*27.6*
Zr	150.9	*144.0*	281.6	*300.0*	10498.1	*11000.0*	217.3	*179.0*
Nb	8.2	*12.0*	41.2	*53.0*	814.4	*960.0*	19.7	*19.0*
Mo								
Cs	3.9	*3.7*	1.0	*1.1*	2.6	*2.8*	0.2	*0.2*
Ba	735.7	*754.0*	122.1	*120.0*	395.3	*450.0*	134.9	*139.0*
La	15.1	*13.0*	104.7	*109.0*	206.4	*250.0*	16.0	*15.8*
Ce	36.1	*33.0*	188.8	*195.0*	262.8	*240.0*	35.5	*39.0*
Pr	4.4	*3.6*	19.6	*19.5*	18.4	*16.4*	5.3	*5.7*
Nd	18.6	*8.0*	71.9	*72.0*	47.0	*48.0*	25.1	*25.2*
Sm	3.9	*3.3*	15.8	*15.8*	4.3	*5.0*	6.3	*6.2*
Eu	1.2	*1.6*	0.3	*0.4*	1.1	*1.2*	2.1	*2.1*
Gd	3.2	*3.2*	13.9	*14.0*	5.4	*3.6*	5.4	*6.4*
Tb	0.8	-	3.1	*3.1*	0.7	*0.7*	1.1	*1.0*
Dy	4.3	*4.6*	17.3	*17.0*	2.9	*3.1*	5.0	*5.2*
Ho	1.0	*1.0*	3.7	*3.6*	0.7	*0.9*	0.9	*1.0*
Er	2.9	*2.5*	10.8	*10.5*	2.1	*2.6*	2.2	*2.4*
Tm	0.5	-	2.1	*2.0*	0.4	-	0.4	*0.3*
Yb	3.6	*3.3*	15.2	*14.2*	2.8	*3.0*	2.3	*2.0*
Lu	0.5	*0.4*	2.2	*2.0*	0.5	*0.4*	0.3	*0.3*
Hf	4.1	*2.3*	12.9	*12.4*	222.0	*231.0*	5.1	*4.4*
Ta	1.0	*0.6*	5.8	*4.9*	26.0	*25.2*	1.4	*1.2*
Tl	0.5	*0.9*	0.7	*0.9*	0.1	*0.1*	-0.1	*0.1*
Pb	17.8	-	39.5	*40.0*	48.4	*43.0*	6.9	*2.6*
Th	11.9	*9.5*	56.2	*51.0*	71.5	*66.0*	1.1	*1.1*
U	2.6	*2.2*	16.8	*15.0*	16.1	*14.0*	0.7	*0.4*

a- Nb and Rb loss occurred for the 2008 standard analyses. Unknown sample Nb and Rb data for samples ending -08 was not used.

Table A.6 continued.

	External standards 2008			
	RGM-1		STM-1	
	Measured	Expected	Measured	Expected
Li	70.7	*57.0*	40.1	*32.0*
Be	2.3	*2.4*	9.4	*9.6*
Sc	4.4	*4.4*	0.6	*0.6*
V	11.6	*13.0*	5.5	*8.7*
Co	3.3	*2.0*	1.6	*0.9*
Ni	2.1	*4.4*	1.4	*3.0*
Cu	10.9	*11.6*	8.4	*4.6*
Zn	33.4	*32.0*	228.2	*235.0*
Rb	112.9	*149.0*	84.4	*118.0*
Sr	102.4	*108.0*	683.4	*700.0*
Y	26.1	*25.0*	42.8	*46.0*
Zr	222.6	*219.0*	1234.6	*1210.0*
Nb	8.9	*8.9*	204.0	*268.0*
Mo				
Cs	9.7	*9.6*	1.6	*1.5*
Ba	818.7	*807.0*	572.4	*560.0*
La	23.0	*24.0*	139.0	*150.0*
Ce	43.2	*47.0*	247.1	*247.0*
Pr	5.3	*4.7*	23.1	*19.0*
Nd	20.0	*19.0*	79.7	*79.0*
Sm	4.2	*4.3*	12.8	*12.6*
Eu	0.8	*0.7*	3.5	*4.2*
Gd	3.4	*3.7*	10.1	*9.5*
Tb	0.7	*0.7*	1.7	*1.6*
Dy	3.6	*4.1*	7.6	*8.0*
Ho	0.8	*1.0*	1.4	*1.9*
Er	2.2	*2.6*	3.8	*4.2*
Tm	0.4	*0.4*	0.7	*0.7*
Yb	2.7	*2.6*	4.7	*4.4*
Lu	0.4	*0.4*	0.7	*0.6*
Hf	6.5	*6.2*	29.3	*28.0*
Ta	1.1	*1.0*	21.6	*18.6*
Tl	0.6	*0.9*	0.1	*0.3*
Pb	26.3	*24.0*	23.3	*17.7*
Th	13.8	*15.1*	34.3	*31.0*
U	5.5	*5.8*	8.4	*9.1*

B. Correction of major element composition to 8.5 wt % MgO

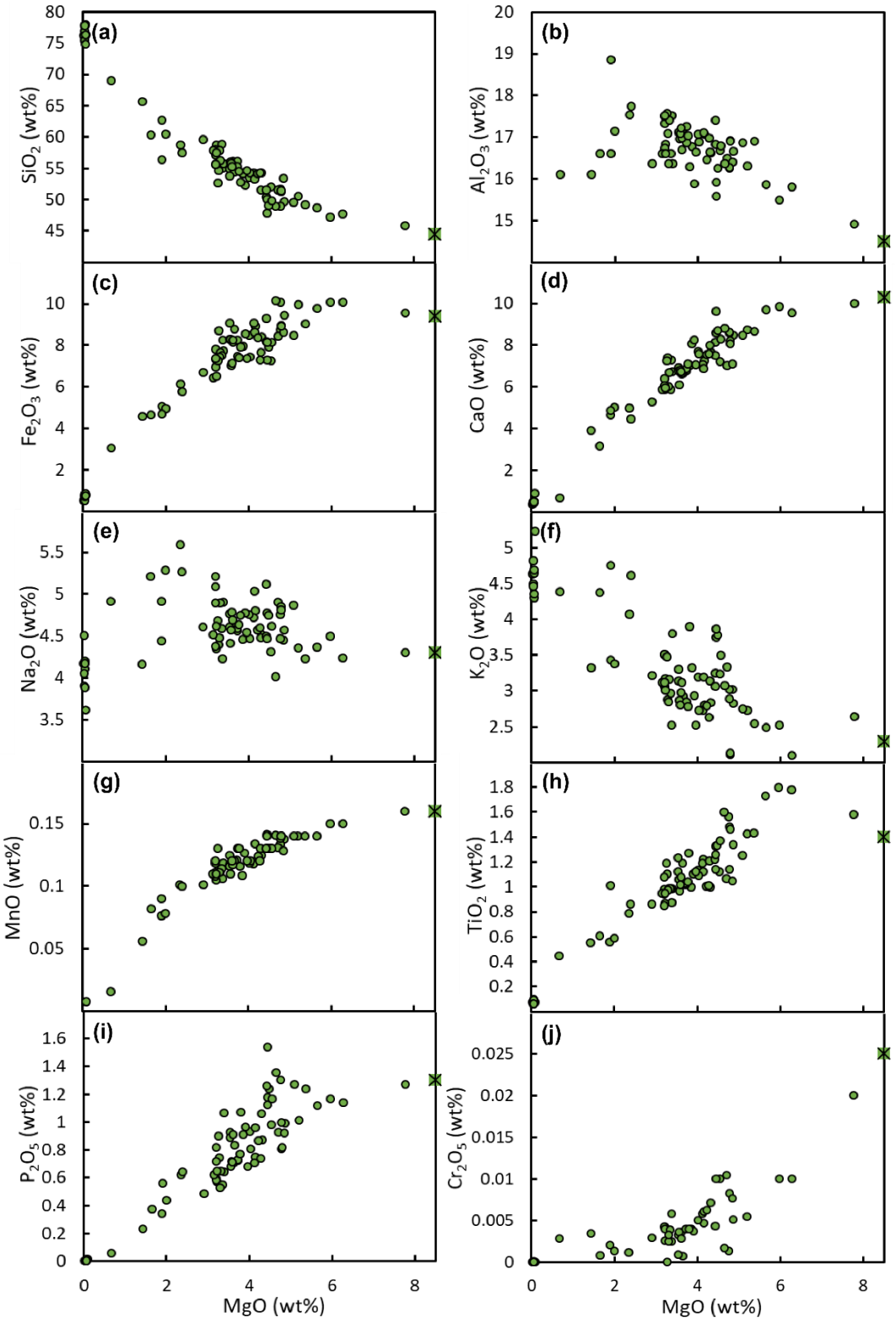

Figure B.1 Extrapolation of major element composition of magmas from Syunik volcanic highland to MgO = 8.5 wt%

Green box with black star represents value used for basalt geothermobarometry in Chapter 3. Green circles are all Syunik major element data. (a) SiO_2. (b) Al_2O_3. (c) Fe_2O_3 (tot). (d) CaO. (e) Na_2O. (f) K_2O. (g) MnO. (h) TiO_2. (i) P_2O_5. (j) Cr_2O_3.

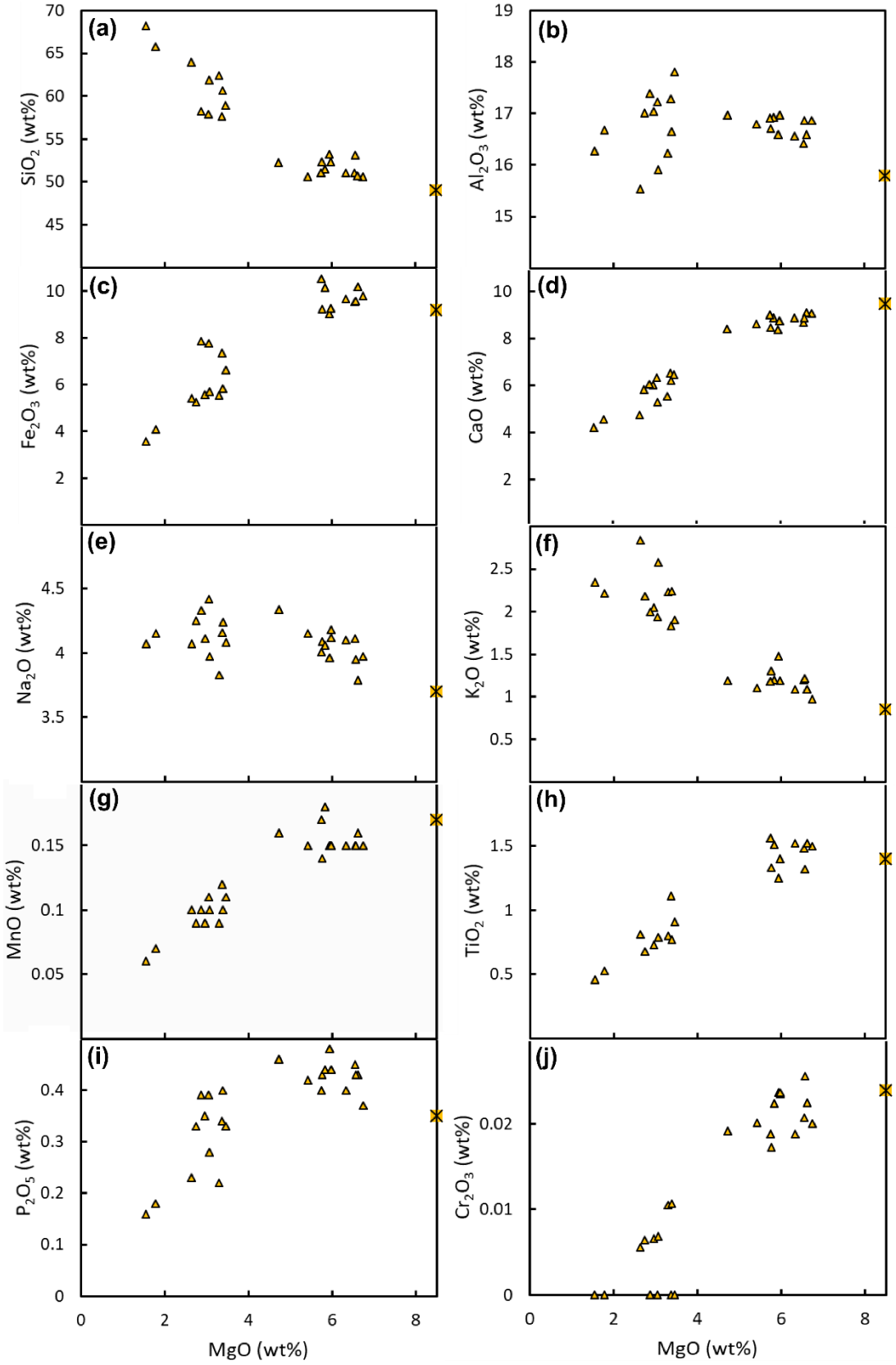

Figure B.2 Extrapolation of major element composition of magmas from Shirak and Lori highland to MgO = 8.5 wt%

Yellow box with black star represents value used for basalt geothermobarometry in Chapter 3. Yellow triangles are the Shirak and Lori highland major element data (Neill et al., 2013, 2015). (a) SiO_2. (b) Al_2O_3. (c) Fe_2O_3 (tot). (d) CaO. (e) Na_2O. (f) K_2O. (g) MnO. (h) TiO_2. (i) P_2O_5. (j) Cr_2O_3.

C. Literature ages of Lesser Caucasus volcanic rocks

Table C.1 Ages of Lesser Caucasus volcanic rocks from both this thesis and the literature Samples shown in bold also have major and trace element data listed in Appendix A.

Sample	Region	Rock Type	Eruptive Type	**Age (Ma)**	Error (2σ)	Technique	Source
2.10.08	Syunik	Basalt	cone	0.861	0.015	Ar-Ar	This study
11.3.15	Syunik	Tephrite	cone	0.048	0.018	Ar-Ar	This study
11.1.15	Syunik	Trachybasaltic andesite	lava	0.37	0.008	Ar-Ar	This study
10.2.15	Syunik	Trachybasaltic andesite	lava	0.167	0.005	Ar-Ar	This study
2.7.08	Syunik	Phonotephrite	cone	0.893	0.012	Ar-Ar	This study
4.15A.08	Syunik	Rhyolite	lava	0.672	0.009	Ar-Ar	This study
6.3.15	Vardenis	Trachybasaltic andesite	lava	1.301	0.014	Ar-Ar	This study
8.3.15	Syunik	Trachybasaltic andesite	cone	0.957	0.012	Ar-Ar	This study
9.1.15	Syunik	Trachybasaltic andesite	lava	0.817	0.011	Ar-Ar	This study
9.2.15	Syunik	Trachybasalt	cone	0.571	0.012	Ar-Ar	This study
5.5.12	Syunik	Trachyandesite	lava	1.316	0.014	Ar-Ar	This study
T5	Syunik		tuff	1.24	0.03	Ar-Ar	Joannin et al., 2010
T7	Syunik		tuff	1.16	0.02	Ar-Ar	Joannin et al., 2010
V0-02	Syunik		lava	0.993	0.022	K-Ar	Ollivier et al., 2010
PR-5	Syunik		lava	0.942	0.02	K-Ar	Ollivier et al., 2010
V0-01	Syunik		lava	0.939	0.02	K-Ar	Ollivier et al., 2010

Table C.1 continued.

Sample	Region	Rock Type	Eruptive Type	**Age (Ma)**	Error (2σ)	Technique	Source
PR-7	Syunik		lava	0.934	0.02	K-Ar	Ollivier et al., 2010
PR-4	Syunik		lava	0.934	0.02	K-Ar	Ollivier et al., 2010
SHAMB-22	Syunik		lava	0.819	0.018	K-Ar	Ollivier et al., 2010
UY-04	Syunik		lava	0.475	0.011	K-Ar	Ollivier et al., 2010
PR-6	Syunik		lava	0.126	0.003	K-Ar	Ollivier et al., 2010
PR-2	Syunik		lava	0.122	0.003	K-Ar	Ollivier et al., 2010
PR-1	Syunik		lava	0.111	0.004	K-Ar	Ollivier et al., 2010
PR-3	Syunik	Trachybasaltic andesite	cone	0		K-Ar	Ollivier et al., 2010
6.26.08	Syunik	Trachyandesite	lava	0.005	0	Archeo-logical	Karakhanian et al., 2002
5.3.15	Vardenis	Trachyandesite	lava	0.003	0	Archeo-logical	Karakhanian et al., 2002
7.29.08	Vardenis	Trachybasaltic andesite	cone	1.4	0.03	K-Ar	Philip et al., 2001
G-43/03	Gegham	Trachybasalt	lava	0.98	0.08	K-Ar	Lebedev et al., 2013
G-44/03	Gegham	Trachybasalt	lava	0.95	0.06	K-Ar	Lebedev et al., 2013
13G/01	Gegham	Rhyolite	lava	0.66	0.04	K-Ar	Lebedev et al., 2013
14G/01	Gegham	Rhyolite	lava	0.74	0.25	K-Ar	Lebedev et al., 2013
24G/01	Gegham	Rhyolite	lava	0.7	0.03	K-Ar	Lebedev et al., 2013
25G/01	Gegham	Rhyolite	lava	0.77	0.12	K-Ar	Lebedev et al., 2013
28G/01	Gegham	Rhyolite	lava	1.2	0.5	K-Ar	Lebedev et al., 2013
G-108/03	Gegham	Trachyte	lava	0.72	0.06	K-Ar	Lebedev et al., 2013
G117/03	Gegham	Rhyolite	lava	0.9	0.3	K-Ar	Lebedev et al., 2013
17G/01	Gegham	Trachybasaltic andesite	lava	0.56	0.04	K-Ar	Lebedev et al., 2013
18G/01	Gegham	Trachybasaltic andesite	lava	0.58	0.05	K-Ar	Lebedev et al., 2013

Table C.1 continued.

Sample	Region	Rock Type	Eruptive Type	**Age (Ma)**	Error (2σ)	Technique	Source
23G/01	Gegham	Trachybasaltic andesite	lava	0.56	0.04	K-Ar	Lebedev et al., 2013
33G/01	Gegham	Trachyandesite	lava	0.53	0.04	K-Ar	Lebedev et al., 2013
34G/01	Gegham	Trachybasaltic andesite	lava	0.56	0.04	K-Ar	Lebedev et al., 2013
G73-03	Gegham	Trachyte	lava	0.54	0.02	K-Ar	Lebedev et al., 2013
G-74/03	Gegham	Trachybasaltic andesite	lava	0.53	0.03	K-Ar	Lebedev et al., 2013
15G/01	Gegham	Rhyolite	lava	0.48	0.05	K-Ar	Lebedev et al., 2013
19G/01	Gegham	Rhyolite	lava	0.38	0.06	K-Ar	Lebedev et al., 2013
26G/01	Gegham	Rhyolite	lava	0.48	0.04	K-Ar	Lebedev et al., 2013
29G/01	Gegham	Rhyolite	dome	0.48	0.05	K-Ar	Lebedev et al., 2013
G-110/03	Gegham	Rhyolite	lava	0.47	0.03	K-Ar	Lebedev et al., 2013
3G/01	Gegham	Trachybasaltic andesite	lava	0.18	0.04	K-Ar	Lebedev et al., 2013
4G/01	Gegham	Trachyandesite	lava	0.16	0.04	K-Ar	Lebedev et al., 2013
6G/01	Gegham	Trachyandesite	lava	0.16	0.04	K-Ar	Lebedev et al., 2013
7G/01	Gegham	Andesite	lava	0.15	0.04	K-Ar	Lebedev et al., 2013
8G/01	Gegham	Trachyandesite	lava	0.16	0.03	K-Ar	Lebedev et al., 2013
30G/01	Gegham	Trachyandesite	lava	0.18	0.04	K-Ar	Lebedev et al., 2013
31G/01	Gegham	Trachyandesite	lava	0.15	0.03	K-Ar	Lebedev et al., 2013
32G/01	Gegham	Trachyandesite	lava	0.16	0.03	K-Ar	Lebedev et al., 2013
G-5/03	Gegham	Trachyandesite	lava	0.15	0.03	K-Ar	Lebedev et al., 2013
G-39/03	Gegham	Trachyandesite	lava	0.16	0.03	K-Ar	Lebedev et al., 2013
G70/03	Gegham	Trachybasaltic andesite	lava	0.25	0.07	K-Ar	Lebedev et al., 2013

Table C.1 continued.

Sample	Region	Rock Type	Eruptive Type	**Age (Ma)**	Error (2σ)	Technique	Source
G93/03	Gegham	Rhyolite	lava	0.2	0.02	K-Ar	Lebedev et al., 2013
2G/01	Gegham	Trachybasaltic andesite	lava	0.07	0.04	K-Ar	Lebedev et al., 2013
9G/01	Gegham	Trachybasaltic andesite	lava	0.08	0.04	K-Ar	Lebedev et al., 2013
G-47/03	Gegham	Trachyandesite	lava	0.07	0.03	K-Ar	Lebedev et al., 2013
G-50/03	Gegham	Trachybasaltic andesite	lava	0.11	0.05	K-Ar	Lebedev et al., 2013
G-51/03	Gegham	Trachybasalt	lava	0.1	0.06	K-Ar	Lebedev et al., 2013
G-83/03	Gegham	Rhyolite	lava	0.13	0.08	K-Ar	Lebedev et al., 2013
G-84/03	Gegham	Rhyolite	lava	0.1	0.02	K-Ar	Lebedev et al., 2013
GaG/01	Gegham	Trachybasaltic andesite	cone	0.06	0.04	K-Ar	Lebedev et al., 2013
5bG/01	Gegham	Trachyandesite	lava	0.02	0.02	K-Ar	Lebedev et al., 2013
4.15A.08	Syunik	Rhyolite	lava	0.61	0.2	AFT	Karapetian et al., 2001
5.20A.08	Syunik	Rhyolite	lava	0.3	0.2	AFT	Karapetian et al., 2001
4.18A.08	Syunik	Rhyolite	lava	0.9	0.2	K-Ar	Karapetian et al., 2001
4.18A.08	Syunik	Rhyolite	lava	0.64	0.2	AFT	Karapetian et al., 2001
4.19.10	Syunik	Trachyte	lava	0.7	0.2	K-Ar	Karapetian et al., 2001

D. ^{40}Ar-^{39}Ar ages experimental data

This appendix summaries the results of Ar-Ar dating at the Scottish Universities Environmental Research Centre. Table D.1 provides a full summary of the key age data for each sample. Table D.2 summarises the results of the step heating experiments, with abundances of each argon isotope reported for each step. Table D.3 reports the results of total fusions of sanidine phenocrysts from sample 5.1.15. Table D.4 shows the assumed isotope ratios, decay constants and nucleogenic production ratios used in age calculations.

Table D.1 Summary of ^{40}Ar-^{39}Ar ages including the J parameter, integrated ages, plateau ages and isochron ages

sample	2-10-08			11-3-15			11-1-15
Instrument	MAP215-50			MAP215-50			ARGUS-V
material	Groundmass			Groundmass			Groundmass
Experiment	1	2	composite	1	2	composite	1
J	0.000490			0.000494			0.000054
± 2σ	0.000002			0.000002			0.000003
int. 40Ar*/ 39ArK	1.001	0.969	0.356	0.045	0.075	0.064	0.356
± 2σ	0.014	0.012	0.010	0.027	0.045	0.044	0.010
int. age (Ma)	0.886	0.857	0.348	0.040	0.067	0.057	0.348
± 2σ	0.024	0.022	0.020	0.049	0.080	0.078	0.020
%rad.	37.1	38.9	9.0	0.7	1.0	0.9	9.0
plateau Ca/K	14.37	20.81	2.530	4.49	4.86	4.78	2.530
± 2σ	0.13	0.08	0.002	0.04	0.03	0.02	0.002
Plat. Age	0.878	0.853	**0.370**	0.042	0.055	**0.048**	**0.370**
± 2σ w/o J	0.024	0.016	0.008	0.024	0.025	0.018	0.008
± 2σ w/J	0.025	0.018	**0.008**	0.024	0.025	**0.018**	**0.008**
MSWD	1.0	1.3	1.0	0.8	1.0	0.9	1.0
Prob.	0.42	0.25	0.47	0.70	0.44	0.63	0.47
Steps	C-M	C-M	E-P	A-M	A-Q	A-Q	E-P
N	11	11	12	13	17	30	12
N-total	14	14	15	13	17	30	15
%gas	81	81	94	100	100	100	94
Isochron age (Ma)	0.913	0.878	0.383	0.057	0.026	0.041	0.383
±2σ w/o J	0.071	0.035	0.010	0.033	0.013	0.015	0.010
±2σ w/J	0.071	0.036	0.011	0.034	0.013	0.015	0.011
n	11	11	13	13	17	30	13
MSWD	1.02	1.09	0.75	0.81	1.01	0.92	0.75
p	0.42	0.37	0.70	0.64	0.44	0.59	0.70
$^{40}Ar/^{36}Ar_{(i)}$	289.6	289.9	296.0	297.7	300.4	299.0	296.0
±2σ	17.2	10.8	1.3	3.9	3.7	2.7	1.3

Table D.1 continued.

sample	10-2-15			2-7-08		
Instrument	ARGUS-V			ARGUS-V		
Material	Groundmass			Groundmass		
Experiment	1	2	composite	1	2	composite
J	0.000528			0.000541		
± 2σ	0.000003			0.000003		
int. $^{40}Ar^*/^{39}Ar(K)$	0.154	0.147	0.161	0.907	0.903	0.915
± 2 σ	0.004	0.008	0.005	0.015	0.016	0.015
int. age (Ma)	0.147	0.140	0.154	0.887	0.883	0.895
± 2σ	0.008	0.016	0.009	0.029	0.032	0.030
%rad.	20.1	9.9	18.0	2.9	2.9	3.0
plateau						
Ca/K	10.64	9.327	9.571	1.9933	2.0261	2.0070
± 2σ	0.02	0.007	0.006	0.0003	0.0004	0.0003
Plat. Age	0.164	0.175	**0.167**	0.894	0.892	**0.893**
± 2σ w/o J	0.006	0.010	0.005	0.010	0.012	0.007
± 2σ w/J	0.006	0.010	**0.005**	0.014	0.015	**0.012**
MSWD	1.5	1.6	1.6	0.8	1.0	0.9
Prob.	0.17	0.09	0.04	0.65	0.41	0.62
Steps	H-O	D-P	D-P	C-P	B-P	B-P
N	8	13	21	14	15	29
N-total	15	15	21	16	15	29
%gas	76	86	100	99	100	100
Isochron						
age (Ma)	0.173	0.157	0.164	0.896	0.901	0.898
±2σ w/o J	0.011	0.022	0.011	0.012	0.015	0.010
±2σ w/J	0.011	0.022	0.011	0.016	0.018	0.014
n	8	13	21	14	15	29
MSWD	1.06	1.45	1.68	0.85	0.86	0.83
p	0.39	0.14	0.03	0.60	0.59	0.71
$^{40}Ar/^{36}Ar_{(i)}$	292.0	304.6	300.3	298.5	298.4	298.5
±2σ	6.4	7.1	5.2	0.2	0.2	0.1

Table D.1 continued.

sample		4-15A-08		6-3-15	8-3-15b	9-1-15
Instrument		ARGUS-V		ARGUS-V	ARGUS-V	ARGUS-V
material		Obsidian		Groundmass	Groundmass	Groundmass
Experiment	1	2	composite	1	1	1
J		0.000532		0.000542	0.000536	0.000535
± 2σ		0.000003		0.000003	0.000003	0.000003
int. 40Ar*/ 39ArK	0.712	0.695	0.699	1.325	0.967	0.787
± 2σ	0.006	0.007	0.006	0.004	0.004	0.006
int. age (Ma)	0.685	0.669	0.672	1.299	0.937	0.761
± 2σ	0.011	0.013	0.011	0.008	0.008	0.011
%rad.	14.7	13.8	14.3	69.6	46.4	63.2
plateau						
Ca/K	0.0845	0.0847	0.0846	2.5963	0.9611	3.569
± 2σ	0.0001	0.0001	0.0001	0.0010	0.0003	0.003
Plat. Age	0.674	0.670	**0.672**	**1.301**	**0.957**	**0.817**
± 2σ w/o J	0.006	0.007	0.005	0.004	0.006	0.006
± 2σ w/J	0.010	0.010	**0.009**	**0.014**	**0.012**	**0.011**
MSWD	1.3	1.5	1.4	1.0	1.7	1.1
Prob.	0.24	0.11	0.10	0.44	0.09	0.39
Steps	E-O	D-P	D-P	B-P	A-I	E-M
N	11	13	24	15	9	9
N-total	15	15	24	15	16	15
%gas	95	99	100	100.0	89	82
Isochron						
age (Ma)	0.807	0.780	0.780	1.307	0.973	0.820
± 2σ w/o J	0.322	0.221	0.140	0.016	0.047	0.019
± 2σ w/J	0.322	0.221	0.140	0.032	0.048	0.021
n	11	13	24	15	9	9
MSWD	1.37	1.56	1.34	0.84	1.84	1.20
p	0.20	0.11	0.13	0.61	0.08	0.30
$^{40}Ar/^{36}Ar_{(i)}$	288.4	290.5	290.5	293.3	293.7	294.8
± 2σ	30.2	19.3	12.0	5.8	14.2	21.8

Table D.1 continued.

sample	9-2-15	5-5-12	5-1-15
Instrument	ARGUS-V	ARGUS-V	MAP215-50
material	Groundmass	Groundmass	Feldspar
Experiment	1	1	
J	0.000543	0.000537	0.000543
± 2σ	0.000003	0.000003	0.000003
int. 40Ar*/ 39ArK	0.571	1.341	-
± 2σ	0.007	0.004	-
int. age (Ma)	0.561	1.303	-
± 2σ	0.014	0.007	-
%rad.	36.0	63.3	-
plateau			**Single grain population age**
Ca/K	15.62	0.9674	
± 2σ	0.01	0.0002	
Plat. Age	**0.571**	**1.316**	**6.014**
± 2σ w/o J	0.010	0.005	0.018
± 2σ w/J	**0.012**	**0.014**	**0.067**
MSWD	1.5	1.2	1.3
Prob.	0.10	0.31	0.08
Steps	A-P	E-L	-
N	16	8	43
N-total	16	15	50
%gas	100	90	-
Isochron age (Ma)	0.569	1.311	6.017
± 2σ w/o J	0.022	0.015	0.071
± 2σ w/J	0.023	0.020	0.030
n	16	8	43
MSWD	1.59	1.27	1.34
p	0.08	0.27	0.07
$^{40}Ar/^{36}Ar_{(i)}$	299.4	302.5	294.0
± 2σ	6.9	11.0	32

Table D.2 Results of step-heating experiments

Errors are 2σ

Sample	10.2.15						
Run	1						
Step	a	b	c	d	e	f	g
Age(Ma)	4260.003	-1.707016	-0.287321	-0.270684	0.1078302	0.1405373	0.1326228
error	82350.61	0.7689077	0.2464183	0.1051251	0.0314107	0.0136264	0.0089188
% 40Ar*	464.9502	-22.76526	-7.638549	-13.75514	10.98236	23.10304	27.69485
Ca/K	-63.82515	1.727209	1.636152	1.645358	1.560644	1.326563	1.119817
Cl/K	-52.7417	-0.000348	0.0174706	0.0124096	0.0020187	-0.000629	-0.001015
40Ar	0.0024414	0.0336033	0.0880558	0.1300949	0.1622144	0.1931449	0.2171633
error	0.0001415	0.0001564	0.0001985	0.0002062	0.0002642	0.0002642	0.000222
39Ar	6.13E-07	0.0042783	0.0223372	0.0630691	0.157538	0.3026021	0.4320292
error	0.0000309	0.0000677	0.0001707	0.0003004	0.0004103	0.0006502	0.0007402
38Ar	-0.000017	0.0000778	0.0004672	0.0011337	0.002125	0.0037238	0.0052237
error	0.0000125	0.0000189	0.0000394	0.0000533	0.0000424	0.0000345	0.0000276
37Ar	-5.73E-06	0.0010573	0.0052211	0.0148191	0.0350544	0.0571487	0.0687734
error	0.0000136	0.0000219	0.0000425	0.0000713	0.0000912	0.0001202	0.0001202
36Ar	-2.99E-05	0.0001392	0.0003224	0.0005096	0.0005166	0.0005512	0.0005906
error	9.90E-06	0.0000115	0.0000193	0.0000232	0.0000173	0.0000144	0.0000134

Sample	10.2.15						
Run	1						
Step	h	i	j	k	l	m	n
Age(Ma)	0.1774579	0.1694759	0.1698076	0.1557447	0.1668223	0.1444905	0.153775
error	0.0088063	0.0065506	0.0057736	0.0053571	0.0074305	0.0107837	0.0306411
% 40Ar*	40.78227	38.56948	35.5988	27.44791	22.46382	12.37731	7.033835
Ca/K	0.9858537	0.9225727	0.9433973	1.071335	1.467461	2.492631	7.815812
Cl/K	-0.001179	-0.00133	-0.001275	-0.001283	-0.000972	0.0003397	0.0024272
40Ar	0.2294302	0.2152399	0.2901545	0.4042509	0.4082767	0.3779346	0.2477574
error	0.000247	0.000222	0.0002555	0.0003734	0.0003922	0.0004016	0.0003362
39Ar	0.502207	0.4665655	0.5794537	0.6788598	0.5240856	0.3088375	0.108342
error	0.0008301	0.0007501	0.0008401	0.0009901	0.0008401	0.0005302	0.0002405
38Ar	0.006014	0.0055665	0.0069388	0.0081747	0.0064252	0.0040191	0.0015631
error	0.0000257	0.0000228	0.0000247	0.0000276	0.0000286	0.0000228	0.0000199
37Ar	0.0702739	0.0610002	0.0773426	0.1027219	0.1084209	0.108297	0.118693
error	0.0001202	0.0000942	0.0001202	0.0001501	0.0001701	0.0001801	0.0002101
36Ar	0.0005213	0.0005004	0.0006989	0.0010795	0.0011633	0.0012126	0.0008855
error	0.0000154	0.0000106	0.0000115	0.0000125	0.0000134	0.0000115	0.0000115

Sample	10.2.15		10.2.15				
Run	1		2				
Step	o	p	b	c	d	e	f
Age(Ma)	0.1511019	0.3881712	-0.1060279	0.0650656	0.1864228	0.1673567	0.1619059
error	0.0977394	0.0936372	0.1424302	0.0166271	0.0067361	0.010145	0.0155922
% 40Ar*	5.1472	14.17586	-4.957916	1.662019	13.18189	36.87758	23.96091
Ca/K	18.47928	18.37559	1.66635	1.472411	0.9869875	0.8998634	1.055224
Cl/K	0.001877	0.0044681	0.0026635	-0.0015215	-0.0013742	-0.0012209	-0.001079
40Ar	0.1471519	0.1178178	0.1044099	1.816655	1.434914	0.3364914	0.2871985
error	0.0001985	0.000214	0.0010479	0.0010921	0.0010809	0.0010409	0.001041
39Ar	0.0481062	0.0412876	0.04658	0.4427411	0.9675457	0.7063122	0.4051064
error	0.000111	0.0001209	0.0001001	0.0000861	0.0001601	0.00025	0.00052
38Ar	0.0007113	0.0006353	0.0006809	0.0063029	0.0121419	0.0084605	0.0049337
error	0.0000189	0.0000171	0.0000154	0.0000183	0.0000262	0.0000233	0.0000174
37Ar	0.1239329	0.105731	0.0134726	0.1129792	0.1654881	0.1099711	0.0738347
error	0.0002201	0.0002101	0.0000311	0.0000411	0.0000331	0.0000511	0.000096
36Ar	0.0005869	0.0004406	0.0003774	0.0060706	0.0042996	0.0007962	0.0007885
error	0.0000164	0.0000134	0.000023	0.0000249	0.0000219	0.0000248	0.0000218

Table D.2 continued.

Sample	10.2.15						
Run	2						
Step	g	h	i	j	k	l	m
Age(Ma)	0.1310503	0.1387977	0.1372305	0.1181921	0.1673066	-0.0785207	-0.3155192
error	0.027179	0.0389586	0.0493116	0.0574928	0.0871777	0.1532904	0.2922802
% 40Ar*	19.87437	18.29003	15.58445	10.28823	8.226057	-2.844687	-8.446575
Ca/K	1.30263	1.58056	1.863452	2.30861	3.827544	10.58889	20.55771
Cl/K	-0.0017042	-0.0004089	-0.0007545	0.0009877	0.0028505	-0.0001091	0.002413
40Ar	0.1764083	0.1416803	0.1302539	0.1964417	0.2090163	0.1313416	0.0964164
error	0.0010282	0.0010192	0.001016	0.0010293	0.001023	0.0010249	0.0010328
39Ar	0.2550065	0.178	0.1410616	0.1631223	0.0981135	0.0455438	0.0247951
error	0.0000991	0.0001101	0.0000832	0.0001401	0.0000552	0.0000752	0.0000542
38Ar	0.0030535	0.002222	0.0017558	0.0021598	0.001417	0.0006422	0.000392
error	0.0000243	0.0000193	0.0000233	0.0000154	0.0000164	0.0000125	0.0000104
37Ar	0.057272	0.0484203	0.0451604	0.0645807	0.0642565	0.0821812	0.0864158
error	0.0000501	0.0000301	0.0000281	0.0000561	0.0000421	0.0001	0.00015
36Ar	0.0005178	0.0004254	0.0004035	0.0006408	0.000693	0.0005173	0.0004186
error	0.0000241	0.0000241	0.0000242	0.0000327	0.0000298	0.0000242	0.000025

Sample	10.2.15			11.1.15			
Run	2			1			
Step	n	o	p	a	b	c	d
Age(Ma)	-0.6025459	0.5509779	0.8056492	-2.983162	-0.8746091	-0.0661219	0.1995192
error	0.4553515	0.6449094	0.6899106	1.709728	0.4044424	0.1402458	0.045874
% 40Ar*	-18.48709	16.16007	22.35833	-5.279627	-1.795483	-0.2227676	1.357257
Ca/K	20.51932	20.68885	18.7903	0.6037398	0.684867	0.802238	0.8692629
Cl/K	0.0082968	-0.0080906	-0.0038457	0.0047684	0.0033884	0.0012582	-0.0011004
40Ar	0.0514842	0.0367609	0.0406539	0.2798001	1.04573	3.6563	4.545623
error	0.0010341	0.0010437	0.0010462	0.0012393	0.0015164	0.0012873	0.0023323
39Ar	0.015175	0.0103553	0.010828	0.0048416	0.0209776	0.1203468	0.3020818
error	0.0000403	0.0000344	0.0000373	0.0000792	0.0001071	0.0000909	0.0002886
38Ar	0.0002686	0.0001184	0.000139	0.0002531	0.0009529	0.0038356	0.0064051
error	0.0000125	0.0000103	0.0000154	0.0000301	0.0000322	0.0000406	0.000032
37Ar	0.0527042	0.0362026	0.0343903	0.0005405	0.0026552	0.0178114	0.048421
error	0.000084	0.000068	0.00007	0.0000357	0.0000369	0.0000416	0.0000571
36Ar	0.0002461	0.000132	0.000133	0.000987	0.0035674	0.0122865	0.0150533
error	0.0000238	0.000023	0.0000258	0.0000279	0.0000273	0.0000493	0.000029

Sample	11.1.15						
Run	1						
Step	e	f	g	h	i	j	k
Age(Ma)	0.3274332	0.3731713	0.3748629	0.3836016	0.3733237	0.3660182	0.3671587
error	0.0225364	0.0143197	0.0107018	0.0093546	0.0093914	0.0074573	0.0112009
% 40Ar*	4.706493	11.06446	21.00447	32.0739	35.75676	28.47632	17.1808
Ca/K	0.8632797	0.8338383	0.8087852	0.8011034	0.8113473	0.8380892	0.9237709
Cl/K	-0.0015274	-0.0015122	-0.0013253	-0.0014012	-0.0014368	-0.0011746	-0.0013244
40Ar	3.635186	2.346483	1.471921	1.072129	0.9354577	1.438246	1.732103
error	0.0012419	0.0016169	0.0013775	0.0012955	0.0012786	0.0013501	1.44E-03
39Ar	0.510405	0.6795095	0.8053673	0.8751865	0.874669	1.092501	0.7915518
error	0.0001063	0.0006239	0.0007533	0.0008728	0.0008828	0.0010024	0.0007234
38Ar	0.0081503	0.0092595	0.0101987	0.0107219	0.0106248	0.0135453	0.0102087
error	0.0000347	0.0000302	0.0000313	0.0000294	0.0000317	0.0000331	0.0000313
37Ar	0.0811178	0.104144	0.1195339	0.1284552	0.1298089	0.167205	0.1333036
error	0.0000433	0.0000927	0.0001049	0.0001338	0.0001436	0.0001533	0.0001145
36Ar	0.011661	0.0070648	0.003981	0.0025325	0.0021074	0.0035673	0.004902
error	0.0000266	0.0000275	0.0000269	0.0000263	0.0000267	0.0000251	0.0000269

Table D.2 continued.

Sample	11.1.15					2.7.08	
Run	1					1	
Step	l	m	n	o	p	a	b
Age(Ma)	0.3644909	0.2985577	0.3649536	0.4359167	0.618011	-2.437842	0.5508247
error	0.0195949	0.0374877	0.0751132	0.196732	0.4828942	0.6481959	0.1018956
% 40Ar*	7.997203	4.011258	4.140002	4.397768	5.404784	-1.002411	0.6767521
Ca/K	1.28077	2.528435	4.159584	5.095046	5.949055	0.6201099	0.6080637
Cl/K	-0.0008432	-3.96E-06	0.0006767	0.000322	-0.000941	0.002482	0.003213
40Ar	2.336007	1.882351	0.9854682	0.4178774	0.1933215	2.342065	4.027745
error	0.0012449	0.001556	0.0014596	0.0013101	0.0012353	0.000472	0.0005048
39Ar	0.5006955	0.2471878	0.1093274	0.041242	0.0165439	0.0094276	0.0484035
error	0.000114	0.0002596	0.0001746	0.0001078	0.0000822	0.0000376	0.0000436
38Ar	0.0073258	0.0041609	0.0019589	0.0007614	0.0003126	0.001617	0.0031709
error	0.0000326	0.0000296	0.0000272	0.0000275	0.0000277	0.0000266	0.0000169
37Ar	0.1166879	0.1134722	0.0823766	0.0379889	0.0177805	0.0009661	0.004862
error	0.0000445	0.000105	0.0001051	0.0000736	0.0000487	0.0000164	0.0000233
36Ar	0.0072841	0.0061357	0.0032253	0.0013664	0.0006258	0.0079239	0.0134031
error	0.0000279	0.0000275	0.0000265	0.0000272	0.000027	0.0000205	0.0000157

Sample	2.7.08						
Run	1						
Step	c	d	e	f	g	h	i
Age(Ma)	0.8586492	0.8893569	0.9426358	0.8852194	0.920381	0.8909577	0.8717973
error	0.0478916	0.0227482	0.0340899	0.0194324	0.0413392	0.0900827	0.0442464
% 40Ar*	1.120598	2.910774	2.78941	3.750291	3.548244	2.560656	1.542188
Ca/K	0.7200139	0.7719848	0.8149249	0.9255916	1.019741	1.088202	1.160669
Cl/K	-0.0000627	0.0014903	0.0010781	0.0018423	0.0022487	0.0016963	0.0010898
40Ar	18.58007	10.23009	10.51735	6.655026	6.562036	8.108064	12.45117
error	0.0019205	0.0011351	0.0011351	0.0006621	0.0008099	0.0008006	0.0012322
39Ar	0.2371701	0.3274828	0.3044053	0.2757788	0.247453	0.2279484	0.2154637
error	0.0000654	0.0000515	0.0000495	0.0000455	0.0000534	0.0000495	0.0000327
38Ar	0.0144924	0.0104389	0.0102863	0.0075875	0.0072103	0.007906	0.0104538
error	0.0000198	0.0000236	0.0000246	0.0000178	0.0000178	0.0000188	0.0000198
37Ar	0.0281588	0.0416687	0.0408181	0.0419289	0.0413776	0.040607	0.0408704
error	0.0000223	0.0000203	0.0000243	0.0000233	0.0000252	0.0000262	0.0000193
36Ar	0.0615574	0.0333008	0.0342771	0.0214883	0.0212326	0.0264948	0.0410942
error	0.0000264	0.0000195	0.0000313	0.0000147	0.0000333	0.0000692	0.0000264

Sample	2.7.08						
Run	1						
Step	j	k	l	m	n	o	p
Age(Ma)	0.9234394	0.9019209	0.875578	0.9112781	0.8992652	0.8986194	0.8933911
error	0.0720425	0.0349565	0.0107366	0.0114154	0.015574	0.014292	0.0183202
% 40Ar*	0.6666121	1.367718	5.584269	15.81826	64.85324	68.44344	67.62453
Ca/K	1.451737	1.909536	2.267362	2.395474	2.492951	2.672287	2.820378
Cl/K	-0.002686	0.0010617	0.003731	0.0042811	0.0044129	0.0046791	0.0052272
40Ar	38.88503	33.08548	16.18684	5.411502	0.797768	0.433435	0.2357378
error	0.0063062	0.00391	0.0021186	0.0005906	0.0003688	0.00035	0.0003225
39Ar	0.2746191	0.4909295	1.010253	0.919186	0.5627878	0.3229379	0.1745644
error	0.0000654	0.0000554	0.0000943	0.0000703	0.0002301	0.0001801	0.0001302
38Ar	0.0274922	0.0267847	0.0232933	0.015464	0.0079097	0.0045534	0.002496
error	0.0000217	0.0000246	0.0000236	0.0000178	0.0000188	0.0000227	0.0000217
37Ar	0.0650372	0.1526452	0.3723149	0.3572927	0.2272821	0.1395637	0.0795851
error	0.0000233	0.0000372	0.0000421	0.0000561	0.0000651	0.0000741	0.0000701
36Ar	0.1294269	0.1094267	0.0514961	0.015554	0.0011283	0.0005745	0.0003221
error	0.0000274	0.0000284	0.0000225	0.0000313	0.0000284	0.0000147	0.0000105

Table D.2 continued.

Sample	2.7.08						
Run	2						
Step	a	b	c	d	e	f	g
Age(Ma)	103.2237	1.010908	0.8597018	0.8716694	0.8348266	0.9178356	0.9146961
error	36.06217	0.1778298	0.0360816	0.0316549	0.0236411	0.0600886	0.0433662
% 40Ar*	1.599669	0.69356	1.7664	3.049251	2.770843	1.657875	1.346179
Ca/K	-2.183537	0.5861316	0.6978797	0.7870868	0.9063843	1.057279	1.264787
Cl/K	-0.336272	-0.0012974	0.0013022	0.0012778	0.0013135	-0.0000308	0.0000946
40Ar	1.202278	5.959376	21.4362	16.16967	14.53554	23.36071	26.86425
error	0.000947	0.0027226	0.0037165	0.0070087	0.0026235	0.0120051	0.0066093
39Ar	0.0001769	0.0399842	0.4307602	0.5532186	0.471872	0.4127318	0.3867487
error	0.0000519	0.0001	0.000146	0.0005017	0.0001038	0.0003624	0.0001081
38Ar	0.0007287	0.0042076	0.0187508	0.0168984	0.0149005	0.0195436	0.0214725
error	0.0000148	0.0000241	0.0000318	0.0000338	0.000027	0.0000347	0.0000279
37Ar	-0.000054	0.003273	0.0419086	0.0606718	0.05949	0.0605909	0.0678002
error	0.0000142	0.0000198	0.0000374	0.0000633	0.0000364	0.0000553	0.0000335
36Ar	0.0039625	0.019825	0.07057	0.052565	0.0473932	0.0770054	0.0888333
error	0.0000122	0.0000202	0.0000377	0.0000475	0.0000279	0.0000634	0.0000289

Sample	2.7.08						
Run	2						
Step	h	i	j	k	l	m	n
Age(Ma)	0.8295272	0.8939174	0.8664052	0.8979601	0.9030076	0.9054398	0.8879806
error	0.0362073	0.0226259	0.0407043	0.0200724	0.0158024	0.0138781	0.0177457
% 40Ar*	1.442088	2.698037	2.392095	5.380097	7.575121	16.1597	31.19772
Ca/K	1.608675	1.829921	1.981395	2.085546	2.150008	2.236946	2.299048
Cl/K	0.0012491	0.0029474	0.0024107	0.0033886	0.0037442	0.0040833	0.0042316
40Ar	25.37798	18.33258	21.39995	9.505357	6.183763	2.454058	0.9686311
error	0.0038161	0.0026235	0.0110056	0.0041149	0.0008641	0.0009008	0.000488
39Ar	0.4316267	0.5413603	0.5781088	0.5572409	0.5075678	0.4285338	0.3329371
error	0.0001362	0.0000673	0.0005116	0.0004717	0.0000871	0.0001554	0.0001845
38Ar	0.0212533	0.0184281	0.020734	0.0131386	0.0104656	0.0071384	0.0049745
error	0.000025	0.0000241	0.0000328	0.000026	0.0000308	0.0000241	0.000027
37Ar	0.0960665	0.1368237	0.1579382	0.1599719	0.1499679	0.1315176	0.1048425
error	0.0000266	0.0000404	0.0001301	0.0001301	0.0000404	0.0000493	0.0000473
36Ar	0.0838683	0.0598793	0.0701161	0.0302803	0.0192894	0.0070201	0.0023351
error	0.0000308	0.0000269	0.0000614	0.0000308	0.000024	0.0000184	0.0000193

Sample	2.7.08		4.15A.08				
Run	2		1				
Step	o	p	a	b	c	d	e
Age(Ma)	0.890853	0.9085945	49.87781	1.635703	1.04233	0.8411039	0.7079765
error	0.0307449	0.015642	30.69014	0.4307275	0.1334095	0.0500329	0.0310225
% 40Ar*	17.70546	35.43891	85.30218	10.57626	12.54475	14.1977	14.25478
Ca/K	2.372215	2.701598	0.5752754	0.0873715	0.087574	0.0870938	0.0854172
Cl/K	0.0040641	0.0041127	0.3511023	0.0062618	0.0042654	0.004123	0.0030175
40Ar	1.338764	1.052637	0.0155833	0.2875635	0.6016789	0.8902496	1.197707
error	0.000481	0.000461	0.0001271	0.0002594	0.0003418	0.0006315	0.0003795
39Ar	0.260344	0.4017171	0.0002528	0.0178695	0.0696029	0.1444426	0.2317997
error	0.000089	0.0001364	0.000018	0.0000404	0.0000513	0.0001901	0.0000613
38Ar	0.0042416	0.0059079	0.0000351	0.0004191	0.0012843	0.0024508	0.0037191
error	0.000025	0.000027	0.0000106	0.0000135	0.0000154	0.0000145	0.0000174
37Ar	0.0844522	0.1483253	0.0000216	0.0002332	0.000909	0.0018753	0.0029469
error	0.0000335	0.0000513	0.0000103	0.0000124	0.0000193	0.0000144	0.0000212
36Ar	0.0037731	0.0024223	7.694E-06	0.0008615	0.0017631	0.0025599	0.003442
error	0.0000269	0.0000202	0.0000276	0.0000268	0.0000323	0.0000248	0.0000245

Table D.2 continued.

Sample	4.15A.08				4.15A.08		
Run	1				2		
Step	m	n	o	p	a	b	c
Age(Ma)	0.6814299	0.6858902	0.6728959	0.7785754	-9.37884	0.9884822	0.1576066
error	0.0121562	0.0137414	0.0226516	0.0272296	18.17353	0.3460573	0.1859313
% 40Ar*	15.02761	15.05872	14.84897	17.8866	-24.64034	5.685358	1.60739
Ca/K	0.0847043	0.0847831	0.0837406	0.0837723	0.0687305	0.1079988	0.094526
Cl/K	0.0025045	0.0026949	0.0026801	0.0022554	-0.3465719	0.0067467	0.005253
40Ar	3.454793	2.574674	1.682087	1.209131	0.0135072	0.3232747	0.3738915
error	0.000408	0.0004368	0.00037	0.0008584	0.0002691	0.0003714	0.0003324
39Ar	0.7323295	0.5433392	0.3567905	0.2669936	0.0003421	0.0178748	0.0366654
error	0.0001002	0.0000932	0.0000782	0.0003301	0.0000256	0.0000384	0.0000344
38Ar	0.0114251	0.008518	0.0055892	0.0040935	-0.0000261	0.0004523	0.0007462
error	0.0000223	0.0000223	0.0000223	0.0000154	0.0000124	0.0000124	0.0000183
37Ar	0.009114	0.0067573	0.0043759	0.0032745	4.717E-06	0.0003862	0.0006926
error	0.0000222	0.0000173	0.0000193	0.0000134	0.0000135	0.0000107	0.0000184
36Ar	0.0098395	0.0073302	0.0048007	0.003328	0.0000564	0.0010214	0.0012326
error	0.0000273	0.0000236	0.0000272	0.0000245	0.0000215	0.0000215	0.0000237

Sample	4.15A.08						
Run	2						
Step	d	e	f	g	h	i	j
Age(Ma)	0.7531114	0.6991314	0.6618367	0.6563599	0.6739096	0.6537939	0.6476056
error	0.09872	0.0655207	0.0442252	0.0390809	0.0242062	0.0215976	0.019403
% 40Ar*	10.60564	12.21002	12.70386	13.09722	13.74375	13.57874	13.53221
Ca/K	0.0876357	0.0849696	0.085869	0.0856135	0.0854033	0.0860023	0.0854685
Cl/K	0.0040883	0.0032417	0.0035969	0.0026656	0.0033825	0.0031146	0.0029565
40Ar	0.4621011	0.5889664	0.7336676	0.9137347	1.413908	1.834738	2.170882
error	0.0005661	0.000522	0.0006096	0.0003834	0.0008989	0.0004456	0.0004073
39Ar	0.0625596	0.0988834	0.1353812	0.1752788	0.2772	0.3663213	0.4360777
error	0.0001101	0.0001401	0.0001701	0.0000652	0.0002901	0.0000682	0.0000752
38Ar	0.0011126	0.0016439	0.0022246	0.0028018	0.0044766	0.0058655	0.0069521
error	0.0000154	0.0000163	0.0000115	0.0000213	0.0000232	0.0000213	0.0000242
37Ar	0.0010955	0.0016764	0.0023156	0.0029842	0.0047004	0.0062447	0.007376
error	0.0000154	0.0000126	0.0000116	0.0000203	0.0000145	0.0000203	0.0000194
36Ar	0.0013842	0.0017328	0.0021465	0.0026613	0.0040875	0.0053144	0.0062914
error	0.0000213	0.0000223	0.0000205	0.0000235	0.0000222	0.0000262	0.0000277

Sample	4.15A.08						5.5.12
Run	2						1
Step	k	l	m	n	o	p	a
Age(Ma)	0.6528835	0.6504539	0.6603907	0.6823923	0.6820896	0.6834678	0.423648
error	0.0118676	0.0106587	0.0083856	0.0077178	0.0084652	0.0128227	0.784972
% 40Ar*	13.67305	13.59552	13.66917	14.39048	14.57593	14.81708	1.886607
Ca/K	0.0852369	0.0849453	0.0853252	0.0847961	0.0844855	0.0850708	1.645437
Cl/K	0.0029409	0.0028794	0.00288	0.0029222	0.0026451	0.0027748	0.0194317
40Ar	3.39153	4.303413	7.181648	9.465508	8.467709	3.1488	0.1217896
error	0.001425	0.0019186	0.0007303	0.0009099	0.0007134	0.00046	0.0002163
39Ar	0.6828009	0.8646911	1.429004	1.918885	1.739497	0.6562227	0.0052698
error	0.00056	0.00073	0.0000712	0.0001201	0.00063	0.0000842	0.0000518
38Ar	0.0108747	0.0137599	0.0227748	0.0304701	0.0273844	0.0103307	0.0001751
error	0.0000163	0.0000203	0.0000272	0.0000262	0.0000322	0.0000203	0.0000225
37Ar	0.0114994	0.0144896	0.0240133	0.0319946	0.028851	0.0109546	0.0016429
error	0.0000116	0.0000164	0.0000223	0.0000223	0.0000213	0.0000233	0.0000226
36Ar	0.0098129	0.0124624	0.0207799	0.0271597	0.0242442	0.0089902	0.0004014
error	0.0000229	0.0000242	0.0000249	0.0000257	0.0000319	0.0000252	0.0000142

Table D.2 continued.

Sample	5.5.12						
Run	1						
Step	b	c	d	e	f	g	h
Age(Ma)	1.06106	1.032367	1.22182	1.301395	1.322749	1.319736	1.310013
error	0.459875	0.0704714	0.0201054	0.0140398	0.0080388	0.0092839	0.0081388
% 40Ar*	7.032848	16.20557	43.89068	66.87601	77.22496	81.9209	83.1689
Ca/K	1.388353	1.353458	1.26789	1.161068	1.061953	0.9796908	0.9187697
Cl/K	0.0346798	0.0081974	0.0013149	-0.0008858	-0.0011174	-0.0012592	-0.0012574
40Ar	0.2366362	0.5245109	0.6798976	0.8599658	1.049125	1.218392	1.305398
error	0.0002683	0.0007398	0.0008188	0.0005142	0.0008287	0.0003418	0.0006708
39Ar	0.0152356	0.0799728	0.2371746	0.4290701	0.5946392	0.7342044	0.8045214
error	0.0000815	0.0002502	0.0004901	0.0003101	0.0008	0.0002402	0.00081
38Ar	0.0005072	0.0014802	0.0032446	0.0052881	0.0071825	0.0087848	0.0096127
error	0.0000353	0.0000353	0.0000313	0.0000264	0.0000225	0.0000157	0.0000254
37Ar	0.0040065	0.0204688	0.0568463	0.0940282	0.1190031	0.1353413	0.1388633
error	0.0000334	0.0000622	0.0001201	0.0000722	0.0001501	0.0000552	0.0001301
36Ar	0.0007397	0.0014866	0.0013181	0.0010211	0.0008853	0.0008347	0.0008355
error	0.0000241	0.0000192	0.0000152	0.0000182	7.75E-06	0.0000162	0.0000123

Sample	5.5.12						
Run	1						
Step	i	j	k	l	m	n	o
Age(Ma)	1.314519	1.312569	1.332987	1.319085	1.195939	1.267716	1.328621
error	0.0096896	0.0085164	0.0134109	0.0196866	0.0214174	0.0484522	0.1088933
% 40Ar*	82.91689	77.56032	68.92378	53.33289	33.91502	22.24907	16.77882
Ca/K	0.8752504	0.8482613	0.8697692	1.176043	2.592333	6.349966	9.11604
Cl/K	-0.0011251	-0.0011556	-0.0007649	-0.000436	0.0007925	0.0018369	0.0012241
40Ar	1.361465	1.923726	1.751771	1.481126	0.8864073	0.4387995	0.2258832
error	0.00037	0.0003231	0.0003511	0.0003324	0.0003606	0.000389	0.0002683
39Ar	0.8336546	1.103499	0.8793363	0.5814767	0.2442327	0.0749283	0.0277822
error	0.0001702	0.0001602	0.0001303	0.0000924	0.0001104	0.0001203	0.0000606
38Ar	0.0100017	0.0133056	0.0108478	0.0074494	0.0034209	0.0011799	0.0004709
error	0.0000215	0.0000264	0.0000235	0.0000313	0.0000166	0.0000119	0.0000176
37Ar	0.13686	0.1752943	0.1429924	0.1276151	0.1178775	0.0883137	0.0468863
error	0.0000255	0.0000542	0.0000413	0.0000383	0.0000642	0.0001101	0.0000722
36Ar	0.0008773	0.0015718	0.0019261	0.0024069	0.0020472	0.0012068	0.0006637
error	0.0000202	0.0000202	0.0000351	0.0000371	0.0000172	0.0000123	0.0000103

Sample	5.5.12	6.3.15					
Run	1	1					
Step	p	a	b	c	d	e	f
Age(Ma)	0.5812951	175.9083	1.564101	1.265927	1.291006	1.299438	1.306557
error	0.1688981	753.3331	0.8381649	0.0201183	0.0093049	0.0084168	0.0078958
% 40Ar*	4.944053	-107.2796	8.725755	43.2323	71.00573	80.06863	83.85415
Ca/K	8.961716	7.63273	1.4117	1.310959	1.141407	1.062025	1.06532
Cl/K	0.0038798	-1.388485	0.0616045	0.0007588	-0.0012359	-0.0012087	-0.0011816
40Ar	0.1681257	0.0029032	0.1953454	1.014585	1.829248	2.229771	2.035124
error	0.0002594	0.0011071	0.001111	0.0011638	0.0011753	0.0011593	0.0011126
39Ar	0.013929	-0.0000166	0.0106816	0.3395586	0.9857579	1.346063	1.279608
error	0.0000518	0.0000685	0.0000955	0.0001995	0.0002186	0.00019	0.000238
38Ar	0.0002902	0.0000115	0.00047	0.0045996	0.011953	0.0161573	0.0153123
error	0.0000119	0.0000246	0.0000266	0.0000394	0.0000217	0.0000188	0.0000236
37Ar	0.0231012	-0.0000172	0.0020521	0.0605334	0.1529587	0.1940342	0.1847264
error	0.0000522	0.0000207	0.0000275	0.0000463	0.0000592	0.0000573	0.0000384
36Ar	0.0005521	0.0000201	0.0005992	0.0019888	0.0019278	0.0016811	0.0012843
error	8.03E-06	0.0000147	0.0000304	0.0000215	0.0000205	0.0000215	0.0000157

Table D.2 continued.

Sample	6.3.15						
Run	1						
Step	g	h	i	j	k	l	m
Age(Ma)	1.302808	1.282947	1.297978	1.3137	1.393052	1.269417	1.214011
error	0.0079309	0.0170544	0.0212264	0.0416067	0.0960014	0.0942424	0.2354122
% 40Ar*	82.56162	75.02837	61.95656	47.41872	40.32839	34.70885	30.17397
Ca/K	1.103679	1.204637	1.611872	2.637194	4.215441	5.208562	5.900705
Cl/K	-0.0009173	-0.0003904	0.0004487	0.0011843	0.0037637	0.0010925	0.0042134
40Ar	1.442057	0.8433003	0.4749012	0.3069348	0.2247898	0.1352455	0.1065018
error	0.0011023	0.001201	0.0010927	0.0010832	0.0010767	0.00109	0.0010863
39Ar	0.8953211	0.4832038	0.2221513	0.1086218	0.06384	0.0362914	0.0259856
error	0.0001618	0.000306	0.0001343	0.0001051	0.0000833	0.0000822	0.0000753
38Ar	0.0108092	0.0059691	0.002862	0.0014737	0.0009482	0.0005134	0.0004027
error	0.0000246	0.0000246	0.0000236	0.0000207	0.0000217	0.0000104	0.0000236
37Ar	0.1336832	0.0786154	0.0482717	0.0385358	0.0361216	0.0253213	0.0205015
error	0.0000374	0.0000622	0.0000344	0.0000423	0.0000334	0.0000483	0.0000236
36Ar	0.0009755	0.0007837	0.0006533	0.0005791	0.0004855	0.0003212	0.0002697
error	0.000011	0.0000254	0.0000147	0.0000147	0.0000205	0.000011	0.0000205

Sample	6.3.15			8.3.15			
Run	1			1			
Step	n	o	p	a	b	c	d
Age(Ma)	1.422381	1.623376	1.253372	0.8860785	0.9732782	0.948073	0.9505563
error	0.1517402	0.2204549	0.1099794	0.0482213	0.0150868	0.0080483	0.0091151
% 40Ar*	34.25552	37.55219	27.88299	27.88011	39.78999	46.08365	51.3897
Ca/K	6.523261	7.06539	7.784943	0.5115471	0.5120427	0.6150617	0.8463523
Cl/K	-0.0018194	0.0012348	0.0022493	0.0086323	0.0066272	0.0051488	0.0038351
40Ar	0.1096097	0.0946075	0.1640838	0.3026951	0.9540711	2.852746	2.690973
error	0.0010922	0.0011016	0.0011087	0.0003625	0.0006671	0.0002267	0.00025
39Ar	0.025918	0.0214903	0.0358577	0.0922219	0.3776456	1.342548	1.4086
error	0.0000724	0.0000681	0.0000744	0.0001401	0.00031	0.00025	0.00026
38Ar	0.0003466	0.0003096	0.0005417	0.0015382	0.005836	0.0197453	0.0198872
error	0.0000114	0.0000114	0.0000178	0.0000183	0.0000302	0.0000741	0.0000901
37Ar	0.0225639	0.0202272	0.0371627	0.0079965	0.0327638	0.1396569	0.201492
error	0.0000295	0.0000256	0.0000423	0.0000311	0.0000491	0.0000521	0.000094
36Ar	0.0002641	0.0002183	0.0004339	0.0007374	0.0019497	0.0052618	0.004541
error	0.0000129	0.0000157	0.0000129	0.0000152	0.0000182	0.0000281	0.0000361

Sample	8.3.15						
Run	1						
Step	e	f	g	h	i	j	k
Age(Ma)	0.9632441	0.9674129	0.9883264	0.8879145	0.9251609	0.7337947	0.6868592
error	0.0073984	0.0127685	0.021379	0.0436044	0.073966	0.0431855	0.0416848
% 40Ar*	52.84308	50.95317	49.60676	41.68247	41.21407	30.65662	28.09957
Ca/K	1.061544	1.256654	1.436463	1.595955	1.785207	2.839686	4.911066
Cl/K	0.0018594	0.0014808	0.0017242	0.0019722	0.0041933	0.0057304	0.0077376
40Ar	1.758117	0.997677	0.5557219	0.3266727	0.2105767	0.2218237	0.2345543
error	0.0005894	0.0006282	0.000446	0.000522	0.000283	0.0003354	0.0003089
39Ar	0.9339179	0.5088555	0.2701318	0.1485317	0.0908645	0.0898063	0.0930575
error	0.00043	0.00045	0.00035	0.0002001	0.0000931	0.0002001	0.0001701
38Ar	0.0125261	0.0067828	0.0036365	0.0020354	0.0013194	0.001372	0.0014928
error	0.0000292	0.0000223	0.0000252	0.0000252	0.0000233	0.0000164	0.0000135
37Ar	0.1672541	0.1076906	0.0652359	0.0397844	0.0271775	0.042638	0.0762244
error	0.000067	0.000088	0.0001	0.0000571	0.0000551	0.000087	0.00013
36Ar	0.0029099	0.0017248	0.0009901	0.0006699	0.0004364	0.0005495	0.0006264
error	0.0000162	0.0000202	0.0000192	0.0000222	0.0000232	0.0000133	0.0000133

Table D.2 continued.

Sample	8.3.15					9.1.15	
Run	1					1	
Step	l	m	n	o	p	a	b
Age(Ma)	0.7645058	0.9281299	0.7875724	0.8427004	0.9369979	-98.87807	-2.653485
error	0.0223139	0.0650826	0.0432485	0.0906054	0.0909684	58.95488	0.5996133
% 40Ar*	33.20745	45.15058	37.37372	40.64415	41.20036	261.2003	-44.52832
Ca/K	6.481966	7.168562	7.748772	8.311905	8.746556	1.604346	1.481586
Cl/K	0.0072422	0.0084648	0.0076273	0.0104499	0.0100035	0.3139079	0.0889608
40Ar	0.3602102	0.2664955	0.1664663	0.1246716	0.0849054	0.005539	0.1485186
error	0.0003716	0.000283	0.0002267	0.0001803	0.0001921	0.0001938	0.0006485
39Ar	0.1518136	0.1258097	0.0766798	0.0583779	0.0362512	-0.0001454	0.0241146
error	0.0002401	0.0001101	0.0001501	0.0000532	0.0000861	0.000072	0.0007528
38Ar	0.0023887	0.0019993	0.0012062	0.0009718	0.0006005	-0.0000231	0.0011696
error	0.0000154	0.0000223	0.0000154	0.0000164	0.0000125	0.0000162	0.0001801
37Ar	0.1637679	0.1498112	0.0985181	0.0803081	0.0524477	-0.0000453	0.0069395
error	0.00023	0.00014	0.00015	0.0000571	0.000087	0.0000251	0.0001714
36Ar	0.0009384	0.0006111	0.0004292	0.0003132	0.0002099	-0.0000299	0.0007238
error	0.0000113	0.0000281	0.0000113	0.0000182	0.0000113	0.0000137	0.0000494

Sample	9.1.15						
Run	1						
Step	c	d	e	f	g	h	i
Age(Ma)	0.0430977	0.4806364	0.8131024	0.7980142	0.8145501	0.816657	0.8265599
error	0.0576029	0.0630696	0.014862	0.0106951	0.0077958	0.0074395	0.0096989
% 40Ar*	1.710808	32.75138	71.5977	77.24025	80.48715	80.45666	79.89532
Ca/K	1.100803	0.8151028	0.6320218	0.5301696	0.4905568	0.491485	0.5346896
Cl/K	0.0409017	0.0100836	-0.0000629	-0.0008321	-0.0008086	-0.0008483	-0.0005865
40Ar	0.3518532	0.5799081	0.7843058	0.8211475	0.8003452	0.6848316	0.5409977
error	0.0006964	0.0007834	0.0006198	0.0006008	0.0007834	0.0007446	0.0007157
39Ar	0.1350004	0.3817813	0.6670408	0.7675851	0.763737	0.651575	0.5050236
error	0.0005638	0.0019011	0.0006532	0.0006135	0.0012018	0.0011019	0.0009323
38Ar	0.0037707	0.0062348	0.0082692	0.0092678	0.0092085	0.0078476	0.0061315
error	0.0002101	0.0004	0.0000504	0.0000257	0.0000415	0.0000296	0.0000296
37Ar	0.0288243	0.0603491	0.0816418	0.0786934	0.072337	0.06173	0.0519628
error	0.0001516	0.0003806	0.0000897	0.0000801	0.000122	0.0001122	0.0001014
36Ar	0.0011783	0.0013478	0.0008027	0.0006806	0.0005734	0.0004913	0.0004006
error	0.0000268	0.0000833	0.0000327	0.0000259	0.0000164	0.0000128	0.0000146

Sample	9.1.15						
Run	1						
Step	j	k	l	m	n	o	p
Age(Ma)	0.8259995	0.8188458	0.8188969	0.7934865	0.7675519	0.803835	0.8732847
error	0.0081671	0.0108127	0.0108761	0.0202803	0.0172606	0.0213492	0.0343954
% 40Ar*	77.18999	73.37044	65.28399	56.8589	53.64338	54.00955	54.55919
Ca/K	0.6532529	0.9164217	1.975964	4.370763	5.340892	5.100247	4.895878
Cl/K	-0.0007405	-0.0005548	-0.0005183	-0.0001803	-0.000596	-0.0002711	-0.0002978
40Ar	0.5851249	0.5059694	0.5305055	0.5056616	0.4452924	0.2753786	0.1931727
error	0.0006676	0.000658	0.0006294	0.0003895	0.0003302	0.000314	0.0002907
39Ar	0.528113	0.4379185	0.4087055	0.3504757	0.3011272	0.1790181	0.1167604
error	0.0008824	0.0008126	0.0006931	0.0002198	0.0001727	0.0002972	0.0002294
38Ar	0.0063965	0.005348	0.0050357	0.0044019	0.0037527	0.0022532	0.0014717
error	0.0000267	0.0000219	0.0000248	0.0000257	0.0000277	0.00002	0.0000219
37Ar	0.0662675	0.0769399	0.1544804	0.2922623	0.3062385	0.1735872	0.1086461
error	0.000122	0.0001417	0.0002609	0.0001813	0.0001714	0.000241	0.0001813
36Ar	0.0004934	0.0005053	0.0007257	0.0009372	0.0009082	0.0005473	0.0003711
error	0.000012	0.0000146	0.0000137	0.0000239	0.0000173	0.0000128	0.0000137

Table D.2 continued.

Sample	9.2.15						
Run	1						
Step	a	b	c	d	e	f	g
Age(Ma)	-0.001507	0.3995155	0.5604758	0.5492108	0.5903884	0.5852194	0.5458707
error	0.4076944	0.122305	0.0144841	0.0122017	0.0113686	0.0176064	0.0208344
% 40Ar*	-0.0334316	16.74822	45.77584	55.13118	57.03262	50.93558	46.90047
Ca/K	1.187665	0.9564469	0.8953066	0.8947949	0.8933842	0.9717511	1.088801
Cl/K	0.0176749	0.017628	0.0035536	0.0014884	-0.0017736	-0.0014809	-0.0009641
40Ar	0.1084071	0.2698985	0.7444452	0.8720396	0.6316913	0.4657157	0.3683551
error	0.0009119	0.0011022	0.0010634	0.0010186	0.0009935	0.0010673	0.00092
39Ar	0.023624	0.1111073	0.5968521	0.8591954	0.5989551	0.3978959	0.3106892
error	0.0001106	0.000485	0.0007532	0.0007432	0.000604	0.0006138	0.0003466
38Ar	0.0005009	0.002174	0.0082738	0.0111788	0.0071182	0.0047995	0.0038141
error	0.0000477	0.00009	0.0001436	0.0001339	0.0000461	0.0000439	0.0000416
37Ar	0.0045187	0.0171108	0.0859051	0.1235439	0.0858172	0.061906	0.054068
error	0.0000368	0.0000915	0.0001225	0.0001422	0.0001031	0.0001127	0.0000807
36Ar	0.000367	0.0007668	0.0014236	0.0014136	0.0009808	0.0008171	0.0007005
error	0.0000327	0.0000462	0.0000285	0.0000344	0.0000219	0.0000231	0.0000216

Sample	9.2.15						
Run	1						
Step	h	i	j	k	l	m	n
Age(Ma)	0.5638513	0.5903357	0.5880107	0.5963811	0.5617224	0.5072614	0.8092482
error	0.0218064	0.0275715	0.0181706	0.0241058	0.0275801	0.0611045	0.1425909
% 40Ar*	45.96818	41.30402	30.08526	23.10429	17.71199	15.07739	22.13178
Ca/K	1.241387	1.48213	2.115547	3.98784	8.957653	16.05244	22.52415
Cl/K	-0.0013699	-0.0015887	0.0000707	0.0016109	0.0030598	0.0021566	0.0051444
40Ar	0.3459038	0.3663349	0.7224881	0.7889157	0.712758	0.4050702	0.2237976
error	0.000937	0.0008731	0.0009041	0.0010309	0.0009487	0.0008956	0.0008696
39Ar	0.2768566	0.2516795	0.3631045	0.3004397	0.2213276	0.11887	0.0605617
error	0.0003268	0.0002295	0.000356	0.0001914	0.0003561	0.0001116	0.0000816
38Ar	0.0033682	0.0030717	0.0047638	0.0042234	0.0033157	0.0017667	0.0009635
error	0.0000381	0.0000373	0.000035	0.0000409	0.0000348	0.0000359	0.000037
37Ar	0.0548376	0.0594133	0.1221135	0.1900071	0.3133354	0.3003247	0.2138585
error	0.0000816	0.0000626	0.0000901	0.0001321	0.0004307	0.0001618	0.0001618
36Ar	0.0006721	0.0007703	0.0017951	0.0021932	0.0022314	0.0014086	0.0007666
error	0.0000201	0.0000233	0.0000218	0.0000241	0.0000202	0.0000243	0.000029

Sample	9.2.15		11.3.15				
Run	1		1				
Step	o	p	a	b	c	d	e
Age(Ma)	0.5589822	-0.0264852	0.0547509	0.059541	0.0319139	0.0729988	0.0917934
error	0.2344003	0.3809428	0.0762187	0.039261	0.0630411	0.0331481	0.0434933
% 40Ar*	15.36829	-0.7220001	1.25313	0.6027506	0.7781339	0.7349286	0.8342301
Ca/K	25.5454	26.67637	0.6270128	0.7005388	0.9894307	0.9219205	1.330167
Cl/K	0.0054782	0.0059428	-0.0001658	0.0032487	0.0051302	0.0053546	0.0096331
40Ar	0.1096549	0.0584629	1.0566	3.986142	2.673323	3.363984	2.148535
error	0.0008603	0.0008521	0.0026173	0.0054083	0.0040112	0.0046098	0.0040112
39Ar	0.0298645	0.0157963	0.1608244	0.6306534	0.3228222	0.7357614	0.3981839
error	0.0000802	0.0000801	0.0003809	0.0022002	0.0016002	0.0024001	0.0017002
38Ar	0.0004833	0.0002644	0.0026168	0.0109036	0.0061975	0.012437	0.0075213
error	0.0000374	0.0000336	0.0002505	0.0002904	0.0002705	0.0004003	0.0003004
37Ar	0.1192834	0.0658336	0.0016306	0.0071374	0.0051542	0.0109232	0.0085193
error	0.0001126	0.0001223	0.0001756	0.0002736	0.0002048	0.000244	0.0004124
36Ar	0.000413	0.0002537	0.0035192	0.0132687	0.008958	0.0111561	0.0071302
error	0.0000235	0.0000201	0.0000434	0.0000782	0.0000682	0.0000812	0.0000583

Table D.2 continued.

Sample	11.3.15						
Run	1						
Step	f	g	h	i	j	k	l
Age(Ma)	0.0730979	-0.0491248	0.0898748	0.0180669	0.0360371	0.0322268	0.07417
error	0.0508624	0.0436307	0.0762544	0.0432472	0.0280061	0.0349606	0.0564207
% 40Ar*	0.614156	0.4566718	0.5137088	0.4716932	0.6248265	0.9807357	1.13105
Ca/K	1.808209	2.5248	3.158423	3.761942	4.821878	5.299554	6.075207
Cl/K	0.0017223	0.0068041	0.0050066	0.0069738	0.0086776	0.0040857	0.0024635
40Ar	3.497231	5.491642	8.29182	7.229322	4.615683	1.983583	1.446391
error	0.0044102	0.0058078	0.0070064	0.0069065	0.005009	0.0037121	0.002816
39Ar	0.4334936	0.6491704	0.6035039	0.8787043	1.056187	0.5283783	0.2712843
error	0.0016002	0.0022002	0.0021002	0.0027001	0.0029001	0.0020002	0.0011003
38Ar	0.0077431	0.0129529	0.0136224	0.0174188	0.0189767	0.0084544	0.0044524
error	0.0002006	0.0003504	0.0003703	0.0004203	0.0005402	0.0002605	0.0002805
37Ar	0.0125866	0.0262873	0.0304988	0.0528324	0.081289	0.044592	0.0262157
error	0.0003032	0.0008412	0.0013007	0.0021005	0.0013007	0.000951	0.0009111
36Ar	0.0116998	0.018734	0.0278258	0.0245998	0.0160037	0.0069573	0.0049912
error	0.0000702	0.0000812	0.0001401	0.0001101	0.0000942	0.0000633	0.0000533

Sample	11.3.15						
Run	2						
Step	a	b	c	d	e	f	g
Age(Ma)	-0.0208241	0.0305339	0.027286	0.0549298	0.1044774	0.0731953	0.1411529
error	0.0820234	0.1084132	0.0309828	0.035456	0.0658979	0.0481525	0.0783088
% 40Ar*	2.073751	0.6776361	0.4398422	0.5459653	0.3523065	0.4547574	0.343365
Ca/K	5.748855	0.6599073	0.7990146	0.9172866	1.567559	2.556721	3.196678
Cl/K	0.0108731	0.0004785	0.0031804	0.0035688	0.0041733	0.0055964	0.013851
40Ar	0.5788916	4.459213	6.941541	6.195086	12.22871	9.429569	16.83529
error	0.0021213	0.00563	0.00563	0.007323	0.0094179	0.008021	0.0100168
39Ar	0.1326823	0.3338171	1.496601	1.268336	1.157726	1.322932	1.333435
error	0.0004408	0.0016003	0.0031001	0.0034001	0.0028002	0.0030001	0.0031001
38Ar	0.0024896	0.0069427	0.0242849	0.0209241	0.0234557	0.0246186	0.0331796
error	0.0002106	0.00035	0.00046	0.00024	0.00063	0.00052	0.00046
37Ar	0.0121165	0.0034915	0.0189335	0.0184023	0.0286315	0.0532909	0.0670421
error	0.000323	0.0002507	0.0004604	0.0005303	0.0010002	0.0015001	0.0009902
36Ar	0.0020522	0.0149265	0.0232554	0.0206431	0.0407481	0.0316751	0.0562571
error	0.0000394	0.0000992	0.0001002	0.0001102	0.0001402	0.0001402	0.0001901

Sample	11.3.15						
Run	2						
Step	h	i	j	k	l	m	n
Age(Ma)	0.088347	0.0175059	0.0793497	0.1151992	0.1510921	0.02608	-0.0430356
error	0.0547754	0.0493276	0.0423821	0.0487456	0.0523461	0.0630312	0.0788677
% 40Ar*	0.395117	0.4612782	0.979849	1.204427	1.452934	1.680239	2.222597
Ca/K	3.560826	3.867912	4.391445	4.58054	4.72216	5.311475	6.059174
Cl/K	0.0052069	0.0033216	0.0041362	0.0087035	0.0070783	0.0050788	0.0035965
40Ar	9.4676	6.682595	2.14714	1.428708	0.9429802	0.774769	0.4929883
error	0.0085198	0.0065258	0.0033506	0.0032521	0.0026639	0.0026639	0.0022752
39Ar	1.115632	0.9252975	0.5209302	0.3522746	0.2526008	0.1963716	0.1289239
error	0.0029001	0.0028002	0.0022002	0.0017002	0.0008505	0.0005008	0.000401
38Ar	0.0215619	0.0165909	0.0084454	0.0062425	0.004277	0.0032339	0.0020542
error	0.0006	0.00023	0.00017	0.00017	0.00021	0.00016	0.0000421
37Ar	0.0624172	0.0561047	0.0358223	0.025244	0.0186208	0.0162643	0.0121605
error	0.0021001	0.0009602	0.0004005	0.0002707	0.0006703	0.000181	0.0003905
36Ar	0.0318761	0.0228039	0.0073448	0.0048507	0.0031761	0.0027164	0.0017773
error	0.0001202	0.0001002	0.0000693	0.0000564	0.0000445	0.0000425	0.0000356

Table D.2 continued.

Sample	11.3.15			2.10.08			
Run	2			1			
Step	o	p	q	a	b	c	d
Age(Ma)	-0.0284236	-0.0387611	0.1062169	-0.0133552	1.092168	0.9806702	0.9053371
error	0.0815296	0.0613094	0.0540595	0.0611017	0.0700631	0.0346392	0.0231201
% 40Ar*	2.437418	1.705168	1.461939	1.846075	1.321293	1.715673	1.074344
Ca/K	6.212212	6.283971	6.197995	5.107979	3.059337	2.465599	1.569605
Cl/K	0.0005894	0.0049397	0.0028144	0.0002988	0.0598966	-0.0007988	-0.0015465
40Ar	0.4117699	0.7637652	0.9540468	0.8242546	1.233684	0.7022665	1.446299
error	0.0020824	0.0024691	0.0028594	0.0024691	0.0043702	0.0030031	0.0034883
39Ar	0.113525	0.2021015	0.2494116	0.2345917	0.2075663	0.3117284	0.6089885
error	0.000431	0.0005008	0.0005907	0.0007905	0.0011005	0.0016003	0.0021003
38Ar	0.001676	0.0033076	0.0038808	0.0034192	0.0074438	0.0039514	0.0076387
error	0.0000831	0.00012	0.00017	0.00013	0.0003915	0.000292	0.0003417
37Ar	0.0109686	0.0197105	0.0239722	0.0185702	0.0108688	0.0131452	0.0163408
error	0.0002906	0.0004504	0.0003106	0.0009702	0.0004539	0.0004439	0.0012014
36Ar	0.0014863	0.0027587	0.0033045	0.0029339	0.0033609	0.0012984	0.0028848
error	0.0000327	0.0000425	0.0000455	0.0000495	0.0000522	0.0000385	0.0000494

Sample	2.10.08						
Run	1						
Step	e	f	g	h	i	j	k
Age(Ma)	0.8638675	0.9051424	0.8654575	0.900314	0.8843413	0.9002346	0.7639219
error	0.0234144	0.0310803	0.0373607	0.0443122	0.0573053	0.0708	0.0754889
% 40Ar*	1.445089	1.683421	1.670209	1.893341	2.313981	2.72285	2.775713
Ca/K	2.473705	4.44799	6.678092	9.447433	11.35911	12.44456	14.40606
Cl/K	-0.0028455	-0.0029687	-0.0009698	0.0015804	0.005762	0.0102327	0.0015849
40Ar	0.8576538	0.7993056	0.6872571	0.6453376	0.4628374	0.4174741	0.4256832
error	0.002508	0.0027857	0.0023514	0.0023514	0.0021291	0.0022233	0.0021291
39Ar	0.477681	0.388333	0.2750281	0.2459944	0.1661852	0.1426826	0.1393334
error	0.0018011	0.0017012	0.0013023	0.0008435	0.0004743	0.0003952	0.0004347
38Ar	0.0056196	0.0046098	0.0035423	0.0034015	0.0025575	0.002427	0.0019823
error	0.000283	0.0001749	0.0001558	0.0001751	0.0001346	0.0001736	0.0001154
37Ar	0.0201492	0.0294056	0.0311968	0.0394007	0.0319139	0.0299819	0.033841
error	0.0013008	0.0005718	0.0005319	0.0015007	0.0006908	0.0010006	0.0017003
36Ar	0.0014695	0.0015803	0.0016498	0.0016384	0.00125	0.001153	0.0012947
error	0.0000389	0.0000435	0.0000371	0.000038	0.0000345	0.0000362	0.0000362

Sample	2.10.08			2.10.08			
Run	1			2			
Step	l	m	n	a	b	c	d
Age(Ma)	0.9012017	0.7029241	0.8391897	0.6972421	1.040189	0.9436376	0.8691728
error	0.10263	0.0882795	0.0733779	0.0708751	0.1646117	0.0214117	0.013193
% 40Ar*	3.527981	2.906203	2.44816	2.200214	1.789409	0.9096828	0.843692
Ca/K	19.06697	18.5351	18.74244	19.18022	2.648971	2.480788	2.140854
Cl/K	0.0095937	0.0059849	0.0005268	0.0025281	0.1161381	-0.0003463	-0.0020766
40Ar	0.3087144	0.3612048	0.357197	0.3981905	0.9170008	1.790425	1.459647
error	0.0017933	0.0022508	0.0020655	0.0023444	0.0040997	0.0041857	0.0036257
39Ar	0.0945337	0.1058864	0.1061551	0.1101285	0.0894198	0.7046798	0.8894274
error	0.0003321	0.000352	0.0003419	0.0002229	0.0004719	0.0013007	0.0027003
38Ar	0.0016104	0.0016971	0.0014894	0.0016495	0.0051885	0.0091894	0.0106079
error	0.0002012	0.0001516	0.0001526	0.0001526	0.0003109	0.0003209	0.0001321
37Ar	0.0302755	0.0329438	0.0333471	0.035368	0.0036559	0.0269603	0.0293447
error	0.001202	0.0007433	0.0006035	0.0004349	0.0002716	0.0005155	0.0004284
36Ar	0.0009557	0.0011935	0.0011285	0.0013286	0.0027523	0.0037149	0.0022181
error	0.0000345	0.0000336	0.0000278	0.0000278	0.000053	0.000052	0.0000383

Table D.2 continued.

Sample	2.10.08						
Run	2						
Step	e	f	g	h	i	j	k
Age(Ma)	0.8365637	0.8784527	0.8364222	0.8737623	0.7601505	0.8729312	0.8170345
error	0.0163086	0.0208561	0.0281849	0.03726	0.0550905	0.0746278	0.0657784
% 40Ar*	1.035065	1.135313	1.315213	1.542956	2.034561	2.624855	2.130529
Ca/K	2.621575	3.935443	6.524961	10.11299	13.21208	16.68724	20.72616
Cl/K	-0.0021609	-0.0028096	0.0014797	0.0009451	0.0042213	-0.0007516	0.0043504
40Ar	1.154904	1.015719	0.9131805	0.7578782	0.59637	0.4769192	0.5661185
error	0.0032481	0.0031528	0.0030552	0.0025349	0.0026932	0.0026058	0.0025201
39Ar	0.6827155	0.5100124	0.3886528	0.283995	0.1973471	0.1498999	0.164688
error	0.0025003	0.0021004	0.0018004	0.0012006	0.0004715	0.0004416	0.0004117
38Ar	0.0081623	0.0060689	0.0053048	0.0038796	0.0029816	0.0020147	0.0025386
error	0.0002809	0.0001715	0.0002112	0.0001024	0.0000907	0.0000936	0.0001023
37Ar	0.0275185	0.0308175	0.0388443	0.0438977	0.0397224	0.0380289	0.0517753
error	0.0007301	0.0004948	0.0004944	0.0007888	0.000455	0.0008083	0.0002308
36Ar	0.0019471	0.0019773	0.0021717	0.0019886	0.0017828	0.0014409	0.0018486
error	0.0000373	0.0000363	0.0000382	0.0000372	0.0000391	0.0000401	0.0000391

Sample	2.10.08			
Run	2			
Step	l	m	n	o
Age(Ma)	0.7269971	0.9377069	0.7980912	0.5723412
error	0.0807839	0.1019018	0.095426	0.1359993
% 40Ar*	2.465996	3.088362	2.822366	4.36441
Ca/K	28.0198	23.67405	23.55483	22.64504
Cl/K	0.006001	0.0091665	-0.0049735	-0.0038694
40Ar	0.4234006	0.3633514	0.3978832	0.2231134
error	0.0025192	0.0024375	0.0025238	0.0022058
39Ar	0.1161659	0.0984764	0.1053796	0.0639199
error	0.0003918	0.0003321	0.0003421	0.0002825
38Ar	0.0018832	0.0016891	0.0013134	0.0008192
error	0.0001219	0.0001417	0.0000877	0.00006
37Ar	0.0491432	0.0352225	0.0374502	0.0218274
error	0.0004838	0.0004547	0.0004065	0.0003875
36Ar	0.0015375	0.001183	0.0013497	0.000804
error	0.0000333	0.0000362	0.0000362	0.0000314

Table D.3 Results of total fusion experiments on sanidine phenocrysts from sample 5.1.15

Crystal	1	2	3	4	5	6	7
Age(Ma)	6.066832	5.974484	6.011923	6.039755	6.039046	6.023179	5.941588
error	0.0507752	0.0666493	0.0535723	0.0596648	0.0661087	0.0876555	0.051211
% 40Ar*	99.19546	87.13902	91.27459	99.45987	97.99086	98.00257	94.8452
Ca/K	0.0288327	0.0234496	0.0259984	0.0143724	0.0343858	0.0195976	0.0199098
Cl/K	0.0026928	-0.002768	-0.001442	-0.001707	-0.002783	-0.004189	0.0018093
40Ar	1.426961	1.154773	1.593223	1.016037	0.9217995	0.566045	1.487099
error	0.002601	0.0017015	0.0028009	0.0014018	0.0013019	0.0012021	0.0019013
39Ar	0.2285777	0.1650123	0.2369815	0.1639193	0.1465377	0.0902314	0.2325724
error	0.00056	0.0003701	0.0007	0.0004	0.00039	0.0002501	0.00069
38Ar	0.0030106	0.0019509	0.0028633	0.0019083	0.0016602	0.0009784	0.0030333
error	0.0000842	0.0000802	0.0000523	0.0000464	0.0000792	0.0000355	0.0000623
37 Ar	0.0003653	0.0002148	0.000341	0.000132	0.000277	0.0000979	0.0002562
error	0.0000425	0.000024	0.0000268	0.0000366	0.0000268	0.0000192	0.0000259
36Ar	0.0000394	0.0004979	0.0004664	0.0000187	0.0000627	0.0000381	0.0002574
error	0.0000262	0.0000311	0.0000291	0.0000262	0.0000272	0.0000242	0.0000272

Crystal	8	9	10	11	12	13	14
Age(Ma)	6.115057	5.938254	6.044483	6.047332	6.262717	5.956153	6.08484
error	0.0520732	0.0681603	0.0645153	0.0545946	0.1078489	0.0556023	0.0563614
% 40Ar*	94.64547	97.91578	96.96687	98.68353	98.43688	98.03642	96.54499
Ca/K	0.0261589	0.0161899	0.0202945	0.0321427	0.0376089	0.0175643	0.0345836
Cl/K	0.0015767	-0.001044	0.0009359	0.0015632	0.0046943	-0.0033855	0.0012402
40Ar	1.589303	0.7795417	0.9309821	1.430347	0.4622055	1.054026	1.451962
error	0.0016016	0.0013019	0.0012021	0.0027009	0.0015017	0.0015017	0.0019013
39Ar	0.2409866	0.1259321	0.1463181	0.228673	0.0711704	0.1699704	0.2256966
error	0.00042	0.00038	0.00039	0.0006	0.0001401	0.00042	0.00059
38Ar	0.0031273	0.0015025	0.0018516	0.0029273	0.0009888	0.0018898	0.002884
error	0.0001002	0.0000474	0.0000474	0.0000633	0.0000345	0.0000782	0.0000583
37 Ar	0.0003463	0.000113	0.0001636	0.0004011	0.0001456	0.0001644	0.000424
error	0.0000259	0.0000366	0.0000211	0.0000259	0.000022	0.000022	0.0000455
36Ar	0.0002859	0.0000547	0.000095	0.0000641	0.0000246	0.0000697	0.0001691
error	0.0000311	0.0000242	0.0000262	0.0000301	0.0000242	0.0000242	0.0000321

Crystal	15	16	17	18	19	20	21
Age(Ma)	6.115854	6.08901	6.058329	5.9179	6.065429	5.904314	6.018215
error	0.0739114	0.0804833	0.1005025	0.0583458	0.0644074	0.0850387	0.0709867
% 40Ar*	97.76811	99.8644	98.80447	94.78043	98.09562	84.04371	96.87461
Ca/K	0.0249189	0.0297301	0.0246697	0.019753	0.0185964	0.0095514	0.029469
Cl/K	-0.0002264	0.0015483	-0.0082261	0.0002774	-0.002455	0.0021315	-0.0049958
40Ar	0.7224436	0.6687209	0.4762101	1.035115	0.9334141	0.791041	0.8169327
error	0.0012021	0.0019013	0.0017015	0.0016016	0.0020013	0.0017015	0.0014018
39Ar	0.113143	0.1074472	0.0760872	0.1624223	0.1478938	0.1103179	0.1288318
error	0.0003301	0.0003301	0.0002901	0.00038	0.0003301	0.0003301	0.0003701
38Ar	0.0013828	0.0013699	0.0007166	0.0020328	0.0016917	0.0015078	0.001367
error	0.0000494	0.0000375	0.0000553	0.0000513	0.0000892	0.0000474	0.0000782
37 Ar	0.0001537	0.0001735	0.0001021	0.000175	0.0001501	0.0000587	0.0002049
error	0.000022	0.000024	0.0000259	0.000022	0.0000347	0.0000259	0.0000268
36Ar	0.0000544	3.48E-06	0.0000193	0.0001814	0.0000599	0.0004229	0.000086
error	0.0000242	0.0000252	0.0000232	0.0000252	0.0000262	0.0000281	0.0000262

Table D.3 continued.

Crystal	22	23	24	25	26	27	28
Age(Ma)	5.913361	6.066613	6.048823	6.13284	6.044472	5.994326	5.903864
error	0.0611051	0.1066405	0.0568691	0.072799	0.1273645	0.0707767	0.0613601
% 40Ar*	95.49651	96.69916	99.09459	99.5814	94.33973	99.88838	97.73507
Ca/K	0.0268838	0.0182393	0.0283685	0.0122393	0.0195186	0.0288152	0.0267113
Cl/K	0.0015027	-0.0055161	-0.0022285	0.0016553	-0.004217	-0.0001405	-0.0007047
40Ar	0.8808968	0.5021857	1.141198	0.7049064	0.38952	0.750044	0.8776473
error	0.0014018	0.0011023	0.002501	0.0012021	0.0017015	0.0019013	0.0021012
39Ar	0.139375	0.0784202	0.1831595	0.1121309	0.0595602	0.1224492	0.1423441
error	0.0003401	0.0003001	0.00043	0.0001801	0.0001401	0.00038	0.0003601
38Ar	0.0017991	0.0008187	0.002102	0.001435	0.0006545	0.0014897	0.001716
error	0.0000593	0.0000712	0.0000982	0.0000444	0.0000663	0.0000404	0.0000523
37 Ar	0.0002024	0.0000777	0.0002796	0.0000753	0.0000628	0.0001891	0.0002039
error	0.000022	0.000023	0.0000425	0.0000249	0.0000347	0.0000356	0.0000366
36Ar	0.0001334	0.0000557	0.0000353	0.0000101	0.000074	3.28E-06	0.0000671
error	0.0000232	0.0000262	0.0000262	0.0000242	0.0000242	0.0000242	0.0000232

Crystal	29	30	31	32	33	34	35
Age(Ma)	6.173397	6.0551	5.996044	5.832015	5.993363	6.156695	5.91949
error	0.0768081	0.0826089	0.061801	0.0776477	0.0570136	0.0930986	0.0946382
% 40Ar*	99.96552	99.08583	97.52318	91.38504	96.3828	96.04081	92.37831
Ca/K	0.0081358	0.0216244	0.0385544	0.0290237	0.0160315	0.0150654	0.0004487
Cl/K	-0.0082206	0.0012833	-0.0037994	-0.0028598	-0.0014497	0.000922	-0.000665
40Ar	0.6270216	0.584599	0.9371773	0.7093929	1.083251	0.6310783	0.6545591
error	0.0016016	0.0011023	0.0014018	0.0012021	0.0015017	0.0019013	0.0017015
39Ar	0.0994671	0.0937205	0.1493348	0.1089079	0.1706677	0.096442	0.1000773
error	0.0002501	0.0002901	0.0003701	0.0003201	0.00043	0.0002901	0.0003101
38Ar	0.0009324	0.0011892	0.0016422	0.0012609	0.0020232	0.001224	0.0012305
error	0.0000643	0.0000385	0.0000663	0.0000673	0.0000474	0.0000355	0.0000603
37 Ar	0.0000449	0.0001088	0.0003061	0.0001684	0.0001473	0.0000783	4.64E-06
error	0.0000386	0.0000249	0.0000259	0.000022	0.0000192	0.0000249	0.0000337
36Ar	7.80E-07	0.0000182	0.0000785	0.0002051	0.0001316	0.0000839	0.0001671
error	0.0000222	0.0000232	0.0000252	0.0000252	0.0000252	0.0000272	0.0000291

Crystal	36	37	38	39	40	41	42
Age(Ma)	5.888683	6.10365	5.851213	6.003279	5.831989	6.047948	5.735213
error	0.0919647	0.0774391	0.0686722	0.0838412	0.1682102	0.1514637	0.0895714
% 40Ar*	97.00117	99.25191	96.30558	99.77193	96.22703	97.78261	95.2278
Ca/K	0.0459669	0.0217761	0.0240871	0.0184759	0.025489	-0.0002043	0.0330865
Cl/K	-0.0000146	0.0012508	-0.0008724	0.000981	-0.0005154	0.0024787	0.0001847
40Ar	0.536107	0.6492759	0.7499811	0.6181848	0.2748416	0.3093604	0.4838309
error	0.0018014	0.0018014	0.0020013	0.0016016	0.0014018	0.0014018	0.0016016
39Ar	0.0865205	0.1034328	0.1209387	0.1006533	0.0444298	0.0490005	0.0787103
error	0.0002501	0.0002801	0.0003301	0.0003101	0.0002301	0.0001202	0.0002701
38Ar	0.0010661	0.0013106	0.0014578	0.0012639	0.0005411	0.0006445	0.0009807
error	0.0000394	0.0000424	0.0000742	0.0000702	0.0000316	0.0000365	0.0000404
37 Ar	0.0002096	0.0001199	0.0001545	0.0000991	0.0000599	5.97E-07	0.0001368
error	0.0000386	0.0000268	0.000023	0.0000455	0.0000211	0.0000201	0.0000327
36Ar	0.0000544	0.0000166	0.0000932	4.98E-06	0.0000349	0.000023	0.0000777
error	0.0000242	0.0000232	0.0000232	0.0000252	0.0000242	0.0000242	0.0000212

Table D.3 continued.

Crystal	43	44	45	46	47	48	49
Age(Ma)	5.991977	5.858055	5.983673	5.890393	5.923344	6.06463	7.01139
error	0.0661769	0.1280127	0.1211422	0.0843982	0.104114	0.0807588	0.9055906
% 40Ar*	96.72263	94.52522	98.85839	94.26284	97.27056	99.75619	98.01735
Ca/K	0.022187	0.0243764	0.0236856	0.036934	0.0393302	0.0083404	1.78314
Cl/K	0.0001934	0.0011646	0.0014869	0.0012008	0.002167	0.0029929	-0.0415365
40Ar	0.8815572	0.3740373	0.4173614	0.6343069	0.4873844	0.5585395	0.0502722
error	0.0013019	0.0014018	0.0015017	0.0018014	0.0017015	0.0017015	0.0003866
39Ar	0.1394123	0.0591313	0.0675538	0.0994495	0.0784129	0.0900055	0.0068877
error	0.0003301	0.0002201	0.0001901	0.0002701	0.0002901	0.0002601	0.0000802
38Ar	0.0017298	0.0007587	0.0008625	0.0012785	0.0010245	0.0011928	-0.0000139
error	0.0000513	0.0000404	0.0000553	0.0000394	0.0000444	0.0000663	0.0000355
37 Ar	0.0001634	0.0000759	0.0000842	0.0001918	0.0001607	0.0000407	0.0006314
error	0.000024	0.000023	0.0000356	0.000023	0.000022	0.0000396	0.0000514
36Ar	0.0000972	0.0000688	0.0000162	0.0001224	0.000045	4.68E-06	4.98E-06
error	0.0000262	0.0000242	0.0000262	0.0000252	0.0000252	0.0000212	0.0000212

Crystal	50
Age(Ma)	5.958228
error	0.0971492
% 40Ar*	98.54926
Ca/K	0.0220482
Cl/K	0.0015935
40Ar	0.5231611
error	0.0017015
39Ar	0.0847738
error	0.0002901
38Ar	0.0010865
error	0.0000454
37 Ar	0.0000955
error	0.0000201
36Ar	0.0000257
error	0.0000252

Table D.4 Nucleogenic production ratios, decay constants, and constant isotope ratios used in age calculations

Nucleogenic production ratios:		Isotopic constants and decay rates:	
$(^{36}Ar/^{37}Ar)Ca$	2.64×10^{-4}	$\lambda(^{40}K_e)$/yr	$5.757 \pm 0.016 \times 10^{-11}$
$(^{39}Ar/^{37}Ar)Ca$	6.5×10^{-4}	$\lambda(^{40}K_{\beta-})$/yr	$4.955 \pm 0.013 \times 10^{-10}$
$(^{38}Ar/^{37}Ar)Ca$	$0.196 \pm 0.0082 \times 10{-}4$	$\lambda(^{37}Ar)$/d	$1.983 \pm 0.0045 \times 10^{-2}$
$(^{40}Ar/^{39}Ar)K$	8.5×10^{-3}	$\lambda(^{39}Ar)$/d	$7.068 \pm 0.0788 \times 10^{-6}$
$(^{38}Ar/^{39}Ar)K$	$1.220 \pm 0.0027 \times 10^{-2}$	$\lambda(^{36}Cl)$/d	$6.308 \pm 0 \times 10^{-9}$
$(^{36}Ar/^{38}Ar)Cl$	$2.629 \pm 0.011 \times 10^{2}$	$(^{40}Ar/^{36}Ar)_{Atm}$	298.56 ± 0.31
$^{37}Ar/^{39}Ar$ to Ca/K	1.96	$(^{40}Ar/^{38}Ar)_{Atm}$	1583.5 ± 2.5
$^{38}Ar/^{39}Ar$ to Cl/K	2.9	$^{40}K/K_{Total}$	0.1167 00002

E. Major element composition of amphibole and clinopyroxenes- standards and unknowns

Table E.1 Spot analyses of Kakanui Hornblende secondary standard. The sub-headings denote the unknown samples which were analysed in the same EPMA session.

	SiO_2	TiO_2	Al_2O_3	FeO	MnO	MgO	CaO	Na_2O	K_2O	Total
With samples 2-5-08, 2-6-08 and 2-7-08										
S1	40.35	4.84	13.36	10.35	0.06	12.45	10.16	2.79	2.12	96.47
S2	39.89	4.88	13.46	10.47	0.08	12.59	10.25	2.89	2.14	96.65
S3	40.07	4.61	13.50	10.52	0.12	12.43	10.13	2.73	2.13	96.25
S4	39.91	4.71	13.58	10.21	0.09	12.28	10.19	2.84	2.14	95.95
S5	40.04	4.69	13.52	10.44	0.13	12.49	10.24	2.82	2.11	96.49
S6	39.30	4.85	13.58	10.54	0.06	12.58	10.13	2.71	2.15	95.90
S7	39.44	4.32	13.37	10.78	0.09	12.27	10.24	2.69	2.17	95.38
S8	39.54	4.36	13.43	10.62	0.08	12.29	10.19	2.81	2.13	95.44
S9	39.22	4.79	13.46	9.97	0.12	12.09	10.22	2.87	2.16	94.90
S10	39.26	4.75	13.50	10.29	0.12	11.96	10.17	2.70	2.16	94.90
S11	38.88	4.61	13.22	10.26	0.10	11.85	10.34	2.70	2.16	94.11
S12	39.26	4.93	13.32	10.30	0.09	12.09	9.99	2.82	2.14	94.95
S13	39.58	4.70	13.33	10.39	0.09	12.37	10.25	2.77	2.17	95.65
S14	39.37	4.74	13.22	10.34	0.12	11.82	10.19	2.79	2.19	94.78
S15	39.87	4.61	13.22	10.33	0.09	12.36	10.25	2.93	2.18	95.84
With samples 7-4-15 and 9-2-15										
S1	40.63	4.59	13.64	10.49	0.10	12.49	10.22	2.64	2.07	96.87
S2	40.45	4.74	13.55	10.24	0.09	12.51	10.29	2.68	2.06	96.61
S3	40.62	4.59	13.41	10.28	0.09	12.45	10.25	2.62	2.05	96.36
S4	40.63	4.71	13.63	10.50	0.08	12.59	10.33	2.70	2.05	97.23
S5	40.85	4.62	13.40	10.37	0.11	12.36	10.31	2.81	2.09	96.92
S6	39.65	4.72	13.17	10.46	0.09	12.40	10.32	2.60	2.01	95.43
S7	39.31	4.71	13.39	10.40	0.11	9.53	10.30	2.68	2.00	92.42
S8	39.74	4.69	13.36	10.56	0.08	12.20	10.23	2.68	2.03	95.56
S9	39.97	4.76	13.33	10.37	0.09	12.36	10.19	2.65	2.01	95.73
S10	39.72	4.77	13.08	10.36	0.10	12.18	10.34	2.61	2.03	95.19
S11	39.74	4.65	13.24	10.43	0.07	12.31	10.28	2.64	2.03	95.39
Average	**39.82**	**4.69**	**13.40**	**10.39**	**0.09**	**12.20**	**10.23**	**2.74**	**2.10**	**95.67**
Ref. values	*40.37*	*4.72*	*14.90*	*10.92*	*0.09*	*12.80*	*10.30*	*2.60*	*2.05*	*98.75*
SD[a]	0.51	0.13	0.14	0.15	0.02	0.57	0.08	0.09	0.06	
SEM[b]	0.10	0.03	0.03	0.03	0.00	0.11	0.02	0.02	0.01	

a- Standard deviation for all spot analyses
b- Standard error of the mean

Table E.2 Spot analyses of GEO2 Diopside secondary standard. The sub-headings denote the unknown samples which were analysed in the same EPMA session.

	SiO_2	TiO_2	Al_2O_3	FeO	MnO	MgO	CaO	Na_2O	K_2O	Total
With 9-2-15 and 8-3-15 clinopyroxene										
S1	55.75	0.04	0.03	0.71	0.07	17.96	25.46	0.07	0.00	100.10
S2	55.77	0.04	0.03	0.73	0.07	17.98	25.45	0.05	0.00	100.10
S3	55.81	0.04	0.00	0.78	0.08	17.90	25.89	0.08	0.00	100.57
S4	55.67	0.03	0.02	0.73	0.07	18.29	25.55	0.07	0.00	100.42
S5	55.92	0.04	0.00	0.86	0.08	18.13	25.65	0.06	0.00	100.74
S6	55.42	0.05	0.00	0.77	0.08	17.68	25.61	0.07	0.00	99.68
S7	55.52	0.04	-0.01	0.76	0.08	17.69	25.64	0.06	0.00	99.78
S8	55.63	0.04	0.03	0.75	0.08	17.92	25.48	0.05	0.00	99.98
S9	55.72	0.04	0.04	0.76	0.09	17.84	25.37	0.06	0.00	99.92
S10	55.67	0.04	0.00	0.78	0.08	17.66	25.67	0.06	0.00	99.93
With 8-3-15, 9-1-15 and 11-3-15 amphibole										
S1	55.91	0.08	0.03	0.75	0.06	18.57	25.49	0.03	0.01	100.96
S2	55.83	0.10	0.02	0.77	0.07	18.77	25.37	0.07	0.00	101.00
S3	55.34	0.09	0.04	0.70	0.08	18.49	25.46	0.04	0.02	100.24
S4	55.21	0.09	0.02	0.72	0.05	18.49	25.53	0.04	0.01	100.15
S5	55.54	0.09	0.04	0.68	0.08	18.43	25.37	0.07	0.01	100.28
S6	55.70	0.10	0.03	0.72	0.06	18.77	25.45	0.06	0.01	100.89
S7	55.57	0.06	0.01	0.77	0.06	18.62	25.66	0.07	0.00	100.84
With 2-5-08, 2-6-08 and 2-7-08 amphibole										
S1	55.64	-0.01	0.05	0.82	0.07	17.77	25.86	0.07	0.00	100.31
S2	55.30	0.04	0.04	0.74	0.06	18.05	25.79	0.05	0.02	99.99
S3	55.28	0.08	0.02	0.78	0.12	17.97	25.79	0.07	0.01	99.99
S4	55.32	0.01	0.03	0.75	0.07	18.27	25.70	0.07	0.02	100.19
S5	55.15	-0.01	0.04	0.79	0.05	18.05	25.76	0.08	0.00	99.79
S6	55.76	-0.08	0.01	0.78	0.06	18.41	25.96	0.13	0.00	100.96
S7	55.18	0.06	0.04	0.76	0.11	18.43	25.78	0.07	0.02	100.41
S8	54.91	0.05	0.04	0.74	0.07	18.29	25.79	0.05	0.01	99.88
S9	54.19	0.01	0.04	0.82	0.10	18.20	25.75	0.13	0.00	99.24
S10	54.68	0.06	0.04	0.81	0.08	18.12	25.76	0.06	-0.01	99.53
S11	55.47	0.05	0.03	0.74	0.07	18.15	25.47	0.08	0.01	99.53
S12	55.12	0.05	0.05	0.66	0.10	18.22	25.67	0.08	0.01	99.53
S13	54.99	0.09	0.02	0.73	0.06	18.03	25.64	0.10	0.01	99.53
S14	54.68	0.06	0.05	0.77	0.05	17.99	25.63	0.13	0.01	99.53
S15	54.36	0.02	0.05	0.77	0.06	17.73	25.59	0.07	0.01	99.53
With 9-2-15 and 7-4-15 amphibole										
S1	55.28	0.04	0.06	0.82	0.06	18.21	26.05	0.05	0.00	100.57
S2	55.44	0.00	0.02	0.79	0.08	18.03	25.91	0.04	0.02	100.33
S3	55.20	0.01	0.02	0.81	0.07	18.08	25.92	0.05	0.01	100.15
S4	54.97	0.04	0.04	0.83	0.07	17.59	26.01	0.04	0.01	99.59
S5	55.04	0.04	0.02	0.76	0.08	17.55	26.09	0.06	0.01	99.64
S6	55.21	0.05	0.00	0.73	0.09	17.59	26.07	0.03	0.01	99.75
S7	55.12	0.10	0.04	0.77	0.07	18.10	25.92	0.03	0.01	100.17
S8	55.04	0.07	0.06	0.78	0.07	17.89	25.87	0.09	0.02	99.88
S9	55.72	0.07	0.02	0.78	0.08	18.07	25.89	0.10	0.01	100.74
With 7-5-15 amphibole										
S1	55.67	0.04	0.06	0.77	0.08	17.98	25.90	0.09	0.01	100.49
S2	55.47	0.02	0.05	0.76	0.07	17.85	25.96	0.05	0.01	100.14
S3	54.99	0.12	0.02	0.81	0.07	17.67	25.84	0.04	0.01	99.46

Table E.2 continued.

	SiO_2	TiO_2	Al_2O_3	FeO	MnO	MgO	CaO	Na_2O	K_2O	Total
With 11-3-15 clinopyroxene										
S1	55.97	0.04	-0.04	0.74	0.09	18.24	25.81	0.04	0.00	100.87
S2	55.83	0.03	-0.06	0.83	0.09	17.99	25.87	0.04	0.00	100.63
S3	55.88	0.04	-0.02	0.74	0.08	18.19	25.65	0.02	0.00	100.58
S4	56.31	0.05	-0.01	0.81	0.08	18.02	25.56	0.07	0.00	100.86
S5	55.89	0.04	-0.01	0.79	0.08	17.79	25.37	0.06	0.00	100.02
S6	56.54	0.05	-0.02	0.79	0.07	17.92	25.59	0.08	0.00	101.00
Average	**55.42**	**0.05**	**0.02**	**0.77**	**0.07**	**18.07**	**25.71**	**0.06**	**0.01**	**100.37**
Ref. values	*55.36*			*0.90*		*18.13*	*25.72*			*100.11*
SD[a]	0.59	0.03	0.03	0.04	0.01	0.32	0.21	0.02	0.01	
SEM[b]	0.08	0.00	0.00	0.01	0.00	0.04	0.03	0.00	0.00	

a- Standard deviation for all spot analyses
b- Standard error of the mean

Table E.3 Major element composition of spot analyses in amphibole phenocrysts with averages used in Chapter 6 and the applied correction based on the measurements of Kakanui hornblende

Spot	SiO_2	TiO_2	Al_2O_3	FeO	MnO	MgO	CaO	Na_2O	K_2O	Total
2-5-08 cores										
amph1_c1	39.72	3.48	12.53	10.60	0.08	13.24	11.85	2.67	1.40	95.57
amph1_c2	39.86	3.53	12.50	10.41	0.11	13.29	11.78	2.68	1.34	95.49
amph1_c3	40.06	3.43	12.43	9.90	0.12	13.62	12.02	2.59	1.43	95.59
amph1_c4	40.16	3.65	12.19	9.94	0.08	13.68	11.87	2.45	1.39	95.41
amph2_c1	39.20	3.32	12.29	15.62	0.33	9.74	11.77	2.37	2.00	96.65
amph2_c2	39.39	3.19	12.28	15.02	0.29	10.14	11.63	2.41	2.03	96.36
amph3_c1	39.77	3.53	12.11	9.63	0.12	13.81	11.82	2.51	1.70	95.00
amph3_c2	39.78	3.75	12.37	9.75	0.12	13.86	11.73	2.61	1.70	95.67
amph3_c3	40.07	3.75	12.23	10.07	0.09	13.66	11.68	2.70	1.55	95.81
Average	**39.78**	**3.51**	**12.33**	**11.22**	**0.15**	**12.78**	**11.79**	**2.55**	**1.62**	**95.73**
Corrected[a]	*40.33*	*3.54*	*13.83*	*11.74*	*0.15*	*13.38*	*11.86*	*2.42*	*1.56*	*98.81*
SD	0.30	0.18	0.13	2.22	0.09	1.54	0.11	0.12	0.25	
SEM	0.10	0.06	0.04	0.74	0.03	0.51	0.04	0.04	0.08	
2-5-08 rims										
amph1_r1	39.19	3.43	12.69	11.16	0.13	12.80	11.84	2.72	1.35	95.32
amph1_r2	40.29	3.24	11.89	11.16	0.15	12.90	11.86	2.68	1.40	95.57
amph1_r3	40.29	3.31	11.81	11.26	0.15	12.99	11.84	2.63	1.36	95.65
amph1_r4	40.22	2.90	11.93	11.77	0.19	12.74	11.81	2.79	1.33	95.67
amph1_r5	40.30	3.44	12.15	11.23	0.18	12.84	11.75	2.70	1.40	96.00
amph1_r6	40.57	3.25	12.35	11.81	0.14	12.98	11.72	2.81	1.39	97.02
amph1_r7	40.06	3.57	11.98	11.08	0.13	12.68	11.82	2.70	1.40	95.43
amph1_r8	40.49	3.37	12.46	9.55	0.12	13.76	11.92	2.82	1.43	95.92
amph1_r9	40.10	3.21	12.84	11.68	0.11	12.64	11.94	2.56	1.31	96.38
amph1_r10	39.73	3.12	12.75	11.91	0.14	12.43	11.84	2.74	1.34	96.00
amph3_r1	39.62	3.72	11.85	10.74	0.07	12.67	11.77	2.75	1.63	94.82
amph3_r2	39.26	3.78	12.37	11.36	0.11	12.78	11.63	2.78	1.52	95.58
amph3_r3	39.91	3.53	12.18	10.52	0.11	13.51	11.88	2.79	1.49	95.92
amph3_r4	39.52	3.46	12.64	11.00	0.12	12.67	11.77	2.63	1.65	95.45
amph3_r5	39.97	3.46	12.08	9.71	0.09	13.83	11.62	2.75	1.73	95.24

Table E.3 continued.

Spot	SiO_2	TiO_2	Al_2O_3	FeO	MnO	MgO	CaO	Na_2O	K_2O	Total
amph3_r6	39.60	3.34	12.68	11.35	0.15	12.48	11.94	2.60	1.65	95.79
amph3_r7	39.73	3.19	12.35	11.16	0.14	12.82	11.77	2.67	1.67	95.51
Average	**39.93**	**3.37**	**12.29**	**11.08**	**0.13**	**12.91**	**11.81**	**2.71**	**1.47**	**95.72**
Corrected[a]	*40.48*	*3.40*	*13.80*	*11.61*	*0.13*	*13.51*	*11.88*	*2.57*	*1.42*	*98.80*
SD	0.40	0.21	0.33	0.64	0.03	0.40	0.09	0.07	0.14	
SEM	0.10	0.05	0.08	0.15	0.01	0.10	0.02	0.02	0.03	
2-6-08 cores										
amph1_c1	40.44	3.96	12.20	10.80	0.12	13.52	11.63	2.73	1.14	96.54
amph1_c2	40.20	4.00	12.29	9.66	0.08	14.16	11.90	2.72	1.16	96.18
amph1_c3	40.44	3.87	12.18	10.16	0.05	13.51	11.71	2.86	1.21	95.99
amph2_c1	40.48	3.61	11.89	10.89	0.15	13.24	11.56	2.77	1.13	95.73
amph2_c2	40.28	3.55	11.89	10.70	0.17	13.52	11.64	2.88	1.15	95.78
amph2_c3	40.33	3.30	11.68	10.77	0.20	13.53	11.59	2.91	1.10	95.43
amph3_c1	40.30	2.94	12.59	11.29	0.19	13.42	11.35	2.89	1.14	96.11
amph3_c2	40.03	2.65	12.02	11.05	0.15	13.61	11.32	2.77	1.17	94.78
amph3_c3	39.92	3.48	12.41	11.58	0.16	13.08	11.57	2.73	1.17	96.10
amph4_c1	39.90	3.54	12.64	9.23	0.12	13.68	11.62	2.72	1.17	94.61
amph4_c2	40.05	4.10	12.46	9.64	0.10	13.61	11.62	2.72	1.21	95.52
amph4_c3	39.63	3.37	12.95	10.38	0.09	12.91	11.33	2.68	1.34	94.69
amph5_c1	39.86	3.50	12.20	10.99	0.17	13.21	11.61	2.73	1.12	95.38
amph5_c2	40.25	3.53	12.10	11.28	0.21	13.43	11.49	2.77	1.15	96.22
amph5_c3	40.20	3.48	11.49	11.14	0.19	13.46	11.56	2.87	1.09	95.50
amph5_c4	39.72	3.07	11.88	11.68	0.16	13.48	11.45	2.83	1.15	95.42
Average	**40.13**	**3.50**	**12.18**	**10.70**	**0.15**	**13.46**	**11.56**	**2.79**	**1.16**	**95.62**
Corrected[a]	*40.68*	*3.53*	*13.69*	*11.23*	*0.14*	*14.06*	*11.63*	*2.65*	*1.11*	*98.71*
SD	0.26	0.38	0.36	0.69	0.04	0.27	0.14	0.07	0.05	
SEM	0.06	0.09	0.09	0.17	0.01	0.07	0.04	0.02	0.01	
2-6-08 rims										
amph1_r1	40.56	2.63	12.04	12.82	0.22	12.60	11.20	2.76	1.25	96.09
amph1_r2	39.38	2.78	13.58	12.62	0.23	12.22	11.11	2.98	1.14	96.04
amph1_r3	40.05	3.65	12.91	11.56	0.12	13.01	11.32	2.90	1.20	96.72
amph1_r4	39.36	3.63	12.72	11.51	0.17	12.58	11.32	2.67	1.20	95.15
amph1_r5	40.18	2.56	12.16	12.31	0.24	12.55	11.17	2.80	1.26	95.24
amph1_r6	39.52	2.75	13.11	12.59	0.23	12.00	11.17	2.97	1.21	95.54
amph1_r7	39.52	3.12	13.06	11.59	0.13	12.55	11.22	2.75	1.13	95.07
amph1_r8	40.31	3.52	12.57	10.94	0.11	12.74	11.25	2.88	1.22	95.54
amph2_r1	40.18	3.46	11.97	10.96	0.19	13.23	11.47	2.84	1.17	95.48
amph2_r2	40.22	3.77	12.54	10.23	0.09	13.56	11.58	2.77	1.19	95.94
amph2_r3	40.29	3.54	12.50	10.71	0.17	13.61	11.58	2.81	1.11	96.33
amph2_r4	40.21	3.68	12.55	10.15	0.11	13.62	11.58	2.68	1.18	95.77
amph2_r5	40.40	3.71	12.01	10.90	0.14	13.31	11.58	2.73	1.20	95.99
amph2_r6	40.01	3.05	12.22	11.06	0.14	13.20	11.54	2.88	1.10	95.20
amph2_r7	40.46	3.18	12.49	11.60	0.10	13.45	11.54	2.74	1.09	96.65
amph3_r1	40.33	3.41	12.59	10.55	0.18	13.60	11.44	2.77	1.16	96.03
amph3_r2	39.82	3.14	12.20	10.56	0.16	13.59	11.41	2.82	1.14	94.84
amph3_r3	39.88	3.07	12.52	10.97	0.19	13.35	11.44	2.86	1.18	95.46
amph3_r4	39.82	3.05	12.19	10.95	0.13	13.69	11.40	2.81	1.11	95.15
amph3_r5	39.46	3.72	12.64	9.97	0.15	13.83	11.53	2.69	1.18	95.17
amph3_r6	39.55	3.73	12.52	10.01	0.11	13.75	11.59	2.72	1.16	95.15
amph3_r7	40.26	3.20	12.07	10.55	0.13	13.71	11.37	2.73	1.10	95.12
amph4_r1	40.78	2.77	11.75	12.56	0.30	12.52	11.10	2.85	1.29	95.92

Table E.3 continued.

Spot	SiO_2	TiO_2	Al_2O_3	FeO	MnO	MgO	CaO	Na_2O	K_2O	Total
amph4_r2	40.54	2.57	12.00	12.53	0.29	12.60	11.17	3.07	1.28	96.07
amph4_r3	40.24	2.51	12.04	12.83	0.31	12.23	11.10	2.93	1.31	95.50
amph4_r4	39.35	3.07	12.11	11.79	0.23	12.62	11.24	2.93	1.24	94.57
amph4_r5	40.23	2.91	12.24	11.50	0.26	12.61	11.30	3.02	1.18	95.24
amph4_r6	39.97	2.66	12.22	11.92	0.30	12.81	11.24	3.01	1.27	95.41
amph4_r7	39.42	2.88	12.54	11.85	0.18	12.65	11.25	2.79	1.22	94.77
amph5_r1	39.74	3.16	11.90	11.81	0.19	13.24	11.48	2.96	1.14	95.62
amph5_r2	39.62	3.13	11.92	11.94	0.22	13.15	11.41	2.82	1.13	95.33
amph5_r3	40.42	3.23	11.92	11.78	0.17	13.27	11.46	2.82	1.21	96.28
amph5_r4	39.99	2.93	12.07	12.13	0.16	13.01	11.44	2.78	1.14	95.65
amph5_r5	39.75	3.08	11.82	12.37	0.21	12.91	11.39	2.72	1.15	95.40
amph5_r6	39.74	3.50	11.85	12.18	0.19	13.06	11.47	2.72	1.12	95.82
amph5_r7	39.88	3.32	11.53	12.08	0.20	13.08	11.48	2.83	1.15	95.55
Average	**39.98**	**3.17**	**12.31**	**11.51**	**0.19**	**13.04**	**11.37**	**2.83**	**1.18**	**95.58**
Corrected[a]	*40.54*	*3.20*	*13.81*	*12.04*	*0.18*	*13.64*	*11.44*	*2.69*	*1.13*	*98.66*
SD	0.39	0.37	0.42	0.83	0.06	0.49	0.15	0.10	0.06	
SEM	0.06	0.06	0.07	0.14	0.01	0.08	0.03	0.02	0.01	
2-7-08 cores										
amph1_c1	39.89	3.48	12.44	11.33	0.11	13.28	11.82	2.62	1.23	96.20
amph1_c2	39.71	3.48	12.61	11.56	0.14	13.16	11.80	2.56	1.31	96.33
amph1_c3	40.17	3.37	12.65	11.03	0.08	12.98	11.86	2.60	1.28	96.04
amph1_c4	39.48	3.58	12.63	11.25	0.11	12.91	11.89	2.59	1.35	95.78
amph2_c1	39.91	3.61	12.24	9.25	0.10	14.29	11.78	2.68	1.39	95.25
amph2_c2	40.57	3.85	12.48	9.24	0.14	14.14	11.81	2.62	1.40	96.26
amph2_c4	40.26	3.76	12.07	9.28	0.06	14.27	11.60	2.61	1.38	95.29
amph3_c1	39.57	4.00	12.59	9.29	0.11	14.04	11.81	2.59	1.31	95.31
amph3_c2	39.80	3.91	12.64	9.36	0.10	13.99	11.78	2.65	1.32	95.55
amph3_c3	39.79	3.87	12.66	9.31	0.10	13.98	11.77	2.57	1.34	95.39
amph3_c4	39.91	3.94	12.34	9.46	0.09	14.10	11.66	2.64	1.32	95.45
amph4_c1	39.77	3.82	12.25	9.48	0.10	14.09	12.05	2.66	1.40	95.64
amph4_c2	39.92	3.72	11.94	9.55	0.11	14.01	12.23	2.54	1.36	95.38
amph4_c3	39.62	3.99	12.13	10.21	0.07	13.74	11.95	2.65	1.37	95.73
amph4_c4	40.39	3.84	11.79	9.43	0.09	14.34	11.99	2.56	1.41	95.84
amph4_c5	39.86	3.63	11.68	9.56	0.08	14.33	12.11	2.55	1.42	95.23
amph5_c1	39.64	3.13	12.24	11.57	0.17	12.72	11.78	2.79	1.31	95.34
amph5_c2	40.18	3.23	12.65	11.89	0.20	12.61	11.69	2.68	1.33	96.47
amph5_c3	39.57	3.67	12.06	11.09	0.10	13.03	11.55	2.70	1.16	94.95
amph5_c4	39.73	3.47	12.15	11.42	0.14	12.66	11.93	2.81	1.29	95.58
amph5_c5	39.81	3.52	12.34	10.54	0.12	13.56	11.77	2.73	1.29	95.68
Average	**39.88**	**3.66**	**12.31**	**10.24**	**0.11**	**13.63**	**11.84**	**2.64**	**1.33**	**95.65**
Corrected[a]	*40.44*	*3.69*	*13.82*	*10.77*	*0.11*	*14.23*	*11.91*	*2.50*	*1.28*	*98.74*
SD	0.28	0.24	0.29	0.96	0.03	0.60	0.16	0.07	0.06	
SEM	0.06	0.05	0.06	0.21	0.01	0.13	0.03	0.02	0.01	
2-7-08 rims										
amph1_r1	39.16	3.22	12.65	12.55	0.18	12.03	11.80	2.61	1.33	95.52
amph1_r2	38.95	3.22	12.62	12.56	0.12	12.48	11.74	2.78	1.27	95.74
amph1_r3	38.90	3.63	12.63	12.00	0.13	12.30	11.67	2.78	1.22	95.26
amph1_r4	39.04	3.25	12.52	12.22	0.17	12.29	11.80	2.65	1.27	95.19
amph2_r1	40.56	3.55	11.66	9.28	0.09	14.62	12.00	2.67	1.23	95.67
amph2_r2	39.96	3.47	12.23	10.92	0.11	12.95	11.73	2.84	1.27	95.49
amph2_r3	39.82	3.49	12.35	10.84	0.16	13.18	11.74	2.65	1.31	95.55

Table E.3 continued.

Spot	SiO_2	TiO_2	Al_2O_3	FeO	MnO	MgO	CaO	Na_2O	K_2O	Total
amph2_r4	39.99	3.45	12.58	11.46	0.15	12.85	11.49	2.81	1.25	96.04
amph2_r5	39.70	3.45	12.32	11.14	0.08	13.23	11.75	2.64	1.32	95.62
amph2_r6	39.66	3.34	12.23	10.91	0.11	13.31	11.77	2.74	1.28	95.36
amph2_r7	40.06	3.63	11.98	10.67	0.11	13.18	11.71	2.85	1.27	95.46
amph3_r1	40.27	3.71	12.27	9.37	0.10	14.13	11.75	2.61	1.42	95.64
amph3_r2	40.63	3.51	12.21	9.34	0.06	14.30	11.80	2.59	1.36	95.81
amph3_r3	40.43	3.66	12.04	9.30	0.11	14.35	11.77	2.50	1.37	95.52
amph3_r4	40.69	3.48	12.23	9.33	0.09	14.10	11.75	2.63	1.36	95.66
amph3_r5	40.48	3.84	12.26	9.35	0.11	14.42	11.68	2.66	1.38	96.18
amph3_r6	40.58	3.68	12.06	9.22	0.06	14.27	11.68	2.63	1.37	95.55
amph3_r7	40.55	3.87	12.35	9.25	0.09	14.05	11.76	2.73	1.31	95.95
amph4_r1	39.64	3.74	12.19	11.37	0.13	12.64	11.96	2.63	1.40	95.69
amph4_r2	39.58	3.60	12.23	11.53	0.14	12.88	11.95	2.68	1.36	95.95
amph4_r3	39.93	3.44	12.15	11.33	0.14	12.74	12.00	2.56	1.36	95.65
amph4_r4	39.34	3.55	12.24	11.13	0.14	12.63	12.02	2.57	1.36	94.99
amph4_r5	39.46	3.51	12.24	11.01	0.16	13.03	11.95	2.54	1.37	95.28
amph4_r6	39.63	3.52	12.11	10.86	0.15	12.92	12.01	2.59	1.42	95.22
amph4_r7	40.07	3.73	12.27	10.95	0.15	13.00	12.01	2.57	1.38	96.12
amph5_r1	40.59	3.74	12.02	9.62	0.12	14.08	11.71	2.70	1.36	95.92
amph5_r4	39.89	3.67	12.35	10.98	0.13	13.28	11.75	2.62	1.27	95.94
amph5_r5	39.52	3.50	11.88	11.38	0.18	12.73	11.72	2.62	1.30	94.83
amph5_r6	38.99	3.28	12.67	13.15	0.20	12.26	11.68	2.84	1.24	96.32
amph5_r7	39.01	3.07	12.85	12.57	0.19	12.43	11.62	2.73	1.28	95.75
Average	**39.84**	**3.53**	**12.28**	**10.85**	**0.13**	**13.22**	**11.79**	**2.67**	**1.32**	**95.63**
Corrected[a]	*40.39*	*3.56*	*13.78*	*11.38*	*0.12*	*13.82*	*11.86*	*2.53*	*1.27*	*98.71*
SD	0.56	0.19	0.25	1.15	0.04	0.75	0.13	0.09	0.06	
SEM	0.10	0.04	0.05	0.25	0.01	0.16	0.03	0.02	0.01	
7-4-15 cores										
amph1_c1	42.39	3.21	11.23	10.15	0.11	14.39	11.45	2.58	0.86	96.37
amph1_c2	41.11	3.31	11.87	10.48	0.12	13.79	11.61	2.64	0.86	95.80
amph1_c3	42.09	3.21	11.71	10.23	0.12	14.36	11.46	2.83	0.84	96.85
amph1_c4	41.40	3.27	12.44	10.46	0.12	13.73	11.61	2.95	0.86	96.84
amph1_c5	41.37	3.37	12.11	10.44	0.12	14.06	11.63	2.73	0.88	96.70
amph1_c6	41.06	3.31	12.23	10.45	0.12	13.79	11.60	2.68	0.91	96.13
amph2_c1	41.53	3.27	11.97	10.30	0.11	14.12	11.40	2.84	0.85	96.37
amph2_c2	41.69	3.31	12.04	10.30	0.11	14.34	11.52	2.72	0.91	96.95
amph2_c3	42.46	3.24	11.27	9.83	0.10	14.34	11.46	2.75	0.85	96.29
amph2_c4	42.05	3.28	11.70	10.00	0.10	14.30	11.48	2.92	0.87	96.70
amph2_c5	41.60	3.26	11.85	10.46	0.11	14.05	11.45	2.91	0.88	96.58
amph3_c1	41.34	3.29	12.14	10.46	0.11	13.88	11.62	2.79	0.87	96.51
amph3_c2	41.17	3.29	12.03	10.51	0.12	14.00	11.63	2.73	0.87	96.37
amph3_c3	41.32	3.24	11.92	10.47	0.12	14.15	11.41	2.87	0.87	96.38
amph3_c4	40.75	3.34	12.32	10.50	0.12	13.87	11.52	2.88	0.87	96.17
amph3_c5	40.86	3.28	12.23	10.80	0.14	13.64	11.64	2.85	0.91	96.35
amph4_c1	42.37	3.02	11.91	10.22	0.12	14.35	11.24	2.64	0.85	96.73
amph4_c2	41.41	3.11	11.88	10.57	0.14	13.99	11.24	2.89	0.87	96.09
amph4_c3	41.78	2.86	12.10	10.19	0.12	14.26	11.17	2.85	0.84	96.18
amph4_c4	41.04	3.16	12.64	10.78	0.14	13.91	11.39	2.81	0.89	96.76
amph4_c5	41.67	3.11	11.73	10.02	0.13	14.52	11.15	2.90	0.81	96.03
amph4_c6	40.39	3.28	12.05	10.36	0.12	13.91	11.33	2.94	0.88	95.27
amph5_c1	41.00	3.19	12.13	10.11	0.11	14.35	11.46	2.69	0.88	95.93

Table E.3 continued.

Spot	SiO_2	TiO_2	Al_2O_3	FeO	MnO	MgO	CaO	Na_2O	K_2O	Total
amph5_c2	41.23	3.19	12.20	10.08	0.12	14.32	11.39	2.63	0.90	96.06
amph5_c3	40.90	3.32	11.96	9.66	0.11	14.31	11.58	2.65	0.89	95.38
amph5_c4	41.47	3.22	12.09	9.98	0.12	14.31	11.45	2.82	0.88	96.33
amph5_c6	40.77	3.09	12.18	10.35	0.12	14.26	11.43	2.69	0.91	95.80
amph6_c1	40.86	2.76	12.00	9.92	0.11	14.09	11.46	2.60	0.88	94.68
amph6_c2	40.92	2.83	12.31	10.00	0.13	14.27	11.41	2.66	0.88	95.40
amph6_c3	40.92	2.78	11.98	10.25	0.13	13.96	11.54	2.79	0.89	95.24
amph6_c4	41.78	2.80	12.00	9.85	0.11	14.40	11.46	2.66	0.88	95.94
amph6_c5	41.86	2.81	11.95	9.87	0.10	14.43	11.52	2.56	0.87	95.97
Average	**41.39**	**3.16**	**12.01**	**10.25**	**0.12**	**14.14**	**11.46**	**2.76**	**0.87**	**96.16**
Corrected[a]	*41.94*	*3.19*	*13.51*	*10.78*	*0.11*	*14.74*	*11.53*	*2.63*	*0.82*	*99.24*
SD	0.51	0.18	0.28	0.27	0.01	0.23	0.13	0.11	0.02	
SEM	0.10	0.04	0.06	0.06	0.00	0.05	0.03	0.02	0.00	
7-5-15 cores										
amph1_c1	40.15	4.00	11.78	11.02	0.14	13.17	11.34	2.58	1.03	95.21
amph1_c2	41.24	4.00	11.81	10.87	0.14	13.27	11.08	2.56	1.06	96.04
amph1_c3	40.71	3.83	11.81	10.86	0.16	13.28	11.22	2.52	1.08	95.47
amph1_c4	40.19	4.21	11.74	11.06	0.12	13.18	10.99	2.50	1.05	95.04
amph1_c5	40.31	4.12	11.99	11.27	0.13	12.98	11.17	2.60	1.05	95.61
amph1_c6	40.55	3.85	11.67	11.15	0.13	13.46	11.18	2.71	1.08	95.78
amph2_c1	41.59	3.82	12.10	10.81	0.13	13.48	11.33	2.58	1.08	96.91
amph2_c2	40.29	3.87	12.27	11.10	0.12	13.18	11.25	2.55	1.07	95.71
amph2_c3	41.12	3.73	11.77	11.37	0.15	13.51	11.35	2.70	1.08	96.79
amph2_c4	40.93	3.25	11.48	11.47	0.17	13.42	11.21	2.79	1.01	95.73
amph2_c5	40.76	3.74	11.76	11.05	0.11	13.35	11.30	2.59	1.09	95.75
amph2_c6	40.42	3.83	11.79	11.18	0.12	13.51	11.32	2.67	1.07	95.90
amph3_c1	40.47	4.23	12.12	10.27	0.12	13.61	11.43	2.78	1.07	96.10
amph3_c2	39.76	4.06	12.31	10.50	0.11	13.18	11.33	2.68	1.04	94.97
amph3_c3	40.27	4.09	12.10	10.45	0.11	13.47	11.31	2.64	1.12	95.57
amph3_c4	40.73	3.96	12.00	10.48	0.10	13.34	11.38	2.69	1.08	95.76
amph4_c1	40.59	4.27	11.35	11.35	0.15	13.48	11.08	2.62	1.01	95.89
amph4_c2	40.11	4.10	11.36	11.11	0.16	13.30	11.12	2.66	1.03	94.96
amph4_c3	40.04	4.14	11.35	11.19	0.14	13.29	11.05	2.68	1.01	94.89
amph5_c1	38.73	3.98	11.54	11.70	0.12	12.33	11.19	2.67	1.07	93.32
amph5_c2	38.98	4.12	11.64	11.76	0.12	12.35	11.19	2.50	1.08	93.74
amph5_c3	39.92	3.83	11.84	11.70	0.14	12.64	10.99	2.66	1.05	94.77
amph5_c4	40.16	4.12	11.92	11.82	0.13	12.56	11.24	2.61	1.06	95.62
amph5_c5	38.92	3.73	11.95	11.99	0.14	12.55	11.01	2.53	1.01	93.82
Average	**40.29**	**3.95**	**11.81**	**11.15**	**0.13**	**13.16**	**11.21**	**2.63**	**1.06**	**95.39**
Corrected[a]	*40.84*	*3.98*	*13.32*	*11.67*	*0.13*	*13.76*	*11.28*	*2.49*	*1.00*	*98.47*
SD	0.68	0.22	0.27	0.45	0.02	0.38	0.13	0.08	0.03	
SEM	0.13	0.05	0.06	0.10	0.00	0.08	0.03	0.02	0.01	
8-3-15 cores										
amph1_c1	39.74	3.62	12.26	11.40	0.24	13.38	11.72	2.80	1.18	96.35
amph1_c2	39.95	3.55	12.25	11.42	0.14	13.28	11.68	2.76	1.12	96.16
amph2_c1	40.37	3.75	12.00	9.90	0.11	14.04	11.75	2.66	1.13	95.72
amph2_c2	39.79	3.77	12.53	10.33	0.09	13.82	11.80	2.63	1.19	95.96
amph3_c1	39.66	3.56	11.92	11.77	0.16	13.21	11.75	2.70	1.26	95.98
amph3_c2	40.42	3.71	12.18	11.15	0.15	13.73	11.80	2.70	1.18	97.01
Average	**39.99**	**3.66**	**12.19**	**10.99**	**0.15**	**13.58**	**11.75**	**2.71**	**1.18**	**96.20**
Corrected[a]	*40.54*	*3.69*	*13.70*	*11.52*	*0.14*	*14.18*	*11.82*	*2.57*	*1.12*	*99.28*

Table E.3 continued.

Spot	SiO_2	TiO_2	Al_2O_3	FeO	MnO	MgO	CaO	Na_2O	K_2O	Total
SD	0.30	0.09	0.20	0.66	0.05	0.30	0.04	0.06	0.05	
SEM	0.12	0.04	0.08	0.27	0.02	0.12	0.02	0.02	0.02	
8-3-15 rims										
amph1_r1	39.72	3.65	12.06	9.93	0.10	13.85	11.68	2.69	1.27	94.95
amph1_r2	39.98	3.70	12.13	10.06	0.12	13.86	11.69	2.77	1.28	95.58
amph1_r3	40.21	3.57	12.16	10.44	0.11	13.94	11.69	2.61	1.21	95.95
amph1_r4	40.22	3.67	12.26	9.73	0.10	14.15	11.85	2.51	1.24	95.72
amph1_r5	40.02	3.11	12.54	11.79	0.16	12.86	11.56	2.66	1.26	95.97
amph1_r6	39.57	3.00	12.15	12.11	0.17	12.52	11.47	2.77	1.27	95.04
amph2_r1	39.55	3.37	12.64	11.63	0.14	12.88	11.62	2.77	1.19	95.79
amph2_r2	39.70	3.55	12.92	11.34	0.14	12.85	11.56	2.87	1.18	96.11
amph2_r3	39.94	3.62	12.29	10.94	0.14	13.05	11.72	2.91	1.23	95.85
amph2_r4	40.31	2.28	11.61	14.28	0.33	11.51	11.12	2.88	1.54	95.86
amph2_r5	39.76	3.61	12.46	10.94	0.16	13.29	11.67	2.67	1.32	95.88
amph2_r6	39.63	3.55	12.71	10.69	0.12	13.34	11.64	2.71	1.30	95.69
amph2_r7	40.05	3.67	12.38	10.26	0.11	13.62	11.71	2.92	1.23	95.96
amph3_r1	40.70	3.69	11.64	9.67	0.11	14.98	11.89	2.66	1.13	96.47
amph3_r2	40.30	3.99	11.45	9.78	0.09	14.49	11.95	2.66	1.05	95.77
amph3_r3	40.18	3.84	11.70	10.21	0.12	13.67	11.77	2.75	1.17	95.41
amph3_r4	40.94	3.60	11.63	9.43	0.13	14.01	11.47	2.69	1.47	95.36
amph3_r5	40.63	3.76	11.53	9.76	0.09	14.64	12.07	2.60	1.11	96.18
amph3_r6	40.43	3.74	11.38	9.86	0.08	14.65	12.09	2.64	1.10	95.96
Average	**40.10**	**3.52**	**12.09**	**10.68**	**0.13**	**13.59**	**11.70**	**2.72**	**1.24**	**95.76**
Corrected[a]	*40.65*	*3.56*	*13.59*	*11.20*	*0.13*	*14.18*	*11.77*	*2.58*	*1.18*	*98.85*
SD	0.39	0.37	0.45	1.14	0.05	0.83	0.22	0.11	0.12	
SEM	0.09	0.08	0.10	0.26	0.01	0.19	0.05	0.03	0.03	
9-1-15 cores										
amph1_c1	39.89	3.54	12.09	11.32	0.14	13.60	11.40	2.67	1.15	95.80
amph1_c2	39.97	3.71	12.04	11.01	0.13	13.73	11.61	2.88	1.15	96.22
amph1_c3	40.20	3.63	12.01	10.93	0.14	13.60	11.44	2.86	1.19	95.99
amph2_c1	39.96	3.74	12.47	10.22	0.09	13.87	11.73	2.86	1.20	96.13
amph2_c2	39.92	3.78	12.31	10.06	0.12	14.07	11.57	2.94	1.18	95.94
amph2_c3	39.19	3.92	12.89	11.87	0.13	12.79	11.60	2.81	1.17	96.36
amph2_c3	40.18	3.67	12.36	10.38	0.12	14.06	11.57	2.82	1.20	96.36
amph2_c4	40.26	3.73	12.25	10.46	0.15	14.11	11.63	2.76	1.18	96.53
amph3_c1	40.35	3.73	11.97	10.32	0.13	13.92	11.58	2.87	1.22	96.08
amph3_c2	40.22	3.67	12.05	10.07	0.11	14.04	11.60	2.72	1.20	95.67
amph3_c3	40.53	3.51	11.83	10.72	0.14	14.25	11.55	2.84	1.20	96.57
amph3_c4	40.54	3.41	12.01	10.56	0.12	14.14	11.56	2.81	1.18	96.32
Average	**40.10**	**3.67**	**12.19**	**10.66**	**0.13**	**13.85**	**11.57**	**2.82**	**1.18**	**96.16**
Corrected[a]	*40.65*	*3.70*	*13.69*	*11.18*	*0.12*	*14.45*	*11.64*	*2.68*	*1.13*	*99.25*
SD	0.35	0.13	0.28	0.52	0.02	0.38	0.08	0.07	0.02	
SEM	0.10	0.03	0.06	0.12	0.00	0.09	0.02	0.02	0.00	
9-2-15 cores										
amph1_c1	40.37	3.91	12.18	9.37	0.09	14.20	11.86	2.71	0.99	95.68
amph1_c2	39.54	3.85	12.87	11.92	0.11	12.70	11.72	2.64	1.03	96.37
amph1_c3	40.31	3.81	12.41	10.35	0.11	13.80	11.80	2.70	1.01	96.29
amph1_c4	39.21	3.95	12.97	11.82	0.12	12.60	11.57	2.81	1.01	96.06
amph1_c5	40.46	3.92	12.10	9.60	0.08	14.38	11.86	2.79	1.01	96.20
amph1_c6	40.19	3.83	12.23	10.35	0.09	13.66	11.66	2.60	0.94	95.54
amph2_c1	40.80	3.28	11.81	10.70	0.12	13.78	11.47	2.72	0.99	95.68

Table E.3 continued.

Spot	SiO_2	TiO_2	Al_2O_3	FeO	MnO	MgO	CaO	Na_2O	K_2O	Total
amph2_c2	39.59	3.55	12.09	10.78	0.12	13.42	11.54	2.76	0.99	94.84
amph2_c3	40.80	3.43	12.18	10.86	0.12	13.45	11.75	2.69	0.99	96.28
amph2_c4	40.10	3.64	12.34	10.74	0.11	13.62	11.61	2.77	1.01	95.94
amph2_c5	47.54	1.54	6.31	7.77	0.14	13.18	21.44	0.72	0.01	98.65
amph2_c6	40.23	3.65	11.88	10.65	0.12	13.80	11.49	2.93	0.91	95.67
amph3_c1	40.55	3.63	12.27	10.74	0.10	13.73	11.61	2.82	0.98	96.44
amph3_c2	40.06	3.62	12.31	10.62	0.11	13.53	11.62	2.75	1.01	95.63
amph3_c3	40.35	3.61	12.31	10.59	0.11	13.66	11.73	2.66	1.01	96.04
amph3_c4	40.30	3.93	12.46	10.71	0.10	13.63	11.64	2.65	1.03	96.45
amph3_c5	40.43	3.96	12.61	10.24	0.10	13.68	11.66	2.71	0.98	96.38
amph3_c6	40.05	3.72	12.32	11.19	0.14	13.11	11.71	2.63	1.01	95.88
amph4_c1	40.65	3.53	12.06	10.71	0.11	13.59	11.67	2.75	0.95	96.01
amph4_c2	41.33	3.53	12.11	10.39	0.11	13.98	11.64	2.74	0.97	96.80
amph4_c3	40.36	3.90	12.26	10.17	0.11	13.90	11.74	2.75	0.96	96.16
amph4_c4	39.80	3.87	12.17	10.18	0.09	13.66	11.76	2.64	1.02	95.18
amph4_c5	39.66	3.16	12.64	12.29	0.16	12.39	11.64	2.72	0.94	95.61
amph4_c6	40.36	3.75	11.89	10.43	0.12	13.79	11.56	2.82	0.98	95.69
amph5_c1	40.03	3.82	12.63	10.31	0.10	13.84	11.31	2.71	0.98	95.73
amph5_c2	39.86	3.61	12.71	10.46	0.11	13.69	11.52	2.70	0.99	95.66
amph5_c3	39.92	3.79	12.49	10.28	0.11	13.93	11.52	2.73	0.98	95.75
amph5_r1	40.01	3.84	12.62	10.21	0.10	13.90	11.66	2.79	0.98	96.12
amph5_r3	39.95	3.75	12.75	10.71	0.11	13.38	11.58	2.57	0.99	95.79
amph5_r2	40.50	3.77	12.71	10.47	0.10	13.64	11.66	2.65	0.99	96.49
amph5_r4	40.05	3.56	12.84	11.51	0.12	12.86	11.51	2.78	0.98	96.21
amph5_c4	40.87	3.84	12.69	10.39	0.12	13.99	11.29	2.80	0.97	96.96
amph5_c5	40.90	3.82	12.66	10.33	0.11	13.77	11.43	2.80	0.94	96.77
amph5_c6	40.29	3.81	12.48	10.34	0.11	13.79	11.34	2.60	0.98	95.76
Average	**40.45**	**3.65**	**12.22**	**10.53**	**0.11**	**13.59**	**11.90**	**2.67**	**0.96**	**96.08**
Corrected[a]	*41.01*	*3.68*	*13.72*	*11.06*	*0.11*	*14.19*	*11.97*	*2.53*	*0.90*	*99.16*
SD	1.30	0.41	1.07	0.75	0.02	0.43	1.67	0.35	0.17	
SEM	0.22	0.07	0.18	0.13	0.00	0.07	0.29	0.06	0.03	
11-3-15 cores										
amph1_c1	39.89	2.99	12.70	10.50	0.08	13.89	11.71	2.61	1.40	95.78
amph1_c3	39.75	3.08	12.72	10.43	0.13	14.03	11.58	2.61	1.39	95.72
amph2_c1	40.98	3.69	11.48	11.30	0.17	13.49	10.88	2.76	1.49	96.24
amph2_c2	40.97	3.80	11.50	11.60	0.13	13.53	11.00	2.77	1.54	96.85
amph3_c1	39.30	4.00	12.07	9.76	0.06	13.95	11.70	2.73	1.29	94.87
amph3_c2	39.44	3.81	12.46	9.93	0.08	14.05	11.69	2.70	1.26	95.43
amph4_c2	39.26	3.65	12.16	11.78	0.14	13.05	11.69	2.69	1.17	95.59
Average	**39.94**	**3.58**	**12.16**	**10.76**	**0.11**	**13.71**	**11.46**	**2.70**	**1.36**	**95.78**
Corrected[a]	*40.50*	*3.61*	*13.66*	*11.28*	*0.11*	*14.31*	*11.53*	*2.56*	*1.31*	*98.86*
SD	0.69	0.36	0.48	0.75	0.04	0.35	0.34	0.06	0.12	
SEM	0.26	0.14	0.18	0.28	0.01	0.13	0.13	0.02	0.05	
11-3-15 rims										
amph2_r1	40.12	4.03	11.84	11.81	0.16	12.86	10.97	2.62	1.60	96.01
amph2_r2	40.44	3.96	11.93	11.27	0.13	13.20	10.98	2.55	1.57	96.02
amph2_r3	40.57	3.66	11.62	11.27	0.18	13.37	10.79	2.70	1.55	95.70
amph2_r4	40.27	3.86	12.01	12.13	0.17	12.59	10.82	2.60	1.67	96.13
amph2_r5	40.44	3.70	11.97	12.49	0.17	12.70	10.92	2.58	1.62	96.58
amph2_r6	40.16	3.62	12.07	12.49	0.19	12.57	10.86	2.58	1.60	96.15
amph3_r1	39.21	3.59	12.76	14.89	0.16	11.27	11.49	2.73	1.21	97.30

Table E.3 continued.

Spot	SiO_2	TiO_2	Al_2O_3	FeO	MnO	MgO	CaO	Na_2O	K_2O	Total
amph3_r2	40.04	3.76	11.99	9.82	0.10	14.27	11.68	2.63	1.26	95.55
amph3_r3	40.25	3.74	11.92	9.93	0.10	14.29	11.66	2.76	1.25	95.90
amph4_r1	40.14	3.60	11.95	11.12	0.12	13.51	11.57	2.67	1.18	95.87
amph4_r2	40.83	3.59	11.76	10.84	0.13	13.74	11.78	2.61	1.20	96.48
amph4_r3	40.26	3.54	11.38	10.60	0.11	13.85	11.70	2.78	1.24	95.46
amph4_r4	39.14	3.82	12.10	10.81	0.12	13.30	11.78	2.71	1.27	95.06
amph4_r5	38.97	3.83	12.15	10.82	0.11	13.42	11.70	2.68	1.23	94.91
amph4_r6	39.62	3.69	12.54	11.79	0.14	12.81	11.63	2.71	1.15	96.07
Average	**40.03**	**3.73**	**12.00**	**11.47**	**0.14**	**13.18**	**11.35**	**2.66**	**1.37**	**95.95**
Corrected[a]	*40.58*	*3.76*	*13.50*	*12.00*	*0.13*	*13.78*	*11.42*	*2.52*	*1.32*	*99.03*
SD	0.53	0.14	0.32	1.21	0.03	0.74	0.39	0.07	0.19	
SEM	0.14	0.04	0.08	0.31	0.01	0.19	0.10	0.02	0.05	

a- Average composition corrected to the Kakanui Hornblende composition

Table E.4 Major element composition of spot analyses in clinopyroxene phenocrysts with averages used in Chapter 6. Only those spot analyses with totals between 99 and 101 wt% were accepted.

Spot	SiO_2	TiO_2	Al_2O_3	FeO	MnO	MgO	CaO	Na_2O	Cr_2O_3	Total
2-5-08 cores										
cpx1_c1	50.16	0.33	4.91	8.42	0.28	12.88	20.99	1.05	0.17	99.19
cpx1_c2	50.81	0.26	4.40	8.20	0.25	13.29	21.17	1.04	0.15	99.58
cpx1_c3	51.10	0.28	3.87	8.05	0.26	13.51	21.59	0.93	0.18	99.76
cpx2_c2	48.89	1.14	5.55	6.31	0.12	13.84	22.97	0.55	0.04	99.42
cpx2_c3	50.66	0.84	4.08	5.95	0.13	14.67	22.88	0.57	0.14	99.92
cpx2_c4	50.38	0.84	3.93	5.88	0.11	14.77	22.70	0.58	0.11	99.30
cpx3_c1	53.29	0.23	1.04	7.40	0.54	14.13	22.87	0.64	0.00	100.15
cpx3_c2	52.72	0.37	1.31	8.37	0.62	13.72	22.13	0.90	0.01	100.16
cpx3_c3	53.10	0.33	1.33	8.24	0.58	13.52	22.57	0.90	0.01	100.59
cpx3_c4	53.29	0.37	1.35	8.27	0.56	13.70	22.26	0.91	0.00	100.71
Average	**51.23**	**0.51**	**3.38**	**7.51**	**0.32**	**13.81**	**22.21**	**0.80**	**0.09**	**99.87**
SD	1.47	0.30	1.64	1.00	0.20	0.56	0.69	0.19	0.07	
SEM	0.47	0.10	0.52	0.32	0.06	0.18	0.22	0.06	0.02	
2-5-08 rims										
cpx1_r1	46.75	1.75	6.97	7.86	0.14	12.75	22.33	0.53	0.02	99.09
cpx1_r2	47.70	1.55	5.91	7.61	0.15	13.33	22.15	0.45	0.02	98.87
cpx1_r3	47.12	1.62	6.22	7.65	0.13	13.19	22.30	0.50	0.01	98.75
cpx2_r1	49.45	1.01	4.98	6.51	0.11	14.19	22.07	0.63	0.04	98.99
cpx2_r2	48.79	1.27	5.80	6.20	0.08	13.86	22.59	0.60	0.12	99.31
cpx2_r3	49.60	1.17	5.35	6.09	0.10	14.03	22.55	0.59	0.07	99.56
cpx2_r4	49.26	1.18	5.45	6.16	0.10	13.95	22.61	0.64	0.09	99.45
cpx2_r5	49.99	1.14	5.22	6.07	0.11	14.13	22.55	0.62	0.08	99.91
cpx3_r1	51.42	0.61	3.13	8.21	0.23	13.68	22.16	0.71	0.01	100.15
cpx3_r2	51.39	0.66	3.04	8.01	0.24	13.74	22.19	0.69	0.02	99.98
cpx3_r3	48.50	0.98	4.88	9.79	0.28	11.91	21.87	0.88	0.01	99.09
cpx3_r5	52.96	0.29	1.36	8.22	0.65	13.43	22.68	0.91	0.00	100.49
cpx3_r6	49.56	0.98	4.60	8.55	0.21	12.77	22.04	0.79	0.03	99.53
cpx4_r3	47.86	1.34	7.64	7.04	0.13	14.01	20.23	0.91	0.06	99.21
Average	**49.31**	**1.11**	**5.04**	**7.43**	**0.19**	**13.50**	**22.16**	**0.67**	**0.04**	**99.46**
SD	1.68	0.39	1.58	1.08	0.14	0.63	0.59	0.14	0.04	
SEM	0.45	0.10	0.42	0.29	0.04	0.17	0.16	0.04	0.01	
2-6-08 cores										
cpx1_c1	50.61	0.96	4.86	6.62	0.15	14.69	21.68	0.62	0.09	100.28
cpx1_c2	50.80	0.90	4.73	6.53	0.14	14.74	21.54	0.65	0.14	100.19
cpx3_c3	49.65	0.88	4.65	6.30	0.14	14.58	21.58	0.63	0.61	99.01
Average	**49.89**	**0.93**	**4.95**	**6.59**	**0.15**	**14.56**	**21.41**	**0.66**	**0.33**	**99.46**
SD	0.64	0.08	0.36	0.18	0.01	0.21	0.21	0.03	0.18	
SEM	0.21	0.03	0.12	0.06	0.00	0.07	0.07	0.01	0.06	
2-6-08 rims										
cpx1_r1	51.99	0.69	3.61	6.83	0.18	15.39	20.94	0.58	0.19	100.41

Table E.4 continued.

Spot	SiO_2	TiO_2	Al_2O_3	FeO	MnO	MgO	CaO	Na_2O	Cr_2O_3	Total
cpx1_r2	52.03	0.70	3.60	6.94	0.19	15.33	20.81	0.60	0.19	100.40
cpx1_r3	52.41	0.68	3.49	6.75	0.16	15.35	21.14	0.57	0.19	100.74
cpx1_r4	51.91	0.59	3.39	6.84	0.15	15.49	20.96	0.59	0.17	100.09
cpx1_r5	49.48	1.09	5.35	7.30	0.17	13.92	21.19	0.70	0.27	99.47
cpx1_r6	49.23	1.08	5.44	7.21	0.15	14.06	21.12	0.64	0.25	99.18
cpx2_r1	49.72	0.94	5.16	7.27	0.17	14.15	21.02	0.70	0.17	99.30
cpx3_r2	48.14	1.33	5.48	8.25	0.21	13.26	21.77	0.57	0.03	99.04
cpx3_r3	52.15	0.64	3.23	6.86	0.20	15.54	20.82	0.57	0.18	100.19
cpx3_r4	52.17	0.57	3.28	6.59	0.17	15.44	21.14	0.61	0.25	100.22
cpx3_r5	51.90	0.65	3.25	6.62	0.18	15.50	20.96	0.56	0.24	99.87
cpx3_r6	51.55	0.60	3.26	6.46	0.17	15.37	21.16	0.59	0.30	99.46
Average	**51.06**	**0.80**	**4.05**	**6.99**	**0.18**	**14.90**	**21.09**	**0.61**	**0.20**	**99.86**
SD	1.41	0.24	0.94	0.46	0.02	0.77	0.24	0.05	0.07	
SEM	0.41	0.07	0.27	0.13	0.01	0.22	0.07	0.01	0.02	
8-3-15 cores										
cpx1_c1	51.30	0.60	3.63	6.39	0.14	15.35	21.16	0.61	0.17	99.35
cpx1_c2	50.65	0.70	4.33	6.58	0.14	14.99	21.05	0.67	0.20	99.33
cpx2_c1	49.26	1.17	5.19	7.13	0.13	14.04	21.85	0.58	0.14	99.49
cpx2_c2	50.11	0.99	4.28	6.57	0.12	14.44	22.06	0.53	0.14	99.24
cpx3_c1	51.49	0.54	3.43	6.11	0.12	15.49	21.30	0.63	0.27	99.39
cpx3_c2	49.87	0.76	5.20	6.33	0.12	14.56	21.20	0.76	0.47	99.28
cpx4_c1	50.68	0.76	4.32	6.11	0.13	14.93	21.63	0.63	0.12	99.31
cpx4_c2	50.89	0.74	4.32	6.26	0.12	14.92	21.39	0.67	0.07	99.38
Average	**50.53**	**0.78**	**4.34**	**6.44**	**0.13**	**14.84**	**21.45**	**0.64**	**0.20**	**99.35**
SD	0.70	0.19	0.59	0.31	0.01	0.45	0.34	0.07	0.12	
SEM	0.25	0.07	0.21	0.11	0.00	0.16	0.12	0.02	0.04	
8-3-15 rims										
cpx1_r1	47.84	1.63	5.79	8.14	0.16	13.62	21.56	0.51	0.08	99.35
cpx1_r2	47.46	1.70	6.07	8.38	0.16	13.25	21.47	0.54	0.05	99.10
cpx1_r3	47.25	1.72	6.23	8.49	0.17	13.18	21.57	0.53	0.05	99.21
cpx1_r5	48.56	1.40	5.17	7.71	0.16	13.99	21.59	0.48	0.13	99.20
cpx1_r6	49.58	0.97	4.51	7.37	0.16	14.48	21.58	0.45	0.14	99.26
cpx3_r5	49.73	0.93	4.62	6.39	0.13	14.76	21.65	0.53	0.27	99.02
cpx4_r1	49.11	1.24	5.21	7.51	0.16	13.90	21.26	0.51	0.23	99.15
cpx4_r2	49.63	1.08	4.96	6.77	0.14	14.32	21.35	0.54	0.32	99.11
cpx4_r3	49.88	0.99	4.74	6.64	0.13	14.51	21.31	0.58	0.32	99.11
cpx4_r4	48.14	1.51	6.27	7.97	0.15	13.53	20.78	0.59	0.06	99.02
cpx4_r6	48.44	1.43	6.01	8.05	0.17	13.44	20.80	0.63	0.07	99.05
cpx4_r7	50.37	0.82	4.67	6.38	0.12	14.66	21.50	0.61	0.27	99.40
cpx4_r8	49.97	0.82	4.99	6.57	0.14	14.46	21.43	0.67	0.20	99.26
Average	**48.92**	**1.25**	**5.33**	**7.41**	**0.15**	**14.01**	**21.37**	**0.55**	**0.17**	**99.17**
SD	0.99	0.32	0.63	0.75	0.02	0.54	0.27	0.06	0.10	

Table E.4 continued.

Spot	SiO_2	TiO_2	Al_2O_3	FeO	MnO	MgO	CaO	Na_2O	Cr_2O_3	Total
SEM	0.28	0.09	0.17	0.21	0.00	0.15	0.08	0.02	0.03	
9-1-15 cores										
cpx1_c1	52.49	0.29	1.97	8.07	0.32	16.68	18.80	0.44	0.08	99.13
cpx2_c1	50.86	0.71	3.58	7.04	0.17	15.19	20.98	0.52	0.11	99.15
cpx3_c2	51.13	0.65	3.28	6.86	0.17	15.61	20.77	0.50	0.12	99.09
cpx4_c2	48.80	1.17	5.27	7.02	0.12	14.07	21.75	0.60	0.30	99.08
Average	**50.82**	**0.70**	**3.52**	**7.25**	**0.20**	**15.38**	**20.57**	**0.51**	**0.15**	**99.11**
SD	1.32	0.32	1.17	0.48	0.07	0.93	1.09	0.05	0.09	
SEM	0.66	0.16	0.59	0.24	0.04	0.47	0.54	0.03	0.04	
9-1-15 rims										
cpx1_r1	48.92	1.21	5.53	7.46	0.16	13.86	21.25	0.58	0.18	99.15
cpx1_r2	48.61	1.26	5.49	7.61	0.17	13.87	21.38	0.56	0.14	99.11
cpx1_r5	51.53	0.65	3.14	6.93	0.18	15.52	20.93	0.47	0.11	99.47
cpx1_r6	51.53	0.79	2.60	7.26	0.24	15.22	21.64	0.40	0.00	99.68
cpx2_r3	49.57	0.97	4.85	6.88	0.15	14.36	21.56	0.57	0.30	99.23
cpx2_r6	49.17	1.01	5.03	7.06	0.15	14.33	21.43	0.58	0.23	99.00
cpx2_r6	49.34	0.99	5.03	7.02	0.16	14.30	21.41	0.57	0.24	99.07
cpx4_r2	48.74	1.15	5.42	7.60	0.17	13.95	21.21	0.60	0.15	98.99
cpx5_r1	49.93	0.88	4.55	6.96	0.15	14.59	21.41	0.55	0.16	99.19
cpx5_r6	49.58	0.99	4.87	7.05	0.15	14.19	21.58	0.57	0.18	99.16
Average	**49.69**	**0.99**	**4.65**	**7.18**	**0.17**	**14.42**	**21.38**	**0.54**	**0.17**	**99.20**
SD	0.43	0.10	0.31	0.26	0.01	0.23	0.13	0.02	0.04	
SEM	0.22	0.05	0.16	0.13	0.00	0.11	0.06	0.01	0.02	
9-2-15 cores										
cpx2_c1	52.68	0.34	1.57	7.91	0.55	13.46	22.51	0.99	0.00	100.02
cpx2_c2	52.46	0.39	1.63	8.10	0.51	13.26	22.53	0.96	-0.01	99.84
cpx3_c1	50.96	0.83	3.57	6.88	0.14	15.47	20.90	0.48	0.16	99.40
cpx3_c2	51.13	0.77	3.39	7.10	0.15	15.23	21.23	0.50	0.05	99.53
cpx4_c1	49.86	1.03	4.79	6.58	0.11	14.63	21.15	0.59	0.45	99.18
cpx4_c2	49.04	1.18	5.55	7.08	0.13	13.90	21.47	0.62	0.30	99.28
Average	**51.02**	**0.76**	**3.42**	**7.27**	**0.27**	**14.32**	**21.63**	**0.69**	**0.16**	**99.54**
SD	1.30	0.31	1.47	0.54	0.19	0.84	0.65	0.21	0.17	
SEM	0.53	0.13	0.60	0.22	0.08	0.34	0.27	0.09	0.07	
9-2-15 rims										
cpx1_r1	48.32	1.98	5.19	7.64	0.20	13.96	21.75	0.92	0.00	100.02
cpx1_r2	46.96	2.13	5.77	8.64	0.19	13.06	21.74	0.66	0.00	99.18
cpx1_r4	47.64	1.93	5.22	8.36	0.19	13.43	21.83	0.63	0.00	99.25
cpx2_r1	50.90	0.95	3.14	7.05	0.17	14.90	22.20	0.37	0.00	99.68
cpx2_r2	50.50	1.04	3.29	7.23	0.15	14.58	22.18	0.36	0.00	99.34
cpx2_r3	49.29	1.13	4.85	7.67	0.15	13.78	21.78	0.56	0.03	99.25
cpx2_r4	49.04	1.17	5.03	7.63	0.15	13.71	21.70	0.58	0.03	99.04
cpx2_r5	49.49	1.02	4.79	7.81	0.16	13.75	21.63	0.59	0.03	99.26
cpx3_r1	48.44	1.67	4.62	7.92	0.15	13.92	21.95	0.38	0.00	99.05

Table E.4 continued.

Spot	SiO_2	TiO_2	Al_2O_3	FeO	MnO	MgO	CaO	Na_2O	Cr_2O_3	Total
cpx3_r4	49.15	1.49	4.07	7.13	0.16	14.28	22.33	0.50	0.00	99.13
cpx3_r5	47.76	1.75	5.32	8.10	0.15	13.36	22.18	0.43	0.00	99.03
cpx3_r6	47.57	1.85	5.81	7.78	0.15	13.22	22.24	0.55	0.00	99.20
cpx4_r1	49.00	1.40	5.24	7.58	0.12	13.66	21.91	0.51	0.05	99.49
cpx4_r4	48.30	1.48	5.45	7.92	0.14	13.25	22.15	0.48	0.01	99.19
Average	**48.74**	**1.50**	**4.84**	**7.75**	**0.16**	**13.78**	**21.97**	**0.54**	**0.01**	**99.29**
SD	1.07	0.38	0.79	0.43	0.02	0.51	0.23	0.14	0.02	
SEM	0.29	0.10	0.21	0.11	0.01	0.14	0.06	0.04	0.00	
11-3-15 cores										
cpx1_c1	50.53	0.77	4.40	6.56	0.14	14.90	20.66	0.95	0.23	99.16
cpx1_c2	51.48	0.66	3.50	6.81	0.15	15.65	20.13	0.84	0.20	99.42
cpx1_c3	51.22	0.62	3.72	6.78	0.15	15.74	19.86	0.88	0.20	99.18
cpx1_c4	51.20	0.72	3.63	6.65	0.14	15.48	20.71	0.78	0.14	99.47
cpx1_i2	49.15	1.08	6.30	7.04	0.13	13.81	21.06	1.08	0.34	100.04
cpx2_c1	52.00	1.07	2.38	7.74	0.16	14.98	20.87	0.75	0.02	100.01
cpx2_c2	50.72	1.12	3.42	7.54	0.15	14.66	21.17	0.73	0.05	99.63
cpx3_c1	51.93	0.63	3.92	6.70	0.15	15.46	20.20	1.01	0.22	100.25
cpx3_c2	51.43	0.62	3.71	6.73	0.15	15.68	19.94	0.94	0.25	99.48
cpx3_i1	49.34	1.02	6.31	7.06	0.14	13.87	20.28	1.29	0.27	99.60
Opx + cpx1_i1	49.75	1.03	5.97	7.61	0.16	14.03	20.27	1.28	0.09	100.18
Opx + cpx1_i2	49.69	1.05	5.60	7.16	0.14	14.16	20.52	1.17	0.17	99.67
cpx4_c1	50.89	1.03	4.11	6.55	0.11	14.84	21.96	0.65	0.12	100.29
cpx4_c2	49.77	1.10	5.06	6.96	0.14	14.50	21.23	0.92	0.11	99.82
cpx5_c1	51.38	0.72	4.43	6.99	0.14	14.95	20.13	1.13	0.16	100.03
cpx5_c2	50.76	0.93	5.08	6.78	0.12	14.46	21.15	1.01	0.18	100.52
Average	**50.70**	**0.88**	**4.47**	**6.98**	**0.14**	**14.82**	**20.63**	**0.96**	**0.17**	**99.77**
SD	0.88	0.19	1.11	0.36	0.01	0.63	0.56	0.19	0.08	
SEM	0.22	0.05	0.28	0.09	0.00	0.16	0.14	0.05	0.02	
11-3-15 rims										
cpx1_r1	50.39	1.18	3.28	7.03	0.15	14.70	22.32	0.38	0.00	99.46
cpx1_r3	47.48	1.72	5.69	7.84	0.11	13.00	22.68	0.55	0.01	99.10
cpx1_r4	48.07	1.63	5.70	7.74	0.12	13.13	22.49	0.54	0.02	99.45
cpx1_r5	48.12	1.44	5.34	7.50	0.11	13.52	22.34	0.59	0.04	99.03
cpx2_r2	47.06	1.78	5.96	8.07	0.11	13.19	22.21	0.61	0.03	99.07
cpx2_r4	51.43	0.89	3.24	7.33	0.16	14.89	21.37	0.73	0.03	100.14
cpx2_r5	50.69	1.01	3.51	7.31	0.14	14.51	21.49	0.72	0.03	99.46
cpx3_r1	48.01	1.77	5.49	7.45	0.11	13.32	22.65	0.58	0.05	99.45
cpx3_r3	48.60	1.63	5.20	7.37	0.12	13.55	22.58	0.56	0.08	99.69
cpx3_r4	48.05	1.64	5.23	7.36	0.12	13.60	22.50	0.56	0.06	99.14
cpx3_r5	48.91	1.24	5.71	7.09	0.13	14.06	21.40	0.95	0.17	99.69
cpx3_r7	48.96	1.58	4.27	8.21	0.15	14.04	22.23	0.44	0.01	99.93
Opx + cpx1_r1	49.45	1.22	4.02	6.82	0.12	14.30	22.50	0.51	0.11	99.06

Table E.4 continued.

Spot	SiO_2	TiO_2	Al_2O_3	FeO	MnO	MgO	CaO	Na_2O	Cr_2O_3	Total
Opx + cpx1_r2	48.13	1.59	5.12	7.25	0.13	13.59	22.59	0.54	0.08	99.05
Opx + cpx1_r3	47.89	1.81	5.42	7.75	0.14	13.49	22.63	0.66	0.00	99.81
Opx + cpx1_r4	49.21	1.25	4.73	7.05	0.13	14.02	21.92	0.68	0.08	99.08
Opx + cpx1_r5	49.34	1.32	4.34	6.98	0.12	14.11	22.74	0.59	0.21	99.76
Opx + cpx1_r6	49.65	1.30	4.17	7.46	0.15	14.25	21.98	0.56	0.03	99.56
Opx + cpx1_r7	50.40	1.13	3.77	6.81	0.13	14.60	22.61	0.51	0.14	100.12
cpx4_r1	46.23	2.38	6.19	8.32	0.16	12.70	22.27	0.81	0.00	99.08
cpx4_r6	47.70	1.96	5.76	7.94	0.12	13.22	22.19	0.60	0.01	99.54
cpx4_r7	48.43	1.59	5.08	7.30	0.12	13.57	22.35	0.54	0.08	99.07
cpx5_r1	49.09	1.31	5.08	7.37	0.13	13.79	21.95	0.72	0.07	99.53
cpx5_r2	50.80	0.97	3.76	6.81	0.15	14.83	21.62	0.60	0.05	99.59
cpx5_r3	49.59	1.10	5.73	6.89	0.12	14.07	21.15	1.07	0.23	99.98
cpx5_r4	49.89	1.37	4.68	6.94	0.12	14.01	22.55	0.61	0.18	100.38
cpx5_r5	49.67	1.17	5.35	6.88	0.13	14.01	21.24	0.92	0.19	99.58
cpx5_r6	50.52	1.21	4.67	6.82	0.13	14.41	22.22	0.67	0.15	100.83
cpx5_r7	50.62	1.01	4.10	6.65	0.13	14.87	21.56	0.73	0.11	99.80
Average	**49.05**	**1.42**	**4.85**	**7.32**	**0.13**	**13.91**	**22.15**	**0.64**	**0.08**	**99.55**
SD	1.24	0.33	0.83	0.45	0.02	0.58	0.48	0.15	0.07	
SEM	0.23	0.06	0.15	0.08	0.00	0.11	0.09	0.03	0.01	